Andrea Kroner

VCSEL-Based Optical Trapping Systems for Microfluidic Applications

Cuvillier Verlag Göttingen
Internationaler wissenschaftlicher Fachverlag

ulm university universität
uulm

VCSEL-Based Optical Trapping Systems for Microfluidic Applications

DISSERTATION

to obtain the academic degree of

DOKTOR-INGENIEUR

(DR.-ING.)

from the Faculty of Engineering Science and Computer Sciences
Ulm University

by

Andrea Kroner

from Ulm

Referees:	PD Dr.-Ing. Rainer Michalzik
	Prof. Dr.-Ing. Hans-Jörg Pfleiderer
Dean of the faculty:	Prof. Dr.-Ing. Michael Weber

Ulm, 26.11.2010

Bibliografische Information der Deutschen Nationalbibliothek
Die Deutsche Nationalbibliothek verzeichnet diese Publikation in der Deutschen Nationalbibliografie; detaillierte bibliografische Daten sind im Internet über http://dnb.d-nb.de abrufbar.

1. Aufl. - Göttingen: Cuvillier, 2011
Zugl.: Ulm, Univ., Diss., 2010

978-3-86955-627-7

Nonnenstieg 8, 37075 Göttingen
Telefon: 0551-54724-0
Telefax: 0551-54724-21
www.cuvillier.de

1. Auflage, 2011
Gedruckt auf säurefreiem Papier

978-3-86955-627-7

VCSEL-Based Optical Trapping Systems for Microfluidic Applications

Abstract

Optical trapping and manipulation by laser beams offers the unique possibility to handle single micrometer-sized particles such as living cells without any mechanical contact, damage or contamination. A second hot topic in biology is microfluidics, where the examination of biological samples in channel structures with widths below 100 µm reduces the used sample volume significantly. While the combination of both techniques results in attractive lab-on-a-chip structures for particle sorting and analysis, the commonly bulky trapping setup is contradictory to the miniaturized concept. Here, the use of vertical-cavity surface-emitting lasers (VCSELs) as light sources in optical trapping systems allows a strong reduction of the setup complexity owing to the small dimensions, low cost and high beam quality of these devices.

This thesis gives a detailed study on optical manipulation systems based on vertically emitting laser diodes. A standard optical tweezers setup as well as a novel, miniaturized system, the so-called integrated optical trap are investigated. The latter aims for particle separation and sorting in microfluidics resulting in low-cost, portable modules.

A classical optical tweezers system based on a high numerical aperture objective in combination with a VCSEL light source is investigated. Standard multi-mode as well as single-mode surface relief VCSELs are used as laser source. With both kinds of VCSELs, optical trapping of polystyrene particles of sizes ranging from 4 to 15 µm is demonstrated with some milliwatts of optical power at the sample stage. A maximum trapping force of 4.4 pN for 15 µm particles is achieved with the multi-mode laser, proving the suitability of multi-mode lasers for optical manipulation despite their inferior beam profile.

By using two-dimensional VCSEL arrays instead of solitary lasers, the system is extended to a multiple optical tweezers setup in a straightforward manner. To avoid any additional optics, densely packed VCSEL arrangements with a device spacing of less than 25 µm are used, where a novel fabrication process allows the seamless integration of the inverted surface relief technique for enhanced beam quality. By electrical switching between individual devices of the array, non-mechanical particle translation with velocities of up to 12 µm/s is achieved. With a tilted linear VCSEL array, an optical lattice is generated in the optical tweezers setup, and continuous deflection of particles is realized.

By substituting the sample stage in the optical tweezers setup with a microfluidic chip fabricated from polydimethylsiloxane (PDMS), particle redirection at a channel junction is realized using a solitary VCSEL source as well as a tilted linear VCSEL array. For the latter,

the particles are deflected when passing the optical lattice, thus, the position of the lasers is fixed and no moving parts are necessary, which further reduces the setup complexity.

To achieve a drastic miniaturization of the trapping setup, namely the integrated optical trap, the laser source is placed directly underneath the sample chamber. A weakly focused laser beam is generated in the particle solution by integrating an additional microlens on the VCSEL output facet. To determine appropriate lens geometries, the beam propagation inside the integrated trap structure is calculated and the thermal reflow process for lens fabrication is studied in detail concerning lens diameter, reflow temperature and substrate material. By combining the microlens with the inverted relief technique, the quality of the focused beam is strongly improved with respect to divergence, transverse beam profile and beam diameter, where a minimum of 7 µm is measured at the focal point. With first solitary integrated optical traps, deflection, levitation and transverse trapping of 10 µm polystyrene particles is demonstrated for optical powers of 5 mW.

In a next step, integrated optical trap arrays are realized based on closely spaced two-dimensional arrangements of lensed relief VCSELs. To transfer the continuous deflection scheme demonstrated in the classical tweezers setup to the integrated trap, linear arrays of parallel working VCSELs are investigated. To support the design of the multiple integrated trap structure, a simulation of the optical deflection process is performed. Here, a dependence on the geometric and material properties of the particles is predicted, so applications in microfluidic particle sorting are intended. Compact and portable modules are obtained by integrating the laser chip with the microfluidic chip using flip-chip bonding. Although the finished modules show strong heating of the VCSEL chip resulting in a significant reduction of the device performance, simultaneous trapping as well as continuous particle deflection was successfully demonstrated with a total optical power of just 5 mW.

The results presented in this work demonstrate the potential of VCSELs as laser sources for optical trapping and microparticle manipulation. In conventional optical tweezers setups, the use of VCSELs reduces the setup complexity significantly, while first prototypes of ultra-compact integrated optical traps based on VCSELs confirm the feasibility of portable and inexpensive microfluidic sorting systems.

Contents

1 Introduction

During the past century, fundamental physical, chemical and biological studies have been advanced, subdivided and improved, leading to countless specializations. Many of these resulted in successful and productive innovations. Many more esteem from combinations and cross-linking of these separate disciplines, profiting from present knowledge and synergy effects. A prominent example is the laser. Its use beyond classical optical applications, like interferometry or spectroscopy, has led to numerous innovations in various scientific fields. Laser cutting and welding are nowadays established techniques in materials processing, laser printers enable fast reproduction of documents and the laser scalpel is a valuable tool in dermatology.

This thesis wants to adapt this idea by combining three basic components: optical manipulation, microfluidics and vertical-cavity surface-emitting lasers (VCSELs). The oldest of these disciplines is optical manipulation, which was for the first time successfully demonstrated and understood in 1970. It deals with handling and trapping of micrometer-sized transparent particles by radiation force, where the invention of the laser ten years before offered the necessary strong intensity gradient. Even three-dimensional trapping of particles can be achieved, thus the term optical tweezers is commonly used. Shortly after the first demonstration optical manipulation was used on biological material. The direct handling of single cells or DNA bound to microbeads [1] opened up new research possibilities, like cell immobilization during spectral studies [2] or the detailed examination of molecular motor movement [3]. A major advantage of optical tweezers in biophotonics is the avoidance of contamination or mechanical damage. Since biological material shows only minor absorption for wavelengths in the near-infrared spectral region, the risk of thermal damage can be minimized as well [4].

The second component is microfluidics, which is a hot topic in biology for a few years. The examination of biological samples in channel structures with widths below 100 µm reduces the used sample volume and enables parallel cycles [5, 6]. Various ongoing work deals with the combination of different analysis steps like mixing, reaction and detection on one chip, often referred to as lab-on-a-chip or micro total analysis system (µTAS). An important requirement is the handling and manipulation of particles in these channels for fixing, selection and sorting purposes. Besides electrical and hydrodynamic approaches, combinations of microfluidics and optical manipulation were successfully demonstrated [7, 8]. While the contactless and biocompatible properties are favorable, the commonly extensive optical setup is contradictory to the miniaturized concept.

A fundamental step is to reduce the size of the laser source itself, since the commonly used Nd:YAG lasers are quite bulky. Therefore, the use of VCSELs as laser sources gained increasing interest [9, 10, 11]. The first working VCSEL was presented in 1979 and its further optimization was aiming for applications in short distance optical data transmission, where

they are nowadays the established laser source [12]. VCSELs have small dimensions, are inexpensive and their symmetric structure leads to a circular, high-quality output beam. Furthermore, their surface emission allows the comparatively easy fabrication of arbitrary-shaped VCSEL arrangements.

These properties make VCSELs an attractive laser source for optical manipulation. Using two-dimensional arrays of VCSELs, even multiple optical tweezers can be generated without extensive beam steering or holographic techniques. The resulting cost reduction along with the small dimensions support the application in microfluidics. Besides the straightforward approach of introducing a VCSEL array as laser source in a classical optical tweezers setup, a drastically miniaturized setup is imaginable. Here, a direct integration of VCSEL source and microfluidic channel would result in a portable, low-cost device for particle manipulation and sorting. Using different laser sources, a comparable module is hardly realizable.

Within the scope of this thesis, this novel approach called the integrated optical trap is implemented and examined for the first time. Furthermore, a classical optical tweezers setup is realized, where specially adapted, densely packed VCSEL arrays serve as laser source. The thesis is structured as follows: the following chapter covers the basic working principle of optical manipulation, where a calculation of the acting trapping forces based on a ray-optical model is presented. Furthermore, an overview of the historical background as well as state of the art trapping systems is given, with the main focus being set on applications in biophotonics. In Chap. 3 properties of the VCSEL laser source are discussed, including the standard top-emitting device structure as well as surface modifications for improved single-mode emission and beam quality. Present work on optical particle manipulation with VCSELs as well as future potentials are presented. The second part of Chap. 3 covers the fabrication of VCSELs by means of semiconductor microtechnology. Here, a novel fabrication process for densely packed VCSEL arrays is introduced, which enables self-alignment of the crucial elements of the laser. Chapter 4 deals with microfluidic systems concerning their physical properties as well as state of the art applications, in particular systems which combine microfluidics with optical manipulation. Furthermore, the used soft lithography process to fabricate microfluidic channels is explained, as well as the use of hydrostatic pressure to control the particle flow inside the channels.

In the second half of the thesis, layout and fabrication of the realized experimental setups and modules are described and the performed experiments are presented. Chapter 5 contains the work on the classical optical tweezers setup. Besides solitary VCSELs, densely packed arrays are used as laser sources, so multiple optical tweezers are generated. Here, non-mechanical movement of polystyrene particles as well as continuous deflection at a tilted optical lattice are investigated. Furthermore, application in microfluidics is demonstrated. In Chap. 6 realization of the integrated trap based on a solitary VCSEL source is described. A key component of the structure is a photoresist microlens on top of the laser output facet, which is fabricated by thermal reflow. Development and analysis of this process is preceded by a simulation of the beam propagation of lensed top-emitting VCSELs. Output characteristics and beam propagation of the fabricated devices are intensively studied, where multi-mode as well as surface relief single-mode VCSELs are used as laser source. Both types of lasers are applied for first particle manipulation experiments. The advancement of these structures is described in Chap. 7, where a stable connection

between laser chip and microfluidic chip is achieved by flip-chip bonding. Furthermore, the solitary laser source is substituted with densely packed linear arrays of VCSELs, since compact modules for continuous particle deflection and sorting are intended. The layout of the devices is based on simulations of the particle deflection process. The finished modules are characterized concerning their electrical and optical properties and first experiments on particle manipulation are performed.

2 Optical Particle Manipulation and Trapping

Optical manipulation describes the exertion of force on matter by light. As early as four centuries ago this kind of light-matter interaction was observed by Johannes Kepler. He noticed that tails of comets always point away from the sun, which he attributes to a sort of radiation pressure [4]. However, it was not until the invention of the laser that this effect could be demonstrated in laboratories as well. In experiments, mesoscopic particles were not only moved and guided by light, but also fixed in space over a long period, hence the terms optical trap or optical tweezers are often used.

Since its first demonstration optical manipulation has gained increasing interest in various scientific fields. In atom physics laser trapping enabled atom cooling and the generation of Bose-Einstein condensates [13]. Furthermore, sophisticated optical tweezers systems can be used for force measurements on particles with sub-piconewton resolution [14]. In the field of biophotonics, the direct handling of single cells or DNA bound to microbeads [1] opened up new research opportunities like cell immobilization during spectral studies [2].

2.1 Theory of Optical Manipulation

2.1.1 Basic Working Principle

To estimate the maximum force that can be exerted on matter by radiation pressure, a ray of light hitting a totally reflecting mirror is assumed. When reflected straight back, the change in momentum of a single photon of this ray is

$$\Delta p_{\mathrm{ph}} = 2\frac{\hbar\omega}{c} = 2\frac{E_{\mathrm{ph}}}{c}, \tag{2.1}$$

where c is the vacuum velocity of light, $\hbar$ is the reduced Planck constant, ω is the angular frequency and $E_{\mathrm{ph}} = \hbar\omega$ is the photon energy. Since the total momentum must be conserved, momentum is transferred from the photon to the mirror. Thus, the mirror experiences a total force of

$$F = N\frac{\Delta p_{\mathrm{ph}}}{\Delta t} = \frac{2}{c}\frac{NE_{\mathrm{ph}}}{\Delta t} = \frac{2}{c}P_{\mathrm{r}}, \tag{2.2}$$

with N being the number of photons hitting the mirror during the time period Δt and P_{r} being the optical power of the incident ray. For an optical power of 1 mW, this force is around 10 pN. Although this is too small to affect a macroscopic mirror, it could be enough to accelerate microscopic particles whose weight is in the same order of magnitude.

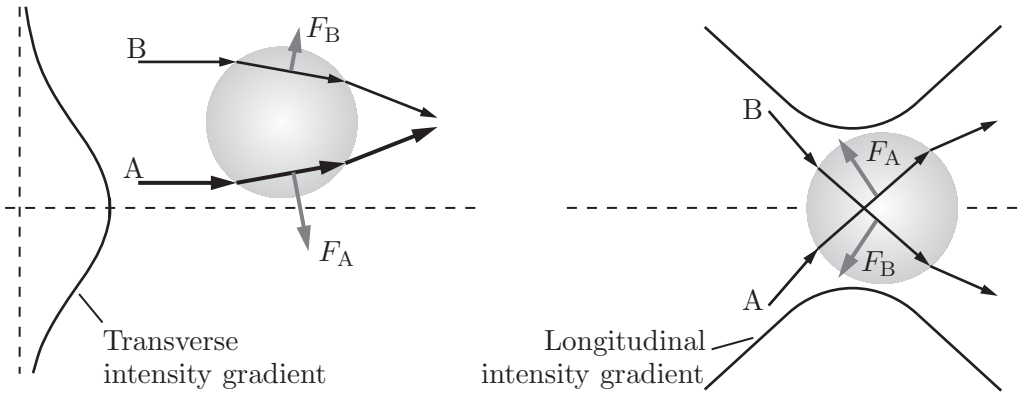

Fig. 2.1: Working principle of a two-dimensional optical trap (left). The refraction of a parallel laser beam with a transverse intensity gradient at a spherical, transparent particle leads to the forces F_A and F_B. Since ray A is stronger than ray B, the net force points toward the intensity maximum. With a tightly focused laser beam (right) even three-dimensional trapping can be realized.

Based on this estimation, Arthur Ashkin performed an experiment on particle manipulation at Bell Laboratories, New Jersey in 1970 [15]. In former experiments, radiation forces were obscured by thermal forces, which arise due to temperature gradients in the illuminated particle and the surrounding medium [16]. Therefore, Ashkin used transparent, micrometer-sized latex spheres suspended in transparent water, so heating by absorption could be avoided. With a mildly focused laser beam of some milliwatts of optical power, particle motion in propagation direction with velocities of some µm/s was observed [13]. However, an additional force was found, which pulled particles from the fringe of the beam toward the center of the beam. Once there, they stayed stable on beam axis, while pushed forward by radiation pressure. The left hand side of Fig. 2.1 illustrates the occurrence of this unexpected force with a ray-optical model. Refraction of a ray at a particle surface is accompanied by a change in momentum of the corresponding photons as well. Thus, conservation of momentum demands a momentum transfer to the particle. For a parallel laser beam with a transverse intensity gradient, as shown in Fig. 2.1 (left), the rays A and B lead to the forces F_A and F_B on the particle. Caused by the offset between beam axis and particle center, ray A has higher power than ray B, so F_A is larger than F_B. Therefore, the particle experiences a net force toward the intensity maximum, where it remains fixed in transverse direction. A two-dimensional or transverse optical trap is thus established. Since the net force in transverse direction arises from the intensity gradient, it is often termed gradient force, while the forward directed force, mainly caused by reflection at the particle surface, is commonly named scattering force.

For a focused laser beam, as shown on the right side of Fig. 2.1, also a longitudinal gradient force arises. If the beam is tightly focused and the corresponding intensity gradient is high, this force can overcome the scattering force. In this case, a three-dimensional optical trap, also called optical tweezers, is generated by a single laser beam. Here, the particle stays fixed near the focal point. Optical tweezers were demonstrated for the first time by Arthur Ashkin in 1986 [17], where different kinds of transparent particles with diameters of

10 µm down to 25 nm were stably trapped with optical power ranging from some milliwatts up to 1.4 W. In later experiments, trapping of biological matter like Escherichia coli (E. coli) bacteria and yeast cells was demonstrated, where even a reproduction of living cells during trapping could be observed [18]. It is important to note, that for stable trapping the gradient force must not only exceed the scattering force, but also any thermal motion of the particle [4, 17].

The way to describe trapping forces in more detail depends on the size of the trapped particle relative to the size of the incident wavelength. In the **Rayleigh regime**, where particles whose diameter a is much smaller than the wavelength λ are considered, a dielectric particle can be treated as a point dipole. The dipole moment of the particle, which is induced by the electrical field, scales with the polarizability α_p of the dielectric material. In a spatially inhomogeneous electromagnetic field, a Lorentz force is exerted on the dipole, in order to minimize its energy in the intensity field [4, 19]. The gradient force acting on a spherical particle is given by [20]

$$\boldsymbol{F}_\mathrm{g} = \frac{2\pi}{\bar{n}_\mathrm{m}^2 c}\,\alpha_\mathrm{p}\,\nabla\mathcal{I} = \frac{\pi a^3}{4\,c}\left(\frac{m^2-1}{m^2+2}\right)\nabla\mathcal{I}, \tag{2.3}$$

where m is the ratio of the refractive index of the particle $\bar{n}_\mathrm{p}$ to the index of the surrounding medium $\bar{n}_\mathrm{m}$, and $\mathcal{I}$ is the light intensity field. The gradient force is proportional to the polarizability of the particle and the strength of the intensity gradient. It is oriented along the gradient for $m > 1$ and reverse for $m < 1$, that is, particles with a lower refractive index than the surrounding medium are repelled by the beam. Additionally, Rayleigh scattering gives rise to a scattering force oriented along the propagation direction of the incident light. Without loss of generality, this is assumed to be in z-direction, so [20]

$$\boldsymbol{F}_\mathrm{s} = \frac{\bar{n}_\mathrm{m}\mathcal{I}}{c}\frac{\pi^5 a^6}{3\,\lambda^4}\left(\frac{m^2-1}{m^2+2}\right)^2 \boldsymbol{e}_z. \tag{2.4}$$

The scattering force scales with the light intensity and increases for increasing contrast in refractive index $m = \bar{n}_\mathrm{p}/\bar{n}_\mathrm{m}$.

In the **Lorentz-Mie regime**, where the dimensions of particles are comparable to the wavelength of the trapping laser, the above given point-dipole approximation is no longer valid. Instead, a full electromagnetic theory is required, which gives consideration to diffraction issues and includes a description of light propagation and polarization at the focal point [4]. Although optical trapping and tweezing is most often used to handle particles in the Lorentz-Mie regime and experiments show no significant qualitative difference to behavior of Rayleigh particles, optical manipulation in the Lorentz-Mie regime is difficult to model.

A closed description of trapping forces can again be found for particles with dimensions much larger than the laser emission wavelength, the so-called **Mie regime** [4, 20]. Here, a ray-optical model can be used, as already done qualitatively in Fig. 2.1. For an accurate quantitative description of trapping forces it is however necessary to consider the Fresnel equations for reflection and refraction as well as multiple reflections inside the particle. Since most of the particles examined in the scope in this thesis have diameters in the range of about ten times the laser wavelength, this regime is discussed in more detail in the following section.

2.1.2 Description of Light Forces in a Ray-Optical Model

In the simple estimation of the radiation force on a totally reflecting mirror in Sect. 2.1.1, the considered ray was assumed to be reflected straight back. However, this is certainly not true for a ray hitting a spherical, transparent particle, due to the curved surface and the partly transmitted power. Therefore, only a certain fraction Q_s of the incident power of the ray P_r contributes to the forward scattering force [21]

$$F_\mathrm{sr} = \frac{\bar{n}_\mathrm{m} P_\mathrm{r}}{c} Q_\mathrm{s}, \tag{2.5}$$

where $\bar{n}_\mathrm{m}$ is the refractive index of the surrounding medium. Same holds true for the transverse gradient force

$$F_\mathrm{gr} = \frac{\bar{n}_\mathrm{m} P_\mathrm{r}}{c} Q_\mathrm{g}. \tag{2.6}$$

To calculate the scaling factors Q_s and Q_g, Fig. 2.2 has to be considered. A single ray hits the particle surface under an angle θ_i and splits into the reflected ray of power $P_\mathrm{r}\mathcal{R}$ and an infinite number of emergent refracted rays of decreasing powers $P_\mathrm{r}\mathcal{T}^2$, $P_\mathrm{r}\mathcal{T}^2\mathcal{R}$, $P_\mathrm{r}\mathcal{T}^2\mathcal{R}^2$, ... The quantities $\mathcal{R}$ and $\mathcal{T}$ are the Fresnel coefficient for reflection and transmission at the interface under the angle θ_i, respectively. By summing up the contributions to momentum transfer in forward and transverse direction in an infinite series, Q_s and Q_g can be determined as [22]

$$Q_\mathrm{s} = 1 + \mathcal{R}\cos(2\theta_\mathrm{i}) - \frac{\mathcal{T}^2\left[\cos(2\theta_\mathrm{i} - 2\theta_\mathrm{t}) + \mathcal{R}\cos(2\theta_\mathrm{i})\right]}{1 + \mathcal{R}^2 + 2\mathcal{R}\cos(2\theta_\mathrm{t})}, \tag{2.7}$$

and

$$Q_\mathrm{g} = -\mathcal{R}\sin(2\theta_\mathrm{i}) + \frac{\mathcal{T}^2\left[\sin(2\theta_\mathrm{i} - 2\theta_\mathrm{t}) + \mathcal{R}\sin(2\theta_\mathrm{i})\right]}{1 + \mathcal{R}^2 + 2\mathcal{R}\cos(2\theta_\mathrm{t})}, \tag{2.8}$$

where θ_t is the angle of refraction. More details on the derivation and the following calculation of the trapping force can be found in App. D.

Figure 2.3 shows the magnitude of both scaling factors depending on the position of incidence of the ray on the particle, which can be described by the radial component r and the angular component φ. A large radial component thus corresponds to a large angle of

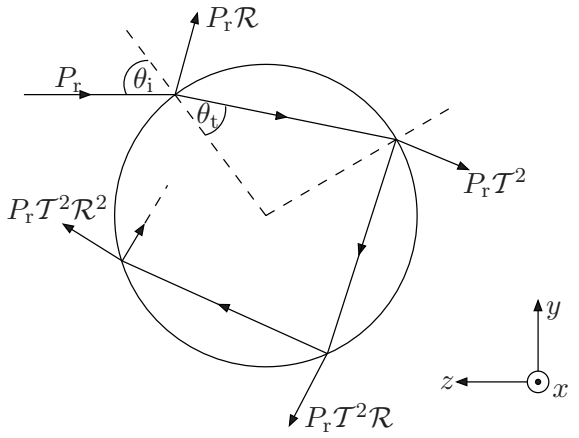

Fig. 2.2: Momentum transfer of a single ray of power P_r to a spherical particle: the ray hits the sphere under an angle θ_i and splits into one reflected ray and an infinite number of refracted rays.

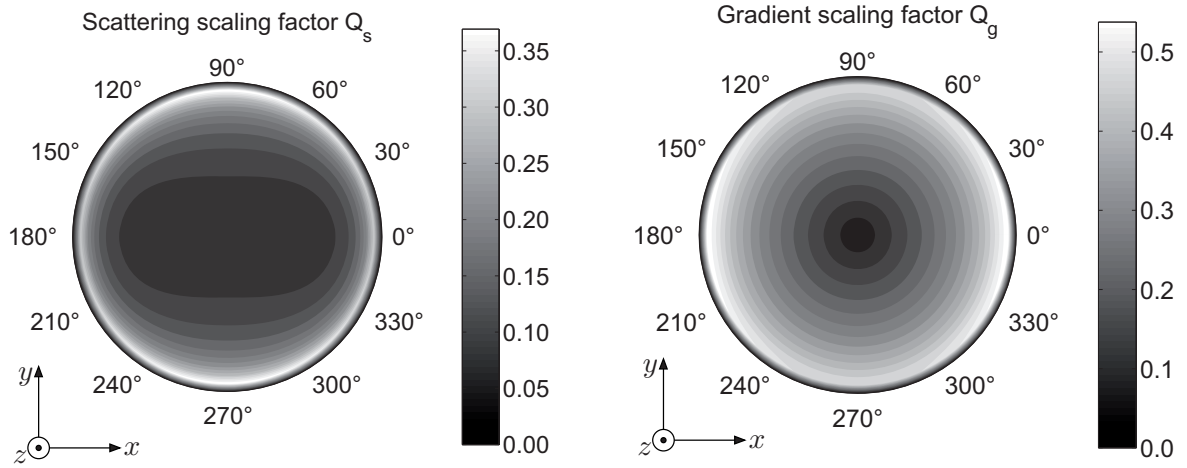

Fig. 2.3: Magnitude of the scaling factors for scattering (Q_s, left) and gradient force (Q_g, right) depending on the position of incidence of the ray on the particle.

incidence θ_i. The calculation is done for a polystyrene sphere ($\bar{n}_\mathrm{p} \approx 1.6$) in water ($\bar{n}_\mathrm{m} = 1.33$). The angular asymmetry arises from the dependence of the Fresnel coefficients on the polarization of the light, which is assumed to be linear and oriented in x-direction. Both scaling factors show high values close to the fringe of the particle. For the scattering component, this is due to the strong increase of the Fresnel reflection coefficient for large angles of incidence. The increase of the gradient component is caused by the strong deflection of the beam when refracted, corresponding to a high transfer of momentum. Accordingly, the gradient scaling factor decreases to zero for rays hitting the center of the particle, since the transmitted portion of the beam is not deflected. However, the reflected portion contributes completely to the scattering force, since the ray is reflected straight back. Thus, Q_s is slightly larger than zero at the particle center (not visible in the figure).

For the further calculation of the trapping force it is assumed that the particle is illuminated by a parallel laser beam with a transverse Gaussian power density distribution S. The beam axis is shifted by an offset of length s to the particle center. Figure 2.4 shows a schematic side-view of the arrangement (left) as well as a projection of the power density distribution on the particle surface. The example is given for a sphere of $a = 6\,\mu\mathrm{m}$ diameter, a total optical power of $P = 5\,\mathrm{mW}$, a beam diameter of $2w_0 = 5\,\mu\mathrm{m}$ and an offset of $1\,\mu\mathrm{m}$ at $45\,^\circ$. Based on the determined scaling factors $Q_\mathrm{s}(r,\varphi)$ and $Q_\mathrm{g}(r,\varphi)$ and the given power density distribution $S(r,\varphi)$, the scattering and gradient force per area can be calculated according to (2.5) and (2.6) as

$$F_\mathrm{sa} = \frac{\bar{n}_\mathrm{m} S}{c} Q_\mathrm{s} \quad \text{and} \quad F_\mathrm{ga} = \frac{\bar{n}_\mathrm{m} S}{c} Q_\mathrm{g}. \tag{2.9}$$

The results are shown in Fig. 2.5 as a projection on the particle surface. The scattering force is especially strong at the upper right fringe of the sphere, thus, not only a forward movement of the particle is to be expected, but also a rotation. While the scattering force shows a clear contribution at the particle center, the gradient force decreases to zero and shows a donut like behavior. For better understanding, the direction of the gradient force is given by arrows in the graph. The force contributions in $135\,^\circ$ and $315\,^\circ$ direction are

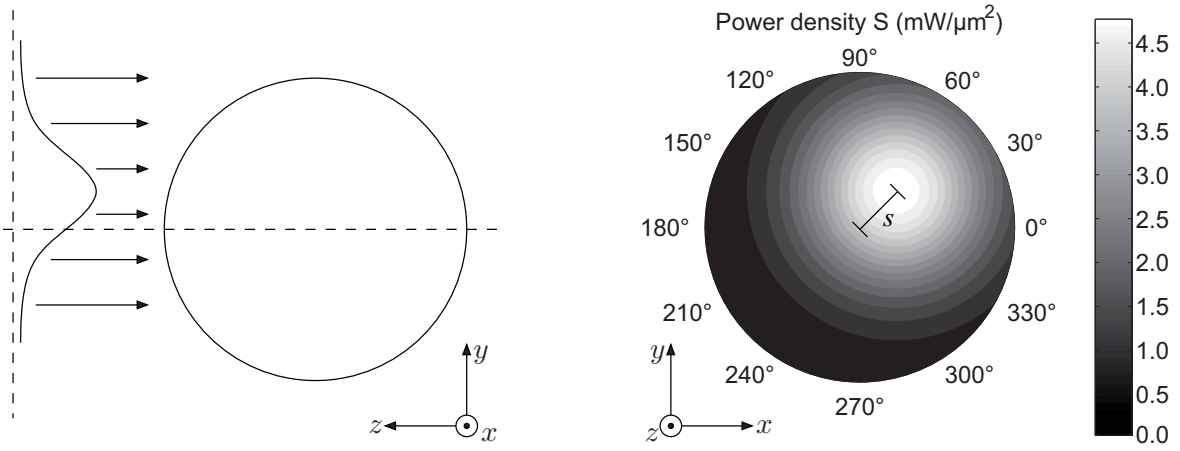

Fig. 2.4: Left: schematic side-view on the particle, which is illuminated by a parallel beam with transverse Gaussian power density distribution. Right: projection of the power density distribution on the particle, showing the offset s between particle center and beam center.

approximately the same and cancel each other out, so no particle movement will occur in those directions. However, the force contribution in 45 ° direction is much stronger than the opposite one, so the particle will effectively be moved towards the maximum intensity of the parallel beam.

The total radiation force on the particle can be determined by integrating the force per area over the projected area of the particle. In case of the gradient force, this has to be done separately for the components in x- and y-direction, where $F_{\mathrm{ga}\,x} = F_{\mathrm{ga}} \cos\varphi$ and $F_{\mathrm{ga}\,y} = F_{\mathrm{ga}} \sin\varphi$

$$F_{\mathrm{s}} = \int_0^{2\pi} \int_0^{a/2} F_{\mathrm{sa}}(r,\varphi)\, r \mathrm{d}r\, \mathrm{d}\varphi, \tag{2.10}$$

$$F_{\mathrm{g}\,x,y} = \int_0^{2\pi} \int_0^{a/2} F_{\mathrm{ga}\,x,y}(r,\varphi)\, r \mathrm{d}r\, \mathrm{d}\varphi. \tag{2.11}$$

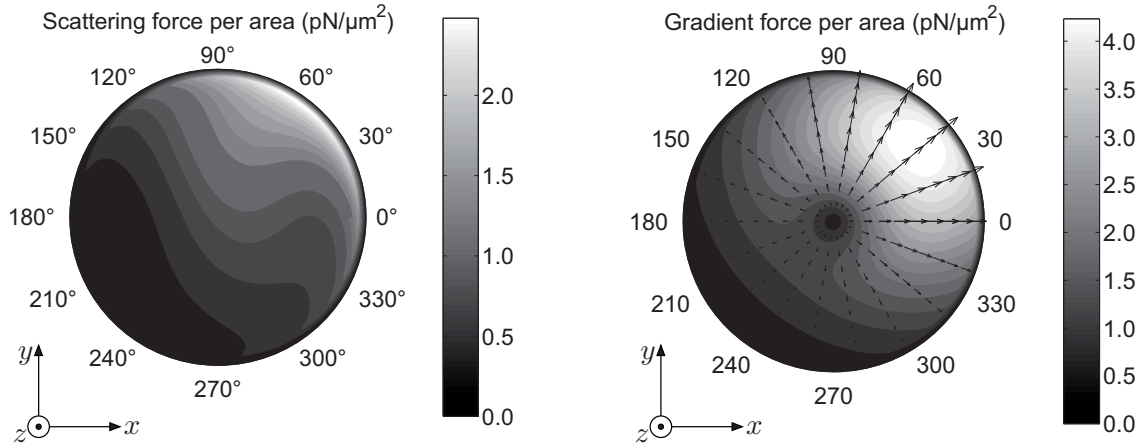

Fig. 2.5: Calculated scattering and gradient fore per area as a projection on the particle surface.

The total gradient force thus is

$$F_{\mathrm{g}} = \sqrt{(F_{\mathrm{g}\,x})^2 + (F_{\mathrm{g}\,y})^2}, \tag{2.12}$$

with orientation

$$\varphi_{\mathrm{g}} = \arctan \frac{F_{\mathrm{g}\,y}}{F_{\mathrm{g}\,x}}. \tag{2.13}$$

Since (2.10) and (2.11) cannot be computed analytically, the integrals were solved numerically using the software package Matlab. For the given example, a scattering force of 1.8 pN and a gradient force of 2.1 pN with almost 45 ° orientation can be determined. Since the mass of the polystyrene particle is only about 120 pg, these forces are large enough for a significant acceleration of the sphere.

To determine the force field affecting the particle, the described computation has to be done for varying offsets s between particle and beam center. Figure 2.6 displays the result for a linear variation of s from -8 to 8 µm along $\varphi = 45°$. The scattering force is always oriented in the propagation direction of the laser beam, while a positive gradient force denotes a 45 ° orientation and a negative value the opposite direction. Both force components decay for large distances between sphere and laser beam, so the particle is no longer affected. While the scattering force shows a distinct contribution also for $s = 0$, the gradient force is zero, since opposing transverse force contributions cancel each other out. A stable equilibrium position in the transverse direction is thus found for a particle at the beam center. Therefore, the derived transverse trapping potential $V_{\mathrm{F}} = -\int F_{\mathrm{g}}\,\mathrm{d}s$ in Fig. 2.7 shows a characteristic minimum at $s = 0$. The maximum gradient force $F_{\mathrm{trap}} = 3.3$ pN is obtained for an offset of about 2 µm, which is close to the fringe of the particle.

Figure 2.8 shows the magnitude of the radiation forces for different beam diameters of 8 to 3 µm, while the diameter of the particle is kept constant at 6 µm. The highest transverse

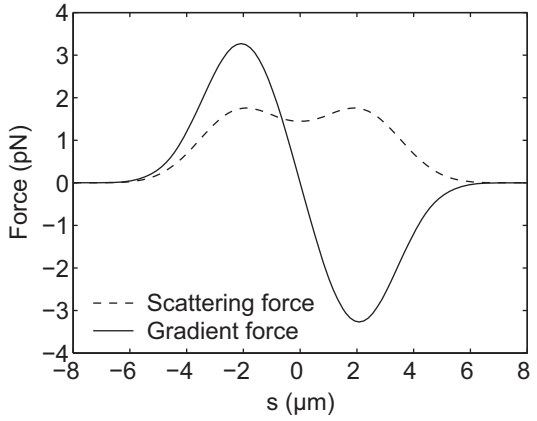

Fig. 2.6: Light forces on an illuminated 6 µm polystyrene particle versus the distance s between particle center and beam axis. The parallel beam has a total optical power of 5 mW and a beam diameter of 5 µm.

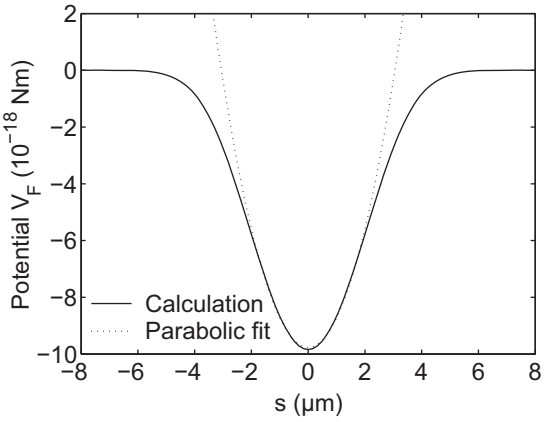

Fig. 2.7: Transverse trapping potential derived from the gradient force given in Fig. 2.8. The dashed line shows the parabolic potential for an ideal harmonic oscillator.

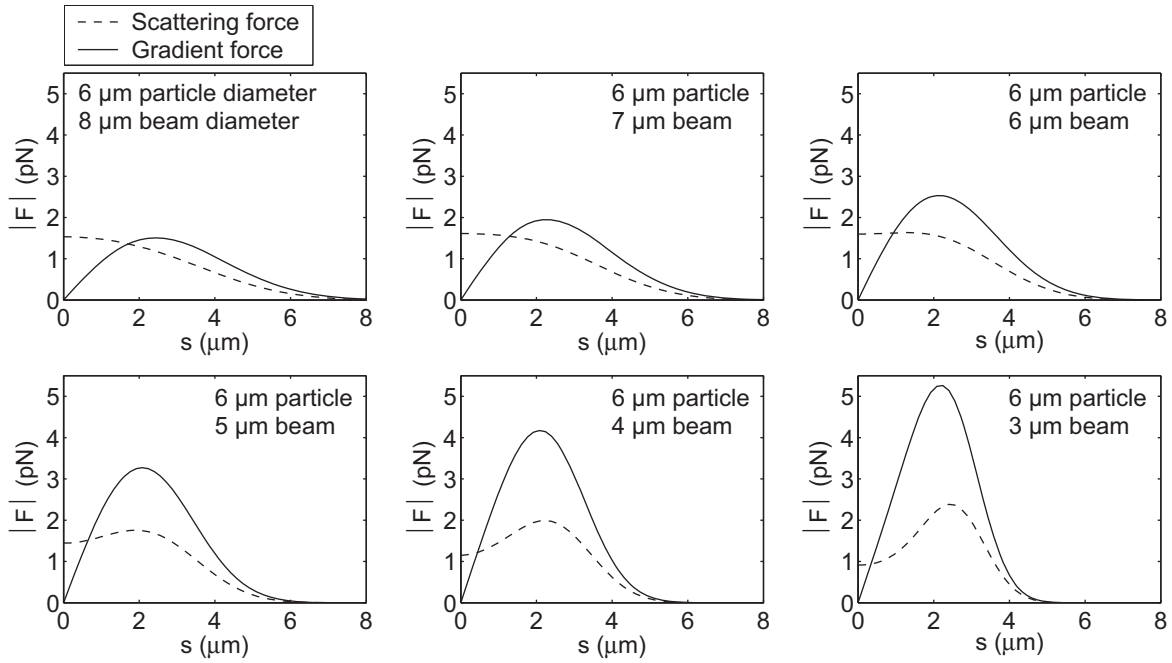

Fig. 2.8: Calculated light forces for a 6 µm polystyrene particle and a beam of 5 mW optical power with varying diameter of 8 to 3 µm.

trapping force of 5.1 pN is achieved for a small beam diameter of 3 µm, since it offers the strongest intensity gradient. However, it is important to regard the diameter of the beam relative to the particle diameter. For small particles, the effective intensity gradient becomes smaller, which results in a weaker gradient force. For example, a 3 µm diameter particle trapped by a 3 µm beam experiences a maximum gradient force of only 2.5 pN, what is similar to the case of a 6 µm particle in a 6 µm diameter beam.

Since the gradient force close to the equilibrium position at $s = 0$ shows approximately linear behavior and the corresponding trapping potential is of parabolic shape (see Fig. 2.7), the deflection of a particle by the distance s from the beam center is often modeled like a Hookean spring [4]

$$F_{\mathrm{g}} = \kappa s, \tag{2.14}$$

where the spring factor κ is called trap stiffness. In addition to the maximum available trapping force F_{trap}, it is a further measure of the strength of the regarded trap. Furthermore, an overall Q-value is defined which connects the maximum trapping force with the total power P of the beam [4]

$$F_{\mathrm{trap}} = \frac{\bar{n}_{\mathrm{m}} P}{c} Q. \tag{2.15}$$

The performed calculation of the trapping forces was done for a simple parallel beam. However, this is not applicable for the commonly used tweezers setups. There, the laser beam is strongly focused to additionally achieve a strong longitudinal gradient force, which could overcome the forward scattering force. Still, the presented simulations display very well the basic properties of an optical trap and help to understand the observed experimental results.

2.2 Systems and Applications

2.2.1 Single Laser Traps

An essential part of a classical optical tweezers setup is a microscope objective of high numerical aperture (NA). It provides strong focusing of the laser beam and thus a high longitudinal intensity gradient, which is required for stable axial trapping. Generally, this is achieved by using immersion objectives. Here, the gap between the objective output lens and the cover glass carrying the particle suspension is filled with a liquid like water or oil to mitigate the difference in refractive index between the glass elements and the gap (see Fig. 2.9). Figure 2.10 displays the working principle by a schematic objective, which carries an immersion only on its left half. For simplification the refractive index of the immersion is assumed to be the same as the one for glass. In this case, a tightly focused beam with a large maximum angle of incidence is achieved. However, the same angle cannot be realized at the right side, where no immersion is applied, due to refraction at the air-glass interface [23]. Since the NA of an objective is defined as $\mathrm{NA} = \bar{n}_\mathrm{i} \sin(\alpha/2)$, where $\bar{n}_\mathrm{i}$ is the refractive index of the immersion liquid and α is the full angle of acceptance of the objective, the NA of an immersion objective can be larger than one. Typical values are in the range of 1.2 to 1.4 [24]. It is however important to note, that the achievable intensity gradient of a laser beam depends on its beam quality as well, since a laser beam of bad quality is less focusable than an ideal Gaussian beam.

To handle particles with optical tweezers, a relative movement of the laser beam to the sample stage is required. In the easiest way, this is achieved by movement of the sample stage itself, offering a large movable range. This can be done computer controlled with servo motors, or, for higher accuracy, using piezo positioners. If movement of the sample stage has to be avoided, steering of the laser beam is necessary. Here scanning mirrors, acousto-optic deflectors or electro-optic deflectors are commonly applied [20], where the range of tweezers movement is limited by the input aperture of the immersion objective.

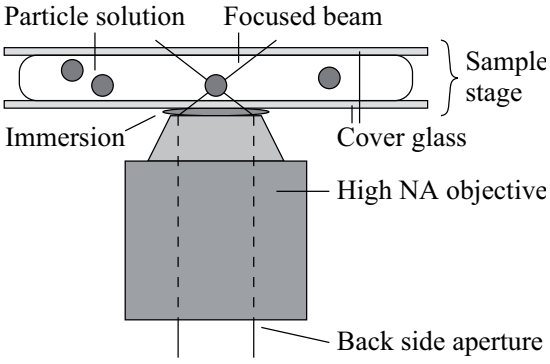

Fig. 2.9: Schematic of the essential part of an optical tweezers setup with the immersion objective and the sample stage containing the particle solution.

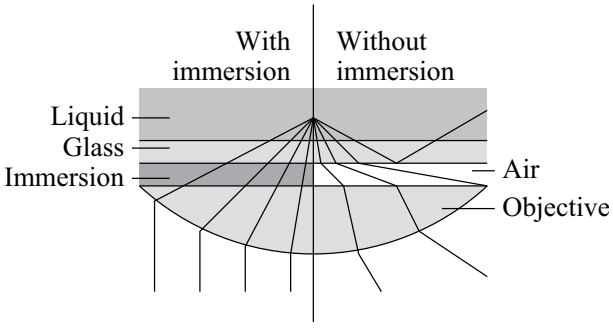

Fig. 2.10: Working principle of a high NA objective with and without immersion, which mitigates the refractive index step and prevents refraction at the objective-air-glass interface.

Typical laser sources in optical tweezers setups are solid state lasers like Nd:YAG or Ti:sapphire, but fiber lasers or semiconductor laser diodes are used as well. Commonly, the fundamental Gaussian mode is preferred, since it can be focused to the smallest beam waist and thus forms a stable harmonic trap [20]. However, also specially adapted laser beams, like Bessel beams, are used [4, 25]. Theoretically, a Bessel beam is propagation invariant, that is, it does not show diffractive spreading like it is typical for a standard Gaussian beam. The beam consists of an infinite number of concentric rings with a bright spot in the center (for the zeroth order mode). In reality, an approximation of a Bessel beam can be created by a conical lens (an axicon) or holographic techniques. The beam shows a drastically reduced divergence of the central core compared to a Gaussian beam. Therefore, optical guiding of particles over a large distance of 3 mm was achieved [26]. Furthermore, a Bessel beam will reconstruct itself after encountering a particle, so the beam reforms after a short distance behind the object. Thus, multiple particles can be trapped and manipulated simultaneously, even if they are separated by a large distance of up to a centimeter [26].

A second specially adapted laser beam is used to trap particles of low refractive index, like air bubbles in water. The beam deflection of a ray transmitting through such a particle is opposite to the deflection at a high refractive index particle. Therefore, the gradient force is directed toward the lowest intensity, and the particle is repelled by the fundamental Gaussian mode [15]. Trapping can be achieved by using a higher-order mode or Laguerre-Gaussian beam, which shows a donut-like intensity profile with an intensity minimum at the beam center. These kinds of traps are therefore often termed dark traps [4, 27].

Since the working distance of the high NA objectives used in standard optical tweezers setups is commonly in the range of only 100 µm, the axial movable range of an optical trap is limited to about 20 µm [20]. This value can be increased by using a counterpropagating-beam trap, as shown in Fig. 2.11. As early as 1970, three-dimensional trapping was achieved by two opposed, mildly focused laser beams, which act as transverse optical traps. A stable axial position is found where the scattering forces cancel each other out [15]. This position can be changed by varying the power ratio between the two beams. Rodrigo et al. [28] improved this concept by using a polarizing beam splitter to create two beams from one circular polarized laser source in combination with a polarization modulator. Therefore, the power ratio of the beams and thus the axial particle position can be controlled by computer

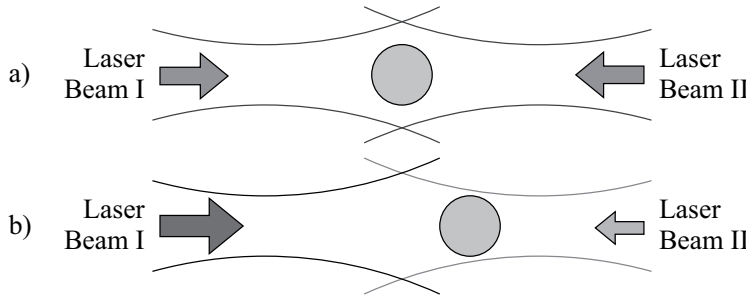

Fig. 2.11: Schematic of a counterpropagating-beam trap, consisting of two opposed, weakly focused beams. The longitudinal particle position can be controlled with the power ratio of beam I and II.

over an axial range of 20 µm. Furthermore, the beam diameter is similar to the particle diameter, so optical damage due to high power densities can be reduced.

2.2.2 Multiple Optical Traps

To study cell interaction or to stretch DNA or cells, it is necessary to have a higher number of optical traps, which are preferable individually controllable. Two traps can be created by splitting a single, circular polarized laser beam in two beams of orthogonal polarization with subsequent individual beam steering [29]. The number of traps can be increased by rapidly scanning a single laser beam between different positions, so that the mean power at each trap is still sufficient. To avoid an influence on the particles, a high scanning frequency and fast beam steering is required, which can be achieved by acousto-optic deflectors for instance [30].

Complex patterns of optical traps can be generated by holographic techniques. Dufresne et al. [31] used a commercial available diffractive optic to produce an array of 4×4 light spots. They focused the pattern using a high NA microscope objective, thus creating an array of optical tweezers in the sample plane. The system becomes more flexible, by substituting the static diffractive optic with a spatial light modulator (SLM), which is based on an array of liquid crystals. With a computer controlled SLM, the phase of a laser beam can be selectively shifted, so a variable intensity pattern is created [32, 33]. The calculation of the required phase pattern for a certain trap arrangement is not straightforward and requires an appropriate algorithm as well as sufficient computing power. However, arbitrary arrangements of optical tweezers can be generated with holographic optical tweezers (HOT) and even an axial adjustment of the trap position is possible. Furthermore, arrays of Bessel beams or dark traps can be realized [34, 35].

Similar results are achieved using the generalized phase contrast (GPC) method. Here, the generated phase pattern is directly transferred to an intensity pattern by introducing a phase shift of π for low spatial frequency components in the Fourier plane [36]. However, an axial variation of the trapping position is not possible. Therefore, the GPC method was used to create dynamic arrays of counterpropagating-beam traps, where the axial position can be varied with the power ratio of the opponent beams, as described in Sect. 2.2.1 [28, 37].

Both systems, HOT and GPC, have been advanced over recent years and include now graphical user interfaces, where particles can be manipulated via drag-and-drop features [38]. Complete systems are meanwhile commercially available [39]. Even a real time interface where the operators fingertips are mapped to the positions of optical tweezers was developed [40]. However, a major drawback of these systems are the bulky and expensive optical setups, which require careful handling and adjustment. Furthermore, the use of numerous lossy optics like SLMs, beam splitters and lenses necessitates lasers with high input powers to generate individual traps of some milliwatts of optical power [33, 41]. This is particularly true for HOT systems, due to unavoidable power contribution to the zeroth order of diffraction.

A different approach is not to split the power of a single laser beam, but to use several individual laser sources, each generating an optical trap. However, this is not feasible with the classically used laser sources, due to too high expenses, large setup dimensions and the issue of multiple beam coupling into the microscope objective. An attractive alternative is given by vertical-cavity surface-emitting lasers (VCSELs). These small-sized laser sources can be directly fabricated as two-dimensional arrays. A detailed discussion is given in Sect. 3.1.3.

2.2.3 Suitability for Biological Applications

Shortly after the first demonstration of optical tweezers, optical manipulation of biological material was examined. Using an argon laser in the visible spectral range, Ashkin et al. trapped living cells with optical powers of up to 100 mW. However, serious optical damage to the cells was apparent, eventually ending in death by light [13]. The reason was the high absorption of biological material in the visible spectral range, leading to internal heating and cell damage. The graph in Fig. 2.12 illustrates the absorption coefficient of biological material in dependence on the wavelength of illumination. At short wavelengths, the absorption of biological chromophores, such as hemoglobin (Hb and HbO_2), dominates the spectral properties. For long wavelengths the absorption of water increases drastically. In-between, a region of relative transparency from about 700 to 1330 nm exists, which is often called biological window [42].

Therefore, the succeeding experiment was performed with a Nd:YAG laser emitting at 1060 nm. Stable trapping of biological matter like E. coli bacteria and yeast cells without optical damage was possible. Furthermore, even reproduction of living cells during trapping could be observed [18]. Nowadays, only lasers with emission wavelengths in the biological window are used for trapping of biological matter. Here, optical damage can be avoided even at long term trapping using optical powers of several hundred milliwatt [7].

A great number of trapping experiments on biological material has been performed since these first experiments, but only a small excerpt can be given in the following. A straightforward application is the handling and separation of certain cells in a cell mixture [13]. Trapped by optical tweezers, cells can be investigated over long time periods without the

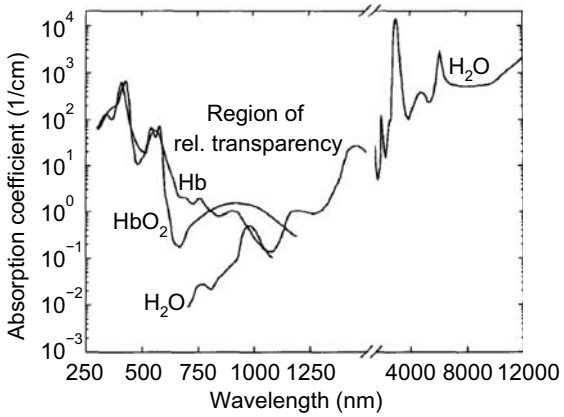

Fig. 2.12: Absorption coefficient of biological matter, showing a region of relative transparency in the range from 700 to 1330 nm, the so-called biological window [42].

risk of damage, contamination or any mechanical contact to glass slides, which leads to deformation or even cell reactions. Single kidney cells suspended in medium have been trapped and their reaction to liquids of different osmolarity was determined by observing the cell volume [43]. Thus, conclusions on the water permeability and the osmotic water transport of kidney cells could be drawn. Optical tweezers can also be used to bring cells in a well defined way into contact with other cells or chemicals. For example, microbeads coated with APCs (antigen-presenting cells) were attached by optical tweezers to different locations on a T-lymphocyte (T-cell), where a large influence on the strength of the resulting reaction could be observed [44].

Using optical tweezers cells can be immobilized during Raman spectroscopy. Raman scattered light exhibits a frequency shift, which reflects specific molecular vibrations, thus providing a chemical fingerprint of the examined sample. However, the signal is very weak and superimposed by the local environment surrounding the sample and by thermal movement of the cell. Both effects can be decreased by investigating trapped cells, which are kept well away from any surface. In this way, the signals of red blood cells, yeast cells or leukemia cells were intensively investigated [2, 45].

Combinations of optical tweezers with optical scissors have also been reported. Optical scissors operate at much shorter wavelength than optical traps to damage and cut biological material at well defined positions. An often referred possible future application is the sperm-egg fusion for in vitro fertilization. Here, the envelope of the egg is cut by the optical scissor, while the sperm is guided through the generated hole by optical tweezers [21].

Since the size of most biological cells is in the range of 5 to 30 µm, they can be handled by optical traps directly. However, for small biological material on the molecular level, like DNA, direct manipulation is no longer possible. Therefore, polystyrene or silica microbeads are commonly attached to the ends of molecules and used as handles. Stretching of DNA or even tying of a molecular knot with multiple optical tweezers was reported [1, 21]. With these experiments, insight into the elasticity and mechanical properties of DNA and other biological molecules can be gained.

The experiments show that beside handling and immobilization optical traps themselves can contribute to the analysis of biological matter. A further impressive example is given by the so-called optical stretcher, whose setup is similar to a conventional counterpropagating-beam trap [4, 46]. Cells between two laser beams were found to be deformed by the light forces. Through the observation of the cell shape, the elasticity of the cytoskeleton can be determined. Thus, not only different cell types can be distinguished, but also abnormalities of the cells can be found, making this a very attractive feature for early cancer detection.

Furthermore, optical tweezers are used to assess the forces acting on a particle. For example, the minimum optical power at which a sperm cell can still be trapped can be taken as a measure for its motility [47]. In more sophisticated setups, an exact measurement of the deflection of a particle or the force applied to it is possible. Commonly, a four quadrant photodiode is used to detect the forward scattered light of the trapped particle. In this way, small deflections down to some nanometers can be determined. Knowing the trap stiffness, conclusions on the force applied to the particle can be drawn, where forces on particles with sub-piconewton resolution were already measured [14]. Such setups are very useful for the

examination of molecular motors. Molecular motors are special enzymes that transform the energy released by chemical reactions into mechanical work and are, for example, the basis of muscle contraction. Using optical tweezers the motion of molecular motors like kinesin or myosin as they move along microtubules could be observed for the first time [21, 3]. Characteristic, regular steps of just some nanometers were determined. The force exerted by the enzyme RNA polymerase during gene transcription was studied in this way as well. The RNA polymerase was attached to a cover glass, while one end of the transcripted DNA molecule was coupled to a polystyrene microbead and trapped by optical tweezers. The RNA polymerase catches the free end of the DNA molecule and pulls it near during transcription. From the deflection of the microbead, forces up to 14 pN exerted from the RNA polymerase could be derived [21].

3 Vertical-Cavity Surface-Emitting Lasers

Vertical-cavity surface-emitting lasers (VCSELs) first emerged in the 1970s and are meanwhile a commonly used laser source in short distance optical data transmission and sensing applications, for example, in optical computer mice [12, 48]. In contrast to standard edge-emitting lasers, the light is emitted orthogonally to the semiconductor wafer surface. This leads to unique device properties like a cylindrical structure with a circular symmetric output beam or the possibility of on-wafer laser tests. The fabrication of two-dimensional laser arrays is possible in a straightforward manner. Typical wavelengths are in the 850 or 980 nm range, but also devices in the visible (660 and 760 nm) as well as in the infrared (1300 and 1550 nm) have been intensively investigated [12]. The small dimensions of just some 10 µm and the low power consumption make VCSELs attractive for integration in complex systems. Thus, new areas of application emerged over the past years, like atomic clocks [49], sensing of biological samples [50] or optical manipulation [9].

3.1 Fundamental Properties

3.1.1 Device Structure and Characteristics

Figure 3.1 shows the cross-section of a typical top-emitting VCSEL structure based on the AlGaAs material system, as it was used in the scope of this thesis. The active region consists of three GaAs quantum wells, which provide gain in the spectral range of about 820 to 870 nm. Unlike edge-emitting lasers, the quantum wells are oriented orthogonally to the direction of light propagation. In addition, the resonator length is much shorter than in edge-emitting lasers. The optical length of the inner cavity surrounding the active layers is chosen to match the design wavelength. Therefore, a standing wave of only one wavelength,

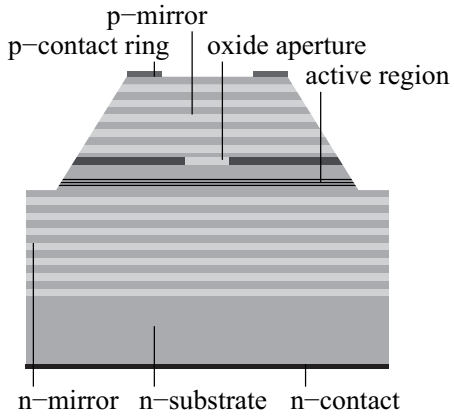

Fig. 3.1: Schematic cross-section of a typical top-emitting, oxide-confined VCSEL structure.

that is the first order mode, is formed inside this cavity. Modes of higher or lower order have a significant spectral splitting to the design wavelength and are thus not amplified by the active material. In this way, longitudinal single-mode emission is guaranteed. However, the length over which the light is amplified is much shorter than in edge-emitting lasers. Therefore, the losses of the resonator must be kept small, in order to provide small threshold gain. The mirror losses can be significantly reduced by using highly reflecting mirrors. In VCSELs this is realized by Bragg mirrors, which surround the inner cavity.

The Bragg mirrors are formed by a stack of alternating layers of AlGaAs with high and low aluminum concentration, corresponding to low and high refractive index, respectively. The electromagnetic wave is partly reflected at each interface, where an additional phase shift of π arises at each transition from low to high refractive index. By choosing the thickness of each layer to be a quarter of the design wavelength, a standing wave pattern between the layers is formed and a high total reflectivity exceeding 99 % can be achieved. For illustration, Fig. 3.2a shows a simplified schematic of the refractive index and the field intensity close to the active region. Since the difference in refractive index between the layers is mostly given by the material system, the magnitude of reflectivity is adjusted by the number of layer pairs. In a top-emitting device, light must couple out mainly at the top mirror, thus its reflectivity must be the lowest. In the used layer structure, the top mirror consists of only 23 mirror pairs while the bottom mirror contains 39.5 mirror pairs. For lossless material, this corresponds to 99.886 % and 99.996 % reflectivity, respectively, [51, 52]. Since VCSELs are electrically pumped laser diodes, it is advantageous to have highly conductive Bragg mirrors. In this case, electrical contact can be easily achieved with a ring shaped p-metalization on top of the laser and a broad n-metalization on the back side of the GaAs substrate, as shown in Fig. 3.1. Since a high concentration of dopants in the complete Bragg mirror would lead to high absorption losses, so-called δ-doping is applied, where the dopant concentration is significantly increased at the position of nodes in the standing wave pattern. Therefore, a compromise between absorption losses and low electrical resistivity can be found [53].

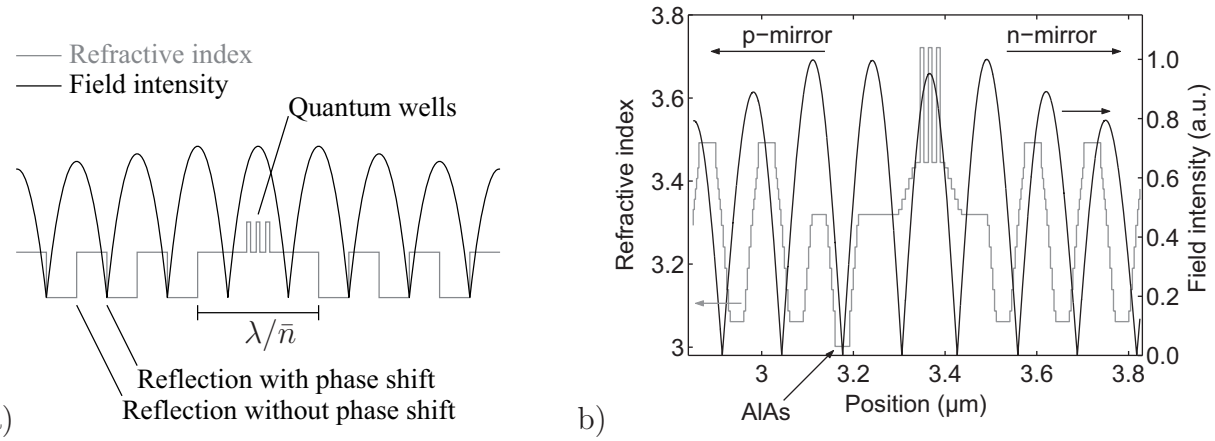

Fig. 3.2: Refractive index and standing wave pattern inside the VCSEL structure. Left: simplified schematic showing the inner cavity with an optical thickness of one wavelength. Right: calculation based on the actual layer structure using the transfer matrix method.

Another issue is the transverse confinement of current to the active region, in order to decrease the threshold current and to reduce carrier losses at the rough side-wall of the VCSEL mesa. For all devices described in this thesis current confinement was achieved by selective lateral oxidation, a technique which proved to enable best laser performance in the past [12]. Here, a layer of very high aluminum concentration in direct neighborhood to the active region is considered in the VCSEL layer stack. Lateral oxidation transforms this layer to an electrically isolating material, thus, the current flow is confined to the remaining aperture at the center of the layer. The size of this oxide aperture strongly influences the laser output characteristics. While devices with small active diameters offer low threshold currents and high quality output beams, VCSELs with large oxide apertures can easily emit high output powers exceeding 100 mW at the cost of significantly reduced beam quality [54].

Besides its isolating properties, the oxidized material shows a much lower refractive index than the semiconductor (1.6 compared to 3.0) [55]. In analogy to a glass fiber, an optical waveguide is formed with a core of high and a cladding of low effective refractive index. However, this effect is commonly unwanted, since strong optical guiding increases the number of propagable transverse optical modes, thus deteriorating the laser beam quality. To minimize the influence of the oxidized layer, it is placed at the position of a node in the standing wave pattern of the optical field. As a negative side effect, this disturbs the exact sequence of high and low refractive index layers [53]. Figure 3.2b depicts the course of refractive index and optical intensity in the actual layer structure, where the transfer matrix method was applied to calculate the electromagnetic field [51]. In all discussed devices, the oxidation layer consists of pure AlAs with no gallium content.

Figure 3.3 shows typical output characteristics of a standard VCSEL device with 6 µm active diameter. The measurements were performed at room temperature, and a collimating objective together with a silicon photodiode was used for optical detection, incurring losses of about 3 % (see App. A). Caused by the p-n-junction in the VCSEL structure, the current–voltage (IV) curve displays a diode characteristic. The threshold voltage of about 1.5 V corresponds to the band-gap energy of 1.43 eV for GaAs. The following linear increase gives a differential resistance of 95 Ω, which is mainly caused by the metal-semiconductor interfaces and the series resistance in the semiconductor layers [12]. Consequently, devices of smaller active diameter have a higher differential resistance.

The light–current (LI) curve shows a threshold current I_{th} of 0.7 mA and a maximum optical output power P_{max} of 6.5 mW at rollover. Thermal rollover is typical for VCSEL devices and is mainly caused by Joule heating of the laser during CW (continuous wave) operation. The heating leads to an increase in carrier leakage, that is, a higher number of carriers can thermally escape the quantum wells without recombination. Furthermore, also the number of nonradiative recombinations increases. Just above threshold, the output power P and the driving current I of the VCSEL are linearly connected by [52]

$$P = \eta_{\mathrm{d}} \frac{\hbar\omega}{q} (I - I_{\mathrm{th}}), \tag{3.1}$$

with q being the elementary charge and $\hbar\omega$ the photon energy. The quantity η_{d} is the differential quantum efficiency, which describes the fraction of the injected carriers which

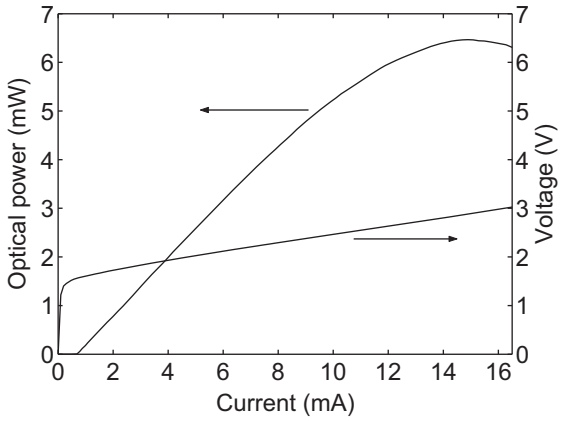

Fig. 3.3: Typical light–current–voltage (LIV) output characteristics of a standard VCSEL with 6 µm active diameter.

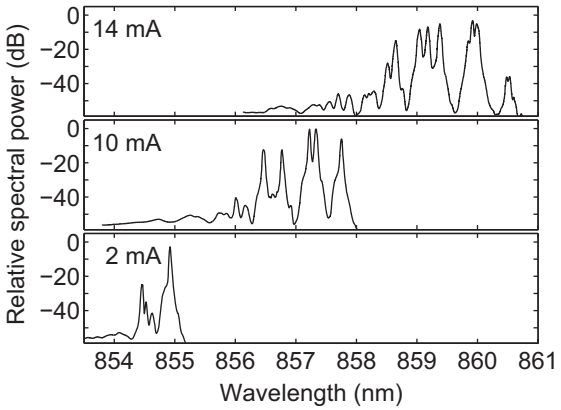

Fig. 3.4: Emission spectrum of the VCSEL from Fig. 3.3 at different driving currents, showing higher-order lasing modes.

contribute to stimulated emission. The given device emits at a wavelength of about 855 nm, so a differential quantum efficiency of 41 % can be determined.

The emission spectrum of the VCSEL at different driving currents is shown in Figure 3.4, where a redshift of the emission wavelength with increasing current can be observed. The temperature dependence of the refractive index and the enlargement of the cavity itself leads to a decrease of the cavity resonance frequency for higher currents. At the same time, the shrinkage of the bandgap causes a redshift of the gain curve. In typical devices this shift is stronger than the shift of the cavity wavelength (typically 0.32 nm/K compared to 0.07 nm/K). However, the emission wavelength of a VCSEL is only determined by the cavity resonance, so the spectrum shifts with just about 0.07 nm/K. Still, the different thermal shifts cause a detuning of the emission wavelength to the gain maximum, whose magnitude and sign depend on the operating point [52].

The appearance of higher-order lasing modes can be observed at higher driving currents. Since VCSELs are as a matter of principle longitudinal single-mode, these are transverse modes which are similar to the linearly polarized (LP) modes in optical fibers [56]. The fundamental mode has a Gaussian-shaped transverse intensity distribution, while higher-order modes show a larger number of radial or azimuthal intensity maxima. The reason for their appearance at higher currents is twofold. The intensity distribution of the fundamental mode leads to a high number of recombinations of carriers at the center of the active region. Therefore, the carrier density distribution becomes donut-shaped, what is known as spatial hole burning. Furthermore, highest temperatures are found at the center of the VCSEL, causing a transverse variation of the refractive index which leads to stronger optical guiding. Thus, this effect is often termed thermal lensing. Both effects support the onset of higher-order transverse modes [52].

A closer study of transverse modes is possible by spectrally resolved near-field measurements, which deliver the intensity distributions of different modes in close proximity to the laser output facet (see App. A). Figure 3.5 shows near-field measurements for the discussed device at 2 and 10 mA driving current. At 2 mA, two different transverse modes can be

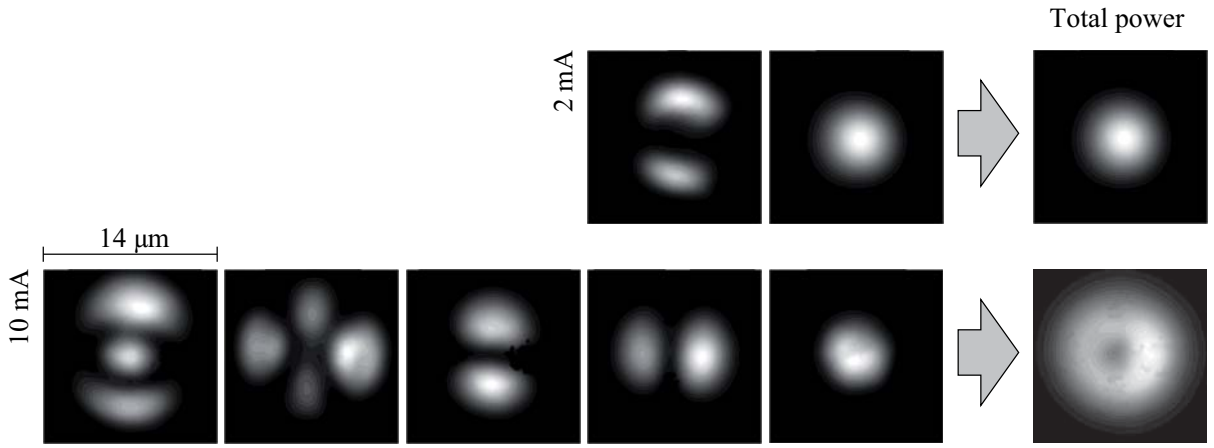

Fig. 3.5: Spectrally-resolved and total near-field intensity distribution of the standard VCSEL, corresponding to the spectra for 2 and 10 mA current in Fig. 3.4.

resolved by the measurement, which can be assigned to the fundamental mode LP_{01} and the first higher-order mode LP_{11}. Other modes, although visible in the spectrum (see Fig. 3.4), cannot be detected due to their low optical power. The total intensity distribution, given on the right side of Fig 3.5, still shows the characteristic transverse Gaussian shape, since the fundamental mode is dominant. At a driving current of 10 mA, five different modes are observable, which can very well be assigned to the five major modes shown in the laser spectrum. The arrangement of the near-field patterns from right to left in Fig. 3.5 corresponds to a decrease in emission wavelength. The second LP_{11} mode, which has its origin in the degeneration of this mode, is now clearly visible. Furthermore, the two modes of lowest wavelength can be associated to the LP_{21} and LP_{02} modes. However, an aberration from their ideal shape is clearly visible. It is caused by asymmetries in the device structure, mainly by a noncircular oxide aperture (see Sect. 3.2.1). Since a large fraction of the total optical power is contained in the higher-order modes, especially in the LP_{11} modes, the total intensity distribution is no longer Gaussian-shaped. Instead, it shows a clear intensity minimum at the center.

The donut-shaped intensity profile will be even stronger at higher currents and is typical for multi-mode VCSELs. Furthermore, higher-order modes show a drastically reduced beam quality compared to the fundamental mode. Therefore, the beam divergence of multi-mode VCSELs is significantly larger than the one of single-mode VCSELs. This complicates fiber coupling in optical data communication. Many novel applications, like optical spectroscopy or optical sensing, require transverse single-mode emission [48]. Therefore, the enhancement of single-mode output power is an important topic, which will be discussed in the following section.

3.1.2 Enhancement of Single-Mode Emission

In standard VCSEL devices, single-mode emission can only be achieved for small oxide apertures, in analogy to single-mode fibers with small core diameters. VCSELs with small diameters below 4 µm commonly show a Gaussian-shaped output beam profile of high

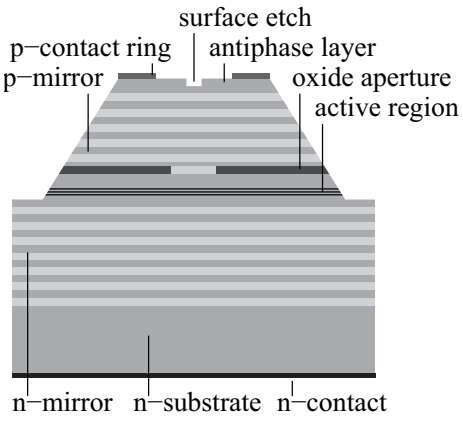

Fig. 3.6: Schematic cross-section of a top-emitting VCSEL structure with integrated inverted surface relief. The Bragg layer stack is terminated by an additional quarter-wave antiphase layer, which is selectively removed in the center of the output facet during the processing.

beam quality, however, the maximum output power of these devices is typically below 3 mW. Furthermore, the small active diameter leads to an increased ohmic resistance and reduced lifetime. More advantageous alternatives to enhance single-mode operation have been demonstrated, like long monolithic cavity VCSELs [57], antiresonant reflecting optical waveguide VCSELs [58] and VCSELs with a triangular holey structure [59]. The latter produced a record-high single-mode output power of 7.5 mW with 30 dB side-mode suppression ratio (SMSR), however, with multi-lobed far-field patterns. For VCSELs with integrated curved mirrors, even higher single-mode powers of 15 mW were achieved [60].

In the so-called surface relief technique, an annular etch of the laser output facet lowers the mirror reflectivity particularly for higher-order modes, which show higher optical intensities outside the device center. The resulting differences in threshold gain then strongly favor the fundamental mode. Therefore, single-mode emission can also be achieved for devices with larger active diameters. An advanced approach is shown in Fig. 3.6. Here, the top Bragg mirror is terminated by an additional quarter-wave antiphase GaAs layer. It reduces the mirror reflectivity significantly, leading to a strongly increased threshold gain. In the course of device processing, the antiphase layer is removed only in the center, so the threshold gain of the fundamental mode with its Gaussian-like beam profile is preferentially decreased compared to other modes. This so-called inverted relief technique requires a less precise etch depth control and higher modes experience additional absorption by the GaAs antiphase layer for emission wavelengths smaller than about 860 nm [57]. The main advantage compared to the above methods is the relatively low fabrication complexity. Furthermore, comparatively small degradations of threshold current, differential resistance or far-field pattern are observed. A high output power of 6.1 mW from a single inverted surface relief VCSEL with continuous single-mode operation and a SMSR above 30 dB has been reported [61]. Even a single-mode power of 6.5 mW was demonstrated, however, the corresponding device showed no continuous single-mode operation. Instead, a higher-order mode was lasing at about three times the threshold current before the VCSEL was single-mode again at higher currents [61].

Figure 3.7 shows the LI curve of a VCSEL, which is nominally identical to the standard VCSEL discussed in the previous section (see Fig. 3.3). It originates from close proximity on the same sample. However, the laser has an inverted surface relief with a diameter of 3.3 µm and an etch depth of 58 nm, as determined by atomic force microscope (AFM)

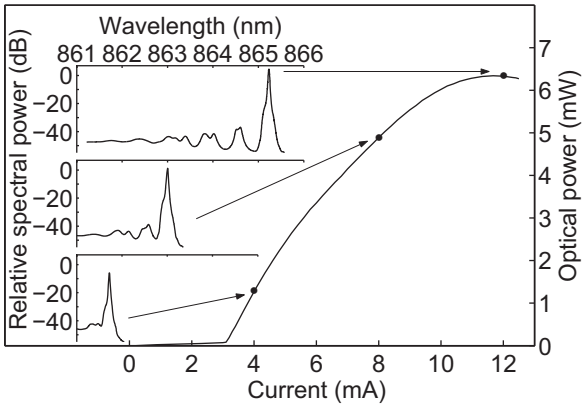

Fig. 3.7: Output characteristics of an inverted surface relief VCSEL with an active diameter of 6 µm and a 3.3 µm wide relief. The emission spectra in the insets show a SMSR of more than 30 dB.

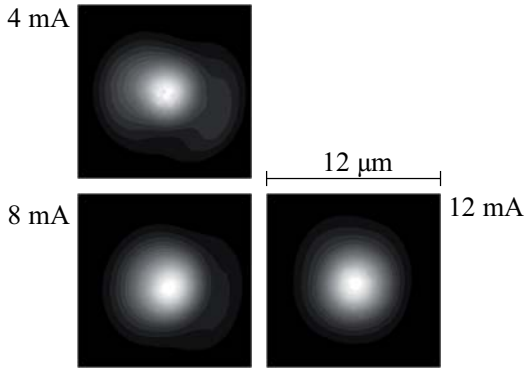

Fig. 3.8: Near-field measurements of the VCSEL from Fig. 3.7 at different driving currents, showing a Gaussian-like intensity distribution.

measurements. For power measurement, an integrating sphere was used, so no additional losses have to be considered. The relief device shows a clearly increased threshold current of 3.1 mA compared to 0.7 mA, due to the effectively decreased mirror reflectivity. On the other hand, the differential quantum efficiency has increased to 92 %, supported by the supply of carriers from the outer part of the active layers underneath the unetched region. Therefore, thermal rollover is nevertheless reached at a lower current compared to the standard device (12 mA and 15 mA, respectively). A maximum output power of 6.3 mW is achieved. The differential resistance of 84 Ω (not shown in the graph) is also similar to the standard device.

However, the optical spectra given for different driving currents in the insets of Fig. 3.7 confirm very different laser emission. Up to thermal rollover, only the fundamental mode is lasing and a SMSR exceeding 30 dB is achieved. Thus, the VCSEL delivers a maximum single-mode output power of 6.3 mW, which is to our knowledge the highest reported value for a relief VCSEL with continuous single-mode operation. Consequently, near-field measurements reveal a Gaussian-like intensity distribution also at thermal rollover (see Fig. 3.8). Figure 3.9 shows the far-field patterns for a standard and a relief device at high currents, where both show similar output powers. The enhanced single-mode operation of the relief device results in a Gaussian-shaped beam profile and a strongly decreased full-width-at-half-maximum (FWHM) of 7.6 ° compared to 21.3 °. Diffraction of light at the relief aperture leads to weak side-lobes in the far-field, which are however negligible.

Although a basic enhancement of single-mode emission is usually easily achieved by the surface relief technique, maximized single-mode output power requires a fine adjustment of relief diameter and oxide aperture size. Relief VCSELs with small active diameter of about 4 µm and a varying relief diameter from 2.6 to 5.0 µm show less output power, owing to the smaller active area. Larger devices of 8 µm oxide aperture with relief diameters from 3.5 to 7.7 µm provide similar single-mode output power as the 6 µm VCSELs, but show much higher threshold currents due to the larger active area and the decreased optical guiding

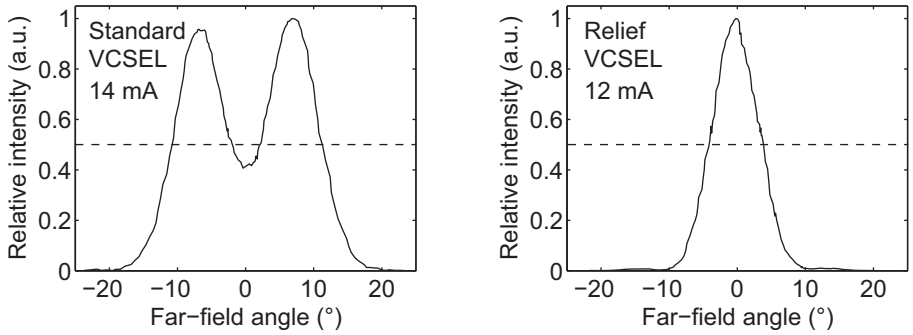

Fig. 3.9: Far-field patterns of a standard and a relief VCSEL with 6 µm active diameter and 3.0 µm relief diameter at similar operating points.

of the fundamental mode. Furthermore, lasing of a higher-order mode close to threshold could be observed.

Concerning the relief diameter, higher single-mode powers are commonly obtained for smaller reliefs, since devices with large reliefs tend to multi-mode emission at high currents. Figure 3.10 shows the output characteristics of four adjacent VCSELs with surface reliefs of 3.6, 3.4, 3.2 and 3.0 µm diameter and 6 µm active diameter. The 3.6 and 3.4 µm devices are single-mode only up to driving currents of 10.9 and 12.3 mA, respectively, as indicated by kinks in the power curves. Therefore, their single-mode output power is limited to 5.4 and 5.5 mW, respectively. For the 3.2 µm relief size, no higher-order mode starts to lase and a maximum single-mode output power of 5.7 mW is reached. However, at the same time, the threshold current increases by 0.6 mA, due to the reduced overlap between the fundamental mode and the surface etch. So a further reduction of the relief to 3.0 µm eventually diminishes the output power by thermal effects.

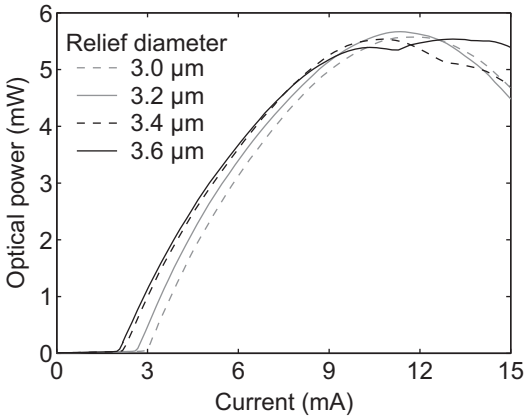

Fig. 3.10: Output characteristics of four adjacent relief VCSELs on the same sample with 6 µm active diameter and varying relief size.

To substantiate the mode-selective effect of the surface relief a significant number of VCSELs similar to the ones discussed above were characterized. Investigation of 75 standard and 160 relief devices with 6 µm oxide aperture from the same sample showed that only one of the standard devices provides a single-mode output power of more than 1.0 mW, whereas a single-mode output power of at least 2.9 mW is achieved for 98 % of the relief VCSELs. These results strongly confirm the reliability of the inverted surface relief technique for single-mode enhancement [62].

3.1.3 Suitability and Application for Optical Particle Manipulation

As mentioned in Sect. 2.2, solid state lasers like Nd:YAG or Ti:sapphire are commonly used as laser sources in optical traps. However, small-sized and low-cost trapping systems are hardly realizable with such components. This is especially true if multiple optical traps should be generated, which require complex beam steering or holographic techniques.

Therefore, the use of VCSELs as laser sources for optical trapping gained increasing interest. Their typical emission wavelengths of 850 or 980 nm are located in the biological window of low absorption and are therefore ideal for manipulation of biological matter (see Sect. 2.2.3). With typical active diameters of about ten micrometers, VCSELs have much smaller dimensions than the commonly used laser sources. They are inexpensive and their symmetric structure leads to a circular, high-quality output beam. However, the requirements on the beam quality limit the output power to some milliwatts. Although VCSELs are thus not suited for applications where high optical forces are necessary, like stretching of DNA or cells, the available optical powers are certainly high enough to handle and immobilize micrometer-sized particles.

Most important, VCSELs offer the unique possibility of straightforward creation of multiple optical traps using two-dimensional, monolithic laser arrays. Unlike other multiple trap concepts, each trap corresponds to an individual laser source, thus no additional losses through beam splitting occur. Furthermore, adjustment requirements and the complexity of the optical setup are strongly reduced. The strength of each optical trap can be easily controlled by variation of the VCSEL driving current.

The straightforward approach is to introduce VCSELs into a classical optical tweezers setup. Stable trapping of polystyrene microspheres, human red blood cells and yeast cells with trapping forces up to 3 pN with a single laser was reported [63]. The VCSEL used was a multi-mode device with a donut-shaped output beam and an available optical power at the sample stage of 5 mW. The direct comparison with a fundamental Gaussian mode trapping beam generated by a AlGaAs diode laser showed no disadvantage concerning the trapping performance. Even a higher axial stability is expected, since the low optical intensity at the beam center leads to a reduction of the scattering force, as discussed in Sect. 2.1.2.

Using a 3×3 VCSEL array originally designed for data transmission, an array of optical tweezers was generated [10]. The device pitch of the VCSEL array conformed to the standard of 250 µm, and a microlens array was used to reduce the VCSEL beam divergence. Parallel trapping of 9 yeast cells was demonstrated, where the whole cell arrangement was moved by 400 µm with a velocity of 8 µm/s. A big rat primary hepatocyte cell with a diameter of 23 µm could be optically manipulated with a velocity of 10 µm/s by combining the beams of the VCSEL array. For this purpose, the inter-tweezers spacing at the sample plane was reduced from 4.25 to 2.5 µm. This was achieved by adjusting the optical lens system with which the VCSEL array is imaged to the back aperture of the high numerical aperture objective.

In a similar setup, also non-mechanical deflection of 10 µm diameter polystyrene particles was reported. Initially, a particle was immobilized by a single optical trap of the array.

Then, an adjacent VCSEL trap was turned on, so the particle moved to a position in-between the two tweezers. By turning the first VCSEL off, the particle is all-optically moved to the position of the second VCSEL trap [64]. A 8×8 commercial VCSEL array was used for the experiment, which generated a tweezers array at the sample plane with a pitch of 3.75 µm and a maximum optical power of about 1.1 mW in each spot. The maximum velocity for non-mechanical translation was 0.48 µm/s. In recent experiments, this value could be significantly increased to 23 µm/s by optimization of the optical setup and using a higher power 12×1 VCSEL array [65]. The VCSELs showed a donut-shaped intensity profile and the generated optical traps had an optical power of 2 mW at the sample stage. Furthermore, by using 2×2 VCSELs of a 8×8 VCSEL array, also stacking of up to seven polystyrene particles was demonstrated. Subsequently, the whole particle stack could be moved non-mechanically across the tweezers array [66]. Similar experiments were also performed with DNA bound to microbeads, where velocities of 38 µm/s for non-mechanical movement of a single microbead was achieved [11, 67].

A more flexible setup was generated by combining a single VCSEL trap with an array of VCSEL tweezers [9, 68]. The single VCSEL trap acts as a collector and distributor, while the trap array enables parallel processing of multiple particles. The superposition of both light sources was achieved by a polarizing beam splitter, where the commonly arbitrary polarization of VCSELs is obstructive. By inserting a tilting mirror in each beam path, the single trap and the trap array could be steered independently. Besides polystyrene particles, yeast cells were manipulated with this system as well.

Since all mentioned experiments were based on commercial available VCSEL arrays with a large device spacing of 250 µm, microlens arrays were essential to decrease the beam divergence of each laser. Otherwise, the losses in the following optical lens system including the high numerical aperture objective would be too high. Therefore, the use of special adapted VCSEL arrays with reduced device pitch is attractive and was further investigated in the scope of this thesis.

Another issue is miniaturization and portability. While the application of VCSELs as laser sources reduces the dimension and the complexity of the optical system significantly, the setup is still bulky compared to the miniature laser and the manipulated microscopic particles. However, using VCSELs a direct integration with the particle stage is possible. Figure 3.11 shows a schematic of this so-called integrated optical trap. To achieve a drastic

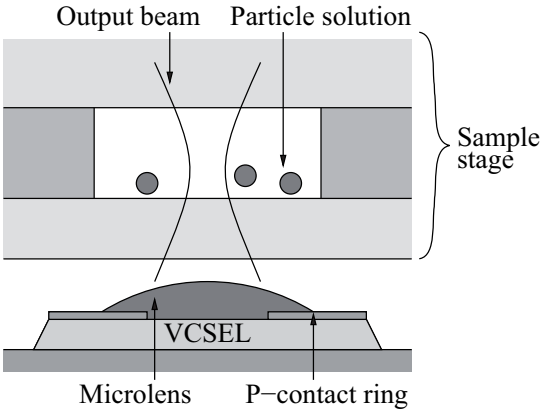

Fig. 3.11: Schematic of the integrated optical trap structure. The VCSEL output beam is focused by a photoresist microlens, so a beam waist of some micrometer diameter is achieved at the sample stage.

miniaturization of the trapping setup, any external optics should be avoided. Instead, shaping of the laser output beam by a photoresist microlens integrated directly on the laser output facet is intended in this thesis. Since the beam focusing achieved by the microlens is expected to be rather weak, no three-dimensional trapping like in optical tweezers can be achieved. However, a transverse optical trap should be sufficient if a thin sample chamber is regarded. The size of the complete setup is expected to be in the range of some centimeters, so portability and parallelization of processes can be achieved. A closer investigation of the integrated trap concept is given in Chaps. 6 and 7.

3.2 Semiconductor Technology for Laser Fabrication

The fabrication of the VCSEL devices used in the scope of this thesis is based on molecular beam epitaxy (MBE) and standard lithographic processes. The starting material is a silicon doped GaAs substrate wafer, on which the layer structure described in Sect. 3.1.1 is successively grown by MBE [53]. For single-mode enhancement by the inverted surface relief technique, the p-mirror has to be terminated by an additional quarter wavelength thick GaAs antiphase layer. Subsequently, the individual VCSEL devices must be defined, where their arrangement on the wafer is in principle arbitrary and can be chosen by the design of the lithographic masks. Besides standard solitary devices, also specially adapted arrays of closely spaced VCSELs have been applied for optical trapping in this thesis. The fabrication processes of both structures are presented in the following sections. Details on the technological procedure can be found in App. C.

3.2.1 Standard Process for Solitary VCSEL Devices

Solitary VCSELs in the present case means, that the devices are separated by a significant distance (250 µm) on the wafer sample, so mutual interference during fabrication and laser operation is unlikely. For standard multi-mode VCSELs, the circular mesa can be easily fabricated by lithographic structuring of photoresist and subsequent semiconductor etching. However, the implementation of the inverted surface relief technique requires a more sophisticated process, since an exact overlap of the shallow relief and the active laser aperture must be guaranteed. The position of the oxide aperture is predefined by the mesa itself, therefore, the alignment of mesa and surface relief is the crucial point.

To relax the tolerances, a self-aligned process was applied [57], which is schematically shown in Fig. 3.12. Mesa and relief are structured within the same lithographic step, therefore, their alignment is given by the high accuracy of the lithographic mask (Fig. 3.12a). Next, the surface relief is etched by a solution of citric acid and hydrogen peroxide, which shows a low etch rate of 1.3 nm/s (Fig. 3.12b). Therefore, a high etching accuracy can be achieved. Standard multi-mode VCSELs can be fabricated from the same sample by etching the antiphase layer across the whole output facet. Before etching the VCSEL mesa, the relief aperture must be protected by a second resist layer, where the alignment to the subjacent structure is not critical (Fig. 3.12c). However, it is important to prevent corrosion of the initial resist structure by developer or the second resist itself. Therefore, a prior strong hard

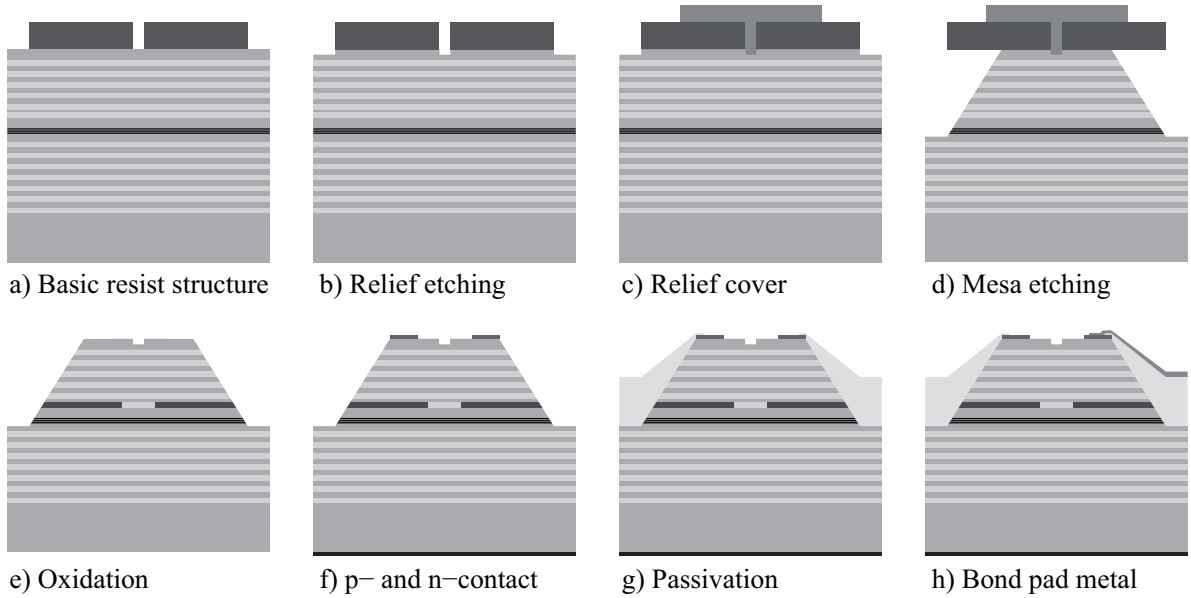

Fig. 3.12: Standard self-aligned fabrication process for top-emitting VCSELs with inverted surface relief.

bake step is applied to the first resist structure. The mesa is etched with a sulfuric acid etch solution, where the etch depth can be controlled in situ by the color change between high and low aluminum containing layers. The isotropic wet etching results in tilted mesa side walls, as indicated in Fig. 3.12d. The used mask set incorporates two different top mesa diameters from about 34 to 45 µm (see App. B).

Next the now uncovered AlAs layer is laterally oxidized to form the active aperture (Fig. 3.12e). This is done in a three zone furnace in a humid ambiance at 370 to 400 °C. The following reaction transforms the semiconductor into the isolating polycrystalline Al_2O_3 [69]

$$2\mathrm{AlAs} + 3\mathrm{H_20} \longrightarrow \mathrm{Al_2O_3} + 2\mathrm{AsH_3}, \tag{3.2}$$

where nitrogen is used as carrier gas for water. To investigate the resulting aperture, infrared light, which can penetrate the upper Bragg mirror is used to illuminate the structure. Caused by the difference in refractive index, the reflectivity between oxidized and nonoxidized areas differs. Therefore, the CCD camera used to detect the reflected light gives an image of the oxide aperture, as shown in Fig. 3.13a. Since the oxidation rate is larger in $\langle 001 \rangle$ than in $\langle 011 \rangle$ direction [70], the aperture has usually a noncircular or rhombic shape, especially for long oxidation depths (see Fig. 3.13b). One effect of this asymmetry is the deviation of higher-order modes from the ideal LP modes, as discussed in Sect. 3.1.1.

Since an in situ control of the oxide growth is not possible in the present setup, stability and linearity of the oxidation process is crucial. A linear relation of time and oxidation depth is given for a reaction limited process, which is in principle dominant for low temperatures, thin AlAs layers and short oxidation time [71, 72]. Since the oxidation setup was rebuilt within this thesis, the time dependence was examined by oxidizing five pieces of the same sample at a temperature of 380 °C. The result shown in Fig. 3.14 confirms a linear behavior with an oxidation rate of 1.58 µm/s, however, a large delay of about 3 min can be observed.

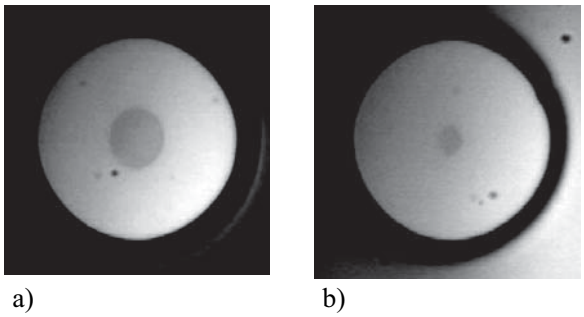

Fig. 3.13: Infrared microscope image of the oxide aperture for short (a) and long (b) oxidation time.

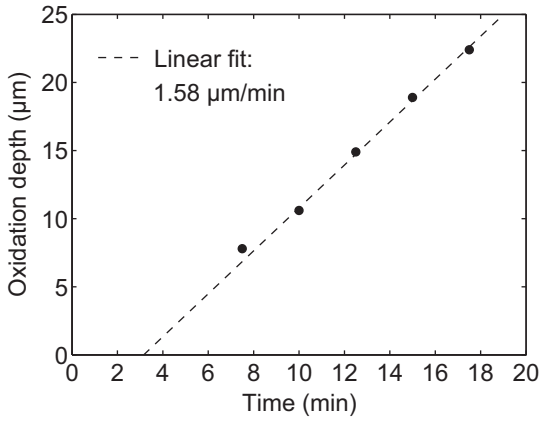

Fig. 3.14: Dependence of the oxidation depth on the process time at 380 °C, revealing a linear behavior with an oxidation rate of 1.58 µm/s.

It was found, that the offset is mainly given by the time it takes the water saturated nitrogen to fill the complete chamber of the furnace. Under consideration of the time delay, the aspired oxide diameters could be realized within deviations of ±1 µm.

Electrical contact of the devices is realized by a common back side n-metalization, where an alloying contact consisting of Ge-Au-Ni-Au is used. On top of the p-mirror a Ti-Pt-Au tunnel contact is evaporated. The contact is formed as a ring, with a 10 µm wide edge (Fig. 3.12f). For structuring, an image reversal resist in combination with a lift-off step is used. The semiconductor surface, apart from the VCSEL output facet, is then passivated by polyimide, which becomes chemically inert during a long hard bake step at 300 °C (Fig. 3.12g). To simplify the electrical contacting, bond pads are structured on top of the polyimide, which overlap with the p-contact ring (Fig. 3.12h). The pads consist of a Ni-Au layer and have an edge length of about 125 µm, so electrical contact can be easily achieved by a standard contact needle.

Figure 3.15 shows two optical microscope top views of finished solitary VCSELs. On the left side, the surface relief and the 10 µm wide p-contact ring on top of the mesa are well visible. The p-contact aperture is typically 10 µm larger than the active diameter to prevent clipping of the output beam at the metal. The right side gives an overview of the complete device including bond pad and device label, which is contained in the polyimide passivation layer.

3.2.2 Fabrication Process for Densely Packed VCSEL Arrays

The generation of multiple optical traps can be achieved in a straightforward manner by using two-dimensional arrangements of VCSELs. Commercially available VCSEL arrays have a typical device pitch of 250 µm. In a classical optical tweezers setup this necessitates the use of an additional microlens array. The realization of the integrated trapping scheme presented in Sect. 3.1.3 is even more critical. Here, the laser distance is much too large to

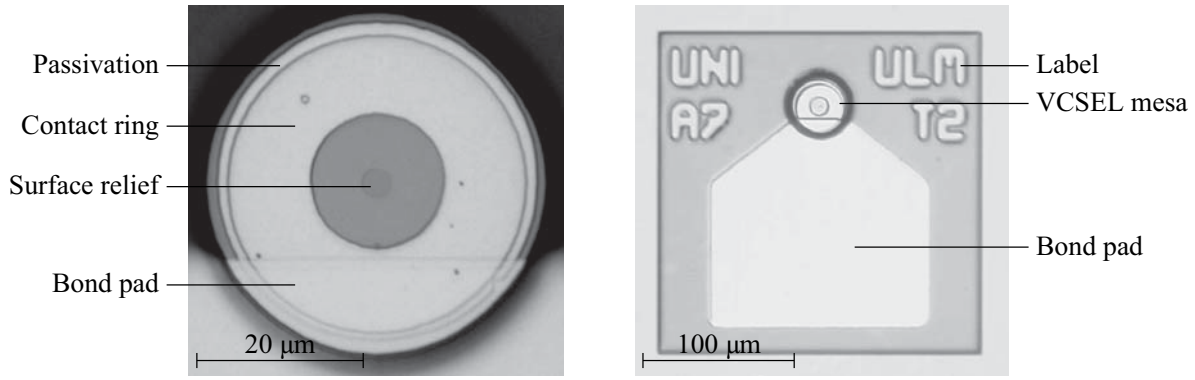

Fig. 3.15: Optical microscope top views on finished surface relief VCSELs.

expect interaction of individual traps. Therefore, special adapted, two-dimensional arrangements of top-emitting VCSELs with a device pitch in the range of 25 µm were fabricated. Figure 3.16 shows a schematic of an exemplary array layout. Since the p-contact ring as well as a potential microlens must be placed on top of the VCSEL mesa, the mesa diameter should be chosen as large as possible. Therefore, the gap between individual devices is reduced to a width of maximum 2 µm. Furthermore, the use of the inverted surface relief technique is considered.

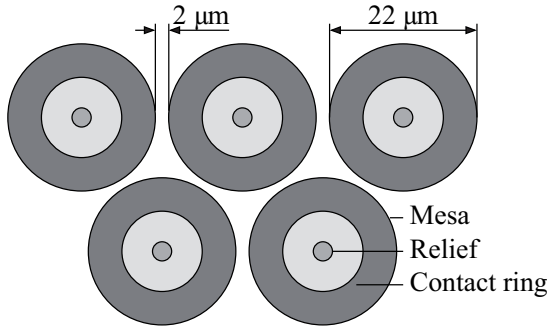

Fig. 3.16: Schematic of an exemplary layout of densely packed VCSEL arrays with inverted surface relief for optical trapping applications, defining the requirements on the fabrication process.

Caused by reduced device distance, the fabrication process for solitary VCSEL devices presented in Sect. 3.2.1 can no longer be applied. Wet-chemical etching of the laser mesa with the unavoidable underetching of the photoresist would lead to tilted side-walls and a strong reduction of the top mesa diameter. Therefore, dry etching techniques must be applied, like reactive-ion etching (RIE) or chemically-assisted ion beam etching (CAIBE). Here, directed, high-energetic ions attack the wafer surface. Material removal is mainly based on the mechanical impact at the semiconductor surface, leading to anisotropic etching and steep side walls. However, also a chemical reaction at the surface takes place, thus, the selectivity between etch mask and semiconductor material can be increased. The ratio between mechanical and chemical attack can be adjusted by process parameters like pressure, gas composition and concentration and RF power.

However, combination of the standard fabrication process with dry etching techniques is not possible. Figure 3.17 gives a schematic explanation. As described in Sect. 3.2.1, the two layer process for the inverted surface relief requires a strong hard bake of the first photoresist. During the bake-out, the resist melts into a spherical shape, with a much

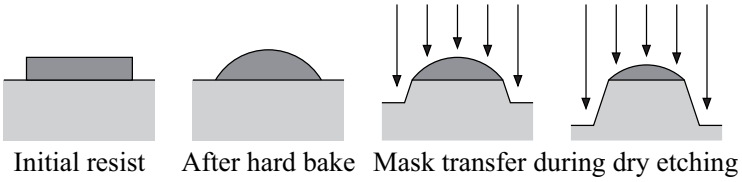

Fig. 3.17: Incompatibility of the standard self-aligned fabrication process with dry etching. The resist hard bake leads to round resist edges, which are transferred into the semiconductor during etching.

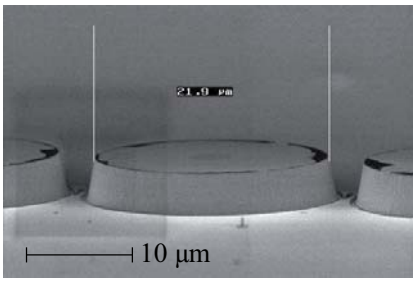

Fig. 3.18: SEM image of the resulting tilted mesa side walls after CAIBE etching.

thinner thickness at the resist edges than in the center. When using a wet etching process, this does not play a role. However, during dry etching, also the resist mask is attacked, thus, the curved resist edge is transferred into the semiconductor, leading to tilted side walls and a decrease of the top mesa diameter. Figure 3.18 shows a scanning electron micrograph of the resulting structures, where a CAIBE etch process was used which is based on argon ions and chlorine. A top mesa diameter of 22 µm can be observed, which is 2 µm smaller than intended. This reduction is not acceptable regarding the demanding process tolerances.

Therefore, a novel fabrication process has been developed, based on multiple resist layers. The process is based on PMGI (polymethylglutarimide) resist, which is not affected by isopropanol, acetone and solvents of most other resists. Especially commonly used novolak-based resists, like AZ or TI resists, show almost no chemical interaction with PMGI. Furthermore, the resists are photosensitive in different spectral ranges. Novolak-based resists are preferably exposed with the i-line of a mercury lamp, that is 365 nm, PMGI on the other hand is photosensitive in the deep ultra violet (DUV) regime (240–290 nm). While this enables complex lithographic processes, it complicates the structuring of the PMGI resist itself, since a mask aligner in the DUV exposer is not available. Instead, a DUV flood exposure in combination with a masking resist is used. Figure 3.19 shows the basic structuring process for PMGI schematically. After spin-coating and prebake of the PMGI resist, AZ resist is placed and structured on top. The AZ structures then serve as mask during the subsequent DUV flood exposure of the PMGI resist. A second flood exposure step at longer wavelengths is used to expose the AZ resist structures. Afterwards, both

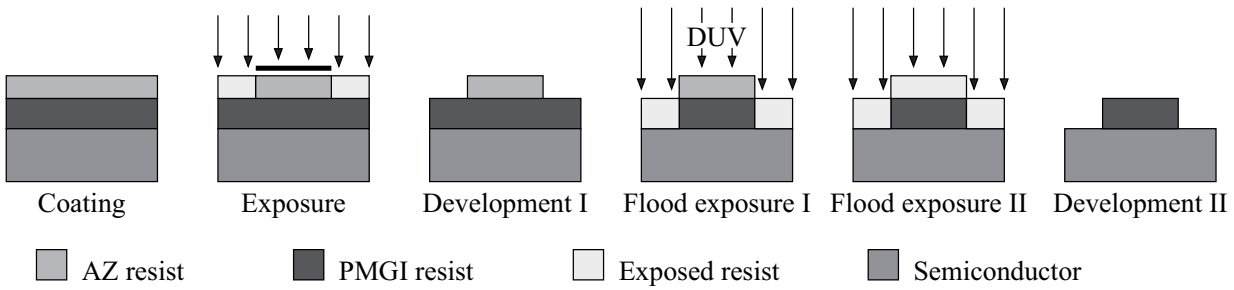

Fig. 3.19: Two layer process necessary for structuring of PMGI resist.

resist layers are developed during the same developing step, where only the non exposed PMGI structures remain.

The basic idea of the novel fabrication process is to use the p-contact metalization as hard mask during mesa dry etching. The stable metal etching mask provides steep side walls, but also an exact alignment of p-contact ring, mesa and oxide aperture is guaranteed. However, this also demands exact alignment of p-contact ring and surface relief. Figure 3.20 shows a schematic of the subsequent processing steps. To achieve self-alignment, relief and p-contact ring are both structured within the first exposure step, as shown in Fig. 3.20a. They are then contained as openings in an otherwise closed layer of PMGI resist. During wet etching of the surface relief, the p-contact area is protected by a novolak-based resist, where only a low alignment accuracy is required. Afterwards, this resist layer can be selectively removed by cold acetone, thus restoring the initial PMGI resist structure. For p-contact metalization, the relief opening is protected likewise, where an image reversal resist with negative resist side walls is used (see optical microscope image in Fig. 3.21). This is important, because the slightly positive side walls of the PMGI resist are covered with metal during evaporation and cannot be attacked by the solvent in the following lift-off step. Here, all resist layers are removed, leading to p-contact rings with centered surface reliefs on a flat wafer surface, as shown by the atomic force microscope (AFM) image in Fig. 3.22. Finally, the VCSEL output facet is protected by resist and the p-contact metal serves as stable hard mask during dry etching. RIE etching based on $SiCl_4$ is used with a high selectivity of up to 1:60 between gold and semiconductor. The following oxidation step leads to a self-aligned oxide aperture. Figure 3.23 presents scanning electron microscope (SEM) images of an array with 24 µm pitch and 3.4 µm surface relief diameter, showing almost vertical mesa edges and exact alignment of mesa, p-contact ring and surface relief. The

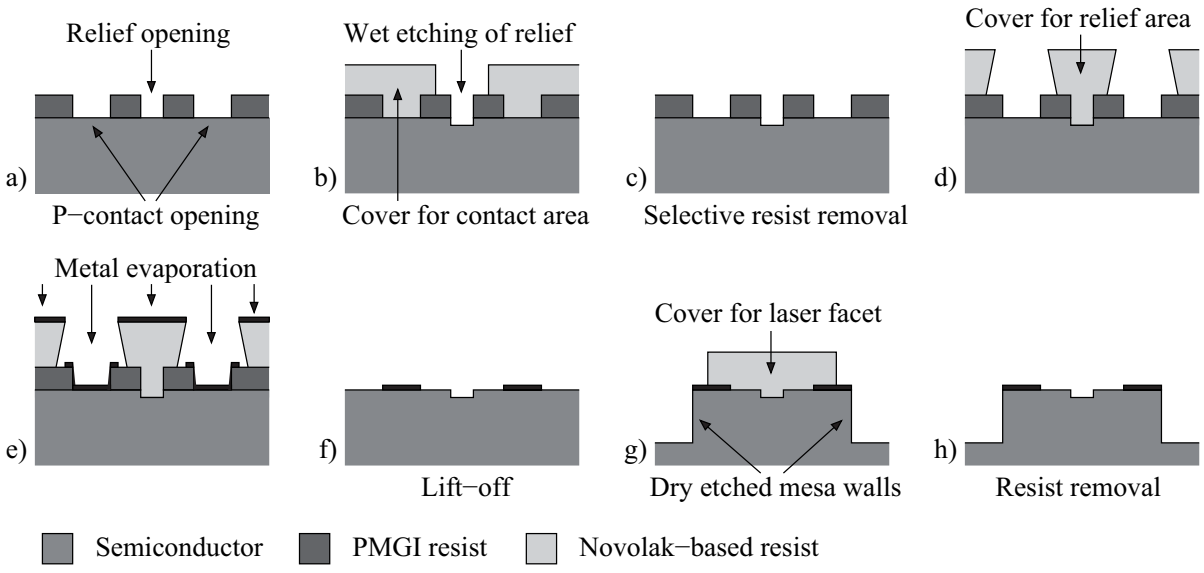

Fig. 3.20: Novel fabrication process, using multiple layers of PMGI and novolak-based resist. Surface relief and p-contact ring are defined simultaneously in the first exposure step (a), thus self-alignment of relief, oxide aperture, and p-contact ring is achieved (h).

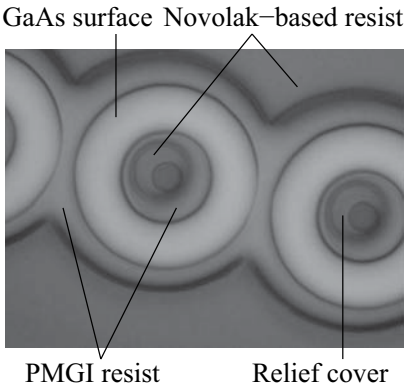

Fig. 3.21: Optical microscope top view on the sample prior to p-contact metal evaporation (see Fig. 3.20d). Only the ring contact area is uncovered, while the surface relief is protected.

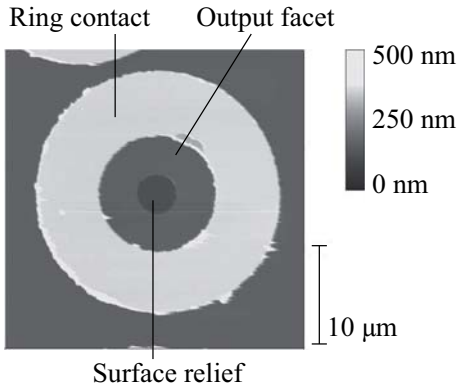

Fig. 3.22: AFM image of the structure after p-contact lift-off, showing optimum alignment of relief and metal ring.

rough p-contact surface arises from metal clustering during the oxidation process, however no influence on the device performance could be observed.

The process is completed by back side metalization, surface passivation and bond pad metalization, analog to the fabrication of solitary VCSELs. The left side of Fig. 3.24 shows an optical microscope image of a finished array of standard top-emitting devices. Here, no relief is etched but the antiphase-layer is completely removed. Besides individually addressable arrays, also parallel working VCSELs have been fabricated, as shown on the right side of Fig. 3.24. Such arrangements create a line or lattice of optical traps.

Finally, Figs. 3.25 and 3.26 show exemplary output characteristics of the fabricated VCSEL arrays. Figure 3.25 corresponds to an array of twelve individually addressable lasers, similar to the one shown on the left side of Fig. 3.24. The devices have no surface relief and an oxide aperture of about 6.5 µm diameter. A maximum output power of about 6 mW is achieved

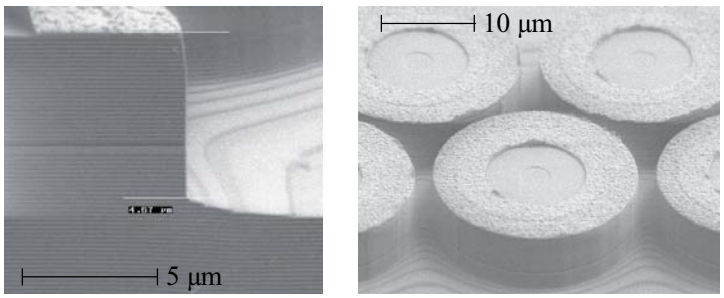

Fig. 3.23: SEM images of the mesa cross-section (left) and an array with 24 µm pitch (right) after RIE dry etching, showing almost vertical sidewalls.

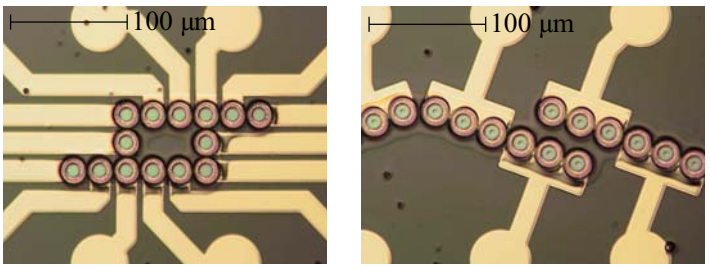

Fig. 3.24: Optical microscope top views on an array of individually addressable standard VCSELs (left) and on arrays of surface relief VCSELs with three devices connected in parallel (right). Both have a pitch of 24 µm.

for all devices, with only minor variation between the LIV curves. The lower graph shows the optical spectrum of a random VCSEL of this array, taken at 12 mA. As expected, the laser emission is strongly multi-mode. In contrast, Fig. 3.26 shows the light versus current curve of three jointly lasing devices, as shown on the right side of Fig. 3.24. The VCSELs have a 6 µm wide oxide aperture and 3.4 µm relief diameter. A mean threshold current of 1.7 mA and a high maximum output power of 3.8 mW per device can be deduced. Owing to the parallel operation of the VCSELs, the differential resistance of 50 Ω is lower than the one for the individually addressable devices of 90 Ω. The lower graph presents the three optical spectra at thermal rollover, revealing single-mode emission with a side-mode suppression ratio above 30 dB owing to the mode-selective effect of the surface relief (see App. A for details of the measurement setup).

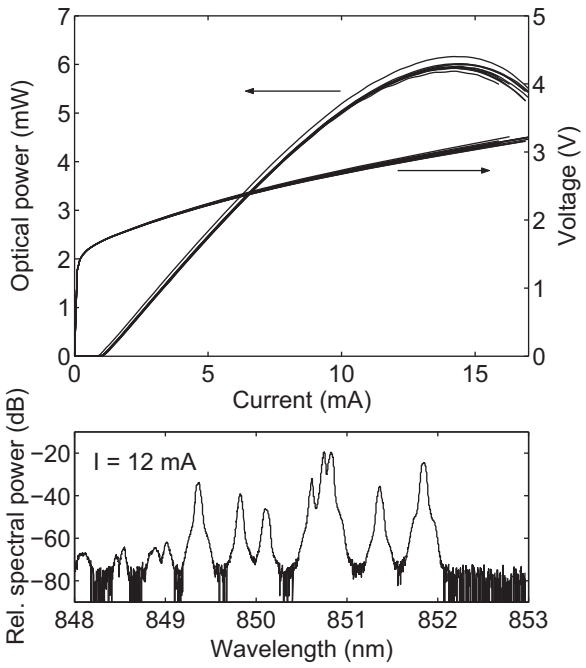

Fig. 3.25: Output characteristics of an array of twelve individually addressable standard devices with 6.5 µm oxide aperture, showing highly multi-mode emission.

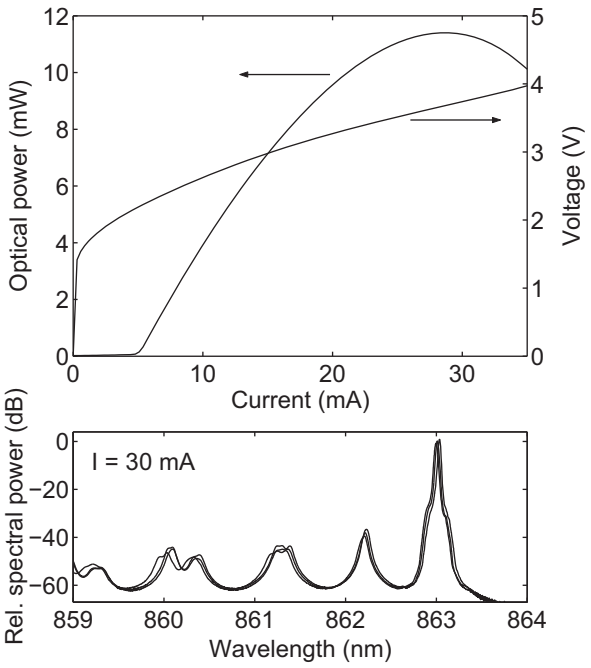

Fig. 3.26: Output characteristics of three jointly lasing VCSELs with 6 µm oxide aperture and 3.4 µm surface relief diameter. The optical spectrum shows a SMSR exceeding 30 dB at thermal rollover.

4 Microfluidic Systems

Microfluidic systems enable the handling of small fluid volumes in channels with typical widths ranging from 1 µm to 1 mm [5]. The technology emerged in the 1980s with the development of inkjet printheads [73]. Nowadays, its use spreads rapidly into the field of chemical, biological and medical analysis. Here, it offers strong cost reduction, owing to a minimum necessary sample volume and miniaturized analysis setups, and enables parallel cycles and exact timing. Furthermore, the constant flow enables the examination of reaction kinetics and mechanisms, down to the single cell or even molecular level.

4.1 Properties and Application of Microfluidic Flow

4.1.1 Laminar Flow of Low Reynolds Number

In contrast to solid materials fluids will deform continuously when exposed to shear stress. In Fig. 4.1 a fluid is placed between two parallel plates, where the upper plate is moved by a tangential force. The fluid layer in contact with this plate moves with the plate velocity, while the lowest fluid layer stays stationary. Therefore, a velocity gradient $\frac{\mathrm{d}v}{\mathrm{d}x}$ arises between upper and lower plate. For a given applied shear stress τ its strength depends on the dynamic viscosity η of the fluid [74]

$$\tau = \eta \frac{\mathrm{d}v}{\mathrm{d}x}. \tag{4.1}$$

The friction force F_R between two adjacent fluid layers of area A and distance $\mathrm{d}x$ is given by

$$F_R = \eta A \frac{\mathrm{d}v}{\mathrm{d}x}. \tag{4.2}$$

The properties of a particular flow depend strongly on the dynamic viscosity of the fluid, more precisely, on the ratio between inertial forces and viscous friction forces. This measure is given by the Reynolds number Re, which is defined as [5]

$$Re = \frac{\rho v D}{\eta}, \tag{4.3}$$

where ρ is the mass density of the fluid, v is the fluid velocity, and D is a characteristic geometry like a channel diameter. For small Reynolds numbers ($Re \ll 2000$), the flow is dominated by viscous forces and is considered laminar, while flow of a high Reynolds number is mainly turbulent. In microfluidic systems, typical Reynolds numbers are well below 1, due to the small geometric dimensions. Therefore, flow in microfluidic channels is in most cases laminar.

Fig. 4.1: Viscous fluid between two parallel plates, where the upper one is moved forward.

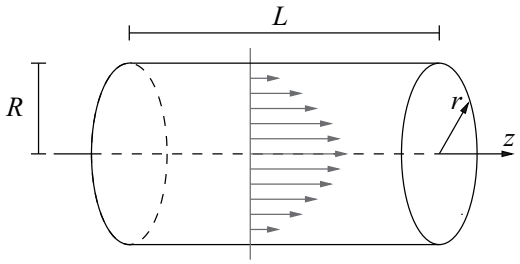

Fig. 4.2: Parabolic velocity profile (arrows) of a laminar flow inside a cylindrical pipe.

The motion of viscous fluids is described by the Navier-Stokes equation, which is based on an equilibrium of forces [5]

$$\underbrace{\rho\frac{\mathrm{d}\boldsymbol{v}}{\mathrm{d}t}}_{\text{inertia}} = \underbrace{\eta\nabla^2\boldsymbol{v}}_{\substack{\text{friction}\\ \text{force}}} - \underbrace{\nabla p}_{\substack{\text{pressure}\\ \text{gradient}}} + \underbrace{\boldsymbol{F}_{\mathrm{ex}}}_{\substack{\text{external}\\ \text{forces}}}, \tag{4.4}$$

where ∇ is the nabla operator and p is the pressure. The given formula is a simplification for incompressible fluids, which can be applied in most cases. The left hand side of (4.4), containing the convective derivative of the velocity $\frac{\mathrm{d}\boldsymbol{v}}{\mathrm{d}t} = \boldsymbol{v}\nabla\boldsymbol{v} + \frac{\partial\boldsymbol{v}}{\partial t}$, gives the inertial force per volume. The right hand side contains the viscous friction force and the pressure force per volume, as well as any additional external forces $\boldsymbol{F}_{\mathrm{ex}}$ per volume, like gravity. For flow of very low Reynolds number inertial forces can be neglected and the flow is dominated by the balance between pressure and viscous force

$$\eta\nabla^2\boldsymbol{v} = \nabla p. \tag{4.5}$$

An analytical solution is found in cylindrical coordinates for a pipe of radius R (see Fig. 4.2). With the assumptions $\boldsymbol{v} = v(r)\boldsymbol{e_z}$ for the velocity field and $p = p(z)$ for the pressure, (4.5) becomes

$$\eta\frac{1}{r}\frac{\mathrm{d}}{\mathrm{d}r}\left(r\frac{\mathrm{d}v}{\mathrm{d}r}\right) = \frac{\mathrm{d}p}{\mathrm{d}z}. \tag{4.6}$$

Integration over the volume of a partial cylinder of length L leads to [75]

$$\eta\cdot 2\pi rL\cdot\frac{\mathrm{d}v}{\mathrm{d}r} = \Delta p\cdot\pi r^2, \tag{4.7}$$

where $\Delta p = p(0) - p(L)$ is the pressure difference between pipe inlet and outlet. The friction force on the left hand side of (4.7) is identical with equation (4.2) in case of a cylindrical surface. By further integration over the pipe radius (4.7) can be solved, where the no slip boundary condition $v(R) = 0$ is imposed. The resulting parabolic velocity profile $v(r)$ is also known as Hagen-Poiseuille formula

$$v(r) = \frac{\Delta p}{4\eta L}(R^2 - r^2). \tag{4.8}$$

Figure 4.2 shows a schematic of the considered structure, including the obtained velocity profile. The volume flow rate Q_V, that is, the volume of fluid which passes through the pipe per unit time, can be derived from (4.8) by integrating over the pipe cross-section A:

$$Q_\mathrm{V} = \int_A v(r)\,\mathrm{d}A = \frac{\pi R^4 \Delta p}{8\eta L}. \tag{4.9}$$

A pressure difference between pipe inlet and outlet will therefore result in a certain volume flow. On the other hand, an applied volume flow leads to a pressure drop along the pipe. The system is therefore comparable to an electrical circuit with an ohmic resistivity [5].

For more complex structures, the incompressive Navier-Stokes equation (4.4) can be solved numerically. Various commercial programs are able to handle this problem, e.g., Comsol Multiphysics, which utilizes the finite element method. The software can analyze static as well as time dependent fluid flow in two- and three-dimensional channel structures. Figure 4.3 shows the velocity profile of water ($\eta = 1000 \cdot 10^{-6}\,\mathrm{kg/(ms)}$) inside a microfluidic Y-junction, where a pressure of 5 Pa for the inlet area (left) and no pressure for the outlet areas (right) is given as boundary conditions. For all other boundaries the no slip condition ($v = 0$) is imposed. The simulation is performed in a two-dimensional environment, however, Comsol Multiphysics provides a thin channel approximation to consider a rectangular channel cross-section of 50 µm height. The channel width is 80 µm. The result shows the typical parabolic velocity profile of laminar flow with a maximum velocity of 57 µm/s at the channel center. In the outlet channels this value decreases to 29 µm/s since the fluid volume splits symmetrically into two channels with the same cross-section as the inlet channel. However, for separation of particles into different channel arms, a constant flow velocity is favorable in order to achieve a fast extraction and to prohibit particle interactions. Therefore, the channel structure shown in Fig. 4.4 with an inlet channel of 80 µm and outlet channels of 40 µm width is more suitable. Here, the maximum fluid velocity at the channel center is about 30 µm/s in all channel sections.

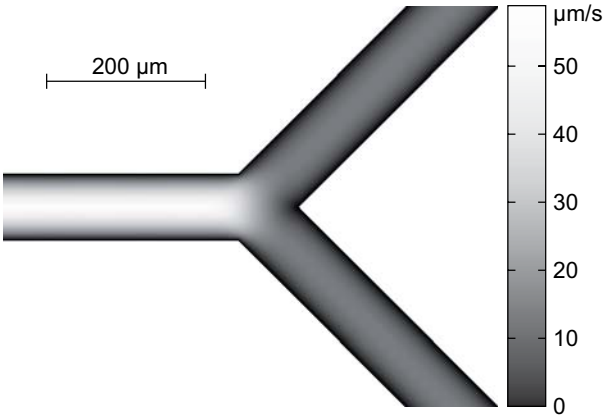

Fig. 4.3: Simulated velocity profile of water inside a rectangular channel (Comsol Multiphysics). The maximum fluid velocity is much lower in the side arms of the channel junction.

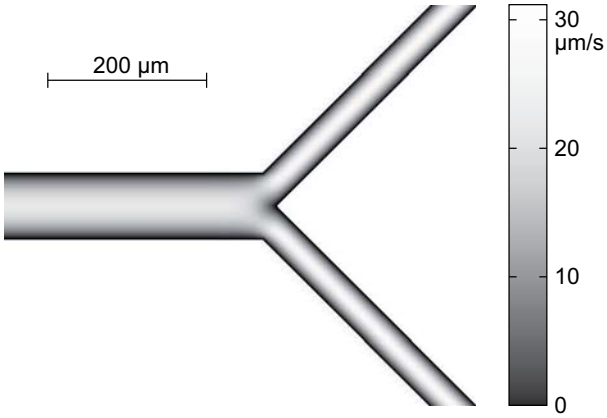

Fig. 4.4: Same as Fig. 4.3, however, an almost constant maximum fluid velocity is achieved by reducing the width of the channel outlets to half of the width of the inlet.

4.1.2 Concept of the Micro Total Analysis System

A major field of application for microfluidics lies in the field of biology and medicine. Various ongoing work deals with the transfer of classically bulky laboratory setups to the microfluidic platform. The aim is to combine different analysis steps like mixing, reaction and optical and electrical detection on one microfluidic chip, often referred to as lab-on-a-chip or micro total analysis system (μTAS). As an example, the microfluidic implementation of fluorescent-activated cell sorting (FACS) is discussed in the following, since it demonstrates the variety of microfluidic integration, as well as its compatibility with optical manipulation.

FACS is an advanced kind of flow cytometry, which is used since the late 1970s to determine and isolate a certain cell species in a biologic sample, where the cells are labeled by a fluorescent marker [21, 76]. The sample is guided through narrow capillaries and after laser excitation and detection, the liquid is dispersed into single, electrically charged droplets, each containing only one cell. Matching cells can then be separated by an electrical field. This technique is well established and offers extremely high throughput rates of more than 50.000 cells/s. However, the acquisition costs of a FACS setup are some 100.000 EUR, thus it is only accessible to well equipped laboratories [76]. For a high yield, a large sample volume of more than 100.000 cells is required, what complicates analysis and increases costs even further [7, 77]. Furthermore, an investigation on a single cell level, like reaction to chemical or electrical influences, is not feasible [8].

The transfer to microfluidics leads to a drastical reduction of setup size, sample volume and overall costs, which is further enhanced by the comparatively simple fabrication processes. The strong decrease in throughput compared to FACS is secondary, since the examined sample volume is reduced at the same time [5, 7, 8]. Furthermore, the required time can be shortened by parallel analysis with multiple microfluidic chips.

An integral part of cell analysis is the separation and sorting of certain cells, however, the classical technique used in FACS cannot be transferred to the microfluidic system. Therefore, alternative methods have been demonstrated, which are based on fluidic, electrical or optical interaction. Fu et al. controlled the flow inside microfluidic channels by pneumatically switched microvalves [78], and Huang et al. achieved continuous sorting by directing the particles over a tilted lattice of obstacles inside the channel [79]. However, the required mechanical components contain the risk of contamination and wearout. Therefore, contactless manipulation is preferable, which is given by electrical methods. Even in electrically neutral liquids, a thin, charged layer is formed at certain interfaces. In small channel dimensions, this layer can be utilized for flow control by an electrical field. Dittrich et al. [80] used this so-called electroosmotic effect to deflect particles into certain channel arms. Particle separation by dielectrophoresis was demonstrated as well, which uses an alternating field for particle manipulation [81]. However, a strong influence of the charge of the particles and the pH-value of the surrounding liquid has to be considered [82]. Furthermore, high field intensities may effect the cell membrane and the lifetime of cells [80, 82].

Therefore, contactless optical manipulation of particles inside microfluidic channels gained increasing interest in recent times, since contamination and damage of biological matter

can be avoided (see Sect. 2.2.3). In the following section, different implementations are discussed in more detail.

4.1.3 Optical Manipulation in Microfluidic Channel Structures

A straightforward way to manipulate particles optically in microchannels is to insert the microfluidic chip into a classical tweezers setup as described in Sect. 2.2.1. Particles flowing through the channels are trapped, redirected and released to a certain arm of a channel junction. Ozkan et al. [83] realized this scheme with an optical tweezers setup based on a laser diode with 27 mW output power. Wang et al. [7] used a similar setup, however, the laser beam could be deflected by an accustoptic modulator, thus an automation of trapping and separation of particles was achieved. An ytterbium-doped fiber laser provided a very high optical power of 13 W in the channel section, making a throughput of up to 100 particles/s possible. Damage to the examined cancer cells could still be avoided by using a short exposure time of 4 ms and weak beam focusing. This leads on the one hand to a loss in longitudinal trapping efficiency, on the other hand, it increases the working depth of the setup, thus the position of the particles inside the channel is less critical.

A different approach is based on the interaction of particles with a tilted array or lattice of optical tweezers, where the drag force of the liquid is in the same range as the trapping force of each trap [41, 84]. Therefore, a particle is not fixed by single tweezers, but deflected at each trap from its initial flow direction. When passing the traps, the particle follows the tilt of the array and is moved all-optically from one side of the channel to the other side (see Fig. 4.5). Since the interaction between optical lattice and particle depends on its material and geometric properties, a continuous sorting of different particles is possible. A big advantage of this scheme is that no relative movement between microfluidic chip and laser spot is necessary.

In first experiments, the optical lattice was generated by interference of laser beams [84, 85] or by holographic techniques [41]. Caused by the losses at optical elements and the splitting of the laser beam, the power of each lattice point at the sample stage was in some experiments below 2 mW [41]. Applegate et al. [8] worked on a similar scheme, however the used light source in this case was a laser bar with a total power of 500 mW, which

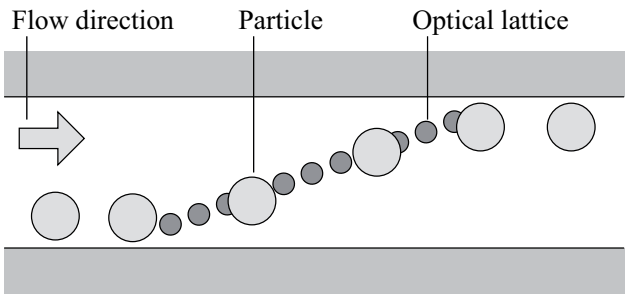

Fig. 4.5: Concept of continuous particle deflection at a tilted, linear optical lattice. While the particle passes the lattice, it follows the tilt of the array.

generated a linear lattice at the particle plane. Since the first demonstration of continuous particle deflection, numerous methods have been investigated to generate appropriate optical landscapes. Among them are standing waves [86], beam elongation by a cylindrical lens [87], the two-dimensional Talbot effect [88], microlens arrays [89] as well as arrays of parabolic micromirrors [90]. Recently, particle deflection was also achieved in the near-field of a microscope objective, which was excited by total internal reflection at the glass-liquid interface [91].

A common drawback of the described optical methods for microfluidic sorting is the still bulky setup, which is caused by extensive optics like objectives, gratings and modulators. It requires a good alignment and trained operators, and increases costs significantly. Losses at numerous optical elements limit the available optical power. Examinations preceding particle sorting are possible [7, 8], however, their number is limited by the space consuming trapping setup. Furthermore, parallelization of the sorting process by increasing the number of chips cannot be realized. Therefore, it is desirable to integrate the optical trap itself into the microfluidic system. A possibility is to guide the laser light by waveguides into the microfluidic channel, where a transverse optical trap is formed at the end of the waveguide. Jensen-McMullin et al. used two opposing glass fibers to achieve also a longitudinal fixation of particles [92]. By varying the power in one of the fibers, the position of trapped particles between the fiber ends could be controlled. In a modified scheme by Kühn et al., the fibers were substituted by planar waveguides and the channel itself was additionally used as bidirectional waveguide [93]. However, these schemes still require an external laser source and the accurate alignment of the waveguides in the fabrication process is demanding.

A higher integration level was achieved by Cran-McGreehin et al. by integrating two opposing edge-emitting AlGaAs laser diodes into the side walls of a microfluidic channel [94]. Optical output powers of 10 mW of each device were reached. Since the channel structure and the laser diodes are based on the same GaAs substrate and fabricated by lithographic techniques, ideal alignment is given. The complete fabrication from GaAs is however expensive and requires a dependable coating of the semiconductor surface to protect the biological material from toxic, electrical and thermal influences and to prevent oxidation of the semiconductor itself. Furthermore, the laser facets have to be fabricated by high quality dry etching, which further complicates the process. Owing to the highly divergent and asymmetric output beam of edge-emitting devices, the channel width was limited to 20 µm.

The VCSEL-based, integrated optical trap scheme presented in Sect. 3.1.3 offers an attractive alternative. The channel itself can be fabricated separately by glass or polymer and the laser chip can be directly attached by flip-chip bonding, for example. Therefore, the risk of chemical, electrical or thermal interaction can be minimized, while an exact alignment is still given. Furthermore, particle deflection and sorting at an optical array or lattice, as shown in Fig. 4.5, can be directly transferred to the integrated optical trap scheme, since two-dimensional laser arrays can be easily realized using VCSELs. A detailed investigation of this approach can be found in Chap. 7.

4.2 Realization of Microfluidic Systems

Materials for microfluidic systems should provide chemical and biological inertness as well as the possibility to structure micrometer-sized channel geometries. Silicon, glass and some types of polymers are most often used, since they offer the further advantage of low-cost fabrication. Silicon and glass are commonly structured by standard optical lithography and subsequent wet-chemical or dry etching. Polymers like polymethylmethacrylate (PMMA) or other thick photoresists can be directly structured via lithography or can be formed by hot embossing. The channels are sealed with bonding techniques, which commonly include high temperature steps and chemical treatment of the samples [5].

A more convenient way is offered by polydimethylsiloxane (PDMS), a transparent and inert elastomer. It can be structured using a molding technique, often referred to as soft lithography. Sealing by glass can be simply achieved due to adhesion, which is sufficient for low pressure applications. For permanent bonding, the connection can be enforced by a prior treatment in oxygen plasma. Although the use of PDMS yields some disadvantages, like swelling in chemical solvents and shrinking during fabrication, it is often used for prototyping of microfluidic channels, owing to straightforward fabrication and low costs [6].

4.2.1 Chip Fabrication by Polymer Molding

Figure 4.6 shows schematics of the soft lithographic fabrication process used in the scope of this thesis. At first, thick and stable SU8 photoresist is structured via standard lithography on a silicon wafer. It contains the negative image of the channel structure and serves as a master. The viscous PDMS is then poured over this mold. Since a cross-linking agent was added to the PDMS base before, it will get solid when cured at 65 °C for one hour. Afterwards, the elastic PDMS, which now contains a cast of the channel structures, can be peeled from the master. The master wafer is not damaged by this process, thus it can be used again for further chip molding. To close the channels, the PDMS is sealed against a cover glass. A prior treatment with oxygen plasma increases the surface energy of both materials by producing silanol groups on PDMS and hydroxyl functional groups (-OH) on glass. When brought into contact shortly after the plasma treatment, covalent

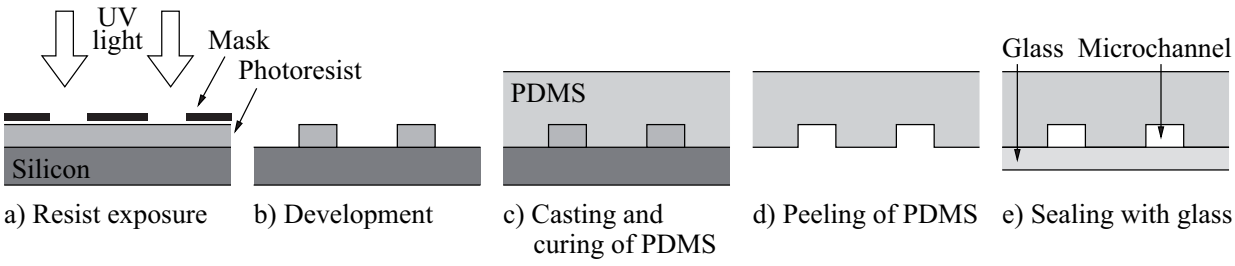

Fig. 4.6: Fabrication of microfluidic channels using a PDMS molding technique.

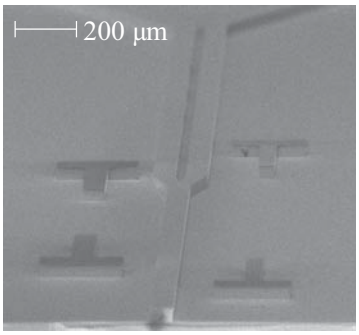

Fig. 4.7: SEM image of structured SU-8 resist of 40 µm height.

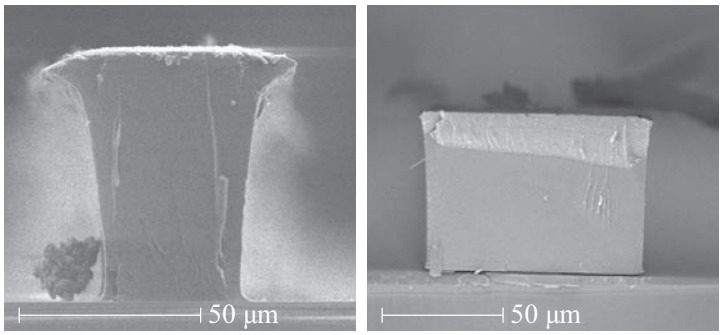

Fig. 4.8: Left: SEM image of a SU-8 structure showing typical T-topping. Right: reduced T-topping by lowering the power density during exposure.

-O-Si-O-bonds are formed between the materials and the connection becomes irreversible [6].

Figure 4.7 shows a scanning electron micrograph (SEM) of SU8 resist test structures with a height of 40 µm on a silicon wafer. SU8 is a negative resist, which is very sensitive in regard to exposure dose and power density. During exposure, acid is formed in the illuminated regions, which cross-links the resist during the following post exposure bake. For a high optical power density, the concentration of acid at the illuminated resist surface gets very high and acid diffuses into regions which were initially not exposed. This effect is enhanced if short wavelengths are used, since the absorption of SU8 increases significantly below 350 nm. This results in a large undercut, typically known as T-topping, which complicates the peeling of PDMS later on. The left side of Fig. 4.8 shows a SEM image of an example, which was caused by too high power density. T-topping could be avoided by exposure in intervals with wavelength of 360 to 400 nm and reduced power density. The SEM picture in the right side of Fig. 4.8 shows a cross-section of a resist structure with almost vertical side walls and reduced T-topping.

In Fig. 4.9, the layout of the fabricated microchannels is sketched. T- and Y-junctions with widths of 30 to 150 µm are considered. The channels have total lengths of about 20 mm and end in larger reservoirs to enable a connection to a macroscale liquid supply. Figure 4.10 presents a finished microfluidic PDMS chip, containing a T-junction with a channel width of 100 µm and a height of 50 µm. In this case the channels can be supplied with liquid via needles. Therefore, small holes are drilled into the PDMS with a thin wire, in which the thicker needles are inserted to connect the microchannel reservoirs. The PDMS tightly surrounds the needles and seals the connection.

4.2.2 Flow Control in Microfluidic Structures

The fluidic drag force on a spherical particle in a laminar flow is given by Stokes' law

$$F_{\text{drag}} = 3\pi\eta a\, v, \tag{4.10}$$

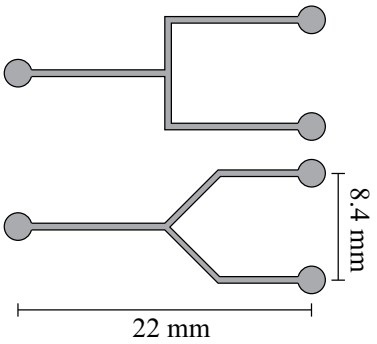

Fig. 4.9: Sketch of the microfluidic channel layout.

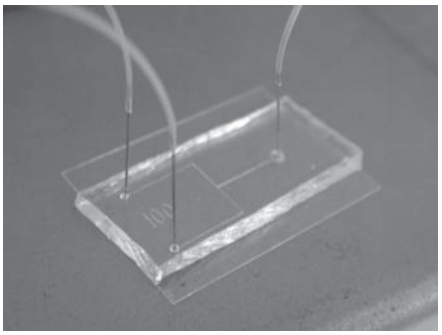

Fig. 4.10: A finished PDMS chip with a microfluidic T-junction. Fluid is injected by needles and micro tubes at the channel ports.

with η being the fluid viscosity, a being the diameter of the particle, and v being the fluid velocity [75]. As discussed in Chap. 2, the trapping force of optical tweezers is typically in the range of some piconewton. That means, a trapped particle can withstand a flow velocity of some 10 µm/s of the surrounding liquid. Therefore, similar fluid velocities should be achieved and controlled inside the microfluidic channels. A direct determination of the fluid velocity is however demanding. Instead, the movement of polystyrene particles inside the channel was observed and recorded by an imaging system with a CCD camera. By analyzing the corresponding video file, the particle velocity can be determined, where an error in measurement of about ±5 % has to be taken into account. It must be kept in mind, that the particles are located at the channel bottom, thus their velocity is smaller than the maximum fluid velocity at the channel center. Furthermore, they represent the mean fluid flow of a certain region rather than a certain point, due to their geometric extent of some micrometer.

A laminar flow inside microchannels can be generated either by applying a constant volume flow or a pressure difference between inlet and outlet, as described in Sect. 4.1.1. The former can be achieved by pumping a defined fluid volume per unit time into the channel. For microfluidic applications, the requirements on pump accuracy and constancy are high, since the considered volume flow is in the range of only some nl/s and a pulsating flow inside the channels has to be avoided. In the scope of this thesis, a high precision syringe pump for flow control was investigated, as shown in Fig. 4.11. Here, the syringe plunger is pushed automatically by a servo-motor with a ball screw, where the forward motion is computer controlled. The generated volume flow then depends on the inner diameter of the syringe. To realize small fluid velocities of some µm/s inside the channels, fragile syringes with plunger diameters of down to 0.1 mm have to be used, which can be easily damaged inside the mechanical setup. Furthermore, when connecting the syringe to the microchannel endings by microtubes, air bubbles inside the tubes are hardly avoidable. Since these bubbles are compressible, they lead to an inert and unstable flow control. Although a flow of polystyrene particles in the range of some 10 µm/s can be achieved, the approach was not further investigated, due to the high sensitivity of the system.

Pressure driven flow requires an accurately adjustable pressure difference between inlet and outlet. From the flow simulations presented in Sect. 4.1.1, a small difference of 5 Pa is

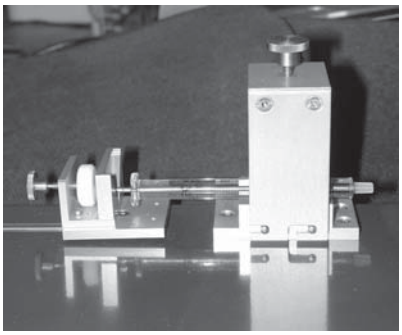

Fig. 4.11: Current driven flow: a syringe pump applies a constant volume flow to the microfluidic channel.

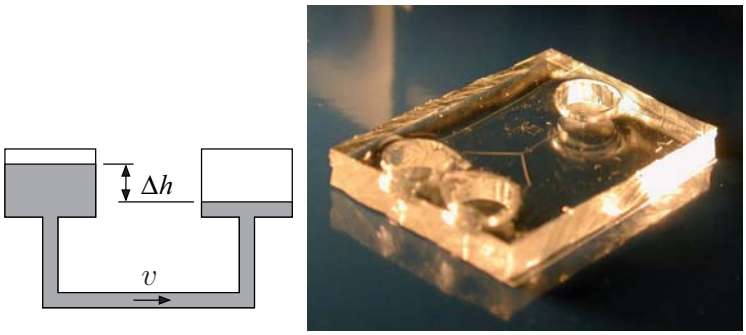

Fig. 4.12: Pressure driven flow: a difference in fluid level between inlet and outlet generates a pressure difference and thus a laminar flow. On the left a schematic of the concept, on the right realization by integrated reservoirs.

expected to create a maximum fluid velocity of about 60 µm/s. Furthermore, a compact setup without tubing is favorable, to decrease the sensitivity on external influences. This can be achieved by hydrostatic pressure, arising from a difference in fluid level between the channel endings. The left side of Fig. 4.12 shows a draft of the intended scheme and the right hand its implementation. The channels end in larger fluid reservoirs, which are easily accessible to enable a careful adjustment of the fluid level. According to (4.8), a height difference of Δh between the fluid levels leads to a maximum velocity of

$$v_{max} = \frac{\Delta p}{4\eta L} R^2 = \frac{\rho g \Delta h}{4\eta L} R^2 \tag{4.11}$$

at the center of a cylindrical pipe of radius R, where g is the gravitational constant and $\rho g \Delta h$ with the mass density ρ gives the difference in hydrostatic pressure. To keep the setup compact, the reservoirs are directly integrated into the PDMS chip by attaching an appropriate stamp during chip molding (see Fig. 4.13). The reservoirs have a diameter of 6 mm and the fluid level can be accurately adjusted by dosing a certain volume of liquid into the reservoirs with the syringe pump.

With this technique, it was possible to vary the particle velocity from only a few µm/s to more than 100 µm/s. On the left side of Fig. 4.14, the velocity of a 6 µm diameter particle inside a 80 µm wide channel is presented depending on the fluid volume dosed by the syringe pump into the reservoir. For better understanding, also the corresponding change in fluid level is given. As expected from (4.11), the relation is approximately linear. To assess the

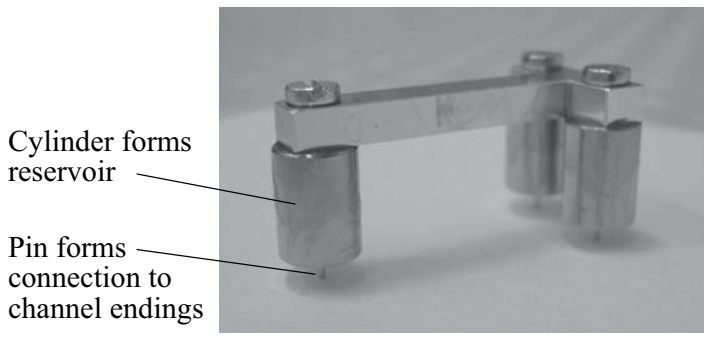

Fig. 4.13: Stamp used during PDMS chip molding. It allows a direct integration of reservoirs into the microfluidic chip.

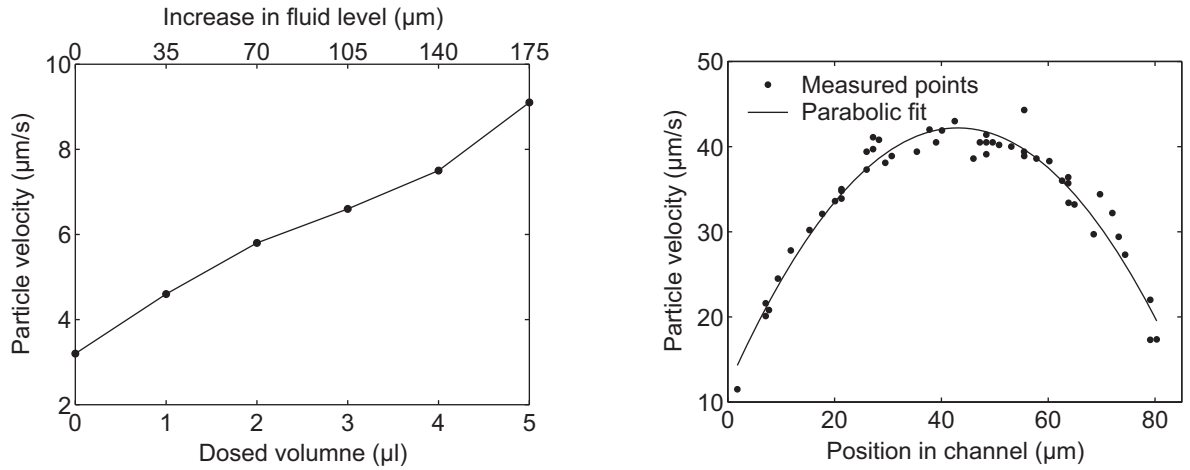

Fig. 4.14: Left: velocity of a 6 µm diameter particle inside a 80 µm wide channel plotted against the dosed fluid volume and the corresponding change in fluid level inside the reservoir. Right: velocities of the particles measured over a period of 10 min depending on their lateral position in the channel.

time stability of the flow, the velocity of the particles was determined in dependence on their lateral position in the channel for a period of 10 min. The result reflects the parabolic velocity profile of laminar flow, as shown on the right side of Fig. 4.14. No significant correlation between velocity deviations and elapsed time was determined.

5 VCSEL Based Optical Tweezers

The straightforward way to realize VCSEL based optical trapping is to insert the laser into a standard optical tweezers setup. In the scope of this thesis, such a setup was constructed and closely investigated. The key component is a high numerical aperture microscope objective, which tightly focuses the VCSEL beam, such that a three-dimensional trap is created in the sample plane. As it is commonly done, polystyrene microspheres solved in water were used for optical particle manipulation. As discussed in Chap. 2, the shape of the focused laser beam has a large influence on the trapping performance, therefore, single-mode as well as multi-mode VCSELs were applied for optical trapping and compared regarding the maximum achievable trapping forces. Besides solitary VCSEL devices, also two-dimensional arrays of standard and closely spaced VCSELs were used as laser sources to generate multiple optical tweezers at the sample stage. Furthermore, experiments on optical particle manipulation inside microfluidic channels were performed.

5.1 Experimental Setup

Figure 5.1 shows a schematic of the implemented tweezers setup. The VCSEL is mounted on a copper block and connected to a current source by a contact needle. The laser output beam is collected and collimated by a standard microscope objective. Then, the beam is tightly focused by an oil immersion microscope objective with a high numerical aperture of NA = 1.25 to form the optical tweezers. The focal point is located at the sample stage containing the microparticles. The diameter of the focal point can be estimated by the magnification V_{setup} of the optical system consisting of the collimating objective and the immersion objective. Assuming an ideally collimated beam, it is given by the ratio of the focal lengths of both objectives as

$$V_{\text{setup}} = \frac{f_{\text{immersion}}}{f_{\text{collimation}}} = \frac{1645\,\mu\text{m}}{12400\,\mu\text{m}} = 0.133. \tag{5.1}$$

A VCSEL with an internal beam waist of 6 µm would thus generate a focal point of about 0.8 µm diameter, if diffraction and imaging errors are neglected.

Unless otherwise noted, the sample stage consists of two cover slips separated by a PDMS spacer with a thickness of about 200 µm. The spacing is filled with polystyrene particles solved in water. The sample stage is connected to a computer-controlled positioning system and is therefore precisely movable in three dimensions. The experiments can be observed by an optical system mainly consisting of a white light illumination, a beam splitter and a CCD camera. An infrared cutoff filter is used to protect the camera from the laser beam, thus the laser light is not visible in the images.

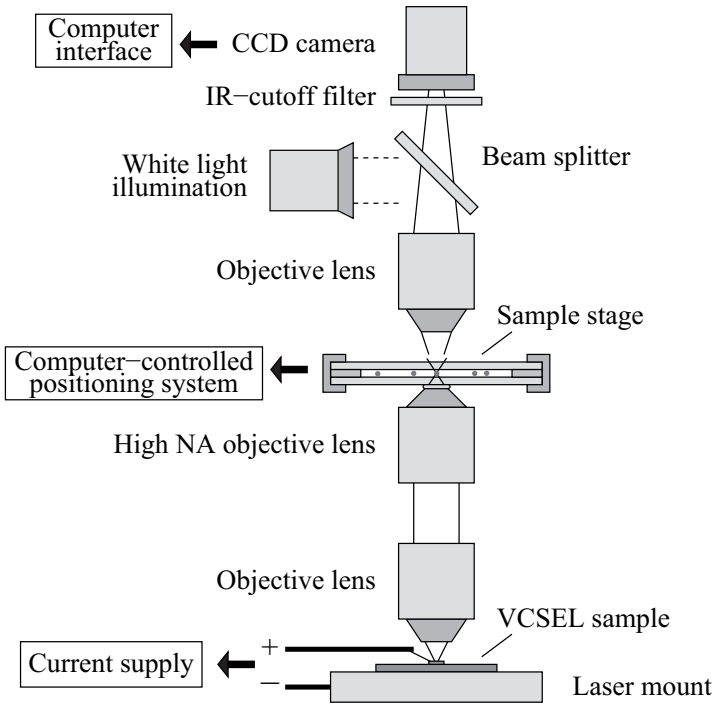

Fig. 5.1: Schematic of the VCSEL based optical tweezers setup.

All experiments were performed using polystyrene microparticles solved in water, which are available in accurately determined sizes with diameters of some ten nanometers up to 100 µm. Optical manipulation of polystyrene spheres is often reported in literature, since they closely resemble biological cells regarding refractive index and mass density (1.57 at 1000 nm wavelength and 1050 kg/m^3, respectively [95]). Like cells, they show only low absorption in the near infrared spectral range but they yield the advantage of much easier handling. However, due to their exact spherical shape and the low deformability, the achieved trapping forces differ to those exerted on living cells.

In Fig. 5.2 a typical trapping sequence taken by the CCD camera is presented. The experiment was performed with a standard solitary VCSEL and polystyrene particles of 10 µm diameter. By the optical system consisting of the collimating and the immersion objective not only the laser beam is imaged onto the sample stage, but also the VCSEL structure itself. Therefore, apart from the particles also an image of the VCSEL with its p-contact ring and part of the bond pad is visible in the picture (see Fig. 3.15 for comparison). This simplifies the adjustment of the setup, since the location of the optical tweezers is almost equal to the position of the VCSEL image. In Fig. 5.2a a particle in close proximity to the tweezers position can be seen. As the laser is turned on the particle is drawn toward the intensity maximum (see Figs. 5.2b and c). After about 3 s, the microsphere remains fixed at the position of the VCSEL image (Fig. 5.2d).

Once the microsphere is trapped, the stability against external forces can be checked by moving the sample stage, therefore also moving the liquid surrounding the particles. In Fig. 5.3a, a particle is already trapped by the VCSEL tweezers. Movement of the sample stage

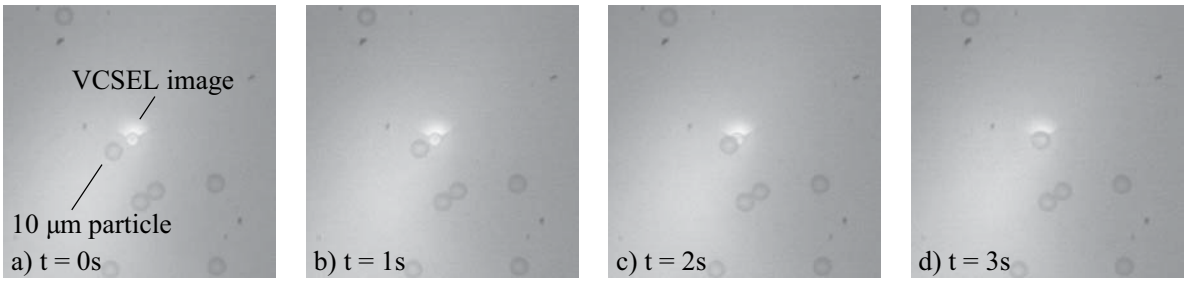

Fig. 5.2: CCD camera images of a typical trapping sequence: Besides the 10 µm polystyrene particles also an image of the VCSEL structure is visible, which marks the position of the optical trap. A particle in close proximity to the tweezers is attracted by the laser beam of 2.5 mW optical power, while other particles remain static.

with a velocity of 34 µm/s (see Figs. 5.3b and c) leads to a translation of the surrounding free particles. The trapped microsphere however is only slightly deflected from its initial position by the fluidic drag force. After the sample stage stops again, the particle returns to the center of the optical trap (Fig. 5.3d). This behavior underlines the analogy of an optical trap to a Hookean spring, as discussed in Sect. 2.1.

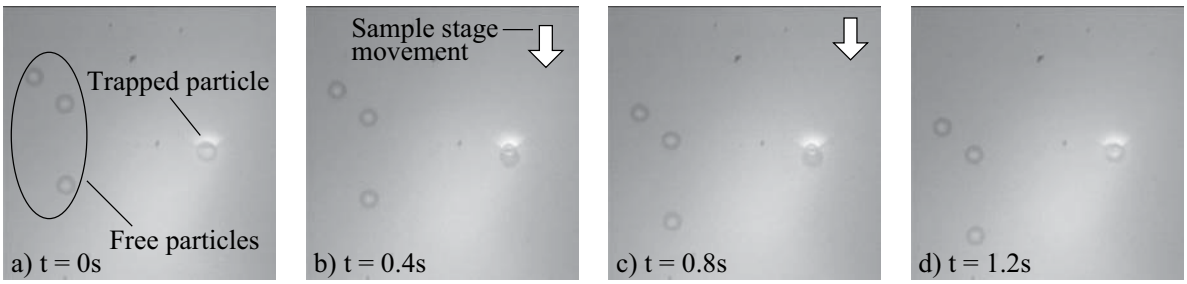

Fig. 5.3: Snapshots of an experiment demonstrating the stability of the trapped particle against external forces: As the sample stage is moved with a velocity of 34 µm/s (Figs. b and c) the free particles follow the movement, while the trapped particle is only slightly displaced from its initial position.

Since polystyrene particles are slightly denser than water, they sink to the bottom of the sample stage and are thus located directly at the lower cover glass. By lowering the sample stage while the position of the optical tweezers is kept constant, the longitudinal radiation forces acting on a trapped particle have to counteract the gravitational force. Thus, the three-dimensional trapping ability of the generated trap can be tested. Figure 5.4a shows a trapped particle which is, just as the free particles, located at the bottom of the sample chamber. Figure 5.4b shows the same arrangement after the sample stage was lowered by about 14 µm. The free particles appear blurred since they moved with the sample stage and are no longer in the focal plane of the imaging system. The trapped particle is however lifted and still well visible, therefore confirming the three-dimensional trapping ability of the setup.

To determine the optical power that is effectively contributing to the optical forces at the sample stage an integrating sphere is used, since the laser beam is strongly divergent after

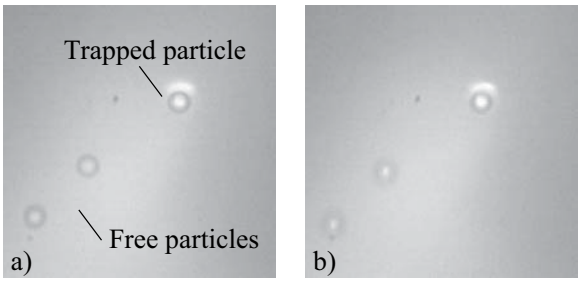

Fig. 5.4: CCD camera image showing a 10 µm particle trapped by the VCSEL tweezers (a). As the sample stage is lowered by about 14 µm, the free particles follow the movement and are thus blurred in the image, while the trapped particle is lifted by the longitudinal radiation force and is still well visible (b).

the tight focusing by the immersion objective. By removing sample stage and imaging optics, the integrating sphere can be placed directly above the high numerical aperture objective, thus collecting all of the laser light. Figure 5.5 shows the LI curve of a VCSEL measured at the position of the sample stage with and without immersion objective. A power loss of about 40 % can be observed. This is partly due to the reduced transmittance of the immersion objective of only 80 % at a wavelength of 850 nm. Furthermore, clipping of the collimated laser beam at the input aperture of the objective has to be considered, which has a diameter of just 4 mm. For the trapping experiments presented in Figs. 5.2, 5.3 and 5.4 an optical power of 2.5 mW was observed using a different VCSEL.

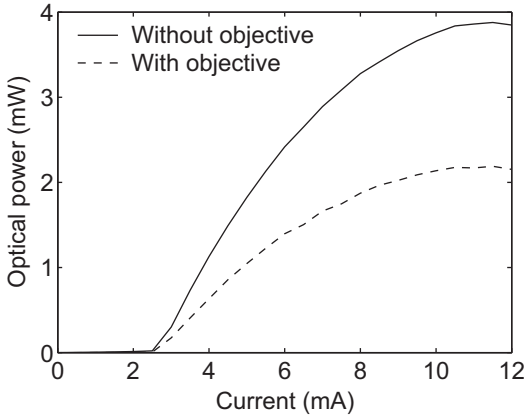

Fig. 5.5: LI characteristics of a VCSEL measured with an integrating sphere at the position of the sample stage with and without the immersion objective. There is a power loss of about 40 %.

5.2 Characterization of Solitary VCSEL Tweezers

To study the trapping properties of VCSELs, optical tweezers based on solitary VCSEL devices were investigated. Besides the comparison of single-mode and multi-mode devices, the attention was directed on the influence of the particle size. Characterization of the optical tweezers demands quantification of the achieved trapping strength. This is often done by assuming a harmonic trapping potential and determining the trap stiffness κ, as given in (2.14). A straightforward way is to apply a known force on a trapped particle and to measure the resulting particle displacement from the trap center, for example by a quadrant photodetector. In most cases, the force is exerted by fluidic drag, but also thermal fluctuations caused by Brownian motion can be utilized. A second quantity displaying the trapping strength is the maximum transverse trapping force, which was investigated in the scope of this thesis.

5.2.1 Measurements of the Transverse Trapping Force

The maximum transverse trapping force is equal to the maximum external force a trapped particle can withstand without leaving the trap. The easiest way to apply an external force in the transverse direction is to move the sample stage including the contained liquid. The fluidic drag force then deflects the trapped particle from its initial position, as already shown in Fig. 5.3. If the fluidic drag force is larger than the transverse trapping force, the particle breaks out of the tweezers. This is comparable to the breaking of a spring under too large stress.

Since a laminar flow can be assumed in the present case, the force on the trapped particle caused by the moving liquid is given by Stokes' law

$$F_{\mathrm{drag}} = 3\pi\eta a\, v_{\mathrm{stage}}, \tag{5.2}$$

where η is the viscosity of the medium, a is the diameter of the trapped particle, and v_{stage} is the fluid velocity, which is equal to the stage velocity [75]. Often a further factor is considered, which accounts for the proximity of the lower glass slide at the bottom of the sample chamber. In contrast to the fluid this wall presents a hard boundary, which cannot adapt to the stationary particle. Therefore, the exerted drag force is increased by a factor c_{faxen}, which is given by Faxen's law as

$$c_{\mathrm{faxen}} = \left(1 - \frac{9}{16}\left(\frac{a}{2l}\right) + \frac{1}{8}\left(\frac{a}{2l}\right)^3 - \frac{45}{256}\left(\frac{a}{2l}\right)^4 - \frac{1}{16}\left(\frac{a}{2l}\right)^5\right)^{-1}, \tag{5.3}$$

with l being the distance between particle center and the surface [96]. However, in the experiment the exact value of l is hard to determine. Furthermore, surface effects or curling of the particle can also influence the result. Therefore, all following experiments were performed with the trapped particle being well above the chamber bottom, what is achieved by lowering the sample stage as already shown in Fig. 5.4. Since c_{faxen} approaches 1 for large distances $l \gg a/2$, it is not further considered (e.g., $c_{\mathrm{faxen}} = 0.91$ for $l = 3a$). The maximum transverse trapping force is therefore given by

$$F_{\mathrm{trap}} = 3\pi\eta a\, v_{\mathrm{stage,max}}, \tag{5.4}$$

with $v_{\mathrm{stage,max}}$ being the maximum stage velocity at which the particle is still trapped.

The measurement procedure is as follows. A particle is trapped and lifted well above the lower cover slip. Then, the sample stage is moved with a certain velocity forward and backward two times. If the particle withstands the resulting drag force, which is applied for at least 5 s, it is considered stably trapped. Subsequently, the stage velocity is increased by 0.7 µm/s and the trapping stability is checked again. The procedure is repeated until the fluid drag becomes too strong and the particle leaves the tweezers. Thereby, the maximum stage velocity $v_{\mathrm{stage,max}}$ and the corresponding trapping force F_{trap} can be found for a given laser current. However, it has to be considered, that the positive error for $v_{\mathrm{stage,max}}$ is equal to the velocity steps during the procedure, that is 0.7 µm/s. This diminishes the measurement accuracy especially for low trapping forces. Furthermore, a change of about 1 % in the viscosity of water due to temperature variations during the measurement has

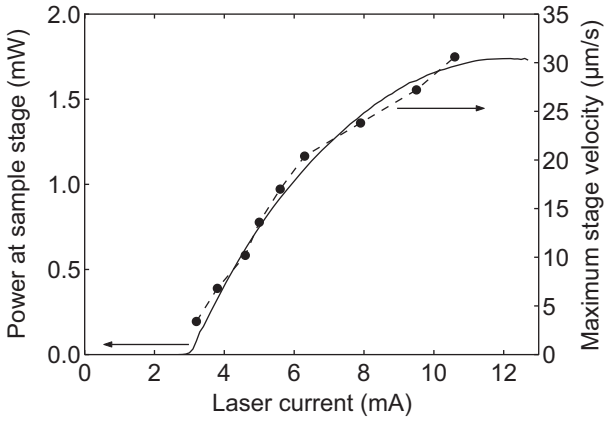

Fig. 5.6: Maximum stage velocity at which a 6 µm particle remains in the optical trap and corresponding optical power at the sample stage depending on the VCSEL driving current.

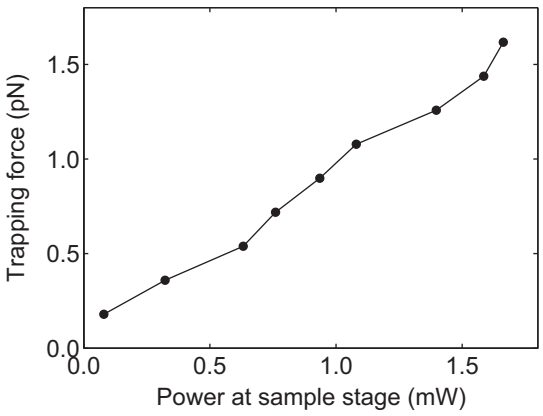

Fig. 5.7: Trapping force calculated from Fig. 5.6 plotted against the optical power at the sample stage.

to be taken into account. This sums up to a positive relative error of about 2 to 8 % for the determined trapping force within one series of measurement, which gets however significantly higher for stage velocities below 10 µm/s. When comparing different series of measurements, where nominally identical but different particles are used, the maximum deviation of the nominal particle radius of ±10 % has to be considered additionally.

Figure 5.6 shows an examplary measurement for a single-mode VCSEL and trapping of 6 µm polystyrene particles. The optical power measured at the sample stage shows a maximum of 1.7 mW. The maximum stage velocity the trap can withstand increases with available optical power and reaches about 30 µm/s. By using (5.4) with $\eta = 935 \cdot 10^{-6}$ kg/(ms), the transverse trapping force equals 1.7 pN at 1.6 mW optical power. Figure 5.7 displays the complete trapping characteristic. As expected from theory, the trapping force scales approximately linearly with optical power.

5.2.2 Influence of the Particle Size on the Trapping Performance

To examine the range of operation of the optical tweezers system, trapping of polystyrene particles of different diameter is investigated by measuring the transverse trapping force as described in the previous section. As laser source, a single-mode VCSEL with an oxide aperture of 6 µm is used, which offers a maximum optical power of 2.3 mW at the sample stage. Single-mode emission is achieved by an inverted surface relief with a diameter of 2.6 µm.

Basically, stable trapping of polystyrene particles with 2, 4, 6, 10 and 15 µm diameter could be demonstrated. Manipulation of even smaller spheres is not limited by the optical trap itself, but by the used imaging system, since structures of only 1 µm size are hardly visible. However, also a detailed characterization of the trapping force exerted on 2 µm particles is complicated. According to (5.2), small particles require higher sample stage velocities to generate a certain fluidic drag force. The measurement procedure requires such high

velocities to be kept for at least 5 s. So the sample stage has to be moved over a large distance in the range of 300 µm, along which collision or interference with free particles is hardly avoidable.

Therefore, the transverse trapping force was studied on four different particle sizes, as shown in Fig. 5.8. Furthermore, the corresponding Q-value is depicted in Fig. 5.9. It was already defined in (2.15) to be

$$Q = \frac{F_{\mathrm{trap}}}{P}\frac{c}{n_{\mathrm{m}}}, \tag{5.5}$$

where F_{trap} is the maximum transverse trapping force, c is the speed of light and n_{m} is the refractive index of the medium surrounding the particle.

According to the theory discussed in Chap. 2, a higher transverse trapping force is expected for larger particles, since they experience a stronger relative intensity gradient. This is confirmed regarding 4, 6 and 10 µm particles. A maximum trapping force of 2.6 pN is achieved for 10 µm particles, corresponding to a Q-value of 0.27. However, the maximum achieved trapping force and the corresponding Q-value for 15 µm diameter particles are only 2.3 pN and 0.24, respectively. This is believed to be caused by the more than three times higher weight of the 15 µm beads compared to the 10 µm beads. The longitudinal position of a trapped particle is given by the equilibrium of scattering force, axial gradient force and gravitational force. Most probably, the 15 µm particle is located at a lower position in the optical tweezers, where the beam is much broader, thus experiencing a smaller transverse gradient force. This agrees with the observation, that for low optical power, also the trapping performance for 10 µm particles decreases significantly.

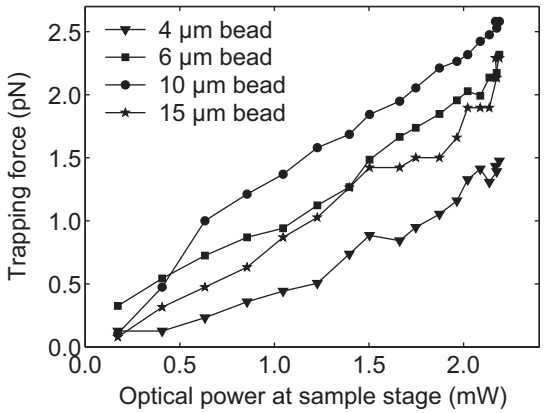

Fig. 5.8: Trapping forces for polystyrene particles of different diameter depending on the optical power at the sample stage.

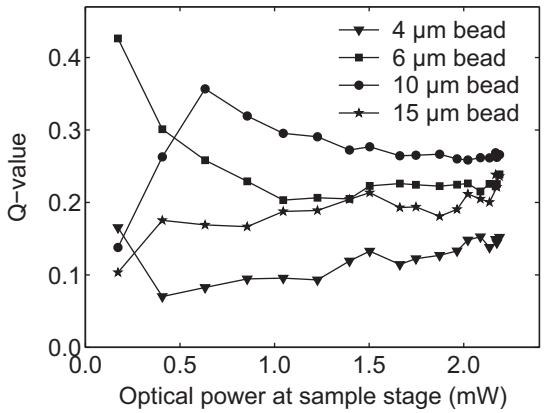

Fig. 5.9: Q-values calculated from the trapping forces in Fig. 5.8, plotted against the optical power at the sample stage for different particle sizes.

5.2.3 Comparison of Single-Mode and Multi-Mode VCSELs

As discussed in Chap. 2 the transverse trapping force does not only depend on particle size and available optical power. Especially the intensity profile of the beam as well as the

strength of the optical gradient have a large influence. Since the beam characteristics of single-mode and multi-mode VCSELs differ significantly, also a difference in their trapping characteristic is to be expected.

Figure 5.10 shows the output characteristics of two VCSEL devices, which are investigated in detail in the following. Both lasers originate from the same sample and have an active diameter of about 6 µm. While a 2.6 µm diameter inverted surface relief is etched into the output facet of the relief device, the antiphase layer is completely removed in case of the standard device. The optical spectra given in Fig. 5.11 confirm the expected multi-mode emission for the standard VCSEL, while for the relief VCSEL only the fundamental mode is lasing up to thermal rollover.

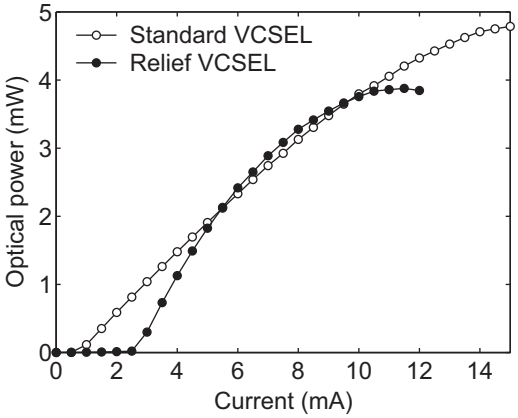

Fig. 5.10: LI characteristics of a standard and a relief VCSEL (2.6 µm relief diameter) from the same sample with 6 µm oxide aperture.

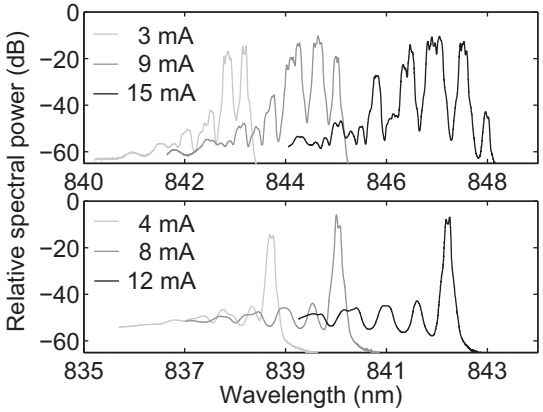

Fig. 5.11: Optical spectra of the standard (multi-mode, top) and relief (single-mode, bottom) VCSELs from Fig. 5.10 at different driving currents.

To describe the beam propagation and beam quality of the lasers, the M^2 quality factor concept introduced in [97] is applied. First, an ideal Gaussian beam with a beam waist of $2\bar{w}_0$ is considered, as shown by the gray line in Fig. 5.12. In the far-field region the beam propagates with the constant divergence or far-field angle $\bar{\theta}_{\mathrm{FF}}$. In free space, the relation of $\bar{w}_0$ and $\bar{\theta}_{\mathrm{FF}}$ is given by

$$\bar{\theta}_{\mathrm{FF}} \approx \tan\bar{\theta}_{\mathrm{FF}} = \frac{\lambda}{\pi\bar{w}_0}, \tag{5.6}$$

with λ being the wavelength of light [98]. A real beam commonly deviates from an ideal Gaussian beam by having a larger beam waist $2w_0$ or far-field angle θ_{FF} or, generally, having both, as shown by the black line in Fig. 5.12. Now, the product of w_0 and θ_{FF} is in contrast to (5.6) given by [99]

$$\theta_{\mathrm{FF}} \cdot w_0 = M^2\frac{\lambda}{\pi}. \tag{5.7}$$

The quality factor M^2 thus describes how similar a beam is to an ideal Gaussian beam. It is commonly larger than one for a real laser beam.

The beam quality factor of both investigated VCSELs was measured using a device called "mode master" (see App. A). Figure 5.13 gives the determined values in dependence on

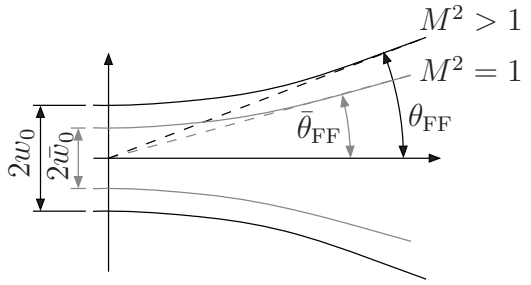

Fig. 5.12: Sketch of an ideal (gray line) and a real (black line) Gaussian beam, where the latter has an M^2 quality factor larger than one.

the laser driving current. While the M^2-factor for the single-mode laser has a low value of about 1.25, which is almost independent of the point of operation, it increases significantly to more than 4.0 for the multi-mode laser. This is due to the onset of higher-order transverse modes, which show a worse beam quality than the fundamental mode.

Furthermore, the far-field of the lasers was examined, where the obtained intensity profiles are similar to the measurements presented in Sect. 3.1.2, that is, the single-mode VCSEL emits a Gaussian-shaped beam profile, while the far-field intensity distribution of the multi-mode laser shows typical side lobes. The strength of these lobes increases with increasing driving current. For a fundamental mode Gaussian beam, the divergence angle can be determined from the $1/e^2$ decay of the maximum in the far-field intensity profile. However, this is not possible if higher-order modes are involved. Therefore, the far-field angle was determined from the intensity distribution $\mathcal{I}(\theta)$ by calculating the second moment or standard deviation σ

$$\theta_{\mathrm{FF}} = 0.5\,\sigma^2 = 0.5\,\frac{\sum \mathcal{I}\cdot(\theta-\bar{\theta})^2}{\sum \mathcal{I}} \quad \text{with} \quad \bar{\theta} = \frac{\sum \mathcal{I}\cdot\theta}{\sum \mathcal{I}}. \tag{5.8}$$

The resulting far-field angles at different driving currents are displayed in Fig. 5.14. Similar to the beam quality factor, an almost constant value is determined for the single-mode laser, while the divergence of the multi-mode laser increases strongly up to 17°.

Using (5.7), the internal beam waist of the VCSELs can be deduced from the values in

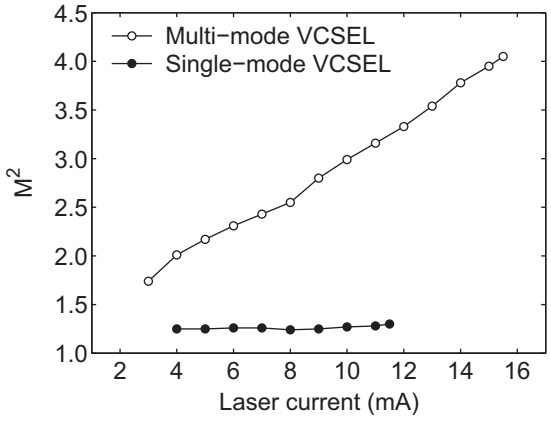

Fig. 5.13: Measured M^2-quality factors for the standard multi-mode and single-mode VCSEL from Fig. 5.10.

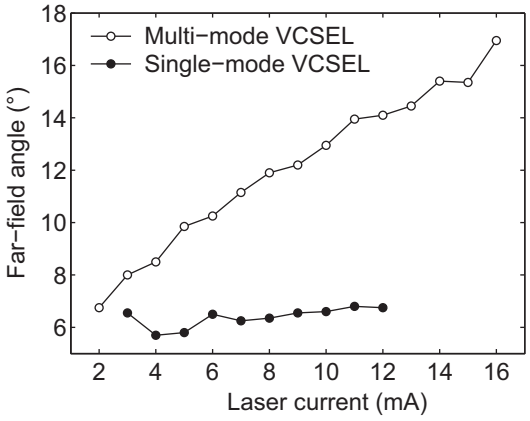

Fig. 5.14: Measured far-field angle for the standard multi-mode and the single-mode VCSEL from Fig. 5.10.

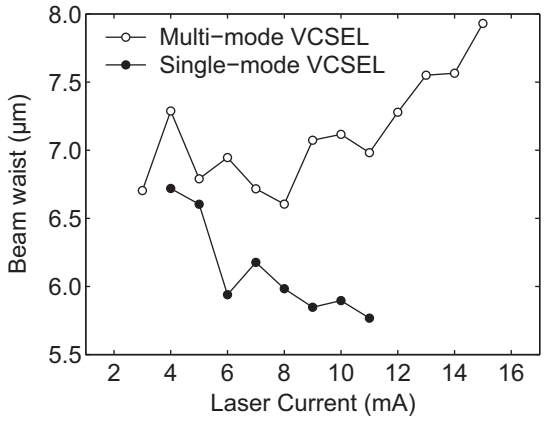

Fig. 5.15: Internal beam waist for the multi-mode and the single-mode VCSEL calculated from Figs. 5.13 and 5.14.

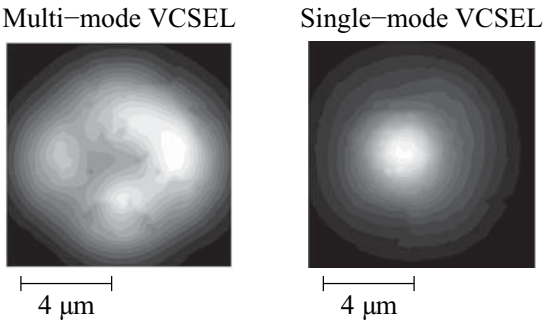

Fig. 5.16: Near-field measurements for the multi-mode and the single-mode VCSEL from Fig. 5.10 taken at 11 mA driving current.

Figs. 5.13 and 5.14. The results shown in Fig. 5.15 appear discontinuous, owing to the measurement errors in the far-field angle and the quality factor. Nevertheless, a shrinkage of the internal beam waist with increasing current can be clearly observed for the single-mode VCSEL, which is also visible in a slight increase of the beam divergence (see Fig. 5.14). The cause is most probably thermal lensing due to internal heating of the device. In contrast, the internal beam waist of the multi-mode VCSEL has an increasing tendency. Although thermal lensing surely occurs as well, the behavior is dominated by the onset of higher-order modes, which penetrate deeper into the VCSEL cross-section. Surprisingly, in both devices the beam waist is found to be partially larger than the 6 µm active diameter of the VCSELs. It has to be mentioned, that both devices show a slightly asymmetric beam propagation and all given values are the average of the values obtained in $\langle 011 \rangle$ and $\langle 0\bar{1}1 \rangle$-direction. The characterization of the beam propagation is completed by near-field measurements for both VCSELs. As expected, the relief laser emits a Gaussian-like intensity profile (see right side of Fig. 5.16), while the multi-mode VCSEL shows the typical donut-shaped profile (Fig. 5.16 left). Both measurements were taken at 11 mA.

Figures 5.17 and 5.18 show the determined trapping forces of both lasers for particles with 6 and 10 µm diameter in dependence on the optical power at the sample stage. Furthermore, the corresponding Q-values are given in the lower graphs. In agreement with the observations in the previous section, both devices lead to higher trapping forces for the larger particles, since they experience a stronger relative intensity gradient. However, a stronger longitudinal gradient force is necessary to overcome their larger weight, leading again to only weak trapping at small powers. Strikingly, the multi-mode laser offers less optical power at the sample stage than the single-mode laser. The power increases to a maximum value of about 1.5 mW at 8 mA and decreases for higher currents, although thermal rollover does not occur up to 15.5 mA (see Fig. 5.10). Nevertheless, for both particle sizes, the multi-mode VCSEL leads to higher or at least similar Q-values at the same power level, indicating a higher stability of the optical trap.

Possible explanations are given by the different beam characteristics of both lasers. Figure 5.19 shows the beam propagation inside the optical tweezers setup for the single-mode and

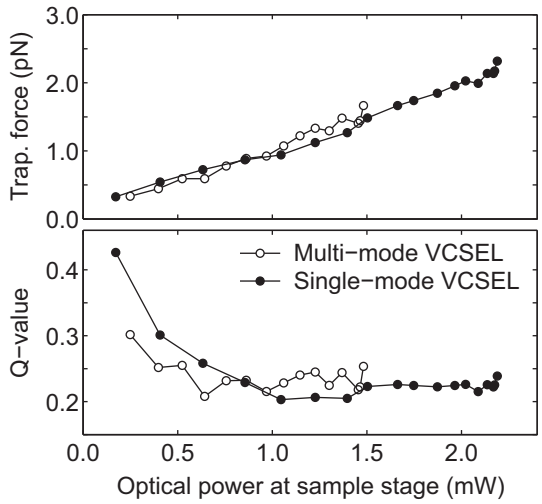

Fig. 5.17: Measured trapping force (top) and corresponding Q-value (bottom) for trapping of 6 µm particles with multi-mode and single-mode VCSELs.

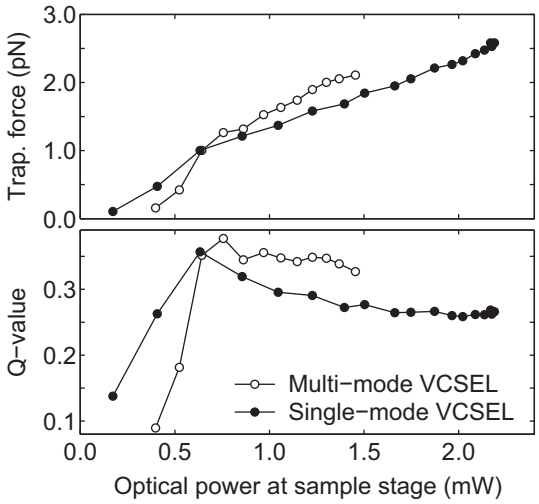

Fig. 5.18: Same as Fig. 5.17 but with particles of 10 µm diameter.

multi-mode VCSEL. The calculation is based on the so-called ABCD matrix method for Gaussian beams, where every optical element, like interfaces or lenses, can be described by a transfer matrix (see App. E). The determined values for the beam quality factor and the beam waist given in Figs. 5.13 and 5.15, as well as the actual dimensions of the setup are included. The lower and the immersion objective are modelled as lenses with focal lengths of 12.4 mm and 1.645 mm, respectively. For the immersion oil and the glass slides $\bar{n} = 1.5$ and for water $\bar{n} = 1.33$ is taken into account. The back side aperture of the immersion objective with a diameter of 4 mm is indicated in Fig. 5.19 as well. The beam propagation of the single-mode VCSEL is almost indifferent about the point of operation, regarding beam quality and divergence. Therefore, the course of the beam waist is given for only one operation point (see dashed line in Fig. 5.19). Owing to the low beam divergence, no significant interaction with the back side aperture of the high NA objective takes place. Since the multi-mode VCSEL shows a much higher divergence, its beam occupies a larger fraction of the aperture, even at a low driving current (see light gray line). This results in a stronger longitudinal intensity gradient at the sample stage and therefore in an increase of the axial stability, as shown in the magnified section of the sample stage area. Because the divergence rises with increasing current, the illuminated area of the back side aperture increases (see dark gray line). Eventually, a cutoff at the aperture occurs at higher currents which reduces the available optical power at the sample stage significantly, as demonstrated by the black line in Fig. 5.19.

A further issue is the transverse beam profile at the sample stage. The larger internal beam waist of the multi-mode VCSEL results in a broader focal point at the sample stage of 0.9 to 1.0 µm compared to 0.8 µm for the single-mode device. Therefore, a lower transverse gradient force is to be expected. However, a donut-shaped output beam has more complex effects on the transverse trapping force compared to a Gaussian beam shape. On the one

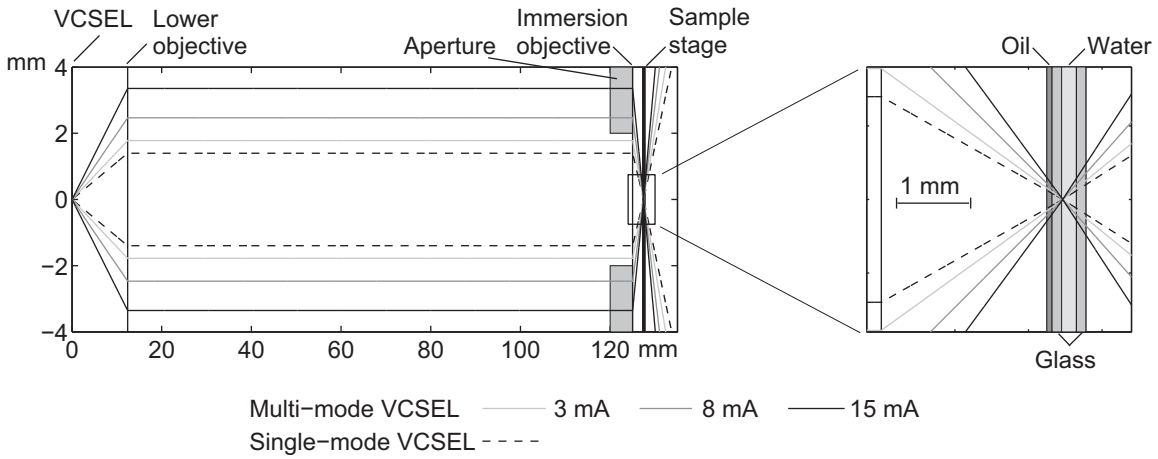

Fig. 5.19: Beam propagation inside the optical tweezers setup for the single-mode and the multi-mode VCSEL calculated with the ABCD matrix method. The calculation is based on the actual setup dimensions and the VCSEL characteristics from Figs. 5.13 and 5.14.

hand, besides the beam center additional equilibrium positions exist at the periphery of the beam, where the particle experiences no transverse net force, resulting in a reduced stability of the trap. On the other hand, those rays of the tightly focused beam which hit the sphere under a large angle contribute strongly to the longitudinal and transverse gradient forces, whereas rays at the beam center induce only a forward scattering force [63]. This effect is also confirmed by the calculations of the trapping force given in Sect. 2.1.2. Therefore, a donut-shaped beam profile offers a higher axial trapping force.

In summary, the properties of the multi-mode output beam support a higher axial trapping force of the tweezers, while the transverse stability is probably reduced. The strength and the ratio of both effects depend however strongly on the operation point of the VCSEL. Therefore, the optical trapping properties of multi-mode VCSELs are much more complex than of single-mode VCSELs. The results however indicate an increased total stability of the trap, especially at higher driving currents.

An unexpected effect on the trapping force is found for the multi-mode VCSEL at driving currents higher than 8 mA. Although the beam cutoff at the back side aperture of the immersion objective already leads to a decrease of the optical power at the sample stage, a further significant increase of the trapping force is observed. Figure 5.20 shows a maximum trapping force for 10 µm particles of 2.6 pN, which is connected to a high Q-value of 0.4. The increase can be explained by the beam cutoff at the objective aperture. Ignoring any diffraction, it results in a cropped focal point at the sample stage, which possesses a high intensity gradient. So even for a low power level at the sample stage a high trap stability can be achieved. Therefore, an overfilled objective aperture is basically beneficial [20].

5.2.4 Trapping Force Optimization for Multi-Mode VCSELs

For a further increase of the trapping forces, the optical power at the sample stage has to be increased, especially with regard to large size particle manipulation where higher weights

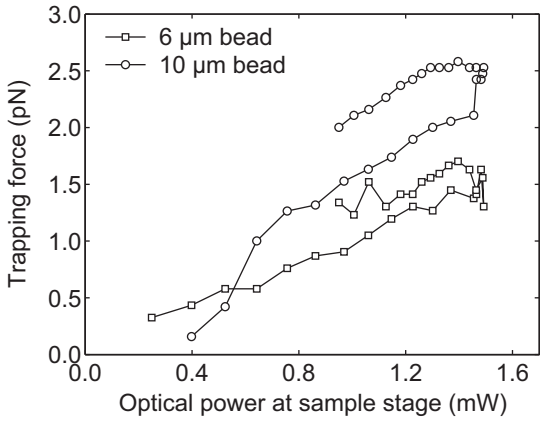

Fig. 5.20: Trapping force achieved with the multi-mode VCSEL for 6 and 10 µm particles. For a laser current of more than 8 mA the optical power at the sample stage decreases due to beam clipping at the objective aperture. However, a further increase of the trapping force is observed.

have to be dealt with. In order to decrease the cutoff losses, the lower objective can be adjusted to focus the VCSEL output beam and to decrease the beam diameter at the input aperture of the high NA objective. Figure 5.21 shows the calculated beam propagation in the tweezers setup for the multi-mode VCSEL at a driving current of 12 mA. By increasing the distance between VCSEL source and lower objective, the desired shrinkage of the beam diameter can be achieved. Figure 5.22 shows measured light-current characteristics for different positions of the lower objective from −0.1 to +0.6 mm, where the 0 mm position refers to a collimated beam. The increase of optical power from 1.5 to 3.7 mW confirms the reduction of beam cutoff. However, by lifting the lower objective, the laser beam is already convergent when entering the immersion objective and thus the longitudinal intensity gradient of the optical tweezers becomes smaller, as shown in the magnified section of Fig. 5.21. Furthermore, the calculations show an increase of the beam diameter at the focal point from 1.0 µm to 1.3 µm, if any cutoff effects at the back side aperture are neglected. Thus, the overall trapping efficiency decreases.

Therefore, an optimum level of focusing for maximum trapping forces has to be determined, which also depends on the particle size. Figure 5.23 shows the trapping characteristics for 6

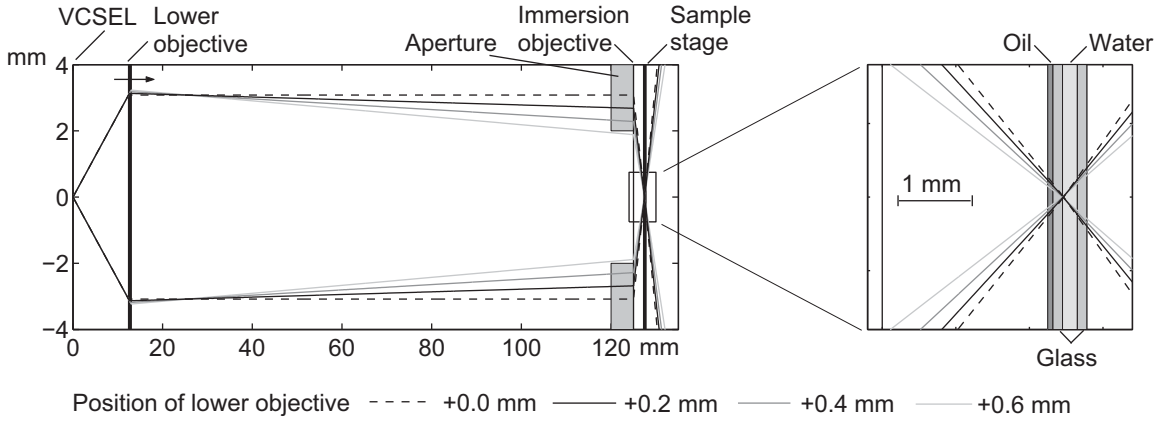

Fig. 5.21: Beam propagation inside the optical tweezers setup for the multi-mode VCSEL at different positions of the lower objective. The calculation is based on the VCSEL characteristics from Figs. 5.13 and 5.14 at 12 mA.

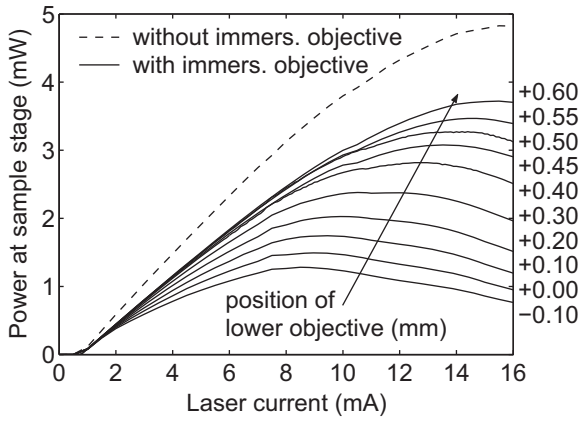

Fig. 5.22: Power at the sample stage for different positions of the lower objective, where 0 mm corresponds to a collimated beam. Here, significant cutoff losses are observed.

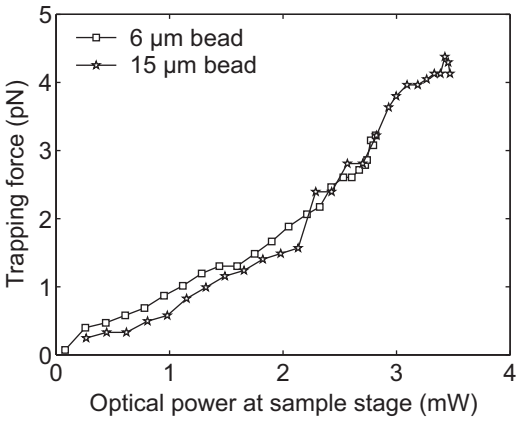

Fig. 5.23: Trapping forces on 6 and 10 µm particles using the multi-mode VCSEL and an optimized adjustment of the lower objective.

and 15 µm polystyrene particles for optimized input beam correction. The highest trapping force for the 15 µm beads is obtained when the lower objective is lifted by +0.55 mm, while the optimum for 6 µm particles is found at a position of +0.4 mm. The corresponding smaller focusing level is attributed to the higher sensitivity of smaller particles to weaker intensity gradients. Therefore, the maximum available output power is only 2.8 mW for the 6 µm beads compared to 3.4 mW for the 15 µm particles, since part of the laser beam is still truncated at the microscope objective. With the optimized adjustment, maximum trapping forces of 3.3 pN for 6 µm and 4.4 pN for 15 µm particles were reached, respectively. The results show that effective trapping can be realized with transverse multi-mode VCSELs, so the power limitation of single-mode lasers can be overcome.

5.2.5 Application in Microfluidics

The easiest way to manipulate particles optically inside a microfluidic channel is to substitute the sample stage in the optical tweezers setup by a microfluidic chip as presented in Fig. 4.12. Figure 5.24 shows the operation characteristics of the VCSEL used for this experiment. It has an active diameter of 8 µm and thus emits higher-order transverse modes at about 865 nm wavelength. A threshold current of 1.8 mA and a maximum output power of 8.7 mW are obtained. The trapping force obtained from this device was optimized as described in the previous section by prefocusing the laser output beam. However, due to optical losses and beam truncation, the power at the sample stage is still significantly smaller than the maximum output power of the laser.

The first trapping experiments revealed a major difference between handling of microspheres inside the commonly used sample stage and catching particles from a microfluidic flow. When trapping 4 µm diameter beads, the particle can withstand sample stage movements of more than 60 µm/s using an optical power at the sample stage of 2.5 mW, corresponding

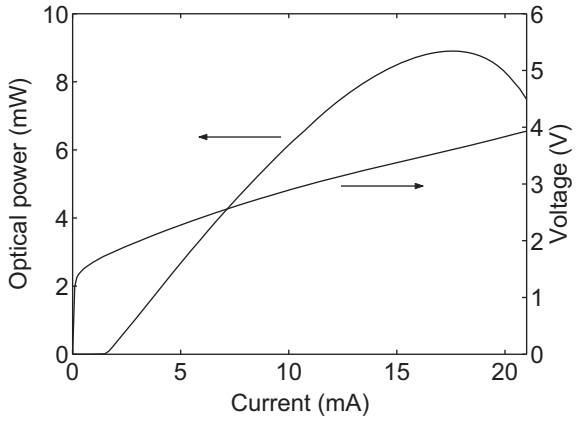

Fig. 5.24: LIV characteristics of the standard multi-mode VCSEL used for particle deflection. The VCSEL has an active diameter of about 8 µm and emits a maximum optical power of 8.7 mW.

to a trapping force of about 2.1 pN. However, when catching 4 µm beads inside a microfluidic channel, where a continuous flow was achieved by applying hydrostatic pressure, the particle velocity must not exceed 25 µm/s. Otherwise the particle escapes the trap. This corresponds to a reduction of the trapping efficiency of 60 %, leading to a strong reduction of the possible particle throughput. A possible explanation is given by the parabolic velocity profile of the laminar flow inside the microfluidic channel. Since the used polystyrene particles are slightly denser than water, they are located at the channel bottom, where they are moved forward by relatively low liquid velocities. If the sphere is moved slightly upwards by the scattering force when attracted by the optical tweezers, it is exposed to a significantly higher drag force. This explanation is also supported by the observation that the particle flows faster after it escapes the optical trap.

Nevertheless, optical particle manipulation inside microfluidic channels was achieved. Figure 5.25 shows snapshots of a particle deflection experiment using the above laser, where the optical power at the sample plane is 2.1 mW. The inlet of the microfluidic T-junction has a width of about 100 µm, the outlet branches are 50 µm wide. The polystyrene particles have a diameter of 4 µm and are flowing from left to right with a velocity of up to 20 µm/s, depending on their position in the channel. Furthermore, the optical image of the VCSEL structure with its rectangular bond pad is visible at the sample stage, which also marks the position of the optical tweezers. In Fig. 5.25a, a particle is already trapped by the laser beam. Now, the microfluidic channel is moved relatively to the laser beam, and in Fig. 5.25b, the trapped particle reaches the lower channel side-wall. By switching off the laser for a moment, the particle is released from the trap (Fig. 5.25c), and in Fig. 5.25d it flows to the lower channel outlet. With the laser switched on again, a second particle is trapped by the tweezers (Fig. 5.25d), which would have reached the lower channel outlet due to the laminar flow in microfluidic channels. Instead, it is now moved to the other side of the microfluidic channel by the VCSEL tweezers (Fig. 5.25e) and, after being released, flows to the upper channel outlet.

With the presented procedure, particle fixation and sorting can be easily performed using a small-sized and low-cost laser source. However, a manual handling of the setup is still necessary and the fluid velocities are comparatively small. Therefore, an advanced scheme using linear VCSEL arrays is investigated in the following section.

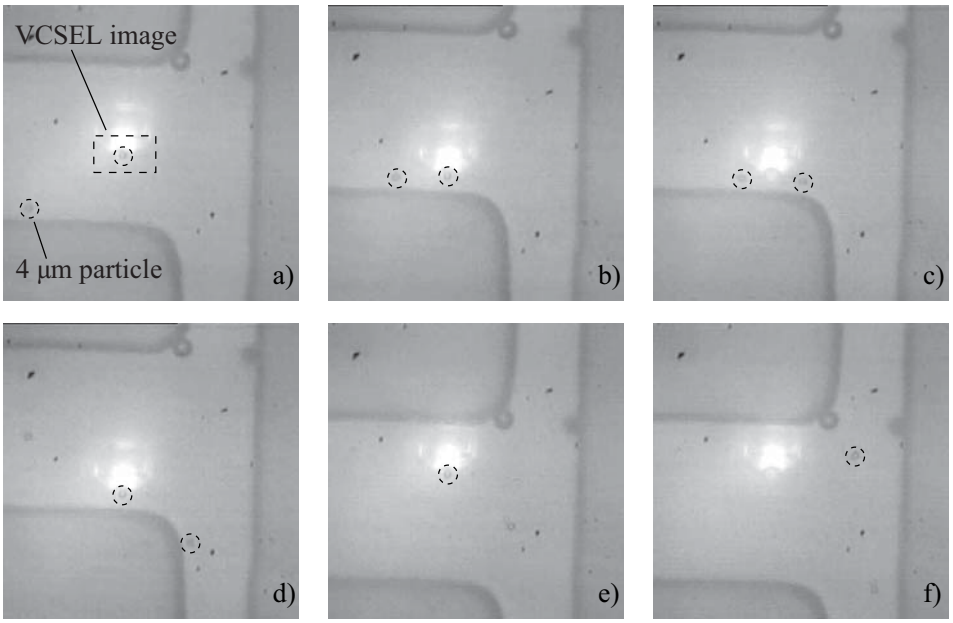

Fig. 5.25: Snapshots of a particle deflection experiment with an optical power of 2.1 mW. The 4 µm diameter polystyrene particles are trapped in the VCSEL tweezers and are redirected to the opposite outlet by relative movements of the laser beam.

5.3 Generation of Multiple Tweezers with VCSEL Arrays

VCSEL sources allow a straightforward generation of multiple optical tweezers by substituting the solitary VCSEL device in the setup shown in Fig. 5.1 by a two-dimensional array. Here, the use of large pitch arrays as well as specially adapted, densely packed VCSEL arrangements was investigated. Eventually, an application in microfluidics is demonstrated.

5.3.1 Application of Large Pitch VCSEL Arrays

The large pitch array used in the experiments was fabricated in the Institute of Optoelectronic by Hendrik Roscher. It contains 4×8 lasers and its device pitch is 250 µm, as customary for VCSELs arrays designed for optical data transmission. Four lasers of the array were contacted, which are arranged in a L-shape, as sketched in Fig. 5.26. Since the VCSELs have different oxide apertures, their maximum output power varies in the range of 1.0 mW to 2.5 mW. All lasers are standard VCSELs and show multi-mode emission at a wavelength of about 850 nm.

The array is inserted into the tweezers setup, with the lower objective adjusted for slightly focused beams. Owing to the relatively large distance between the devices, the lateral position of the array can only be optimized for a single laser. All other lasers are off the optical axis and their beam is therefore distorted and truncated at the optical elements. This leads to an additional reduction of the power level at the sample stage.

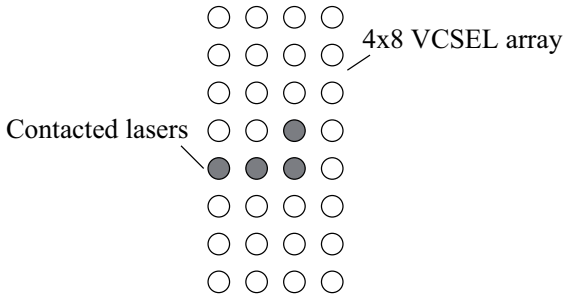

Fig. 5.26: Sketch of the investigated 4×8 VCSEL array. The lasers used in the experiment are highlighted in black.

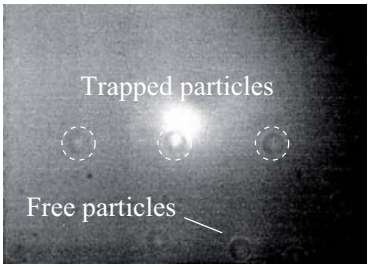

Fig. 5.27: CCD camera image showing simultaneous trapping of three particles of 10 µm diameter with trapping forces of 0.2 to 0.9 pN.

Figure 5.27 shows an image of the sample stage, where three particles with a diameter of 10 µm are trapped simultaneously by the VCSEL array. The adjustment of the optical setup was optimized for the center VCSEL. Optical trapping by the fourth laser was not possible, since its influence at the sample stage was too weak. The achieved trapping forces were in the range of 0.9 pN for the center tweezers, while the trapping force for the left and right traps was limited to only 0.2 pN. This underlines the distortion of the off-axis beams.

The distance between the optical tweezers at the sample stage can be varied by adjusting the lower objective. For ideally collimated beams, it is given by the magnification of the optical system $V_{\text{setup}} = 0.133$ and is therefore 33.25 µm. In the presented experiment, the laser beams were slightly convergent, leading to a larger trap distance of about 45 µm. Such prefocusing of the beams is advantageous, since a larger fraction of the beams can enter the aperture of the immersion objective, and beam distortions can be reduced. However, the large distance of the optical traps at the sample stage inhibits any interaction between them. Although a shrinkage of the trap distance can be easily achieved by decreasing the distance between lower objective and VCSEL array, this approach is not practicable. The divergent beams would experience too high cutoff losses and distortions at the high NA objective. This contradiction can be solved by using a microlens array to decrease the beam divergence of each individual VCSEL [10, 65]. For the here presented experiment, a microlens array with a focal length of 720 µm and a pitch of 250 µm was placed very closely in front of the VCSELs, so the resulting output beams are only slightly divergent. With a following collective lens with a large focal length of 150 mm, the trap distance at the sample stage can now be adjusted.

Figure 5.28 shows sequences of a trapping experiment, where the trap distance was reduced to 6 µm. Below each snapshot, a sketch of the L-shaped VCSEL array marks the actually emitting VCSEL. Furthermore, a schematic of the corresponding optical setup including the microlens array and the ray propagation is given in Fig. 5.29. Figure 5.28a shows a 6 µm bead, which is trapped by the upper right VCSEL of the L-shaped arrangement. By turning this laser off and the adjacent laser on, the particle moves non-mechanically to the next trap (see Fig. 5.28b). So, by switching between the four traps, the particle is eventually moved to the other end of the L-arrangement. However, losses at the various optics leads to a low optical power level at the sample stage of well below 0.5 mW, so stable

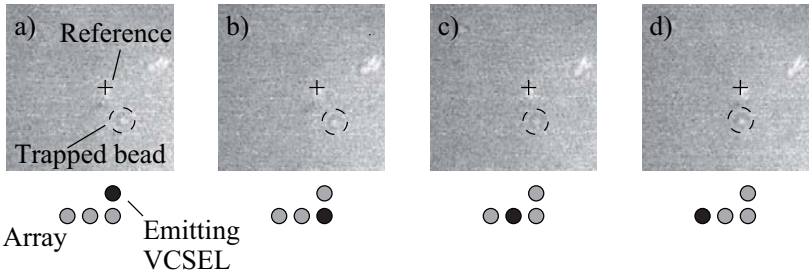

Fig. 5.28: Non-mechanical translation of a 6 µm diameter particle using a L-shaped VCSEL arrangement and a microlens array for reduction of beam divergence.

trapping and a fast movement of the particle is critical. Furthermore, the microlens array needs careful alignment and mounting. Since it has no antireflection coating for 850 nm, the VCSEL output characteristics are also disturbed due to the formation of an external resonator. In summary, the avoidance of the microlens array is highly attractive. This can be achieved by the use of VCSEL arrays with a much smaller pitch.

5.3.2 Densely Packed VCSEL Arrays: Non-Mechanical Particle Translation

When using laser arrays with a small device distance, the downscaling of the VCSEL array in the optical setup can be much weaker than in the previously discussed case. The densely packed VCSEL arrays presented in Sect. 3.2.2 have a device pitch in the range of 25 µm. Introducing such an array into the standard tweezers setup depicted in Fig. 5.1

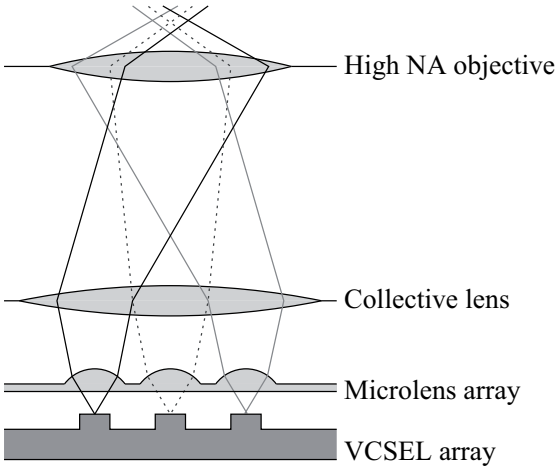

Fig. 5.29: Schematic of the optical tweezers setup based on a standard VCSEL array with large device pitch. The microlens array reduces the laser beam divergence, thus a small trap distance at the sample stage can be achieved.

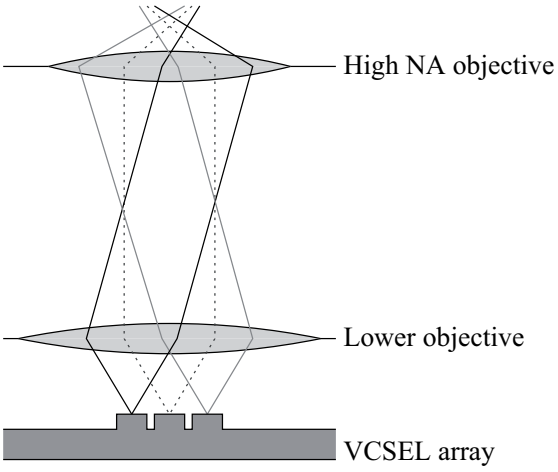

Fig. 5.30: Generation of multiple optical traps using densely packed VCSEL arrays. Owing to the small laser distance, reduction of the beam divergence is not necessary and the use of a microlens array can be avoided.

and adjusting the lower objective for beam collimation results in a small trap distance at the sample stage of about 3.3 µm. Figure 5.30 shows a schematic of the beam propagation in the optical setup. Even slightly focused beams would result in a smaller trap distance than the previously achieved 6 µm, while cutoff losses at the high NA objective can be significantly reduced. Therefore, the divergence of the individual laser is less critical and the use of a microlens array can be avoided.

The left side of Fig. 5.31 shows a microscope image of the VCSEL array used in the following experiments. The array contains 15 individually addressable lasers with a device pitch of 26 µm. The VCSELs are standard multi-mode devices with an oxide aperture of 8 µm. The right side of Fig. 5.31 presents the corresponding operation characteristics. Threshold currents of about 1.6 mA and maximum multi-mode output powers of about 8 mW with only minor variations are observed.

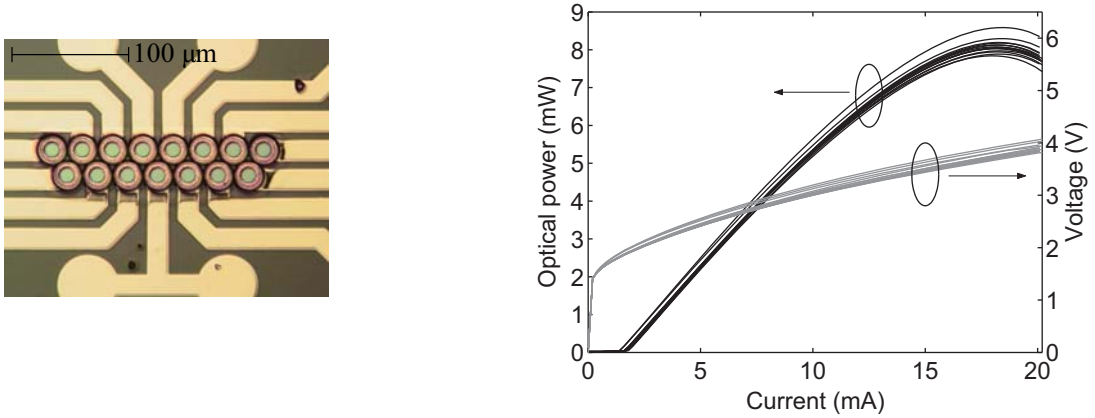

Fig. 5.31: Left: optical microscope image of an array consisting of 15 individual standard VCSELs without relief and an active diameter of 8 µm. Right: corresponding LIV characteristics.

By introducing the array into the optical tweezers setup, the output beams of the lasers are tightly focused by the immersion objective, creating an individually addressable tweezers array at the sample stage. The lower objective was adjusted to focus the output beams, so a tweezers pitch of about 5.5 µm is achieved. The laser current was set to 15 mA, resulting in an optical power at the sample stage of about 2.1 mW from each individual device. Figure 5.32 shows sequences of the experiment as top views on the sample stage, which contains polystyrene particles with a diameter of 10 µm solved in water. A partial image of the VCSEL array can be seen, indicating the position of the optical tweezers. Next to each snapshot, a sketch of the relevant part of the array marks the activated laser. In Fig. 5.32a, the VCSEL in the lower left corner is emitting, trapping a particle in its beam. When switching to the adjacent device, the sphere follows the maximum of light intensity, as shown in Fig. 5.32b. By subsequent switching between the lasers, the particle is thus non-mechanically moved. After 1.5 s, the particle is translated by a distance of about 16 µm to the upper right trap of the array (Fig. 5.32d).

In Fig. 5.33 the same experiment is shown, however, the distance between VCSEL array and lower objective is further increased, thus the laser beams are more convergent when entering the high NA objective. Therefore, the trap distance at the sample stage is increased to about

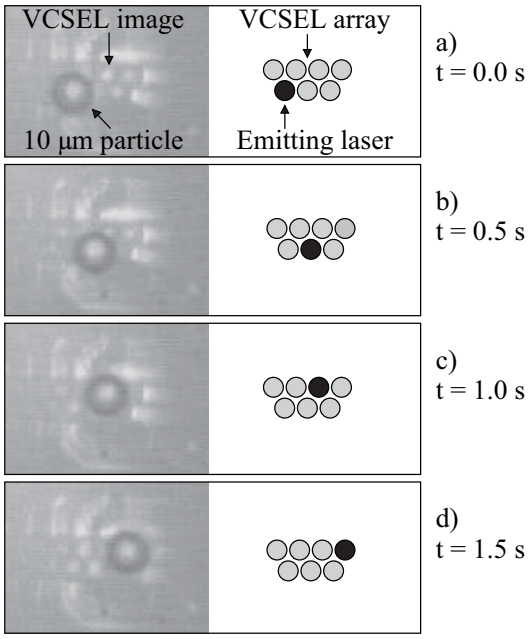

Fig. 5.32: Non-mechanical translation of a 10 µm particle by switching between adjacent lasers. Sequences of the experiment are shown as top views on the sample stage (left) and schematically to highlight the emitting laser in the array (right). The trap distance is 5.5 µm and the optical power is 2.1 mW.

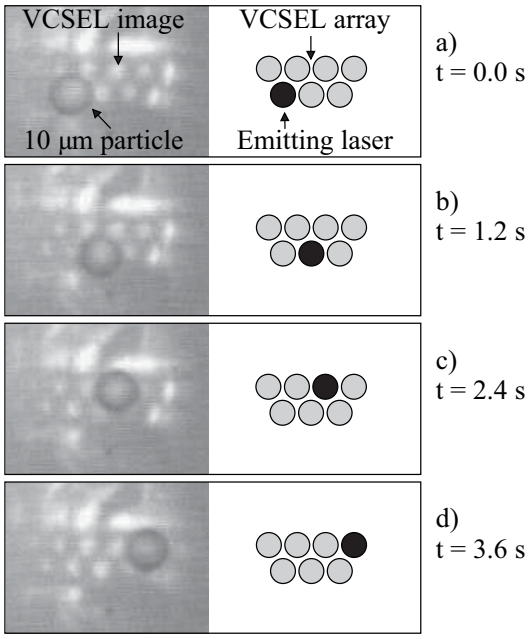

Fig. 5.33: Same as in Fig. 5.32 but the trap distance was increased to 8.0 µm, resulting in a higher optical power at the sample stage of 2.8 mW, due to reduced beam cutoff losses.

8.0 µm. This is also visible by the magnified image of the VCSEL array at the sample stage, since the depicted snapshots have the same scale as in Fig. 5.32. The focusing of the laser beams leads to a further reduction of cutoff losses at the aperture of the immersion objective. Thus, a higher optical power at the sample stage of 2.8 mW from each VCSEL can now be reached for a driving current of 17 mA. In this case, non-mechanical movement of particles can be achieved as well. However, the time it takes for the sphere to move between the four traps is increased to 3.6 s. On the one hand this is caused by the longer total distance of about 23 µm. But also the increased gap between the tweezers reduces the maximum particle speed. After switching between lasers, the sphere is located at the edge of the trapping range of the adjacent trap, where the attractive gradient forces are very small.

Figure 5.34 shows the mean particle speed during the non-mechanical translation for three different tweezers distances at the sample stage. However, the spacing cannot be varied without simultaneously affecting the properties of each individual trap. To achieve a distance of about 4 µm at the sample stage, the VCSEL output beams must be almost collimated by the lower objective before entering the high NA objective. Therefore, severe cutoff losses occur at the back side aperture, resulting in a reduced maximum optical power of only 1.4 mW for an individual trap at a driving current of 8 mA. Although this is accompanied by a stronger intensity gradient at the sample stage, as discussed in Sect. 5.2.3, the mean particle velocity is limited to about 9 µm/s. By slightly focusing the laser

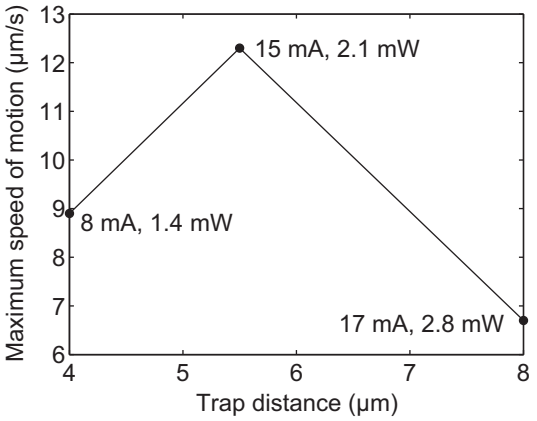

Fig. 5.34: Mean particle velocity during non-mechanical particle translation depending on the trap distance. It is important to note that the available power at the sample stage varies simultaneously.

beams by the lower objective, the trap distance is increased to 5.5 µm and cutoff losses can be significantly reduced. Despite the larger trap spacing, a higher mean particle velocity of more than 12 µm/s can be achieved owing to the stronger optical tweezers. A further focusing of the laser beams results in an even higher power level at the sample stage of 2.8 mW, however, the increased trap distance of 8 µm leads to a decrease of the particle velocity below 7 µm/s.

In the presented experiments just four VCSELs were used for non-mechanical particle translation. Obviously, the scheme can be extended to laser arrays with a much higher number of elements.

5.3.3 Densely Packed VCSEL Arrays: Continuous Particle Deflection

Besides individually addressable arrays, also linear VCSEL arrangements with parallel driven devices have been fabricated, as described in Sect. 3.2.2. By inserting such an array into the optical tweezers setup, a one-dimensional optical lattice of tweezers is generated at the sample stage. In Sect. 4.1.3 the application of tilted optical lattices for continuous particle deflection was described (see schematic in Fig. 4.5). The working scheme is as follows: If the trapping force is smaller than the fluidic drag force, a particle passing the lattice is not retained, but deflected at each trap. Therefore, it follows the tilt of the array and is eventually moved orthogonal to its initial flow direction without any additional mechanical or electrical intervention. Since an individual addressing of lasers is not required in this operation scheme, the number of electrical contacts can be significantly reduced.

The inset in Fig. 5.35 presents an optical microscope image of such a tilted linear VCSEL array, where six devices are driven in parallel. The element pitch is 24 µm and the VCSELs have an active diameter of 6 µm. The corresponding light-current characteristic (see Fig. 5.35) shows a maximum output power of 20 mW and a threshold current of 8 mA for the six jointly lasing VCSELs. Thus, a mean threshold current of 1.3 mA and a mean maximum output power of 3.3 mW per device is deduced. Since the VCSELs have a 3.4 µm diameter inverted surface relief to enhance single-mode emission, the optical spectra of the devices, measured close to thermal rollover, show a SMSR of more than 30 dB (see Fig. 5.36). The wavelength offset for two of the devices is most likely caused by a slight variation of

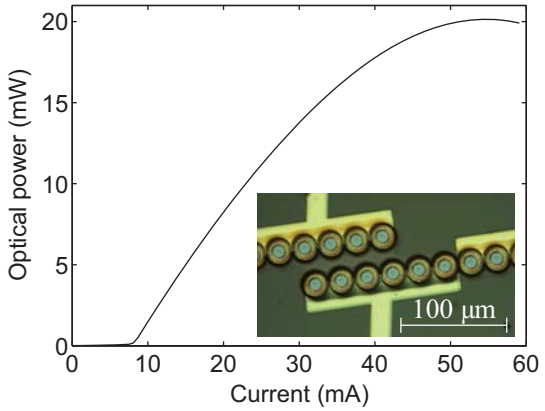

Fig. 5.35: LI characteristic of six relief VCSELs with a 6 µm wide oxide aperture and 3.4 µm relief diameter driven in parallel. The inset shows the corresponding structure.

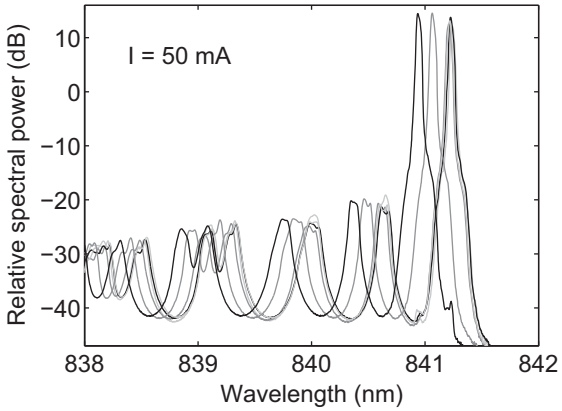

Fig. 5.36: Optical spectra of the six relief VCSELs presented in Fig. 5.35 at 50 mA driving current.

the active diameter, leading to a different amount of heating, inducing different refractive indices and corresponding resonance shifts.

In Fig. 5.37, a particle deflection experiment using the presented array is demonstrated. For this purpose, the laser chip is inserted into the optical tweezers setup to create a linear optical lattice with a tilt of 21°. The lower objective of the tweezers setup is adjusted to slightly focus the output beams to the back side aperture of the immersion objective. Therefore, a trap distance of about 7.5 µm and a total optical power of 6.4 mW is achieved in the sample plane. A 10 µm polystyrene microsphere is then moved from left to right with a velocity of 25 µm/s by the computer-controlled positioning system connected to the sample stage. While passing the optical lattice, the particle follows the tilt of the array (Figs. 5.37b–e) and is eventually deflected by a total distance of about 18 µm orthogonal to its initial flow direction (Fig. 5.37f). In literature, the particle behavior is often called kinetically locked-in to the lattice [41].

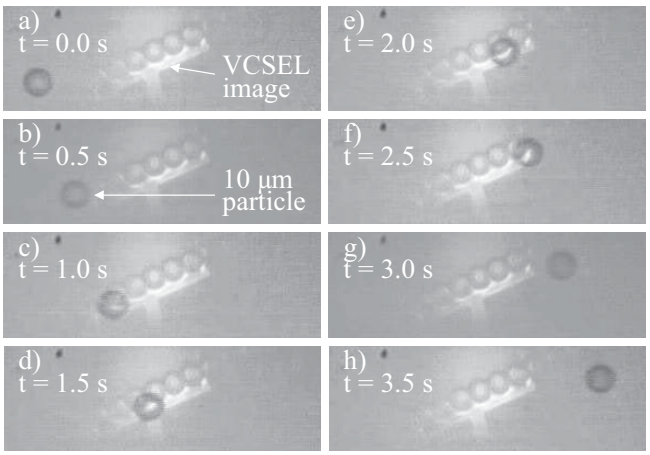

Fig. 5.37: Continuous deflection of a passing particle by a tilted VCSEL array. The 10 µm polystyrene microsphere is moved from left to right with a velocity of 25 µm/s and is eventually deflected by a total distance of about 18 µm orthogonal to its initial flow direction.

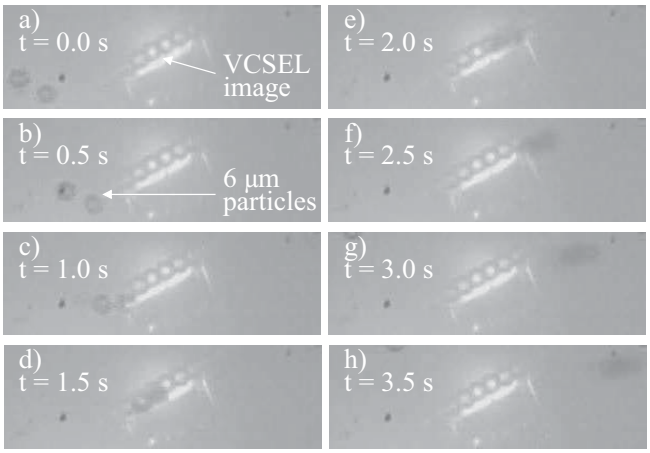

Fig. 5.38: Same as Fig. 5.37 using an array of ten parallel working VCSELs and particles of 6 µm diameter moved with a velocity of 30 µm/s. A blurring of the particles can be observed, which corresponds to the levitation by radiation pressure.

The deflection process depends strongly on the stage velocity. For a fast translation of more than 30 µm/s the fluidic drag is too strong and the sphere does not follow the tilted optical lattice to its end but breaks out earlier. For slow stage movement, the particle is stably trapped by a single trap of the array, most often by the last one of the lattice. Thus, a certain balance of fluidic drag force and trapping force is essential for continuous particle deflection. Furthermore, the array tilt is a critical factor. Beyond a certain maximum tilt of more than 30°, deflection of 10 µm particles at a velocity of 25 µm/s was no longer possible. For 6 µm diameter beads under the same conditions, the critical angle was even smaller. This underlines the sorting capability of this deflection scheme, as it was already reported in [84].

To examine the influence of the trap distance, deflection experiments with 6 µm diameter polystyrene particles were performed. The used array is similar to the one presented in Fig. 5.35, however, it consists of ten single-mode devices. Like in the previous section, the trap distance can be easily controlled by varying the position of the lower objective, thus changing the focusing level of the laser beams before entering the high NA objective. However, one must keep in mind that at the same time the power level and the intensity gradients at the sample stage are affected. Figure 5.38 shows snapshots of an experiment with a tweezers spacing of 5.7 µm and an array tilt of 28°. The power level at the sample stage was 11.9 mW. Two 6 µm beads are moved from left to right with a velocity of 30 µm/s and follow the tilt of the array, so they are eventually deflected by 23 µm from their initial position. In contrast to the deflection of the 10 µm particle presented in Fig. 5.37, a simultaneous blurring of the particle outlines is visible, which corresponds to a lifting of the spheres. This is attributed to the scattering force, which elevates the particles when moving from trap to trap. Caused by the more than four times lower weight of the smaller spheres, the effect is much more apparent.

Figure 5.39 presents the maximum stage velocity at which particle deflection is still possible for four different trap distances at the sample stage. Highest velocities can be achieved for a

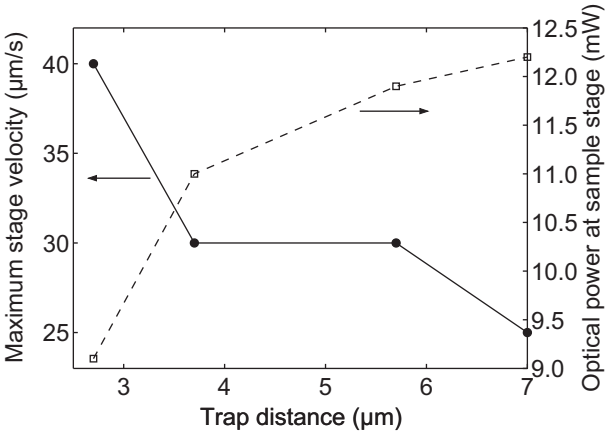

Fig. 5.39: Maximum sample stage velocity at which particle deflection is still possible depending on the trap distance at the sample stage. Furthermore, the corresponding available optical power is plotted.

small spacing of about 2.7 µm. For large trap distances, the particle is no longer kinetically locked-in to the optical lattice, that is, it no longer follows exactly the tilt of the array. Instead it hops from trap to trap, like moving up a staircase. But still, continuous particle deflection is possible. Although the power level at the sample stage is highest in this case, as given by the dashed line in Fig. 5.39, the maximum stage velocity is lowest. However, one has to note, that the total displacement of the particle is about three times larger than for the smallest trap spacing.

5.3.4 Application in Microfluidics

In the previous experiment, the particle velocity was initiated by a movement of the complete sample stage. Now, the continuous particle deflection scheme is translated to a microfluidic flow. Therefore, the sample stage is replaced with a microfluidic chip and the linear VCSEL array of Fig. 5.35 consisting of six devices is used for particle deflection.

Figure 5.40 illustrates sequences of a deflection experiment with 6 µm polystyrene particles at an optical power of about 6 mW. Besides the microfluidic Y-junction with a 150 µm wide inlet and two 50 µm wide outlets, an image of the linear VCSEL array is visible as well. It is placed in the upper half of the channel to redirect particles from the upper to the lower outlet and is tilted by an angle of about 18°. The distance of the tweezers at the sample stage is slightly below 7 µm. The particles are moving from right to left with velocities of about 10 µm/s, depending on their position in the channel. In Figs. 5.40a and b, two closely-spaced particles approach the optical lattice, where the lower one is attracted by the laser beams, while the upper one moves on without interference (Fig. 5.40c). The deflected particle follows the tilt of the optical lattice (Figs. 5.40c and d) and is deviated from its initial path. Thus it eventually moves to the lower branch of the junction (Fig. 5.40e), while the upper particle moves on to the upper outlet (Fig. 5.40f).

However, the particle is not only deflected orthogonal to its initial flow direction, but it is also lifted by the scattering force when moving from one trap to the next, what can be observed by a blurring of the particle image in the experiment. While this was not critical in the former experiment shown in Fig. 5.38, it gets relevant for the laminar flow inside

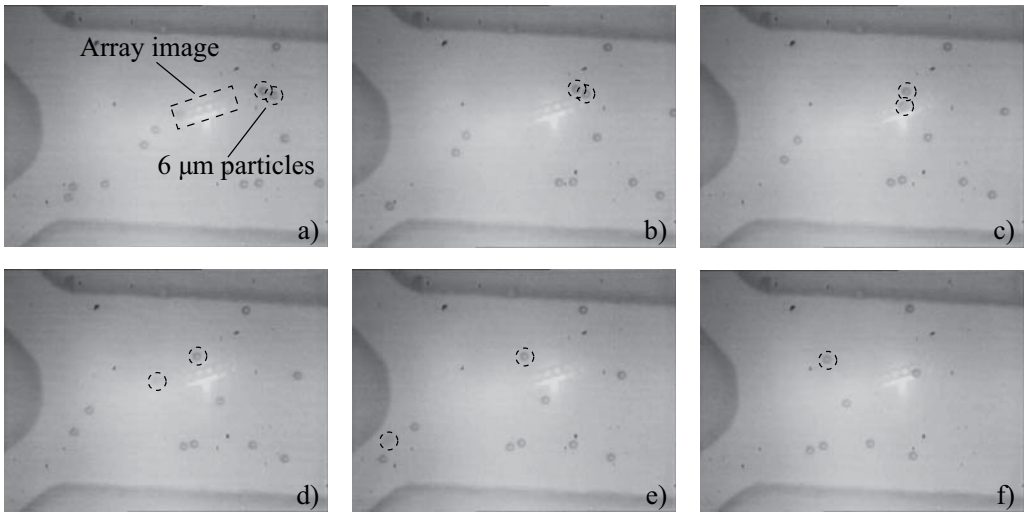

Fig. 5.40: Snapshots of a continuous deflection experiment with an optical power of 6 mW. A 6 µm particle is redirected to the lower branch of the junction while passing the optical lattice.

microfluidic channels. The typical parabolic velocity profile leads to an acceleration of the particle, since it is lifted to a region of higher fluid velocity. Therefore, the influence of the optical tweezers is diminished. To eliminate this effect, smaller channel heights or an electroosmotic-driven flow with a constant velocity profile might be an alternative.

Since levitation by the scattering force is less pronounced for heavy particles, the experiment was repeated using polystyrene particles with 10 µm diameter. In Fig. 5.41 the corresponding snapshots are presented, showing a microfluidic Y-junction with 50 µm wide channels. The particles flow from left to right with a velocity of about 10 µm/s, depending on their position in the channel. Furthermore, an image of the VCSEL array at the stage

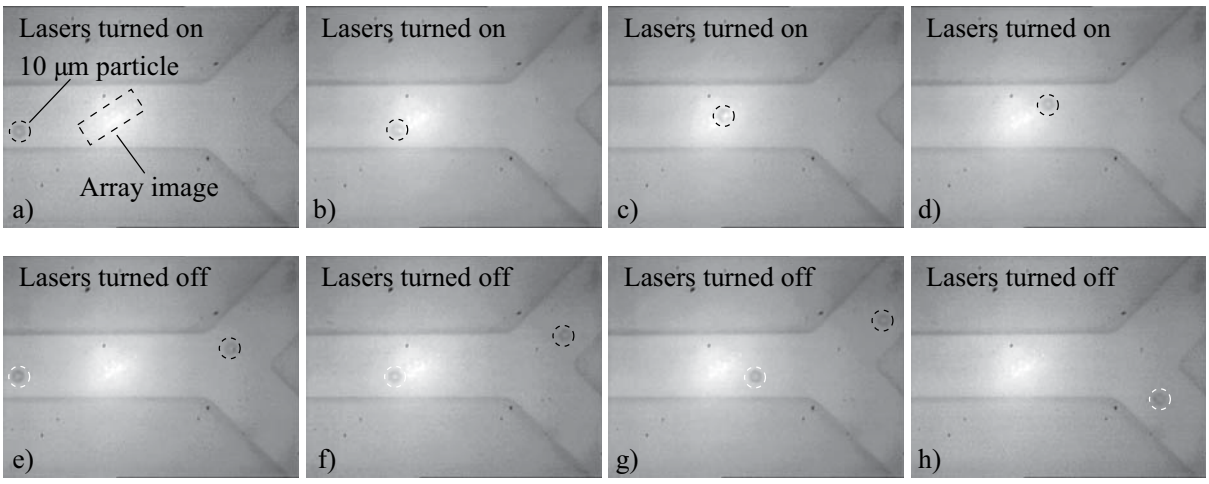

Fig. 5.41: Snapshots of a continuous deflection experiment with an optical power of 8.2 mW. A 10 µm particle (encircled in black) is redirected by the optical lattice to the upper branch of the junction (Figs. a–f). In Figs. e–h the lasers are turned off, thus, the next particle (encircled in white) moves on unaffected to the lower branch.

is visible. The array consists of six lasers and is tilted by about 30° to the flow direction of the particles. The distance of the traps is slightly below 7 µm and the total optical power at the sample stage is 8.2 mW. In Figs. 5.41a–d, the lasers are turned on. Thus, the particle encircled in black, which is initially located at the lower side of the channel (Fig. 5.41a), is redirected by the optical lattice (Figs. 5.41b–d) and leaves the channel through the upper branch (Figs. 5.41e–g). Only weak levitation and associated acceleration of the particle was observed. Next, the laser array is turned off (Figs. 5.41e–h). Therefore, the particle marked in white, which has about the same starting position as the former particle (Fig. 5.41e), does not leave its flow path. It enters the lower channel branch as given by the laminar flow.

By increasing the size of the tilted VCSEL arrays, efficient optical particle separation in microfluidics could be achieved without external intervention. Since the position of the optical lattice is fixed and no moving parts are necessary, the array can be connected to the chip, making this scheme attractive for direct integration. This concept of the integrated optical trap is investigated in more detail in the following chapters.

6 Miniaturization Through Solitary Integrated Optical Traps

The previously presented experiments on optical particle manipulation with VCSEL sources were based on a classical optical tweezers setup. Although the application of VCSELs reduces the dimension and the complexity of the optical system significantly, the setup is still bulky compared to the miniature laser and the manipulated microscopic particles. However, VCSELs offer the unique possibility of a strong system miniaturization by connecting the laser chip directly with the sample, as shortly discussed in Sect. 3.1.3. In this chapter, the concept of this integrated optical trap is studied in detail. For first experiments, only solitary VCSEL devices are employed. An important issue is the shape of the laser beam at the sample stage. Therefore, the focusing effect of integrated microlenses is investigated, both for standard multi-mode VCSELs and single-mode lasers with an inverted surface relief. With both devices, optical particle manipulation in the integrated optical trap is performed.

6.1 Concept and Layout of the Integrated Optical Trap

Figure 6.1 shows a schematic of the integrated optical trap based on a solitary top-emitting VCSEL. A photoresist microlens is integrated directly on the laser facet to focus the laser output beam to a micrometer-sized beam waist at some ten micrometer distance. Thus, any external optics are avoided and a strong reduction of the system dimensions can be realized. The longitudinal intensity gradient achieved by the microlens is expected to be rather weak and not sufficient to realize three-dimensional optical trapping. Instead, only a transverse optical trap is generated. However, at the same time the depth of focus is

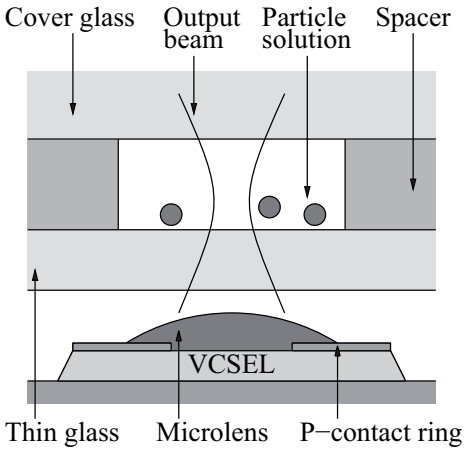

Fig. 6.1: Schematic of the integrated optical trap setup. The output beam is focused by an integrated microlens to manipulate the particles located at the sample stage.

increased, so particle manipulation over a large part of the sample stage cross-section can be achieved. Since the focal point is located close to the lens surface, the sample stage is placed close to the VCSEL at a distance of about 10 µm and only 30 µm thick glass is used to isolate the laser chip from the particle solution. The sample stage consists of the thin glass substrate and a cover glass, which are separated by a PDMS spacer. The size of the complete setup is expected to be in the range of some centimeters, so portability and parallelization of processes can be achieved.

6.2 Calculated Beam Propagation of Lensed Top-Emitting VCSELs

To calculate the necessary lens parameters, the shape of the beam and its propagation was calculated using the matrix method for Gaussian output beams (see App. E). In the present case, the consideration of the Gaussian beam propagation is especially important, since the lens is located well inside the Rayleigh length $z_\mathrm{R} = \pi w_0^2 \bar{n}/\lambda$. Within this length, the beam evolves from near-field to far-field, where it propagates with a constant divergence angle. The beam waist of the VCSEL is assumed to be located at the active region with its diameter $2w_0$ equal to the oxide aperture.

Figure 6.2 shows the calculated beam propagation in the given setup for lensed VCSELs with an emission wavelength $\lambda = 850\,\mathrm{nm}$. The microlens at the laser output facet has a distance of 4 µm to the internal beam waist inside the VCSEL and a focal length of 40 µm in air. The glass substrate with a thickness of 30 µm is separated from the laser by a small gap of 6 µm filled with air. After the glass follows the particle solution, where the refractive index of water is considered. The diameter of the internal beam waist, which is equal to the active diameter d_active, is varied from 6 µm (dashed black line) to 16 µm (solid black line).

For the concept of the integrated optical trap a strong intensity gradient, that is, a small focal spot, as well as a large distance between the glass liquid interface and the position of the focal point are beneficial. Both demands can be satisfied for large internal beam waists, where a small focal diameter of 2.5 µm is achieved for 16 µm oxide aperture. For a small oxide aperture of 6 µm, only a weak reduction of the beam diameter to 4.5 µm is possible, where the focal point is even located inside the glass substrate. However, at a large distance to the glass liquid interface, that is, at the top of the sample chamber, the beam diameters are comparable.

In Fig. 6.3 the influence of the focal length of the microlens is studied for a fixed internal beam waist of 10 µm. As expected, a short focal length of 20 µm leads to a small spot of about 2 µm diameter, however, it is located well inside the glass substrate. The strong focusing is followed by a high beam divergence, so the beam diameter in the particle solution is unacceptably large. For larger focal lengths, the focal point moves into the sample chamber, however, the beam waist increases significantly up to 6 µm diameter for a focal length of 70 µm.

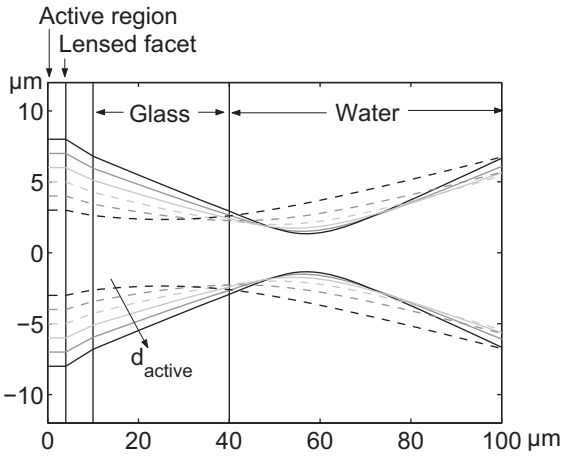

Fig. 6.2: Calculated beam propagation inside the integrated optical trap structure for active diameters of 6 to 16 µm in steps of 2 µm and a focal length of 40 µm.

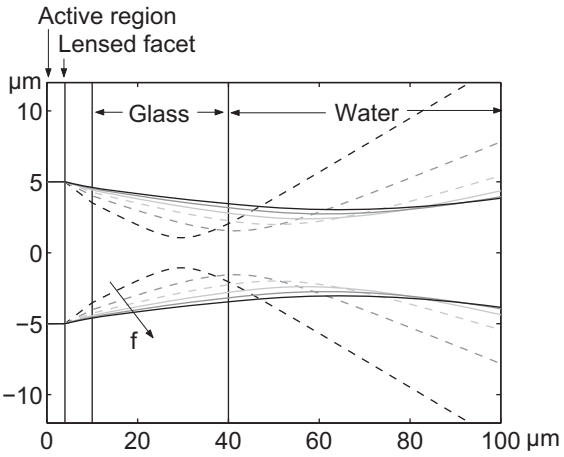

Fig. 6.3: Calculated beam propagation inside the integrated optical trap structure for an internal beam waist of 10 µm and focal lengths of 20 to 70 µm in steps of 10 µm.

Figures 6.4 and 6.5 display the results in more detail. In Fig. 6.4 the distance of the focal point to the glass liquid interface is given in dependence on the focal length of the microlens for different internal beam waists. For 6 µm active diameter (dashed black line), the focal point is always located inside the glass substrate, even for very large focal lengths. For medium internal beam waists of 8 and 10 µm, the focal point is mainly located close to the surface with a only weak dependence on the focal length, while for large diameters the distance scales almost linearly. The corresponding focal diameters are given in Fig. 6.5. According to the trapping force calculations for a parallel beam in Sect. 2.1.2 (see Fig. 2.8), a beam diameter of about 4 µm should be sufficient to handle micrometer-sized particles. For active diameters of 6 to 16 µm this can be achieved with focal lengths of about 40 to 70 µm, where the larger devices have the additional advantage of long working distances.

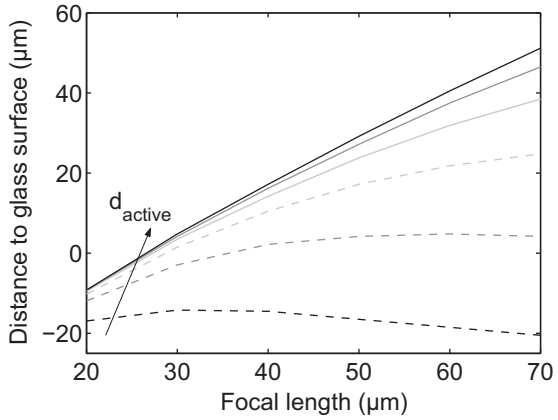

Fig. 6.4: Distance between focal point and glass surface against the focal length for internal beam waists of 6, 8, 10, ..., 16 µm.

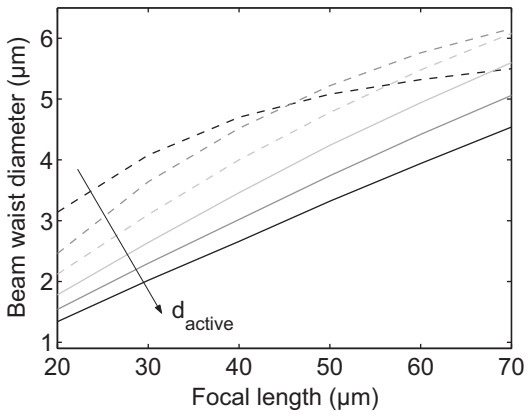

Fig. 6.5: Diameter of the focal point against the focal length of the microlens for beam waists as in Fig. 6.4.

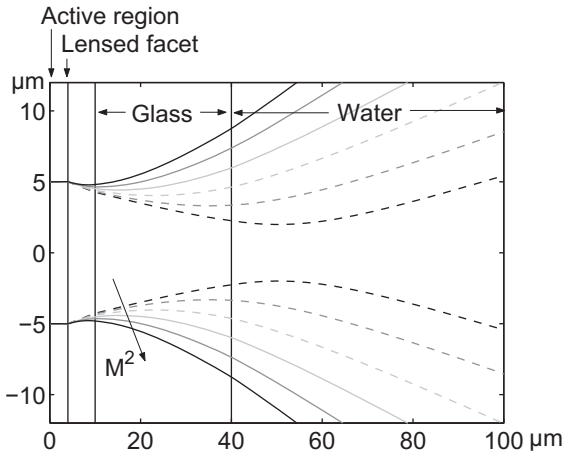

Fig. 6.6: Calculated beam propagation inside the integrated trap structure for an active diameter of 10 µm, a focal length of 40 µm and a varying M^2 of 1 to 6 in steps of 1.

Although large devices seem to be more appropriate for the intended application, one has to keep in mind, that the presented calculations do not include the inferior beam quality, which is typical for VCSELs with large active diameters. In Fig. 6.6, the influence of the beam quality factor M^2 is studied for an internal beam waist of 10 µm and a focal length of 40 µm. For an ideal Gaussian beam with $M^2 = 1$, a small focal diameter of 4 µm well apart from the glass substrate can be achieved. However, with increasing M^2 the size of the focal spot increases and its location moves into the glass substrate. For a high M^2 of 6, the focusing effect of the lens is hardly observable and the beam is strongly divergent, resulting in a very large beam diameter of more than 20 µm at the sample stage. Nevertheless, lensed top-emitting VCSELs with large active diameters of about 14 µm are studied as well, since the particle manipulation can benefit from the higher available optical power.

6.3 Fabrication and Characterization of Photoresist Microlenses

6.3.1 Basic Fabrication by Thermal Reflow

The microlenses are fabricated by a thermal reflow process and are made of PMGI resist. PMGI is transparent in the near infrared and has a smooth reflow behavior at temperatures above 250 °C. Furthermore it shows an above-average chemical and mechanical stability compared to other resists, so it has been used as microlens material in the past, for example for integrated beam collimation of bottom-emitting VCSELs [100].

The lithographic structuring of PMGI resist is done in the same way as described in Sect. 3.2.2 for the VCSEL array processing (see Fig. 3.19), that is, a second Novolak based resist is used to serve as mask during DUV food exposure. For the lenses, simple PMGI resist cylinders are fabricated. After finishing the PMGI process, the sample is placed on a hotplate at a temperature of more than 250 °C, where the cylindrical photoresist "islands" start to melt. Owing to surface tension, the shape of the cylinders changes in order to minimize

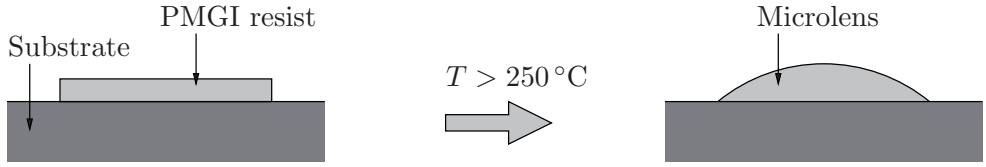

Fig. 6.7: Reflow process: at temperatures of more than 250 °C the PMGI resist cylinders melt into a spherical shape to minimize surface energy.

the surface energy, as shown in Fig. 6.7. The resulting structure is in good approximation spherically shaped and has a focal length in air of [101]

$$f = \frac{R_\mathrm{c}}{\bar{n}_\mathrm{PMGI} - 1}, \tag{6.1}$$

where $\bar{n}_\mathrm{PMGI}$ is the refractive index of the PMGI resist, given as 1.535 at a wavelength of 850 nm. To reach the intended focal lengths of 40 to 70 µm, the radii of curvature R_c have to be in the range of 20 to 40 µm.

Assuming that the bottom diameter as well as the volume of the resist do not change during the reflow process, the resulting radius of curvature is only determined by the height H_i and the diameter D_i of the resist islands before reflow [101]. The volume V_i of the resist in the beginning is

$$V_\mathrm{i} = \pi \frac{D_\mathrm{i}^2}{4} H_\mathrm{i}. \tag{6.2}$$

The volume of the spherically shaped lens after reflow can be calculated by

$$V_\mathrm{l} = \pi H_\mathrm{l} \left(\frac{1}{6} H_\mathrm{l}^2 + \frac{1}{8} D_\mathrm{l}^2 \right), \tag{6.3}$$

where H_l is the maximum height of the lens and D_l is its diameter at the ground [102]. Equating (6.2) and (6.3) and including $D_\mathrm{l} = D_\mathrm{i}$ leads to

$$H_\mathrm{l} = \frac{1}{2} \left(6 D_\mathrm{i}^2 H_\mathrm{i} + \sqrt{D_\mathrm{i}^6 + 36 D_\mathrm{i}^4 H_\mathrm{i}^2} \right)^{1/3} - \frac{1}{2} D_\mathrm{i}^2 \left(6 D_\mathrm{i}^2 H_\mathrm{i} + \sqrt{D_\mathrm{i}^6 + 36 D_\mathrm{i}^4 H_\mathrm{i}^2} \right)^{-1/3}. \tag{6.4}$$

Eventually, the radius of curvature can be calculated by

$$R_\mathrm{c} = \frac{1}{2 H_\mathrm{l}} \left(\frac{D_\mathrm{l}^2}{4} + H_\mathrm{l}^2 \right). \tag{6.5}$$

Figure 6.8 shows the radius of curvature in dependence on the diameter for different initial resist thicknesses H_i. For the present VCSEL structures, the diameter of the lens has to be in the range of about 10 to 40 µm, otherwise it would be smaller than the output facet or larger than the mesa, respectively. Therefore, an initial resist thickness of about 2 µm is best suited to cover the interesting radius of curvature range.

In Fig. 6.9 an optical microscope picture of a PMGI microlens with a diameter of 28 µm and an initial resist thickness of 1.8 µm can be seen. For first steps in process development, the

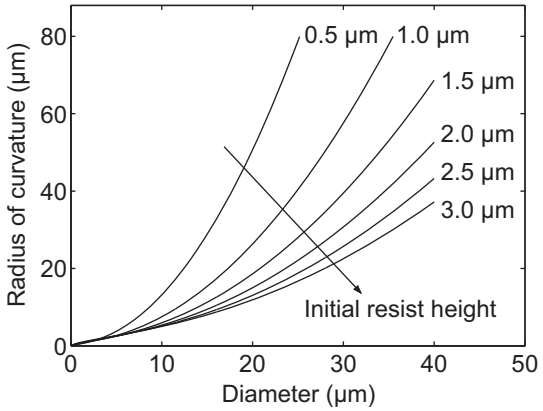

Fig. 6.8: Radius of curvature versus the diameter of the resist islands for different initial resist thicknesses under the assumption that resist volume and bottom diameter do not change during the reflow.

lens was fabricated on a flat GaAs substrate. The concentric interference lines, so-called Newton rings, arise due to interference at thin layers and indicate the spherical shape of the lens. In the upper right corner of Fig. 6.9 a three-dimensional plot of the height profile measured by an atomic force microscope (AFM) is depicted. The bottom left side shows the cross-section of the profile at the center of the lens. The dashed line represents a spherical fit which reveals the nearly ideal spherical shape of the lens with a radius of curvature of about 37 µm. However, this value is about 5 µm larger than the intended radius of curvature. Furthermore, a difference between reflow on a gold surface and on a GaAs substrate was observed. Therefore, a detailed study of the reflow process follows in the next section.

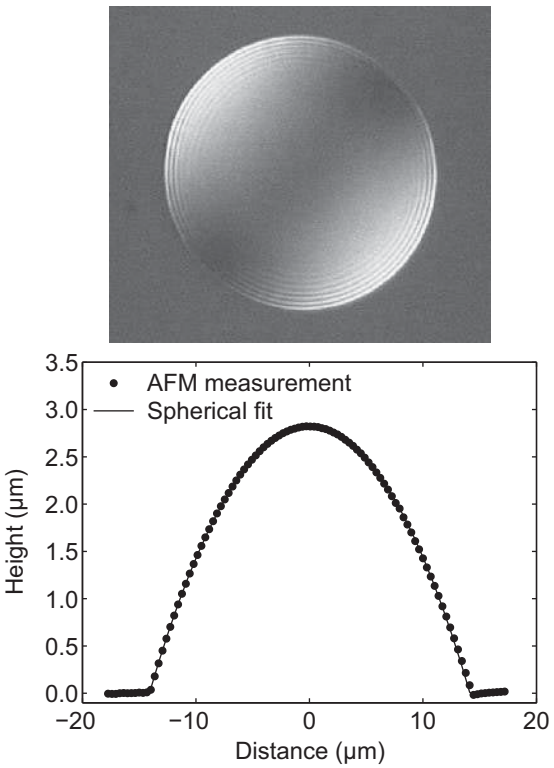

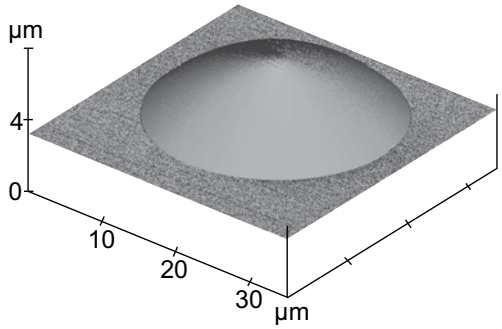

Fig. 6.9: Top left: optical microscope image of a PMGI lens on GaAs substrate with a bottom diameter of 28 µm. Top right: AFM measurement of the height profile. Bottom left: Cross-section of the AFM height scan, where the dashed line represents a spherical fit with a radius of curvature of 37 µm.

6.3.2 Analysis of the Reflow Process

The calculation of the radius of curvature in Fig. 6.8 is based on the assumptions of a constant resist volume and a constant resist diameter at the surface. However, both assumptions are critical. Especially the volume of the resist will decrease during the reflow process due to evaporation of solvents. Both effects are not only dependent on time and temperature of the reflow, but also on the surface material. Here, the difference between gold and semiconductor surface is of special interest, since the lenses will be placed directly on the p-contact ring in the final structure (see Fig. 6.1). To study the reflow process in more detail, lenses with different diameters were fabricated on gold and GaAs surfaces. Reflow temperatures of 250 °C and 270 °C are examined, where the reflow time was kept constant at 20 min. The initial resist thickness for the structures on gold as well as on GaAs was 2.0 µm, so the results can be directly compared.

By AFM measurements of the height profile of each examined structure before and after the reflow the volume change can be determined. The decrease was found to be in the range of 10 to 17 %, where no dependence on the structure size was observed. The mean value for the sample with gold was found to be slightly smaller, while for the larger temperature, the mean value was one percentage point higher than for the low temperature. Furthermore, a change of the resist diameter at the bottom of the lens is observed. Fig. 6.10 shows the ratio between the diameter after and before reflow for the four examined samples. Especially for small lenses, which have the largest aspect ratio, a broadening of the resist islands can be observed. The measurements also indicate a difference in wetting between PMGI resist on GaAs and gold, where the wetting on gold seems to be stronger. A maximum broadening of the resist diameter by a factor of 1.4 is determined at high temperatures of 270 °C on the gold substrate. For even higher reflow temperatures of 290 °C, the smallest lenses of 10 µm diameter do not even keep their circular base, but melt into an irregular shape.

Figure 6.11 shows the measured maximum height of the lenses and the radius of curvature in dependence on the initial diameter of the resist islands. The solid line describes the ideal behavior according to (6.4) and (6.5). For all structure sizes, the lenses are much shallower than expected, resulting in a larger radius of curvature. The highest deviation is found for small lenses on the gold surface, owing to the better wetting and the corresponding increase in resist diameter. In Fig. 6.12 the reflow behavior on the gold sample at 270 °C is studied

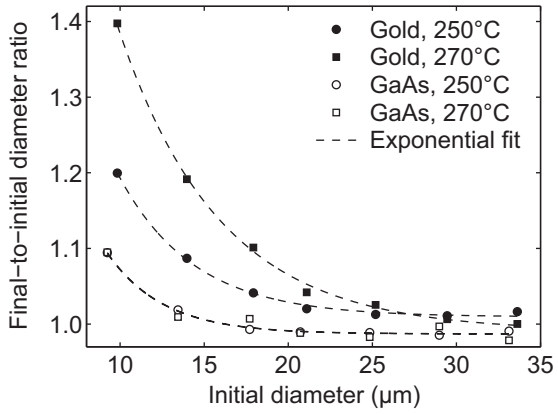

Fig. 6.10: Ratio of the resist diameter before and after reflow plotted against the initial diameter for different substrate materials (gold, GaAs) and reflow temperatures (250 °C, 270 °C).

in more detail. The filled circles give the measured values, while the solid line shows the calculated ideal height and radius of curvature dependence. For the dotted line, a decrease in resist volume of 14 % was considered in the calculation. While a good agreement for large resist diameters can be achieved, the deviation for small lenses is still strong. Next, the broadening of the resist islands during reflow, as given in Fig. 6.10, is taken into account as well. The resulting dashed line shows an improved agreement for all lens sizes. This proves, that the observed difference of the maximum resist height and the radius of curvature to the expected results is mainly caused by the volume loss and the increase in resist diameter.

Despite the observed deviation from the ideal reflow behavior, the desired radius of curvature range of 20 to 40 µm can be still covered, also for lenses on gold surface. Low reflow temperatures are favorable, since the broadening of lenses with a high aspect ratio can be reduced. However, if the temperature is reduced to 230 °C, resist islands of larger diameter

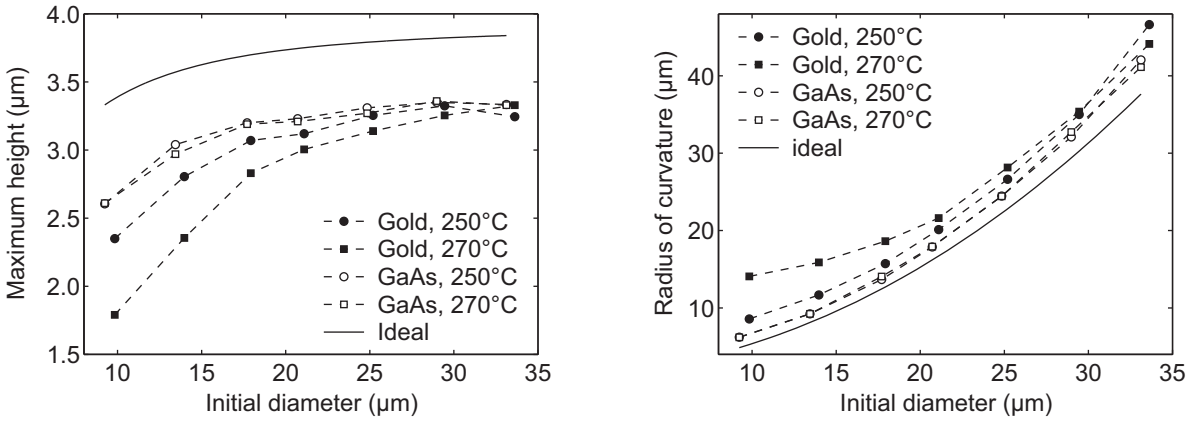

Fig. 6.11: Maximum height (left) and radius of curvature (right) of the lenses plotted against the initial resist diameter for different substrate materials (gold, GaAs) and reflow temperatures (250 °C, 270 °C). The solid line shows the calculation for constant resist volume and diameter.

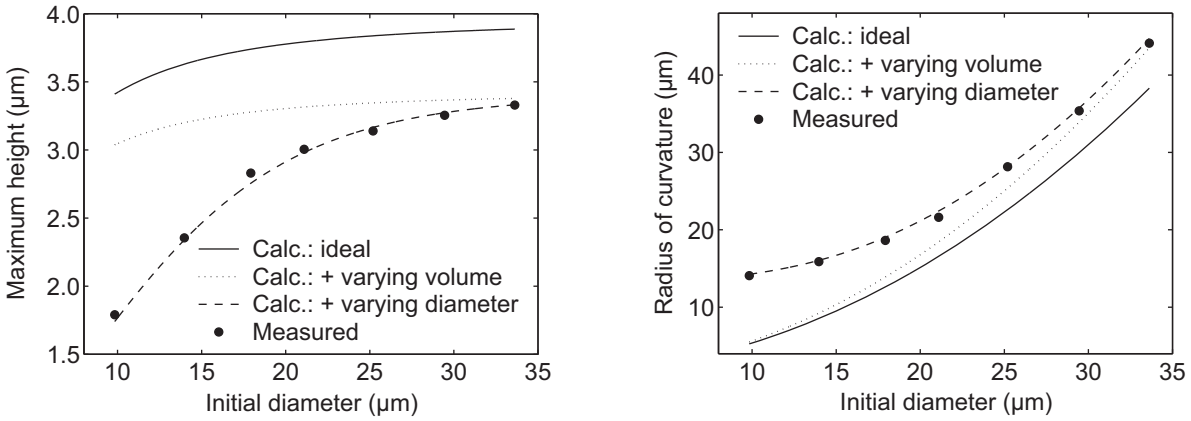

Fig. 6.12: Maximum height (left) and radius of curvature (right) of the lenses against the initial diameter for the gold sample at 270 °C reflow temperature (filled circle). The solid line shows the calculation for constant resist volume and diameter, the dotted line includes the loss in resist volume and the dashed line takes the varying resist diameter into account as well.

do not melt completely, so a spherical shape can be no longer achieved. Therefore, a reflow temperature of 250 °C for 20 min is used in all following processes.

6.4 Multi-mode VCSELs with Integrated Photoresist Microlenses

According to the calculations in Sect. 6.2, smallest focal spots and largest working distances can be achieved with large aperture VCSELs. Furthermore, such multi-mode VCSELs have higher optical output powers, thus offering stronger optical forces on the microparticles. Therefore, VCSELs with oxide apertures of about 14 µm are used for the first realization of the integrated optical trap. Before applying such devices for particle manipulation, the output characteristics as well as the output beam profile of lensed multi-mode VCSELs are investigated.

6.4.1 Device Performance and Beam Propagation

Figure 6.13 shows a schematic cross-section of the investigated devices. After standard VCSEL processing, the PMGI microlens is fabricated on top of the laser output facet. The lens overlaps not only the p-contact ring, but partially the bond pad metalization as well. However, due to the thin metal layer of only 200 nm, no disturbance or asymmetry of the lens shape is observable. Based on the calculations in Sect. 6.2, radii of curvature of the microlens of 20 to 25 µm, corresponding to a focal length of about 40 to 50 µm, should be realized in order to achieve a beam diameter of less than 4 µm at the focal point.

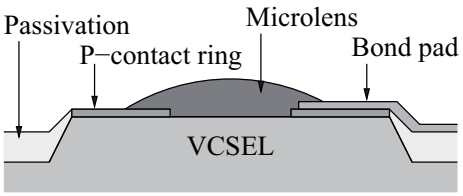

Fig. 6.13: Schematic cross-section of the examined lensed VCSEL structures.

The radius of curvature can be set by the height of the resist islands before reflow, according to Sect. 6.3. It must be considered, that the resist on top of the structured VCSEL mesa is slightly thinner than on a flat substrate, thus the resist spinning speed has to be adjusted. The left side of Fig. 6.14 presents an optical microscope image of a completed device, showing the laser mesa with the p-contact ring and the integrated microlens. Furthermore, the polyimide passivation as well as part of the bond pad are visible. The lenses are characterized by measuring their surface profile with an AFM. The dots in the right side of Fig. 6.14 indicate the AFM data while the solid line shows a spherical fit. The lens profile is again almost ideally spherical, where a radius of curvature of about 22 µm can be determined.

In Fig. 6.15 the operating characteristics of the lensed VCSEL from Fig. 6.14 with an active diameter of 13.5 µm before and after the microlens was placed on its output facet is shown.

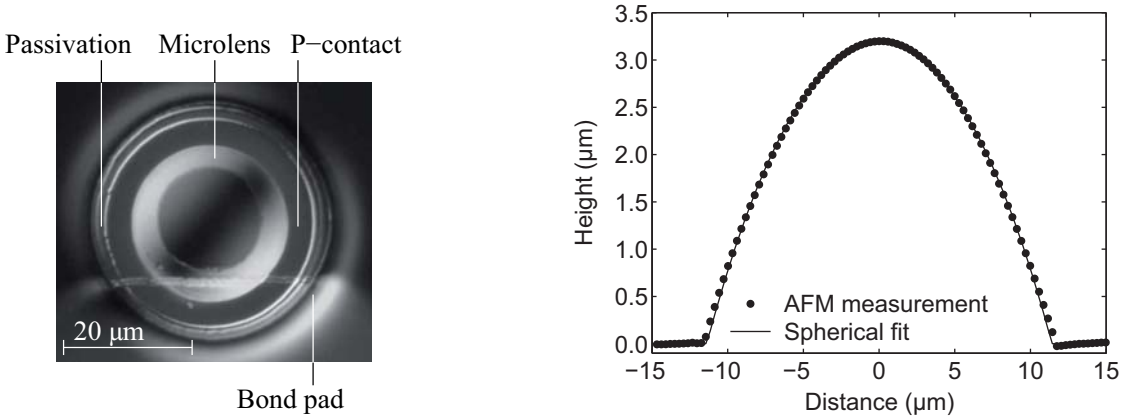

Fig. 6.14: Microscope image (left) and AFM height profile (right) of a lensed VCSEL. The spherical fit of the AFM data shows a nearly ideal spherical shape of the lens with a radius of curvature of about 22 µm.

A small increase of the threshold current (from 3.7 to 4.4 mA) as well as of the differential quantum efficiency (from 51 to 58 %) and the maximum output power is observed. This is caused by the microlens material, which weakens the refractive index step at the former semiconductor–air interface, leading to a reduction of the upper mirror reflectivity. A maximum optical output power of up to 17 mW at 30 mA driving current is available from this device. Caused by the large active diameter, the VCSEL shows transverse multi-mode emission from threshold to thermal rollover with an emission wavelength of about 860 nm.

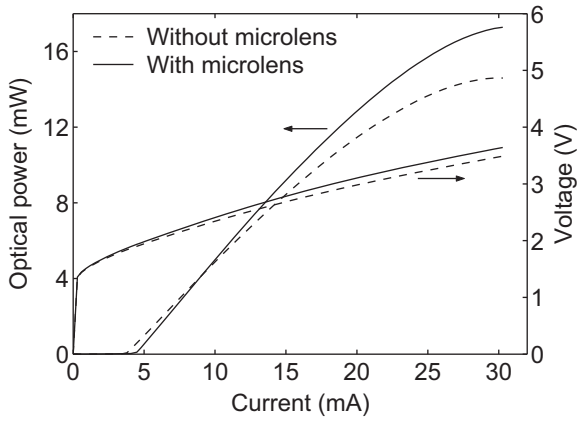

Fig. 6.15: LIV characteristics of a 13.5 µm oxide aperture VCSEL with and without integrated microlens. The increase of threshold current and optical output power is explained by a reduction of the top mirror reflectivity. The voltage increase is probably caused by photoresist residues at the bond pad.

To analyze the focusing effect of the microlens, the transverse output beam profiles at different distances from the laser surface are measured. Therefore, the near-field measurement setup is used, where the laser beam is scanned with a lensed fiber moved by piezo actuators (see App. A). While the longitudinal distance between successive transverse scans is very accurate, the initial distance z_0 to the laser surface is not exactly known. It has to be estimated with a stereo microscope, where an accuracy in the range of ±5 µm must be taken into account.

Besides the presented lensed device, also a reference VCSEL only 750 µm apart on the same sample is investigated. Except for the microlens, it is nominal identical to the lensed

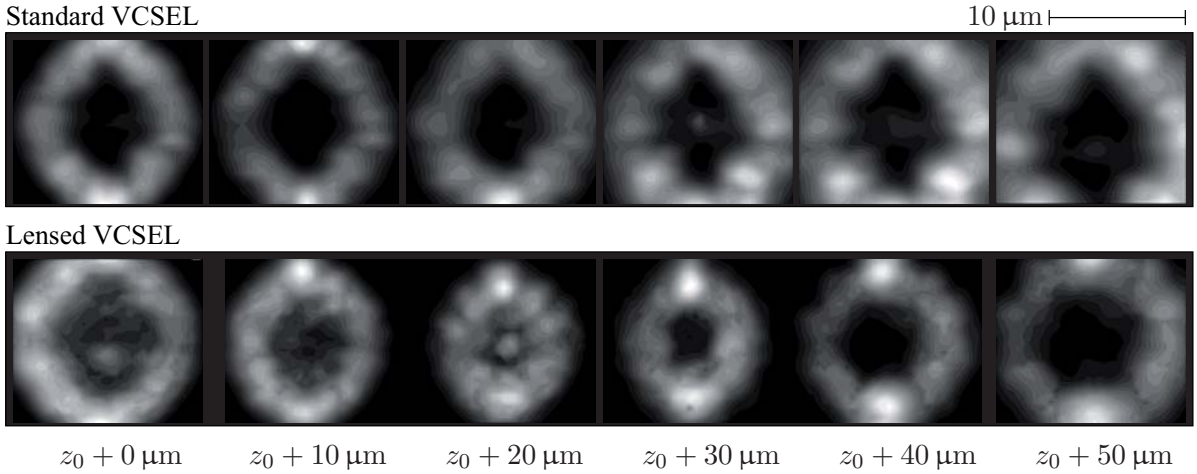

Fig. 6.16: Measurement of the beam profiles of a standard VCSEL (top) and a lensed VCSEL (bottom) at a current of 10 and 6 mA, respectively, at various distances to the laser surface, ranging from about 0 to 50 µm. For the lensed device, a focal point with a beam diameter of about 15 µm and a FWHM of 10 µm is found at a distance of 20 to 30 µm.

VCSEL and its output characteristic is similar to the one presented in Fig. 6.15. The upper part of Fig. 6.16 shows the scanned near-field of the reference VCSEL at distances from $z_0 + 0\,\mu m$ to $z_0 + 50\,\mu m$ to the laser surface, with longitudinal steps of 10 µm. The laser driving current is 10 mA. Owing to the multi-mode emission, a donut-shaped intensity profile is observable. Furthermore, the device shows continuous beam divergence, thus its near-field profile becomes much broader than the fiber scanning range of $14 \times 10\,\mu m^2$.

The lower part of Fig. 6.16 presents the same measurement for the lensed multi-mode VCSEL, where beside the typical donut-shaped profile a distinct shrinkage of the beam is visible. To determine the beam diameter, the mathematical definition of a standard deviation, as given in (5.8), is applied in different spatial directions. A minimum beam diameter of about 15 µm at a distance of only 20 to 30 µm is observed. It has to be considered, that the near-field measurements are taken in air, while the beam calculation presented in Sect. 6.2 includes propagation in glass and water, resulting in a longer focal distance. Still, this could not explain the large deviation between expected focal beam diameter and distance (about 4µm and 60 µm, respectively) and the measured values. Most probably, it is caused by the worse beam quality of the multi-mode VCSEL, as shown in Fig. 6.6. However, the lens still leads to a much smaller beam diameter at the sample stage compared to the reference device and due to the resulting higher intensity gradient, stronger transverse trapping forces can be achieved.

6.4.2 Experimental Results on Particle Manipulation

To examine the suitability of the fabricated lensed VCSELs in optical trapping applications, the above described device is introduced in the integrated optical trapping setup shown in Fig. 6.1. However, the small distance between laser and sample stage prohibits an electrical connection of the VCSEL p-side via a contact needle or wire bonding. Therefore, the

approach shown in Fig. 6.17 was used for first experiments. The back side of the thin 30 µm glass substrate is partly covered with an evaporated NiAu metalization. By adding a drop of conductive glue on the VCSEL bond pad, electrical contact can be achieved for a small gap between semiconductor and sample stage and the VCSEL can be connected via the glass metalization. Since the conductive glue is still liquid, limited movement of the sample stage by a positioning system is possible. To observe the experiments, an imaging system, mainly consisting of a CCD camera and filters, is placed above the sample stage. The experiments are performed with 10 µm-sized polystyrene particles in water.

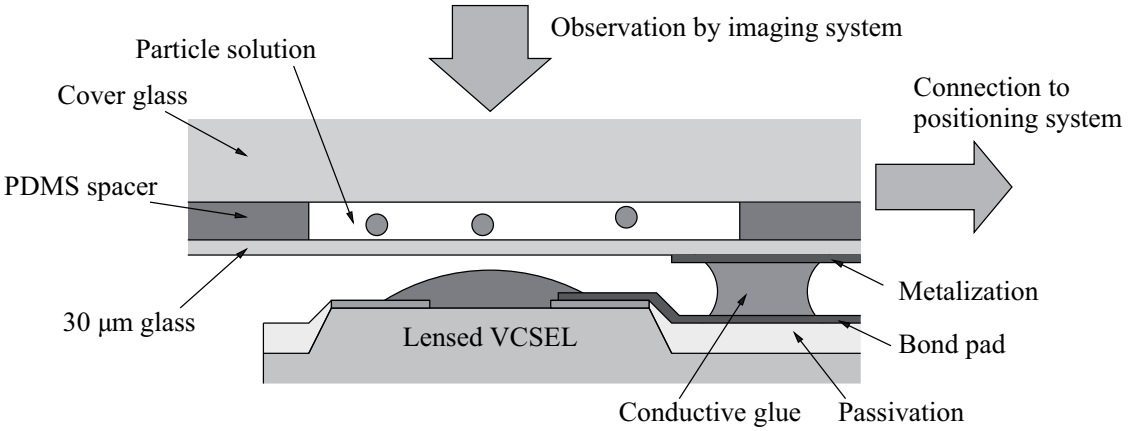

Fig. 6.17: Schematic of the setup used for first trapping experiments with lensed VCSELs. To minimize the distance between VCSEL and sample stage, the metalized glass surface together with conductive glue is used for connection of the VCSEL p-side.

Figure 6.18 shows a typical experimental sequence by means of pictures taken by the CCD camera (top view). For better comparison, corresponding schematic side views are added. Besides the 10 µm diameter particle, also the shape of the VCSEL structure with p-contact ring and part of the bond pad metalization is visible. However, its outlines are blurred, due to the distance of about 40 µm between laser surface and particle solution. Initially the particle is located at the bottom of the sample stage and drifts randomly through the liquid as shown in Figs. 6.18a and 6.18b. This drift is induced by a constant evaporation of liquid from the sample stage and was not found to be influenced by the emission state of the laser. In the present case the VCSEL emits about 9 mW optical output power. When approaching the laser beam, the particle is pulled toward the intensity maximum by the transverse gradient force (Figs. 6.18c and 6.18d). Since the laser beam is only mildly focused, the longitudinal gradient force is not strong enough to overcome the forward scattering force. Therefore, the particle is lifted by the laser beam until it reaches the upper cover slip where it remains trapped. The elevation is observable in Figs. 6.18d and 6.18e by a blurring of the particle as it moves out of the imaging focus. In Fig. 6.18f, the focal point of the imaging system is adjusted to show the particle immobilized at the top of the sample stage. When the laser is turned off, it floats back to the bottom. At lower output power, deflection and elevation of the particles is still observed while stable trapping at the upper cover slip is no longer achieved. Consistent results for manipulation and trapping were obtained for similar VCSELs.

However, a displacement of the trapped particle with respect to the device center is generally observed, much likely caused by the donut-shaped beam profile. Since the beam diameter

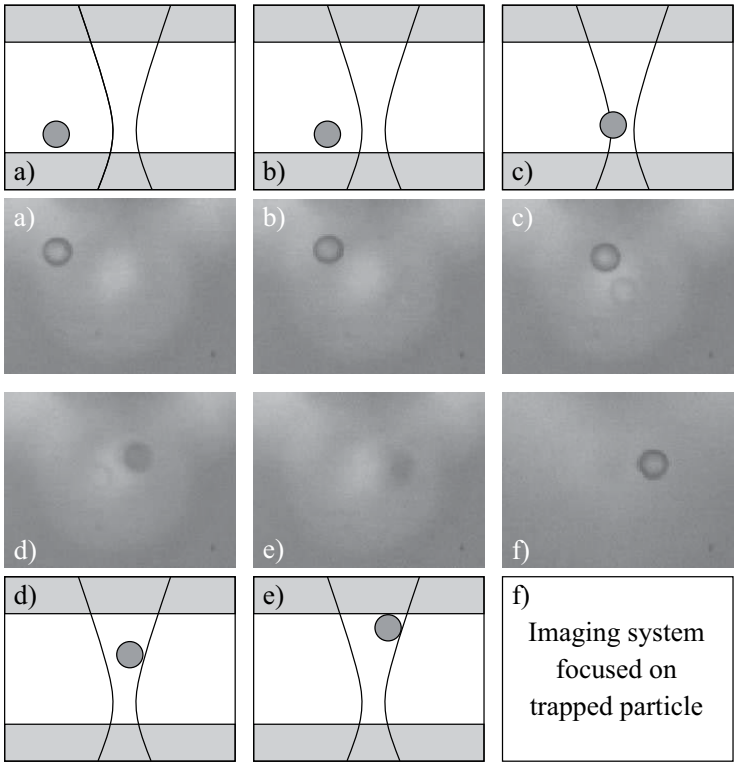

Fig. 6.18: Sequence of a typical trapping experiment with the integrated optical trap using a 10 µm diameter polystyrene microsphere. For better understanding, top views by the CCD camera as well as associated schematic side views are shown. The approaching particle (a, b) is pulled toward the intensity maximum of the laser beam by the gradient force (c, d) and is pushed upwards by the scattering force (d, e). Finally, it remains trapped at the upper cover slip (f) until the laser is turned off again.

is much broader than the particle, the transverse equilibrium position where all transverse trapping forces on the particle cancel each other out is not found at the center of the beam. Instead, the particle is located somewhere along the ring of the donut-shaped beam profile. Thus, the final position of the sphere is not predictable. To achieve a Gaussian-shaped intensity profile and to improve the beam quality of the VCSELs, the surface relief technique is applied as a next step.

6.5 Lensed VCSELs with Additional Surface Etch

6.5.1 Device Performance and Beam Propagation

The results of the beam propagation calculation in Sect. 6.2 show that a larger internal beam diameter leads to a smaller focal spot and a larger working distance. This trend is beneficial for the given design. However, the demand of single-mode emission and a Gaussian-shaped intensity profile is hard to satisfy with oxide apertures of about 10 µm and more, even when using the inverted surface relief technique. Therefore, oxide apertures of about 8 µm in combination with a focal length of 40 µm are targeted as a compromise. A weak focusing to a spot width of 4 to 5 µm at a distance of about 30 to 40 µm to the laser surface is expected.

Lensed top-emitting relief VCSELs with 8 µm active diameter and a 4 µm diameter surface relief were fabricated using the standard processes presented in Sects. 3.2.1 and 6.3.1. Figure

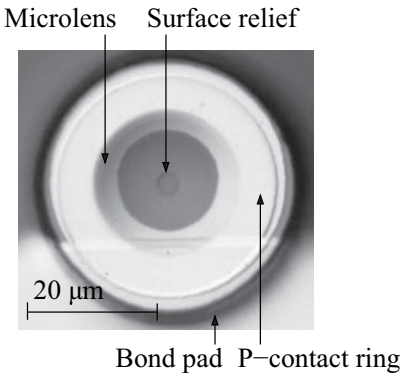

Fig. 6.19: Optical microscope image of a lensed surface relief device.

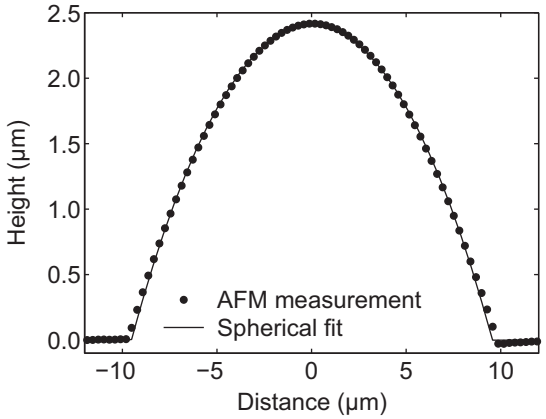

Fig. 6.20: Characterization of the spherical shape by AFM profile measurements (dots). The solid line represents a spherical fit with 20 µm radius of curvature.

6.19 shows an optical microscope image of a finished device with surface relief and lens, where a partial overlap between lens and p-contact ring is recognized. To characterize the lens shape, AFM measurements of the height profile are performed, as shown by the dots in Fig. 6.20. The solid line represents a spherical fit with a radius of curvature of 20 µm which again reveals a nearly ideal spherical shape of the lens.

To investigate the influence of the relief and the microlens on the VCSEL performance, the power characteristics and the optical spectra of a standard reference device as well as a relief VCSEL before and after the microlens was placed on the output facet were measured. Figure 6.21 shows the obtained results. The standard device with an oxide aperture of 8 µm and no surface relief has a high maximum output power of 9.2 mW at a driving current of 20 mA and low threshold current of 1.0 mA (see left side of Fig. 6.21a). However, the laser shows strong multi-mode emission even at small currents, as visible in the optical spectra taken at different driving currents (see right side of Fig. 6.21a). Fig. 6.21b shows the same measurements for a VCSEL with 8 µm active diameter and a 3.8 µm large and 57 nm deep surface relief, but still without microlens. A strikingly higher threshold current of 6.4 mA is observed, which is attributed to the decrease of the upper mirror reflectivity due to the surface etch and the small overlap of relief and the relatively large oxide aperture. On the other hand a high differential quantum efficiency of 92 % is found, so the maximum output power of 5.9 mW is reached at a relatively low current of 16 mA. The optical spectra, shown on the right side of Fig. 6.21b, reveal a lasing higher-order mode at small driving currents, which vanishes for higher currents and a SMSR above 30 dB is reached, so the maximum output power is single-mode.

Figure 6.21c shows identical measurements for the same VCSEL after a PMGI microlens with a radius of curvature of 20 µm was placed on its output facet. The graph on the left side showing the LIV characteristic also contains the measurement without microlens as a dashed gray line. A reduced threshold current of 5.9 mA and an increased maximum output power of 6.3 mW is observable. Furthermore, the differential quantum efficiency is reduced to 63 %, indicating a behavior approaching that of a standard VCSEL. This

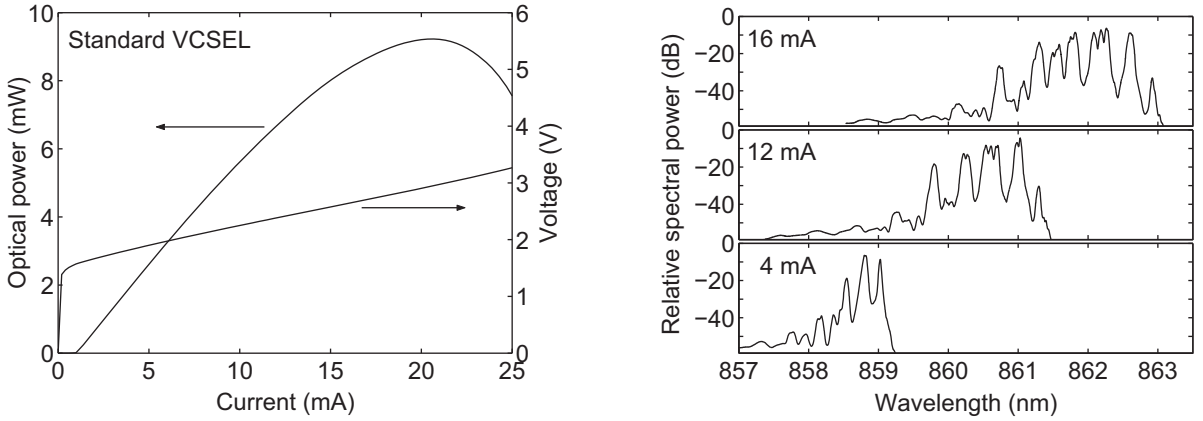

a) Output characteristics and optical spectra of a 8 µm active diameter standard VCSEL without microlens.

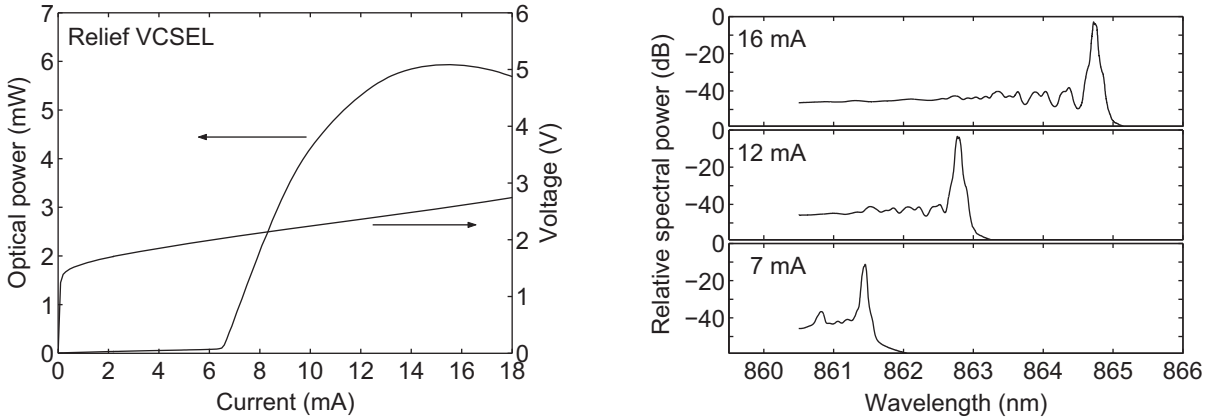

b) Output characteristics and optical spectra of a 8 µm active diameter relief VCSEL with a 3.8 µm surface etch without microlens.

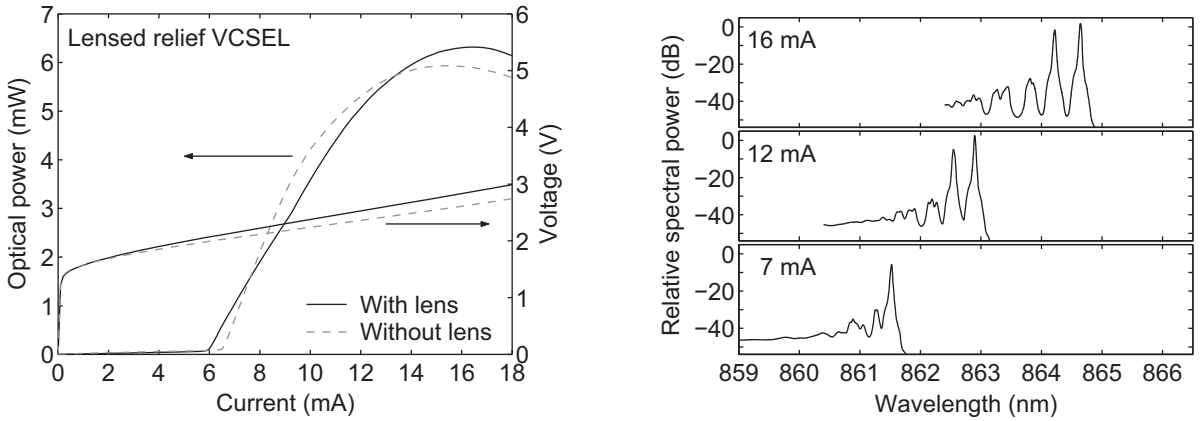

c) Output characteristics and optical spectra of the relief VCSEL presented above after a PMGI microlens was placed on its output facet.

Fig. 6.21: The standard VCSEL shows strong multi-mode emission (a), which can be effectively suppressed by use of the inverted surface relief technique (b). The microlens degrades the single-mode emission of the relief VCSEL but the fundamental mode remains dominant (c).

observation is supported by the optical spectrum, which is shown in the right side of Fig. 6.21c for different driving currents. The laser shows at least one higher-order mode over the whole operating range and is never single-mode. This effect is comprehensible, since the microlens diminishes the refractive index step at the output facet and the reflectivity of the upper mirror is further decreased. So the mode-selective effect of the surface relief, namely the enhanced difference in threshold gain between fundamental and higher-order modes, is reduced. However, the fundamental mode dominates by more than 3 dB up to thermal rollover, indicating a strong improvement compared to the highly multi-mode device without surface relief.

Figure 6.22 shows the spectrally resolved near-field measurement of the lensed relief device at a current of 12 mA and a distance of about 35 µm to the laser surface. Besides the fundamental mode also one LP_{11} mode can be resolved. However, since less than 20 % of the total power are contained in the higher-order mode, the beam still shows a Gaussian intensity distribution. Therefore, the VCSEL is still suited for the use in the integrated optical trap.

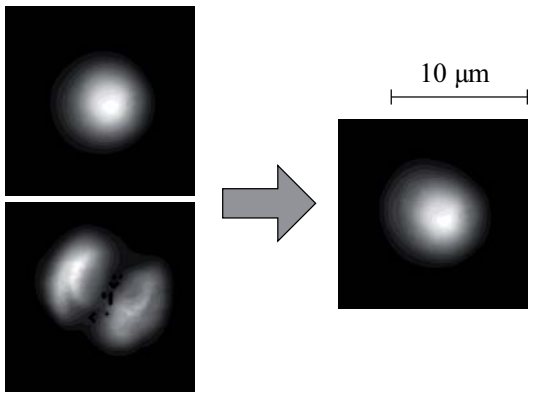

Fig. 6.22: Spectrally resolved near-field measurement of the lensed relief VCSEL from Fig. 6.21c at a current of 12 mA (left). Besides the LP_{01} mode (top) also one LP_{11} mode (bottom) can be resolved. However, the total intensity distribution (right) is still Gaussian-like.

For a further investigation of the focusing effect, near-field measurements at different distances to the laser surface are performed for a standard device, a relief device, and a lensed relief VCSEL on the same sample, all with oxide apertures of 8 µm. The relief diameters are 3.7 and 3.8 µm for the devices without and with microlens, respectively, and the microlens has a radius of curvature of 20 µm. All measurements are taken at 12 mA. Figure 6.23 presents the obtained results. The total intensity profile of the standard device shows constant beam divergence and clear multi-mode emission, as it was to be expected from the spectra in Fig. 6.21a. By contrast, the single-mode spectra in Fig. 6.21b for the relief device suggest a Gaussian-shaped beam profile. However, close to the laser surface a donut-shaped intensity profile can be observed. This is caused by preferred outcoupling of light at the outer regions of the VCSEL facet, where the mirror reflectivity is significantly lower than at the surface relief [103]. After about 20 µm, this profile evolves into a Gaussian-shaped intensity distribution, where a much lower divergence than for the multi-mode VCSEL can be observed. For the lensed relief device, the beam disturbance close to the laser facet is no longer present, since the resist material reduces the influence of the surface relief. Furthermore, a weak shrinkage of the beam diameter is observable, followed by a low beam divergence. Therefore, the beam size at a distance of 40 µm is smaller than for the relief device without microlens.

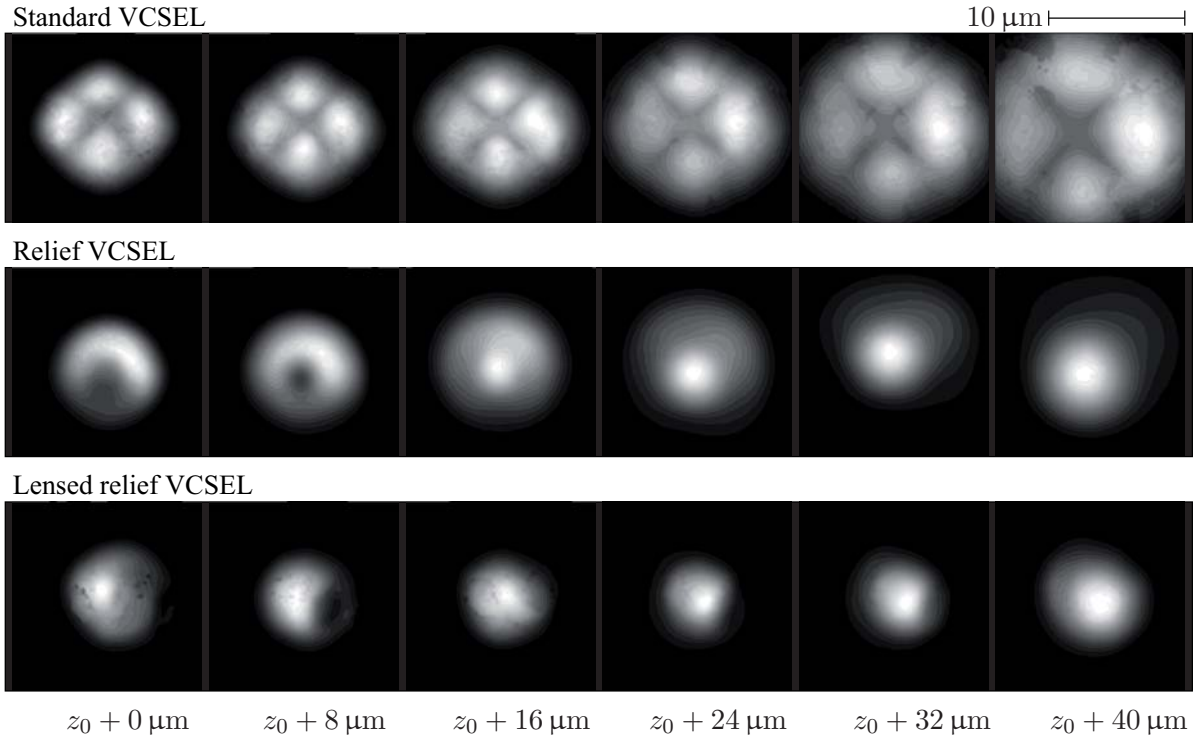

Fig. 6.23: Near-field measurements at different distances to the laser surface for three VCSELs with active diameters of 8 µm, all taken at a driving current of 12 mA. Besides the standard device (top), also a relief device without lens (3.7 µm relief, middle) and with lens (3.8 µm relief, 20 µm radius of curvature, bottom) are examined.

From the near-field profiles the beam diameter at each distance can be determined. Therefore, the mathematical definition of a standard deviation is applied, as given in (5.8), in different spatial directions. However, for a broad output beam, a significant portion of the beam is not scanned by the fiber, hence, the determined beam diameter is too small. This is especially true for the standard device at large distances to the laser surface. Figure 6.24 shows the resulting beam propagation for the different devices. Compared to the standard VCSEL, the relief device has a reduced beam diameter and a lower divergence, due to the absence of higher-order modes. While both lasers show a constantly diverging beam, the lensed device possesses weak focusing of the output beam at a focal distance of about 15 µm (in air) to a beam waist of 7 µm. This leads to a delayed divergence of the beam, so a reduced beam diameter compared to the device without lens is observed, for example 8.5 µm compared to 11.5 µm at 40 µm distance. This reduction of the beam diameter at a distance where the particles are placed in the final setup enhances the transverse stability of the integrated optical trap.

6.5.2 Experimental Results on Particle Manipulation

The above described lensed relief VCSELs are inserted into the setup shown in Fig. 6.17 to investigate their suitability for particle manipulation. The experiment is observed by a CCD camera which is protected from the laser beam with an infrared cutoff filter. The

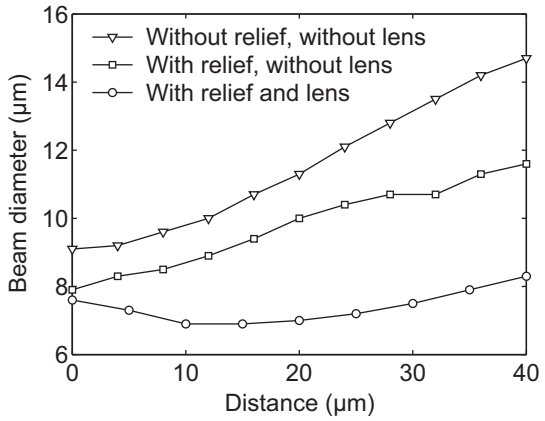

Fig. 6.24: Beam diameters at different distances to the laser surface for three different VCSEL types with active diameters of 8 µm. The relief diameters are 3.7 µm (without lens) and 3.8 µm (with lens), where the microlens has a radius of curvature of 20 µm. Weak focusing and a delayed divergence for the lensed relief VCSEL is observed.

volume between the thin glass substrate and the upper cover slip is filled with a solution of 10 µm polystyrene particles which drift through the liquid due to thermally induced evaporation of the solution. Again, this drift was found to be random and no correlation to the emission status of the VCSEL is observed. Figure 6.25 shows a typical sequence of the performed experiment, employing a 8 µm active diameter VCSEL with a 3.9 µm surface relief and a 20 µm radius of curvature microlens. Furthermore, corresponding schematic side views are added.

Initially, the polystyrene particles drifts randomly through the liquid, in the present case from the right to the left (Figs. 6.25a and b). When a particle comes close to the lensed VCSEL, which emits about 5 mW of optical power, it is drawn toward the center of the beam by the transverse gradient force (Figs. c and d). Since the longitudinal gradient force

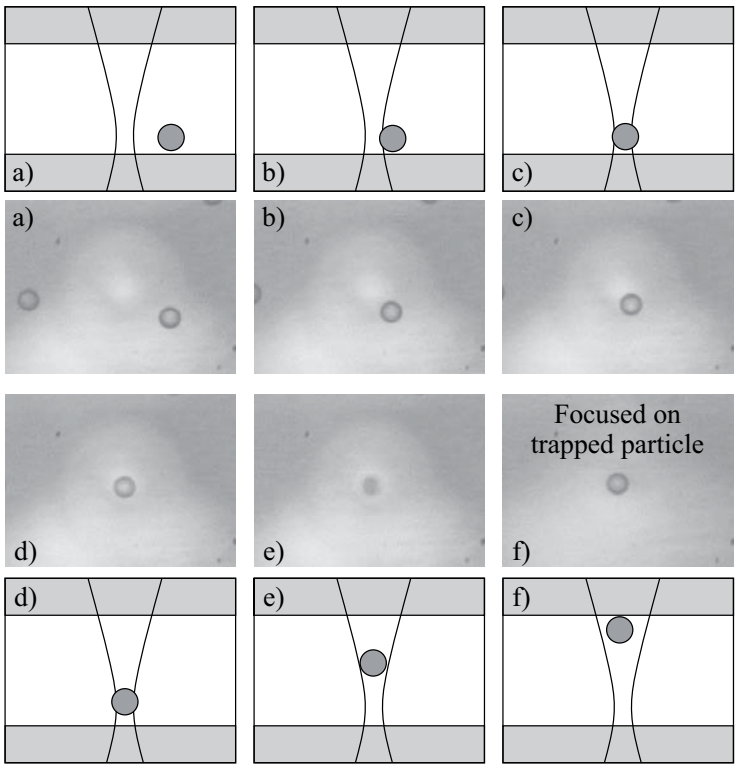

Fig. 6.25: Sequence of a trapping experiment with the integrated optical trap based on a lensed relief VCSEL at 5 mW of optical power. Initially the 10 µm particle drifts randomly through the liquid (a,b), then it is drawn toward the center of the laser beam (c,d) and elevated by radiation pressure (e). Finally it remains trapped at the upper cover slip (f).

of the only weakly focused beam is not large enough to compensate the forward scattering force, the particle is then pushed upwards by radiation pressure, which can be observed by a blurring of the particle as it moves out of the focus of the imaging system (Fig. e). After adjusting the imaging system, the particle is found to be trapped at the upper cover slip where it remains immobilized until the laser is turned off. Similar results were obtained for higher output powers and similar lasers. At lower optical power or high drift velocities, only transverse deflection and elevation of the particle can be accomplished but no immobilization is possible.

Although the basic flow of the experiment is very similar to the trapping experiment presented in Fig. 6.18 for the multi-mode VCSEL, a difference regarding the transverse trapping position exists. For highly multi-mode lensed VCSELs, an offset between laser center and trapped particle is generally observed, as mentioned earlier. Figure 6.26a shows a typical picture of these experiments, where the particle is trapped by the laser beam at the upper cover slip and the imaging system is focused on the microbead. The white cross marks the center of the VCSEL. A distance of more than 15 µm between VCSEL center and trapped particle is visible. The added schematic side view illustrates the origin of this offset, showing the particle placed on the ring of maximum intensity. The final position of the particle is determined by the movement of the surrounding liquid, which is oriented from left to right in the case of Fig. 6.26a. Figure 6.26b shows the same picture for the experiment with a lensed surface relief VCSEL with reduced multi-mode emission. Here, only a small deviation between particle center and laser is found, since the intensity maximum coincides with the laser center, as indicated by the schematic side view. Furthermore, less optical power is required for trapping (5 mW compared to 9 mW), since the power density at the sample stage is similar, owing to the lower divergence and the smaller beam diameter. Therefore,

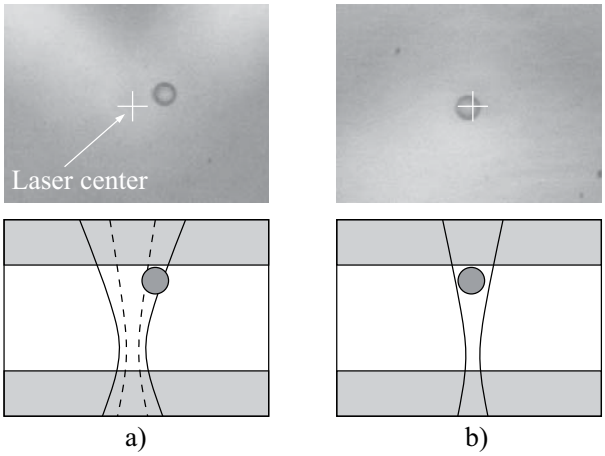

Fig. 6.26: Results of trapping experiments with a highly multi-mode VCSEL (a) and a relief VCSEL with reduced multi-mode emission (b), both with integrated microlenses with radii of curvature of about 20 µm. The pictures show 10 µm particles trapped at the upper cover slip. The dashed line in the schematic side view indicates the ring shaped beam profile of the multi-mode laser. While a large offset between laser center and trapped particle is present for the multi-mode laser, a significant reduction is achieved by the relief device.

the power limitation of the relief device does not affect the trapping stability, while the higher beam quality leads to an improved spatial accuracy.

In the presented trapping experiments, deflection, levitation and trapping of particles were demonstrated, so the concept of the integrated trap could be confirmed. However, the used setup presented in Fig. 6.17 is still experimental and neither stable nor practicable. A major issue is the electrical contact to the VCSEL p-side as well as a reliable connection between sample stage and laser chip. Therefore, an advanced setup is investigated in the next chapter, where also the number of used VCSELs is increased.

7 Integrated Optical Trap Arrays in Microfluidics

In the previous chapter the realization of the integrated trap scheme based on a solitary VCSEL was discussed and successfully demonstrated. The current chapter covers the extension of this concept to multiple optical traps using arrays of vertical-cavity lasers. Continuous particle deflection in a microfluidic environment is intended using a linear optical lattice. To determine appropriate array dimensions, simulations of the deflection process are performed. Furthermore, the still crude experimental setup in Chap. 6 is substituted with a compact and portable one, based on flip-chip technology and indium soldering.

7.1 Continuous Particle Deflection Scheme Using Integrated Optical Traps

7.1.1 Concept and Layout

Figure 7.1 shows a schematic of the intended integrated trap structure. Analogous to the previous chapter, an integrated photoresist microlens in combination with an inverted surface relief is used to generate a Gaussian-like laser beam of small diameter in the particle solution. However, instead of a solitary laser, an array of closely spaced VCSELs is used, which can be fabricated according to the self-aligned process given in Sect. 3.2.2. As in the previous chapter, the photoresist microlens is made of PMGI resist, where the fabrication process has to be adjusted to account for the smaller mesa diameter.

Using a slightly tilted, linear array of integrated optical traps, the deflection scheme shown in Fig. 7.2 can be realized. Instead of being trapped by a single laser beam, the flow path of a particle in the microfluidic channel is altered by the interplay of trapping force and fluidic drag force. While the large particle in Fig. 7.2 passes the array, it is deflected orthogonally to its initial flow direction, so eventually it is redirected to the upper channel arm. Thus, by switching the array on or off, specific particles can be selected from the solution.

However, successful deflection only works in a certain window of parameters, similar to the process in the optical tweezers setup given in Chap. 3. For example, a reduced particle diameter results in a lower fluidic drag force but also in a decreased transverse trapping force. Furthermore, the relative distance between the traps becomes larger, such that successful deflection is no longer possible. Thus, the smaller particle in Fig. 7.2 leaves the channel junction through the lower branch. With the larger particles being deflected, the concentration of smaller particles in the lower channel arm is strongly increased. Therefore, particle fractionation by size is achieved. Furthermore, particle separation dependent on the

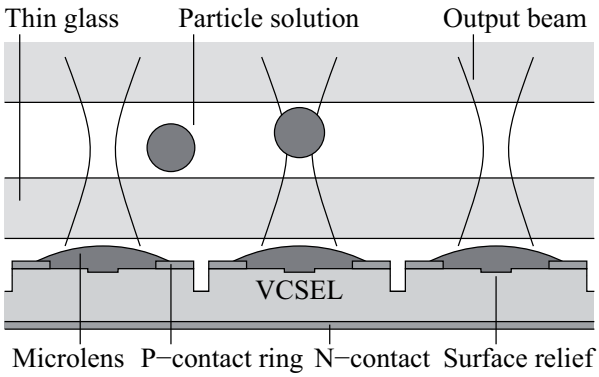

Fig. 7.1: Schematic of the integrated optical trap structure based on a densely packed VCSEL array. Multiple optical traps are generated at the sample stage.

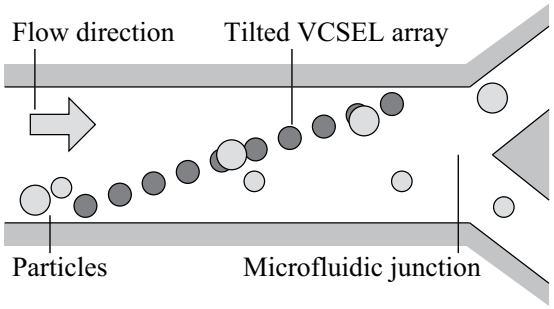

Fig. 7.2: Schematic of the optical fractionation scheme at a tilted array of integrated optical VCSEL traps.

refractive index or the shape of the particle should be possible, since both factors influence the trapping forces.

To design such an optical deflection unit and to determine appropriate laser array geometries, the deflection process is studied in more detail in the following section by simulation of the flow path of the particle.

7.1.2 Simulation of Continuous Particle Sorting

Simulation of the particle deflection requires knowledge of the acting trapping force as a function of the spatial position in the channel. Therefore, the ray optical model presented in Sect. 2.1.2 is used to calculate the gradient force F_g generated by a single VCSEL trap. The weakly focused laser beam is approximated by a parallel beam with a transverse Gaussian profile. Figure 7.3 shows the calculated transverse trapping force as a function of the distance between particle center and optical axis for 8 µm beam diameter, 5 mW optical power, and a 15 µm diameter polystyrene particle. Only far away from the laser beam or exactly at the beam center the particle is in a stationary state, while close to the beam center a force of up to 5 pN is exerted.

Next, the corresponding trapping potential, given by $V_\mathrm{F} = -\int F_\mathrm{g}\,\mathrm{d}s$, is extended to a two-dimensional array. Figure 7.4 shows the potential for an array of six traps with a trap distance of 25 µm and a tilt angle of 10° for a 15 µm particle. By reducing the trap distance to only 15 µm (see Fig. 7.5) and increasing the number to nine lasers, a strong overlap of the individual trapping potentials can be achieved, leading to a connected region with negative potential along the tilted trap array. However, such a small laser pitch cannot be achieved with lensed VCSELs. Therefore, particle deflection will not happen along a straight line, but it is expected to have a staircase-like quality with a certain hopping of the particle between individual traps.

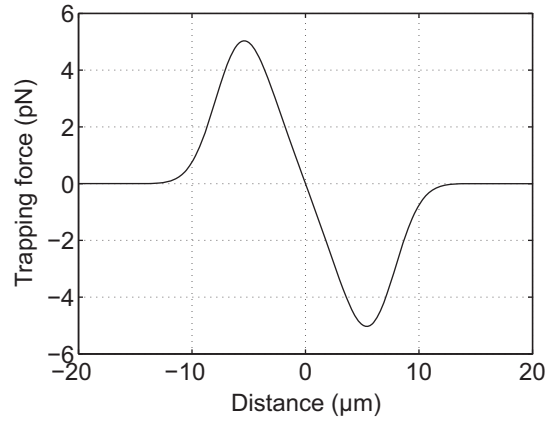

Fig. 7.3: Calculated trapping force versus the distance between particle center and optical axis for 8 µm beam diameter, 5 mW optical power, and 15 µm particle diameter.

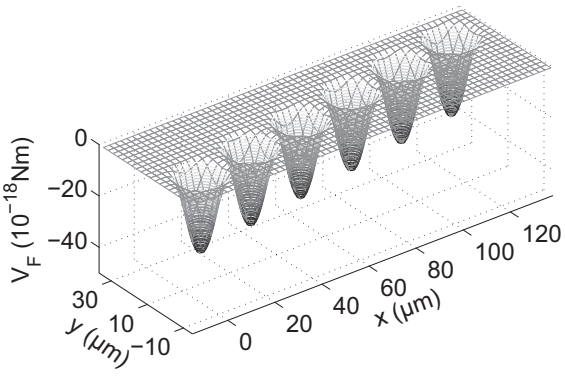

Fig. 7.4: Optical trapping potential V_F of an optical lattice of six traps with a distance of 25 µm and a tilt angle of 10°. All other parameters are as in Fig. 7.3.

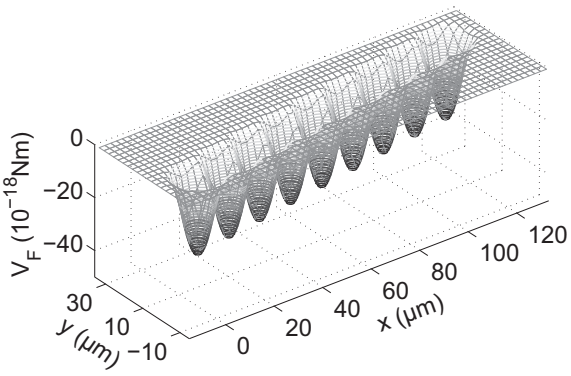

Fig. 7.5: Optical trapping potential V_F of an optical lattice of nine traps with a distance of 15 µm and a tilt angle of 10°. All other parameters are as in Fig. 7.3.

To determine the particle movement through such a potential landscape, the equation of motion [75]

$$m_\mathrm{p}\ddot{\mathbf{x}} = \mathbf{F} + D_\mathrm{f} \cdot (\mathbf{v}_\mathrm{f} - \dot{\mathbf{x}}) \tag{7.1}$$

has to be solved. Here, $\mathbf{x}$ is the position vector, m_p is the particle mass, $\mathbf{v}_\mathrm{f}$ is the fluid velocity and $\mathbf{F}$ is the spatially varying optical force on the particle. The quantity D_f is a damping constant, which for a spherical particle is given by Stokes' law as

$$D_\mathrm{f} = 3\pi\eta a, \tag{7.2}$$

where a is the diameter of the particle and η is the fluid viscosity. Thus, the second right-hand term of (7.1) represents the fluidic drag force. All vectors are only two-dimensional, so the scattering force, which pushes the particle upward, is not taken into account.

Equation (7.1) can be rewritten into the following set of differential equations

$$\dot{x} = v_x \tag{7.3}$$

$$\dot{v}_x = \frac{1}{m_\mathrm{p}} \left(F_x + D_\mathrm{f} \cdot (v_{\mathrm{f}x} - v_x) \right) \tag{7.4}$$

$$\dot{y} = v_y \tag{7.5}$$

$$\dot{v}_y = \frac{1}{m_\mathrm{p}} \left(F_y + D_\mathrm{f} \cdot (v_{\mathrm{f}y} - v_y) \right), \tag{7.6}$$

where x and y are spatial coordinates according to Fig. 7.4 and their first derivatives are the particle velocities v_x and v_y, respectively. The trapping force and the fluid velocity are separated into their x- and y-components as well, leading to the quantities F_x, F_y and $v_{\mathrm{f}x}$, $v_{\mathrm{f}y}$. Equations (7.3)–(7.6) are numerically solved using the software package Matlab, where the viscosity of water $\eta = 935 \cdot 10^{-6}\,\mathrm{kg/(ms)}$ and the mass density of polystyrene of 1050 $\mathrm{kg/m^3}$ are taken into account. As boundary condition, the initial velocity of the particle is chosen to be equal to the velocity of water $v_{x0} = v_{\mathrm{f}x}$ and $v_{y0} = v_{\mathrm{f}y} = 0$, i.e., the particle is carried by the fluid flow.

The left side of Fig. 7.6 shows the result of a calculation by sequences of the determined particle path. A 15 µm diameter polystyrene particle with a refractive index of 1.6 is moved forward by a fluid velocity of 90 µm/s. The trap array consists of six lasers with a distance of 25 µm and a tilt of 10°. Each trapping beam has 5 mW of optical power and a diameter of 8 µm, based on the experimental results on lensed relief VCSELs presented in Chap. 6. While passing the array, the particle is piecewise deflected at each trap. The x- and y-displacements plotted in the right side of Fig. 7.6 show that the sphere is moved by a total distance of more than 20 µm in y-direction, while the movement in x-direction is only slightly disturbed. As expected, the deflection in y-direction has a staircase-like quality, with the particle being accelerated when approaching a trap. Even for an increased array length the

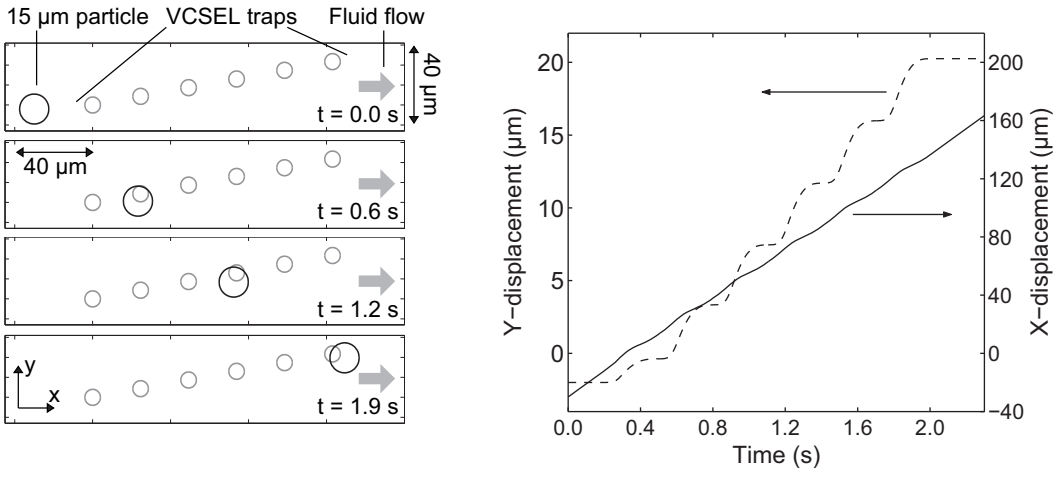

Fig. 7.6: Calculated movement of a 15 µm diameter polystyrene particle shown by snapshots of the particle position (left) and plots of the x- and y-displacement (right). The simulation parameters are as follows: 90 µm/s water velocity, 25 µm trap distance, 10° array tilt, 5 mW power per trap, and 8 µm beam diameter.

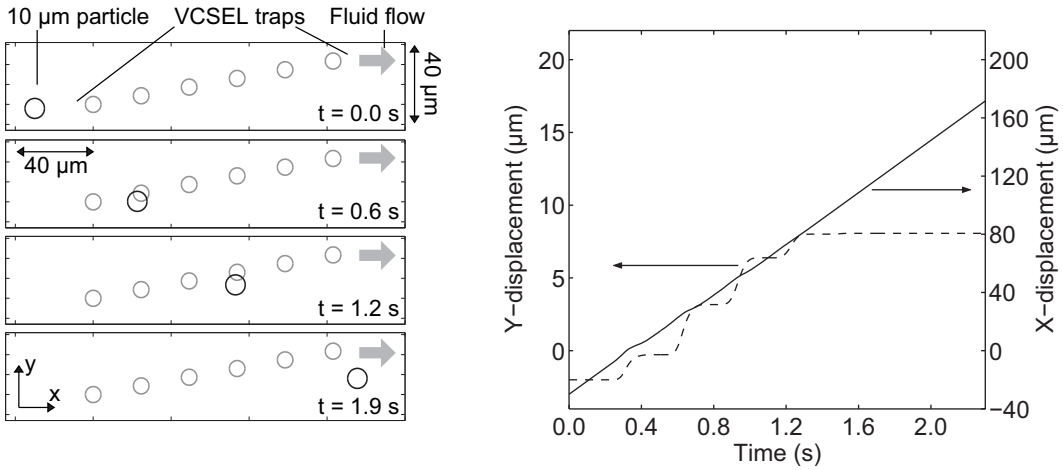

Fig. 7.7: Movement of a 10 µm diameter particle equivalent to Fig. 7.6 using identical simulation parameters.

particle will follow this staircase to its end, since it is stably linked to the optical lattice. This behavior is termed successful deflection in the following. A separation of specific particles can be performed by switching the array on or off. Furthermore, significantly higher particle velocities than in the conventional VCSEL tweezers setup presented in Chap. 3 are expected, mainly due to drastically reduced optical losses and therefore higher optical power.

Figure 7.7 shows the result of a second calculation for a smaller polystyrene particle with 10 µm diameter. All other simulation parameters are retained. In this case, the particle is again deflected by the optical lattice, however, due to the comparatively larger trap distance, the interaction is clearly weaker than for the larger particle. After a distance of about 80 µm, the particle looses contact with the array and is no longer deflected. Therefore, the total displacement in y-direction is only about 10 µm, thus, an added junction in the microfluidic channel according to Fig. 7.2 could be used to separate larger from smaller particles by fractionation.

The same effect can be observed for particles of different refractive index. The upper line in Figure 7.8a gives the maximum fluid velocity at which successful deflection is still possible in dependence on the refractive index for particles with 15 µm diameter. If the fluid velocity is increased beyond this maximum value, the link of the particle to the optical lattice is lost and the particle escapes the deflection. A higher contrast in refractive index between particle and surrounding medium results in a stronger transverse trapping force, as discussed in Chap. 2. Therefore, the maximum possible fluid velocity is much higher for particles with a refractive index of 1.6 than 1.4. It is important to note that also a minimum fluid velocity is necessary to achieve successful deflection. If the fluidic drag on the particle is too weak, it is no longer deflected, but stays trapped by a single laser beam. This minimum fluid velocity is given by the lower line in Fig. 7.8a. Owing to the larger trapping force, it increases with increasing refractive index.

Figure 7.8b shows the same diagram for a particle of 10 µm diameter. Significant shrinkage of the velocity range of successful deflection compared to the 15 µm particle can be observed. The minimum fluid velocity is similar, since the lower fluidic drag force is compensated by

a lower transverse trapping force. The maximum possible velocity however is much smaller, due to the comparatively larger trap distance. So, obviously, there exist certain velocity ranges, where particles of different refractive index or size can be separated.

Figures 7.8c and d give the minimum and maximum fluid velocities for different tilt angles of the optical lattice (10°, 15°and 20°) for 15 and 10 µm particles, respectively. As expected, the maximum possible velocity decreases with increasing tilt angle, while the minimum velocity is independent on the angle. An interesting observation can be made for 10 µm particles at large tilt angles. Here, the range of successful deflection vanishes and the particle is either completely trapped or escapes the link to the optical lattice.

Since the used simulation parameters are based on experimental results and the fabrication of VCSEL arrays with the required geometries was already demonstrated in Chap. 3, integrated VCSEL trap arrays have a strong potential for continuous optical particle sorting in compact, portable devices.

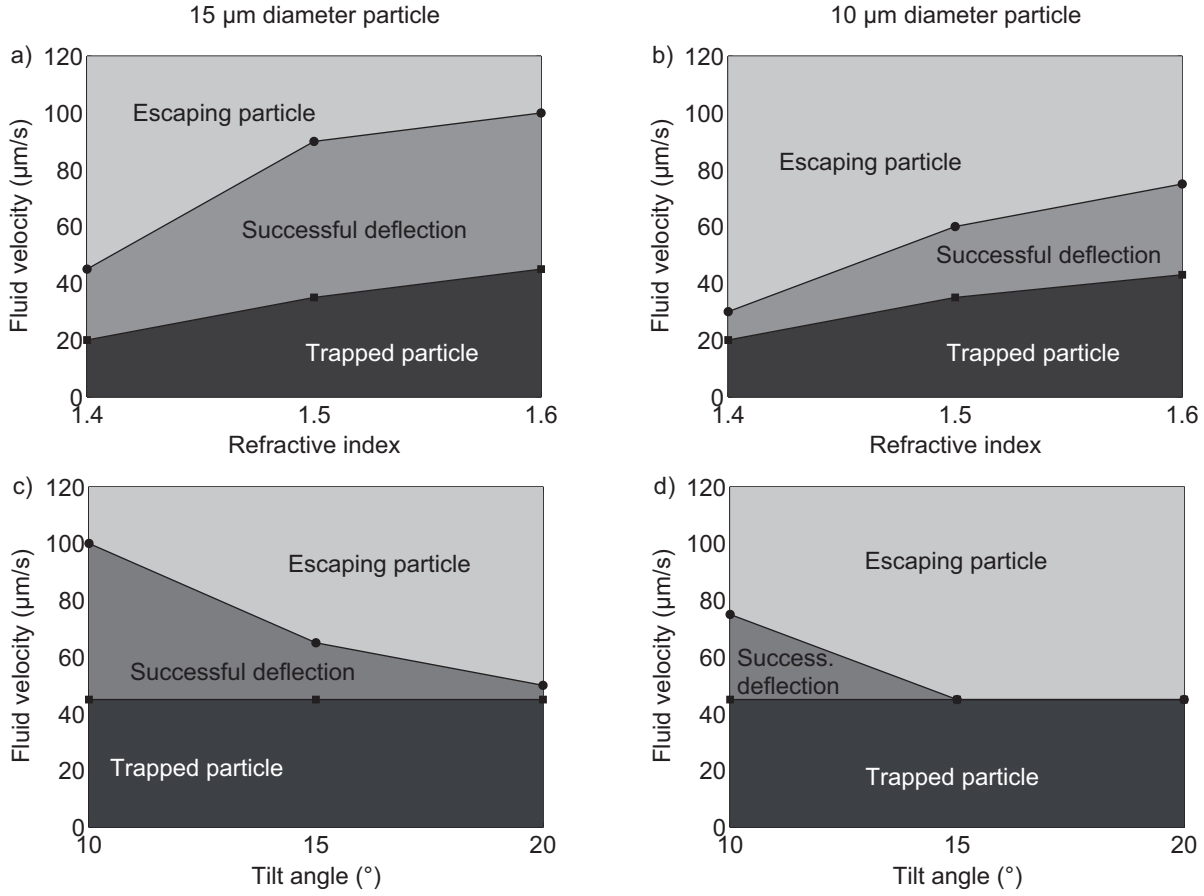

Fig. 7.8: Fluid velocity range for successful deflection depending on the refractive index of the particle (a, b) and the tilt angle of the optical lattice (c, d) for 15 µm (a, c) and 10 µm (b, d) particle diameter. Out of this range, the particle either escapes the lattice (velocity too high) or it is completely trapped (velocity too low). Symbols are simulation results, lines are guides to the eye.

7.2 Integration of a VCSEL Chip with Microfluidic Channels

An efficient operation of the integrated optical trap demands a minimized distance between the laser surface and the microfluidic chip to prevent strong beam expansion. At the same time, electrical contacts to the p-metalization at the top side of the laser chip must be realized. In the previous chapter, these requirements were met by inserting a thin layer of conductive glue between the p-contact pads and the metalized glass of the sample chamber. This setup is however neither stable nor portable and not suited for addressing multiple lasers. Therefore, flip-chip bonding of the laser chip to the microfluidic chip is investigated in the following section.

7.2.1 Concept

Figure 7.9 shows a schematic of the envisioned module. The microfluidic chip is made of PDMS by soft lithography, as described in Chap. 4. However, the cover glass used to seal the microfluidic channel has to be substituted with much thinner glass to conform to the integrated trap scheme shown in Fig. 7.1. The VCSEL array is located directly underneath this glass slide. Indium solder bumps connect the p-contact pad to a metalization layer on the glass, which extends to the edges of the microfluidic chip. With this fan-out, the p-side of the lasers can be easily contacted, while the n-side is accessible by the common back side metalization.

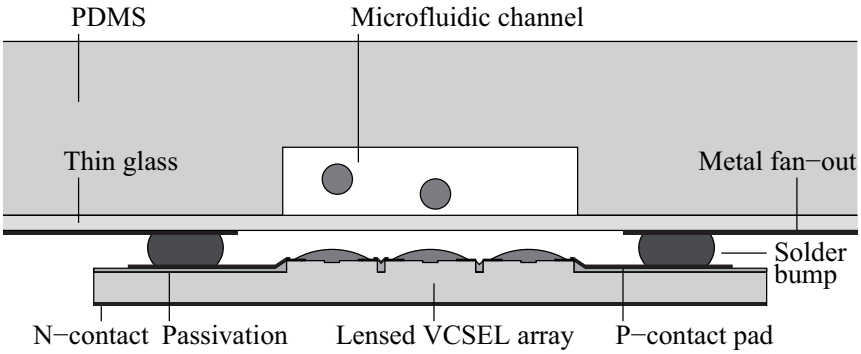

Fig. 7.9: Schematic of the integrated trap array module. The laser chip is directly connected to the microfluidic chip by indium solder bumps, which serve as mechanical as well as electrical contact.

To fabricate this structure, lithography, metalization, and lift-off processes must be performed on the glass side of the microfluidic chip. After completion, the glass contains the metal fan-out as well as small islands of indium. For soldering, the laser chip is flipped and placed on the metalized glass side. When heated, the indium melts and alloys with the p-contact pad on the laser chip. After cooling down, a stable electrical and mechanical contact is formed, where a good alignment of the fan-out structure to the channel can be attained.

Figure 7.10 shows a more detailed schematic of this connection. Additional polyimide passivation layers on the glass as well as on the semiconductor side are necessary to prevent spreading of the indium along the metal stripes during the soldering process. Since indium does not wet polyimide, the indium islands will contract to a bump-like shape to minimize the surface energy. More details on the structuring of the microfluidic chip and the indium soldering follow in Sects. 7.2.3 and 7.2.4, respectively, while the following section gives results on lensed VCSEL arrays.

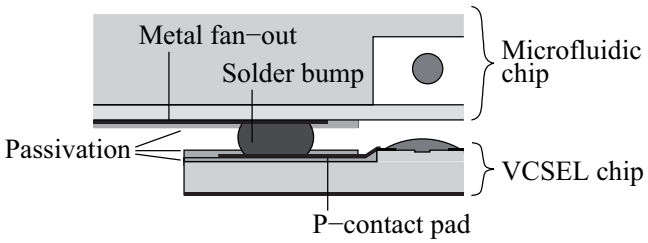

Fig. 7.10: Detailed section of the schematic integrated trap setup. Additional passivation layers are necessary to prevent wetting of the metal lines with indium.

7.2.2 Surface Relief VCSEL Arrays with Integrated Microlenses

Densely packed VCSEL arrays with inverted surface relief are fabricated according to the self-aligned process given in Sect. 3.2.2. Since a second passivation layer is required as shown in Fig. 7.10, the process is terminated by an additional polyimide step. Next, the microlenses are fabricated by thermal reflow of PMGI resist as described in the previous chapter. Since the mesa diameter is in the range of only 22 to 24 µm, the bottom diameter of the lens must be reduced from about 25 µm as in Chap. 6 to about 16 to 18 µm. To achieve a similar radius of curvature of about 20 µm, the resist thickness is reduced according to Fig. 6.8. All other process parameters are retained.

In the upper left corner of Fig. 7.11, an optical microscope image of a finished lensed VCSEL array with a laser pitch of only 24 µm is shown. To analyze the shape of the fabricated microlens, AFM measurements are performed. The obtained height profile of a scanned device is shown in the upper right corner of Fig. 7.11. Three regions can be distinguished on the VCSEL mesa. In the center of the output facet, the photoresist microlens is clearly visible, partly covering the p-contact ring. The following outer ring stems from the overlapping polyimide passivation layer. In the lower left corner of Fig. 7.11, the central cross-section of this measurement is given. A radius of curvature of about 25 µm is obtained from the spherical fit.

To study the effect of the microlens on the VCSEL performance, output characteristics were measured before and after the microlens fabrication. In the upper part of Fig. 7.12 the LIV curves of an array of three simultaneously working VCSELs is shown. The oxide aperture is 6.5 µm wide and the surface relief has a diameter of 3.4 µm. An overall output power of 8.5 mW and a threshold current of 15.4 mA can be observed, leading to mean values per device of 2.8 mW and 5.1 mA, respectively. Owing to the inverted surface relief, the output spectra given below for one VCSEL show a side-mode suppression ratio of more than 30 dB in the whole range of operation. As expected, the near-field measurements in the lower part of Fig. 7.12 show a Gaussian-shaped beam profile.

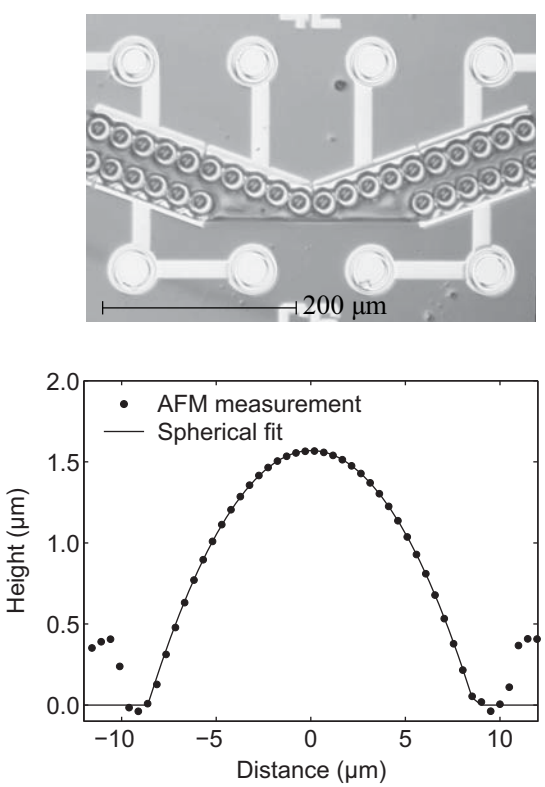

Fig. 7.11: Top left: image of a densely packed array of lensed surface relief VCSELs. Top right: AFM height profile of an individual device. Bottom left: cross-section of the AFM measurement with a spherical fit, showing a radius of curvature of 25 µm.

The corresponding measurements after the microlens fabrication, given in Fig. 7.13, agree with the results of Chap. 6. Since the lens material lowers the refractive index step at the output facet, the effect of the surface relief is reduced. Therefore, the threshold current is strongly decreased to 3.0 mA per device and a slight increase in mean output power to 3.1 mW can be observed. In the optical spectra an onset of various higher-order modes can be observed. However, the fundamental mode is still dominant by at least 20 dB, thus the corresponding near-field measurements show a Gaussian-shaped beam profile.

To analyze the beam propagation of the lensed relief devices, near-field measurements were taken at different distances to the laser output facet. From these measurements, the beam diameter was derived based on the criteria of the second moment, as described in Sect. 5.2.3. Figure 7.14 shows the determined beam broadening for a standard device of 8.5 µm oxide aperture and a nominally identical device except for a 4.0 µm wide surface relief and an integrated microlens with 25 µm radius of curvature. The measurements are taken at similar operating points. Compared to the standard device, the lensed relief VCSEL shows a strongly reduced beam diameter. Although no focal point is visible in these measurements, a delayed divergence can be observed. At a distance of 40 to 50 µm, where the particle solution will be located in the final trap structure, the beam diameter is only about 10 µm wide. At the same distance the standard device shows an output beam diameter of 16 µm, which is furthermore donut-shaped due to highly multi-mode emission.

Although the fabricated lensed relief VCSEL devices show lower output power than expected, they are well suited for the application in the integrated optical trap concerning their beam propagation properties.

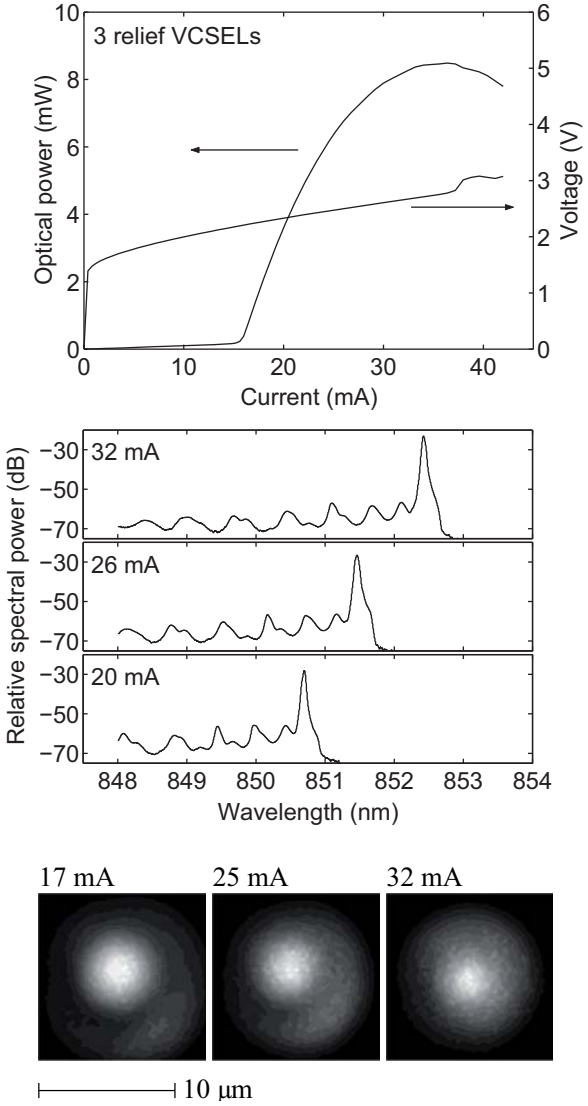

Fig. 7.12: LIV characteristics (top), optical spectra (middle) and near-field profiles (bottom) of three relief VCSELs driven in parallel (6.5 µm active and 3.4 µm relief diameter).

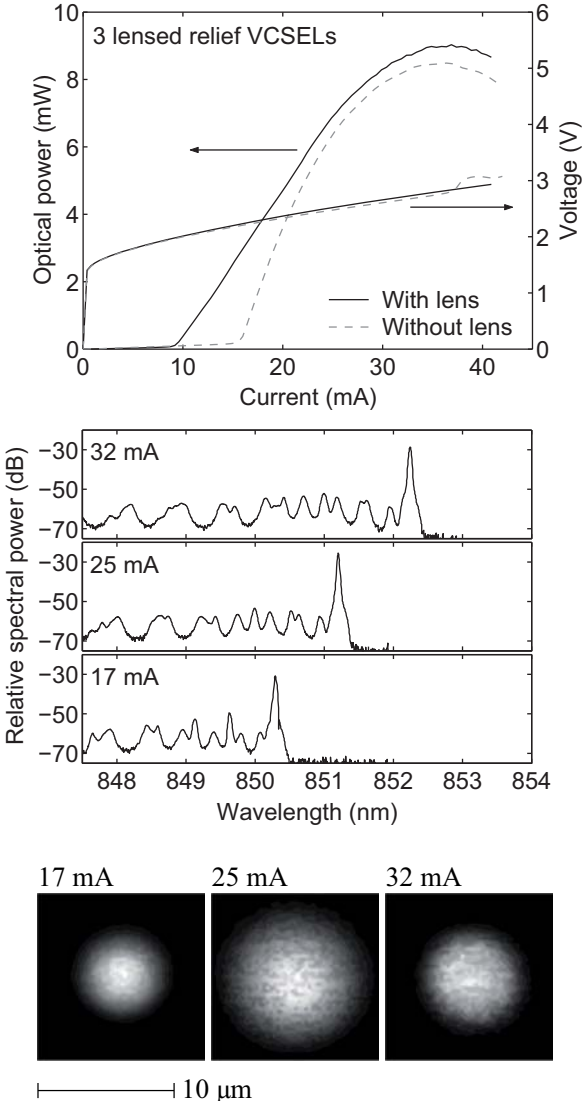

Fig. 7.13: Same as Fig. 7.12 after integration of resist microlenses on the output facets. Despite the onset of higher-order modes, the intensity profile is still Gaussian-shaped.

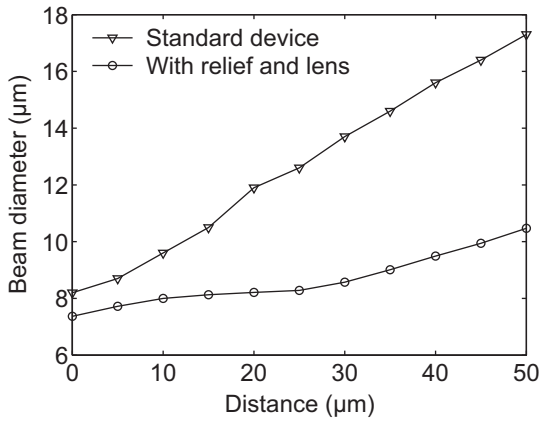

Fig. 7.14: Diameter of the output beam against the distance to the laser facet for a standard device and a lensed relief VCSEL with 8.5 µm active diameter, a 4 µm relief diameter and 25 µm radius of curvature. The beam diameter is determined from near-field intensity profiles.

7.2.3 Structuring of the Microfluidic Chip

The fabrication of the microfluidic chip works according to the soft lithography process based on PDMS described in Chap. 4. The cover glass used so far to seal the channel is substituted by a just 30 µm thin glass slide, to meet the requirements of the integrated trap scheme. While the freestanding glass slide is very fragile, bonding to the PDMS chip stabilizes the thin layer and enables easy handling. However, overlapping glass edges must be carefully avoided, since they are the origin of cracks, which can spread along the whole glass slide.

Flip-chip bonding of the semiconductor chip to the microfluidic chip requires three major processing steps on the glass slide, according to Fig. 7.10. First, the metal fan-out is fabricated by structuring of negative resist, metal evaporation and lift-off. Next, a polyimide layer is structured to passivate the entire glass surface except for the region above the microfluidic channel and the ends of the fan-out lines. Thus, contact pads are formed. Finally, 6 µm thick indium islands for the soldering bumps are generated on top of the contact pads. Here again structuring of thick negative resist, metal evaporation and a lift-off process are used.

To perform lithographic steps on the microfluidic chip the commonly used processes must be modified. First, the channel inlets have to be closed against infiltration of solvents like acetone, which lead to a swelling of PDMS [104]. Especially during lift-off processes the contamination by resist residues must be avoided. Therefore, PDMS cylinders are plugged into the channel reservoirs to seal them. Furthermore, heating processes can no longer be performed on contact hot-plates. Instead, heating furnaces are used. Here, a bowing of the microfluidic chip can be observed, since the temperature expansion of PDMS is larger than the one of glass. This bowing is however reversible and neither the PDMS layer nor the glass slide are affected, even for the hard bake of polyimide at a temperature of 300 °C. Unexpectedly, the fan-out metalization on the glass-slide was found to be a critical step. To achieve a solid metal layer for stable bonding as well as good adhesion to the glass substrate, the metalization is composed of titanium, nickel and gold. After metal evaporation, multiple long cracks were often found in the thin glass slide, which cause a leakage in the microfluidic channels. The cause of these cracks can be either the abrupt heating of the glass substrate during evaporation or the strong shrinkage of the strained Ni layer during cool down. Both effects can be decreased by using a sputtering process instead of evaporation, so a stable metalization process is achieved.

Figure 7.15 shows an optical microscope image of the central part of the fabricated metal fan-out. Underneath the fan-out lines the microfluidic channel with Y-junction is visible. Since the glass slide is already bonded to the PDMS chip during processing, the lithographic structuring guarantees good alignment of the fan-out to the microfluidic channel. This is important, since the fan-out determines the position of the laser chip after flip-chip bonding. Figure 7.16 shows the microfluidic chip with the fan-out metalization on its glass side ready for flip-chip bonding.

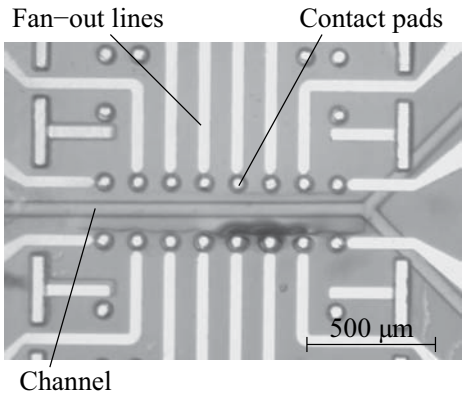

Fig. 7.15: Optical microscope image of the central part of the metal fan-out on the glass slide. Underneath the fan-out lines, the microfluidic channel in the PDMS is visible.

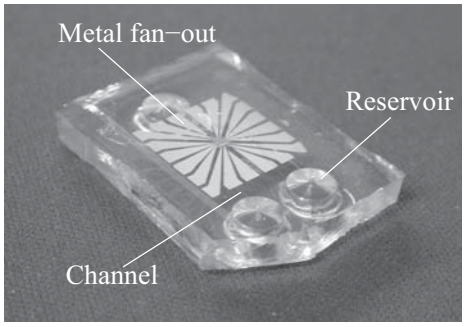

Fig. 7.16: Microfluidic chip with the fan-out metalization on its glass side ready for flip-chip bonding.

7.2.4 Flip-Chip Bonding Using Indium Bumps

Figure 7.17 shows the setup used for flip-chip bonding. The microfluidic chip, with its glass side facing upwards, is stuck to a glass plate by vacuum. The VCSEL chip is flipped and adhered to vacuum tweezers, which are movable in three dimensions by a servomotor-based positioning system. To simplify handling, the cleaved VCSEL chip has a size of about $1.2\times1.2\,\mathrm{mm}^2$, thus it contains three array segments, with only the center one being used. The metal structures on VCSEL chip and microfluidic chip can be viewed and aligned by detecting the infrared transmitted light in a microscope. This is possible, since the VCSEL chip has no complete back side metalization, which would block the infrared light from the imaging system. Instead, small contact stripes were structured on the back side of the chip. Figure 7.18 shows a typical image taken by the CCD camera. Both the fan-out lines on the

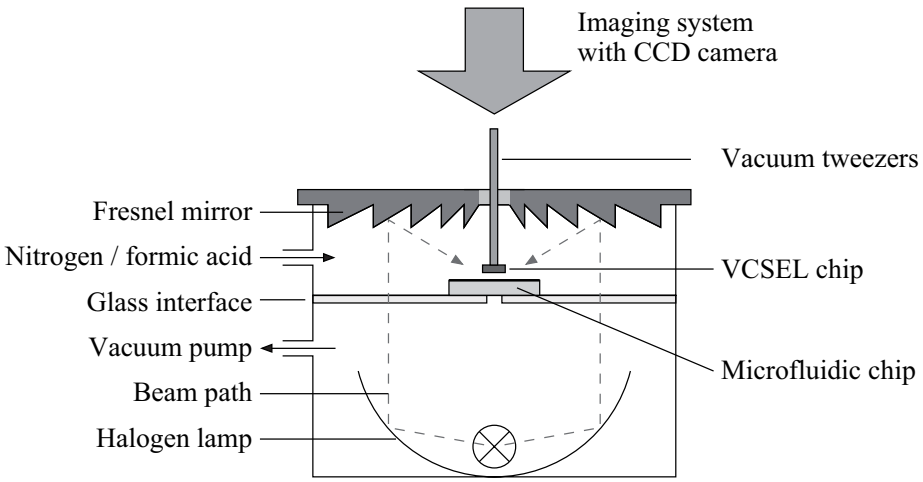

Fig. 7.17: Setup used for flip-chip bonding of microfluidic chip and VCSEL chip. Alignment of the structure is possible by detection of the infrared transmitted light.

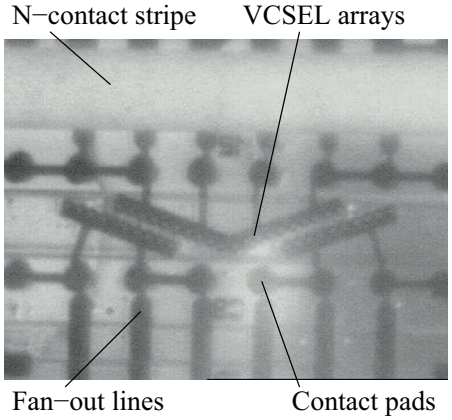

Fig. 7.18: CCD camera image taken in the flip-chip bonding setup, where both the fan-out lines on the glass slide and the VCSEL metalization lines are well visible.

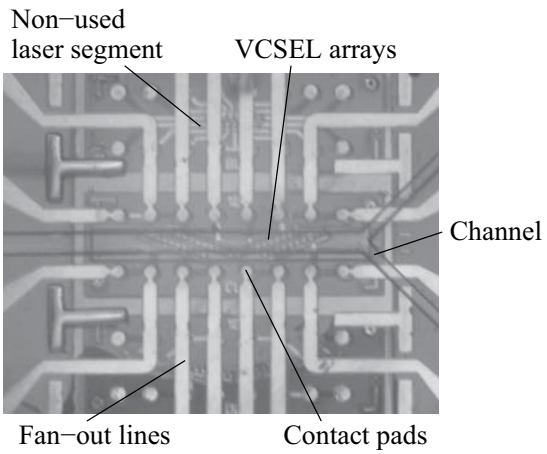

Fig. 7.19: Optical microscope image of the sample after flip-chip bonding. The image is taken through the transparent PDMS layer.

glass side as well as the VCSEL metalization are well visible, so the contact pads can be well aligned.

After the semiconductor chip is aligned and placed on the microfluidic chip, the structure is heated by a halogen lamp, whose radiation is focused to the chip using a Fresnel mirror. Melting of indium, which occurs at a temperature of 160 °C, is observed via alignment markers, so overheating of the structure can be avoided. During the soldering process the sample is rinsed with formic acid to remove indium oxide. In Fig. 7.19 an optical microscope image of the sample after soldering is presented. The image is taken through the PDMS layer, so the channel structure is on top, followed by the metal fan-out lines on the glass slide and the laser chip, with the relevant VCSEL arrays directly below the microfluidic channel. Good alignment of the contact pads on the glass and semiconductor sides can be observed.

Critical parameters during soldering are the process temperature and time. While too cold or too short soldering leads to unstable or non-conductive connections, the opposite can be hazardous for essential parts of the sample, like the photoresist microlenses, or can cause high strain between the different microchip materials. Furthermore, a long soldering time increases the diffusion of indium into the gold layer of the metal stripes. In the extreme, the complete indium island will spread along the fan-out stripes underneath the polyimide passivation. This leads to an unstable connection or at least to a strong shrinkage of the indium bump thickness and therefore to a reduction of the distance between laser and glass substrate. Although a small distance is beneficial, the step in refractive index between air and photoresist microlens is necessary for beam shaping. Thus, the microlens must not contact the glass slide.

To check the distance, a test sample was fabricated, where a semiconductor chip was soldered to a cover glass with fan-out metalization. Next, the sample was molded by a transparent epoxy resin and afterwards sawn and polished such that the cross-section of

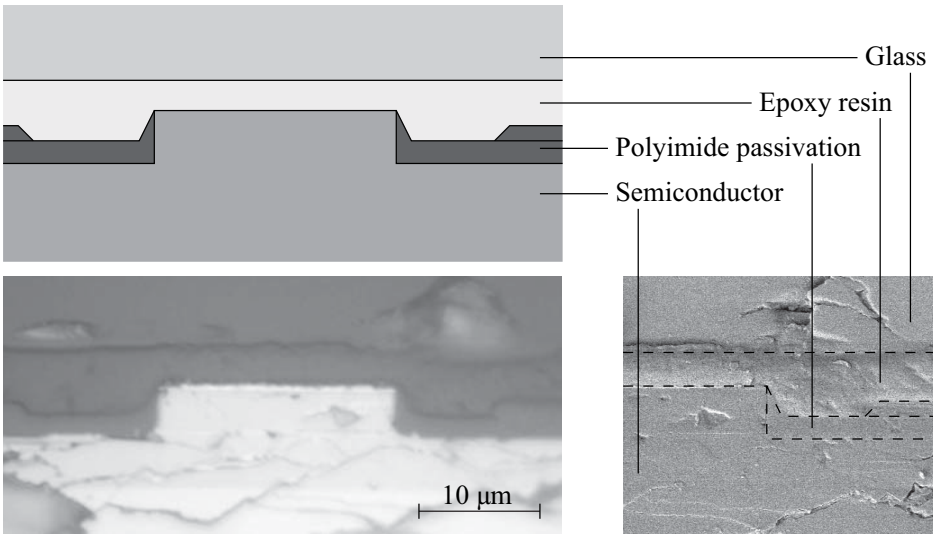

Fig. 7.20: Cross-section through the sample shown as schematic (top left), microscope image (bottom left) and SEM image (bottom right). To stabilize the sample for the polishing process, the gap between glass slide and semiconductor chip is filled with epoxy resin.

the sample is visible. Unfortunately, this cross-section does not contain an indium bump. However, an alignment marker on the semiconductor chip is visible, which has the same height as the VCSEL mesas. Figure 7.20 shows an optical microscope image (bottom left) and an SEM image (bottom right) of this section. Furthermore, a schematic of the visible structure (top left) is included. Although the sample is damaged by the polishing, the gap between semiconductor chip and cover glass, which is now filled by epoxy resin, is clearly visible. A distance of about 3.4 µm can be determined, which is large enough for the 1.5 µm high photoresist microlens.

The inset in the lower left part of Fig. 7.21 shows a photograph of the soldered chip, taken from the laser side. The fan-out on the glass and the semiconductor chip soldered at its center are clearly visible. Directly underneath the semiconductor chip, the PDMS contains a microfluidic T-junction, which ends in reservoirs for fluid injection. To contact the VCSEL, the microfluidic chip is attached to a printed circuit board containing an opening in its center, as shown in the photograph in the upper part of Fig. 7.21. With wire bonding, the fan-out lines of the glass metalization are connected to the metal stripes on the circuit board. A bond wire from the semiconductor back side to the circuit board provides contact to the VCSEL n-side. To increase the stability of the semiconductor–glass connection for this step, the edges of the laser chip are covered with epoxy glue.

Finally, cables are soldered to the circuit board lines and the structure is inserted into a specially adapted plastic housing. Figure 7.22 shows a finished prototype. Its dimensions are about $5\times6\times2.5\,\mathrm{cm}^3$, so easy handling and portability are achieved. A further reduction in size could be realized by using a more sophisticated connection of the circuit board. Electrical contact to the VCSEL arrays is provided by stable cables, which leave the housing on the right hand side in Fig. 7.22. While the laser chip is secured in the inside of the housing, the microfluidic chip with its reservoirs for fluid injection is easily accessible from

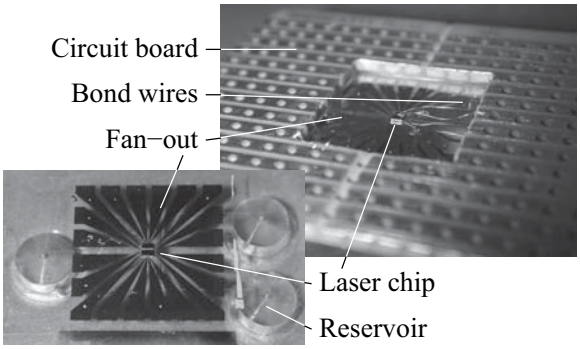

Fig. 7.21: Bottom left: Photograph of the sample after flip-chip bonding. Top right: The sample is attached to a printed circuit board and connected via bond wires.

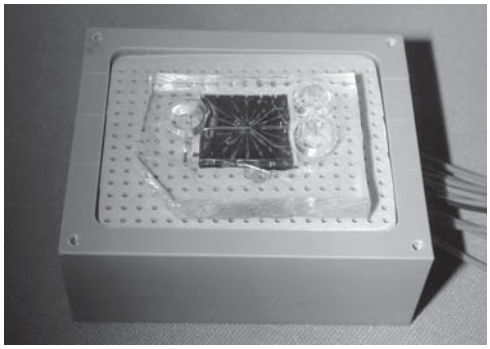

Fig. 7.22: Photograph of the finished integrated trap module. The laser chip is secured inside the plastic housing, while the reservoirs are easily accessible from top. Electrical contact is provided by cables.

top. Observation of particles inside the microfluidic channel is possible from the top side as well, due to the high transparency of PDMS. However, the used microscope must provide an infrared cutoff filter to block the laser light.

7.3 Experimental Results with the Integrated Optical Trap System

The fabricated integrated trap devices are ready for experiments on optical trapping and deflection of particles in the microfluidic channel. To assess these experiments, knowledge of the VCSEL performance after chip integration is essential. Furthermore, the investigation of their electrical and optical properties is necessary to reveal possible problems and drawbacks of the realized concept.

7.3.1 Electrical and Optical Characteristics

To measure the optical power emitted by the integrated VCSEL arrays, an integrating sphere is placed directly above the PDMS chip, such that most of the divergent light is collected. However, various reflections at the different material interfaces as well as scattering inside the PDMS layer have to be considered. Therefore, the determined values are not exact, but can be used to evaluate the power level in the microfluidic channel.

Figure 7.23 shows two exemplary light–current curves of two integrated VCSEL arrays. Both contain six lasers working in parallel with active diameters of 6.5 µm and 3.4 µm wide surface reliefs. A very low optical power level of less than 2 mW can be observed, leading to a mean optical power of only 0.25 to 0.3 mW per device, which could not be explained by measurement errors. The comparison to the LIV curve of a nominally identical VCSEL array prior to wafer cleaving and integration, shown in Fig. 7.24, reveals a power reduction

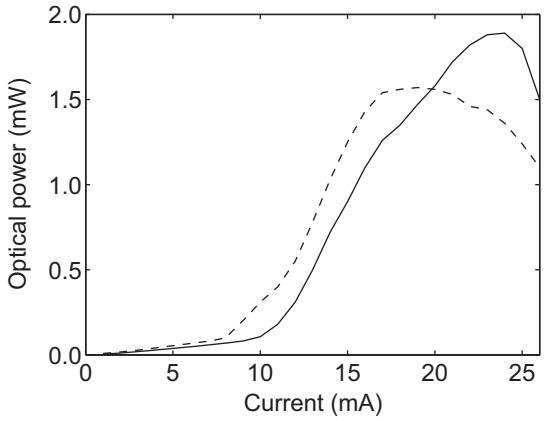

Fig. 7.23: LI curves of two exemplary integrated VCSEL arrays with six lasers working in parallel with active diameters of 6.5 µm and 3.4 µm wide surface reliefs.

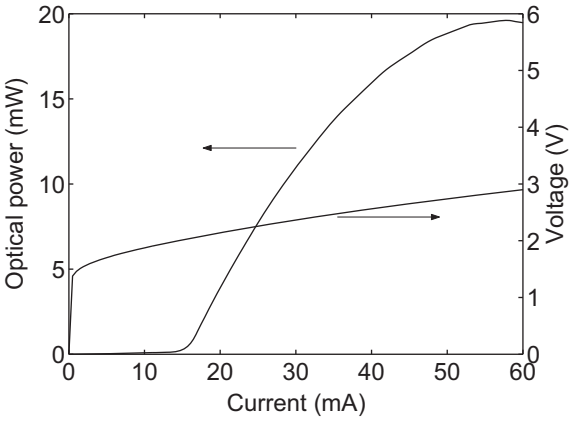

Fig. 7.24: LIV curve of a VCSEL array nominally identical to the ones shown in Fig. 7.23 prior to wafer cleaving and integration.

by a factor of ten. Thermal rollover occurs at a much lower current of 20 to 25 mA instead of 60 mA. Furthermore, light emission of the VCSEL arrays was found to be unstable. After increasing the laser current, the optical power decreases continuously after a first strong increase. When decreasing the laser current from a higher level, a slow increase of the optical power after the first decrease is observed. Moreover, some of the fabricated modules showed only spontaneous emission. Theses observations clearly indicate strong heating of the integrated devices, which does not occur for on-wafer measurements. Various factors lead to a reduction of heat dissipation in the integrated structure. First, the size of the semiconductor substrate is strongly reduced to only $1.2 \times 1.2\,\mathrm{mm}^2$, with no back side connection to a broad-area heat sink. Second, the close proximity of the VCSEL facet to the microfluidic chip impedes laser cooling by convection. This effect is further enhanced by the glue which was used to stabilize the connection of the semiconductor chip to the microfluidic chip. The worst laser performance is indeed observed if the glue completely encloses the layer of air above the VCSELs. In some modules, the strong heating of the semiconductor chip even affected the fluid in the microfluidic channel. Shortly after the lasers were turned on, air bubbles appeared at the channel edges, which expanded fast along the whole channel cross-section.

To decrease heating of the semiconductor chip and to lessen the resulting negative effects, the chip was rinsed with nitrogen gas during laser operation. Figure 7.25 shows the obtained LIV characteristics for an array containing five VCSELs working in parallel with active diameters of 6.5 µm and 3.4 µm wide surface reliefs. Here, a total optical output power of 8 mW is achieved, thus each VCSEL emits a mean power of 1.6 mW. Furthermore, the emitted power level was found to be stable with no significant power increase or decrease over time. Although cooling of the laser chip improved the device performance considerably, the power level is still much lower than for on-waver measurements. Before chip cleaving and integration, the same VCSEL array showed a mean maximum output power of about 3.4 mW per laser at a driving current of 50 mA, so heating of the laser chip is still significant. Comparison of the voltage drop shows a similar behavior before and after integration, with a

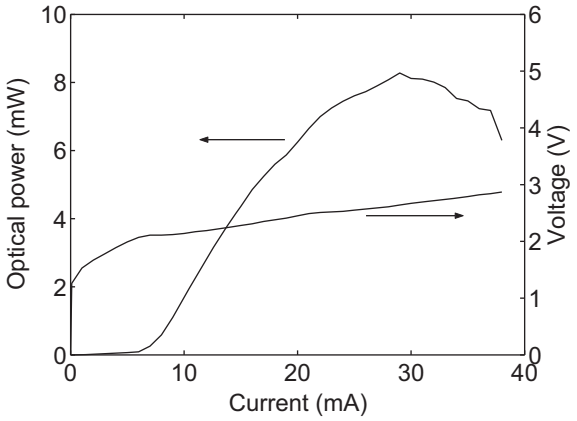

Fig. 7.25: LIV characteristics for an integrated array containing five VCSELs working in parallel with active diameters of 6.5 µm and 3.4 µm wide surface reliefs. The chip was rinsed with nitrogen during laser operation.

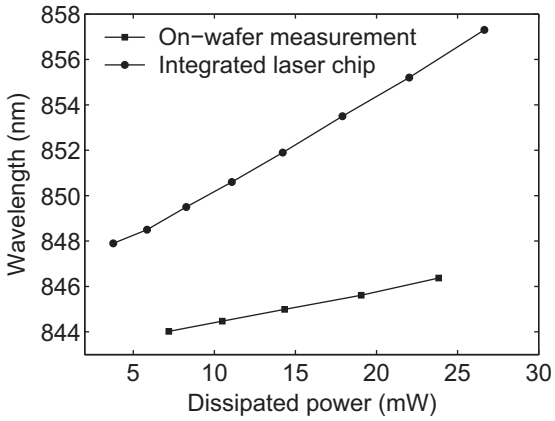

Fig. 7.26: Emission wavelength versus the dissipated power for two nominally identical VCSELs, one measured on-wafer with heat sink, the other integrated after chip cleaving and flip-chip bonding.

differential resistance of about 25 Ω. However, a higher threshold voltage of 1.9 V compared to 1.7 V is observed for the integrated module, which was found to be independent on chip cooling.

A measure for the heating of the laser module is given by its thermal resistance. It is defined as [52]

$$R_{\mathrm{TH}} = \frac{\Delta T}{P_{\mathrm{dis}}}, \tag{7.7}$$

where ΔT is the increase of the internal laser temperature in regard to room temperature and P_{dis} is the dissipated power, which can be easily determined by the difference between electrical input power and emitted optical power. The increase in temperature can be derived from the redshift of the optical laser spectrum. As discussed in Chap. 3, this shift is typically in the range of 0.07 nm/K. Figure 7.26 shows the measured emission wavelength versus the dissipated power for two similar lasers with 6.5 µm oxide aperture and 3.4 µm relief diameter. The square symbols refer to an on-wafer measurement on a copper heat sink, while the circular symbols are related to an integrated laser module after chip cleaving and flip-chip bonding. Obviously the wavelength shift, and thus the increase in temperature, is much stronger for the integrated device, namely 0.42 nm/mW compared to 0.14 nm/mW. Assuming the same temperature red-shift of 0.07 nm/K for both lasers, the integrated laser shows a three times higher thermal resistance and an about 100 °C higher internal temperature at 25 mW dissipated power.

The strong heating of the VCSEL chip is a serious problem, since it does not only worsen the laser performance significantly, but the large generation of heat in close proximity to the microfluidic chip could affect or endanger biological species in later applications. Therefore, modifications of the setup of the integrated trap are necessary to achieve better heat dissipation. Despite the poor optical output power of the VCSEL arrays, the integrated trap modules fabricated so far can be used to investigate the interaction of the generated optical lattice with particles in the microfluidic channel.

7.3.2 Experimental Results on Particle Manipulation

First experiments on particle manipulation are performed using 10 µm polystyrene particles and an integrated trap module with a 100 µm wide microfluidic channel. A slow, pressure driven fluid flow inside the channel is controlled by the fluid level in the reservoirs. The left hand side of Fig. 7.27 shows an optical microscope image of the used VCSEL array structure. Five VCSELs with an active diameter of 8.5 µm and a 4 µm wide surface relief are connected in parallel. The lasers are arranged linearly with a tilt angle of 20° to the microfluidic channel. However, the upper right laser is damaged and only the four lasers marked in the image are working. Furthermore, due to fabrication errors, the glue used to stabilize the connection between semiconductor chip and microfluidic chip presumably covers part of the VCSEL devices. Thus, the focusing effect of the integrated microlens is reduced. The mean output power of each device is about 1.25 mW (with N_2 cooling). Most likely the VCSEL in the lower left corner is driven above thermal rollover, thus its output power is below the mean value.

In spite of these poor preconditions an optical lattice is generated in the microfluidic channel. This is verified by the experiment presented in the right hand side of Fig. 7.27. Shown is a top view on the integrated trap module, with the laser emission being blocked by an infrared cutoff filter. For clarification, the outlines of the microfluidic channel are highlighted, as well as the 10 µm polystyrene particles in the solution. Underneath the channel, a blurred image of the integrated VCSEL array is visible. Each emitting laser creates an optical trap, so particles are immobilized above the VCSELs. Owing to the transverse gradient force they are drawn toward the beam center and withstand the fluidic drag force caused by the fluid flow with 3 µm/s velocity. Furthermore, the traps show a relatively large working distance, so up to three particles can be fixed and stacked by one laser beam. If a fourth sphere is attracted by the optical trap, one of the trapped particles is replaced, since the 35 µm high channel limits the stack height.

Next, the generated optical lattice is used for first experiments on continuous particle deflection. Figure 7.28 shows snapshots of an experiment with 10 µm particles and a flow velocity of 13 µm/s. To highlight the particle movement, a tracking line is inserted, which reveals that the particle flow path is slightly altered by the presence of the tilted optical

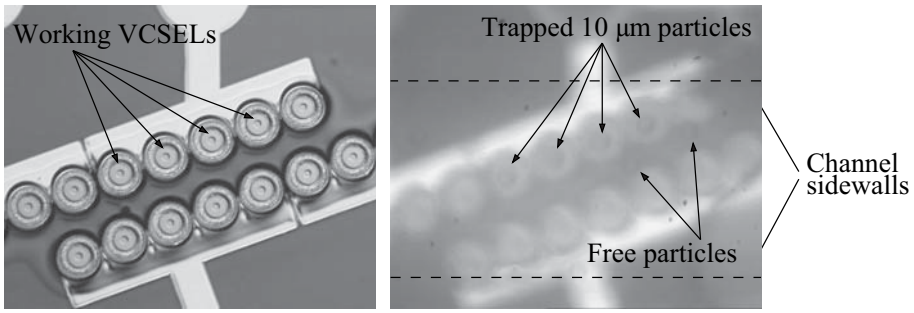

Fig. 7.27: Left: optical microscope image of an array of five VCSELs connected in parallel with a tilt angle of 20°. Right: top view on the integrated trap module using the same VCSEL array. In the experiment, 10 µm particles are trapped simultaneously with the laser beams.

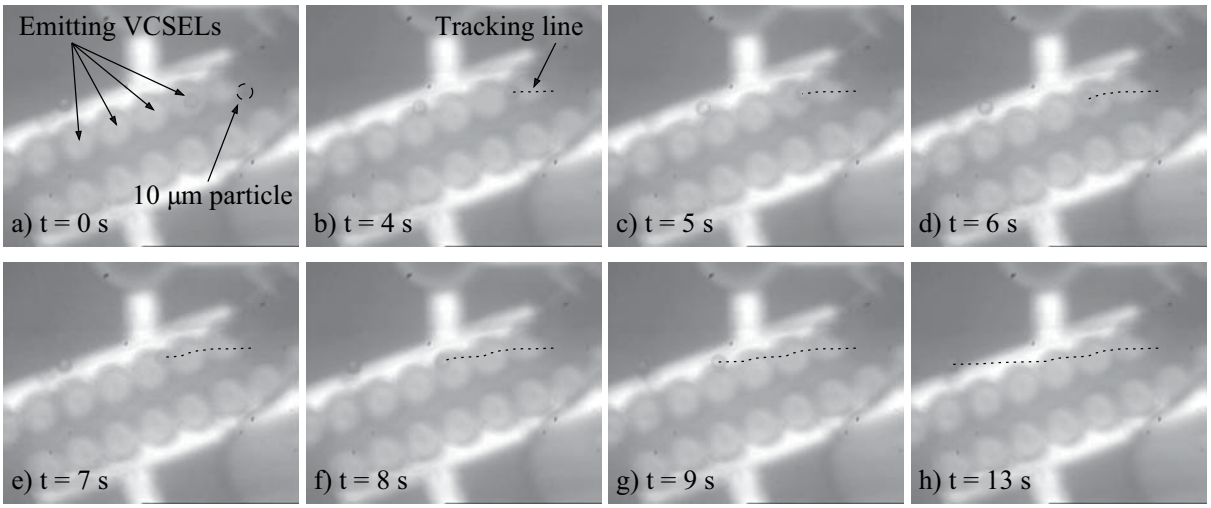

Fig. 7.28: Snapshots of a continuous deflection experiment on a 10 µm large particle with a total optical power of 5 mW. The added tracking line shows that the flow path of the particle is only slightly altered.

lattice. However, the interaction is very weak and the particle loses its link to the trap array quickly. Optimization of the deflection behavior was not successful. If the particle velocity is lowered, the particle is totally trapped by one laser beam. For faster fluid flow, the particle is no longer influenced by the optical lattice. Such a characteristic was already predicted by the simulations presented in Sect. 7.1.2.

According to the simulations, the velocity range for successful deflection is wider for larger particles, since the relative distance between the individual optical traps is reduced. Therefore, the experiment is repeated using larger particles of 15 µm diameter. Figure 7.29 shows corresponding sequences for a particle velocity of about 10 µm/s. Here, deflection of the

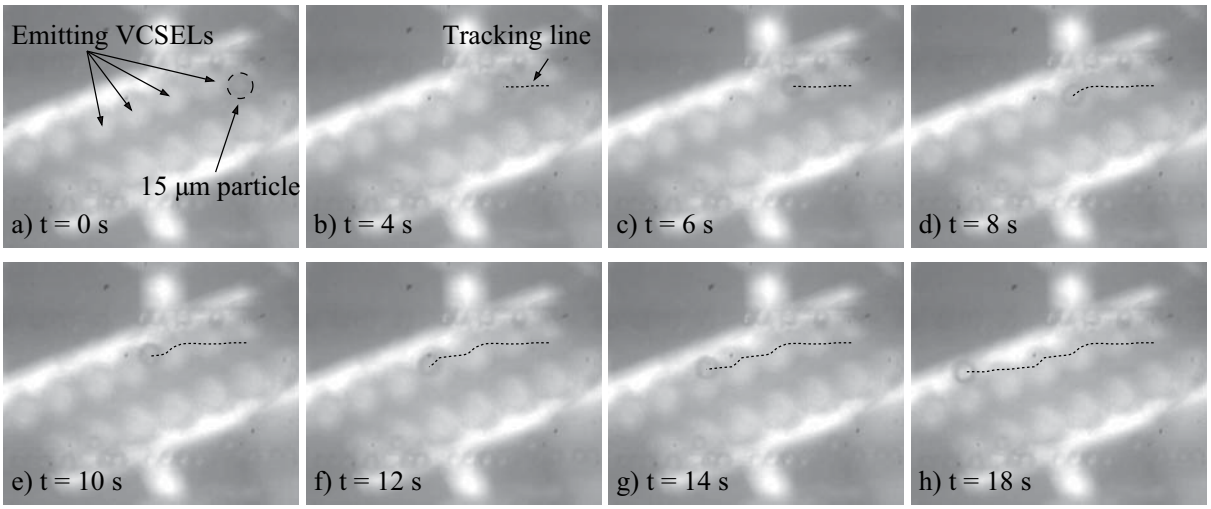

Fig. 7.29: Snapshots of a continuous deflection experiment with a total optical power of 5 mW. The inserted tracking line shows that the 15 µm polystyrene particle is deflected in a staircase-like manner by a total distance of about 20 µm.

particle is clearly visible, which shows the typical staircase-like characteristic known from the simulations. After 18 s the sphere is moved orthogonally to its initial flow direction by a total distance of about 20 µm. Further deflection at the lower left VCSEL of the array was not achieved, owing to the lower output power of this device.

The particle velocity at which continuous particle deflection was achieved is much smaller than expected. This is mainly attributed to the limited optical output power of the lasers, which is about five times lower than expected. Furthermore, the actual shape of the output beams during the experiment is unknown and the resulting effect on the trapping performance cannot be evaluated. To improve the deflection performance, modifications on the integrated trap setup are necessary. Central points are the avoidance of the epoxy glue to enable air exchange above the VCSEL facet and to eliminate any disturbance of the beam shape as well as a heat sink on the back side of the laser chip. The latter, however, can hardly be combined with the flip-chip bonding technique, since size and weight of the laser chip would increase strongly.

An attractive alternative approach is to abandon any direct contact between microfluidic chip and VCSEL chip. Instead, the PDMS chip is plugged on a larger module containing the VCSEL structure, and can thus be disposable. Challenging is however the small distance between laser facet and particle solution required for effective particle manipulation. Furthermore, the VCSEL p-side can no longer be connected via the glass side of the microfluidic chip. Possible alternatives are the use of via holes through the semiconductor substrate or bottom-emitting VCSEL structures.

Despite the restrictions named above, continuous particle deflection was successfully demonstrated. The predicted stair-like characteristic as well as the expected dependence on particle size was observed. Thus, the desired working principle of continuous particle deflection is confirmed. The first experiments with integrated trap prototypes prove the feasibility of a small-sized and portable module for particle manipulation based on densely packed linear VCSEL arrangements. By optimizing the still experimental structure of the trap modules, a significant increase in particle throughput is possible. With the presented results on particle deflection in mind, this future work is very promising.

8 Conclusion

This thesis gives a detailed study on optical manipulation systems based on vertically emitting laser diodes. It includes a discussion of the physical background of this special kind of light–matter interaction, where a simplified ray optical model of the trapping process was presented. It allows a rough estimation of the expected trapping forces and identifies the various parameters which influence the trapping performance, like particle size and refractive index. To examine the suitability of VCSELs as laser source in experiment, a classical optical tweezers system was constructed and set up, whose key component is a high NA objective. The resulting strong intensity gradient is necessary for three-dimensional manipulation of particles. First, solitary VCSELs were used as laser source, where standard multi-mode as well as surface relief VCSELs were fabricated. For the latter, single fundamental mode emission is achieved by a circular, shallow etch at the center of the output facet, where high single-mode output powers of up to 6.3 mW were achieved. With both kinds of VCSELs, optical trapping of polystyrene particles of sizes ranging from 4 to 15 µm was possible with some milliwatts of optical power at the sample stage. Using the escape force method, the acting trapping force could be determined. Maximum trapping forces of 4.4 pN for 15 µm and 3.3 pN for 6 µm particles were reached using the multi-mode laser. Thus, its donut-shaped beam profile is not necessarily a drawback. Since the use of a single-mode VCSELs is not required, higher optical powers and trapping forces are feasible.

The system was extended to a multiple optical tweezers setup by substituting the solitary lasers with two-dimensional VCSEL arrays. Standard VCSEL arrays with a device pitch of 250 µm were successfully used for simultaneous particle trapping. To enable interaction between the individual traps, the optical setup was modified to decrease the trap distance at the sample stage from 45 to 6 µm, so non-mechanical particle translation was realized. However, the necessary microlens array, which reduces the beam divergence of each VCSEL, leads to additional optical losses and increases the complexity of the setup. Using densely packed VCSEL arrangements, multiple optical tweezers are easily created in a straightforward manner, since the use of additional optics can be avoided. A novel, self-aligned fabrication process was developed to realize a device spacing of less than 25 µm as well as a seamless integration of the inverted surface relief technique for enhanced beam quality. By inserting such an array of individually addressable VCSELs into the tweezers setup, non-mechanical particle translation with velocities of up to 12 µm/s was achieved. With a tilted linear VCSEL array, an optical lattice was generated in the optical tweezers setup, and continuous deflection of 6 and 10 µm diameter particles was realized.

An essential part of the thesis is the application of optical particle manipulation in microfluidics. The physical properties of microfluidic flow and its use for cell handling and sorting was discussed. Microfluidic channels with widths of 30 to 150 µm were fabricated

from PDMS using soft lithography. The fluid flow inside the channels was controlled by hydrostatic pressure using integrated fluid reservoirs. By substituting the sample stage in the optical tweezers setup with a microfluidic chip, particle redirection at a channel junction was realized using a solitary VCSEL source as well as a tilted linear VCSEL array. For the latter, the particles are deflected when passing the optical lattice, thus, the position of the lasers is fixed and no moving parts are necessary.

To achieve a drastic miniaturization of the trapping setup, the laser source is placed directly underneath the sample chamber. A weakly focused laser beam is generated in the particle solution by integrating an additional microlens on the VCSEL output facet. To determine appropriate lens geometries, the beam propagation inside this integrated trap structure was calculated, aiming for a small focal point as well as a large working distance. To obtain the necessary radii of curvature of about 20 µm, the thermal reflow process for lens fabrication was studied in detail concerning lens diameter, reflow temperature and substrate material. By combining the microlens with the inverted relief technique, the quality of the focused beam was strongly improved with respect to divergence, transverse beam profile and beam diameter, where a minimum of 7 µm was measured at the focal point. With lensed relief devices of 8 µm active diameter, deflection, levitation and transverse trapping of 10 µm polystyrene particles was demonstrated for optical powers of 5 mW. An earlier observed offset between laser center and particle could be almost eliminated owing to the Gaussian-shaped beam profile.

In a next step, closely spaced arrays of lensed relief devices were fabricated. The focus was on linear arrays of parallel working VCSELs to transfer the continuous deflection scheme realized in the classical tweezers setup to the integrated trap. The deflection process was simulated to support the layout of the structure. The results show that higher particle velocities can be expected. Furthermore, a dependence on the geometric and material properties of the particles was predicted, so applications in microfluidic particle sorting are intended. To obtain compact and portable modules, a process was developed to integrate the laser chip with the microfluidic chip using flip-chip bonding. The indium solder bumps serve as mechanical as well as electrical connection, since a metal fan-out is structured on the glass side of the microfluidic chip. However, the finished modules showed strong heating of the VCSEL chip resulting in a significant reduction of the device performance. Nevertheless, simultaneous trapping of 10 µm particles as well as continuous particle deflection of 15 µm particles was successfully demonstrated with a total optical power of just 5 mW.

The results presented in this work demonstrate the potential of VCSELs as laser sources for optical trapping and microparticle manipulation. By introducing individually addressable or parallel working VCSEL arrays into a conventional tweezers setup, low cost multiple tweezers systems can be realized in a straightforward manner. In such systems compact non-mechanical particle movement, interaction, or multiparticle fixation is achieved. Furthermore, novel ultra-compact modules suited for microparticle analysis were fabricated. First results confirm the feasibility of the system. Therefore, portable and inexpensive microfluidic devices for particle manipulation in biological cell studies are within reach.

A Measurement Setups

Light–Current–Voltage (LIV) Measurements

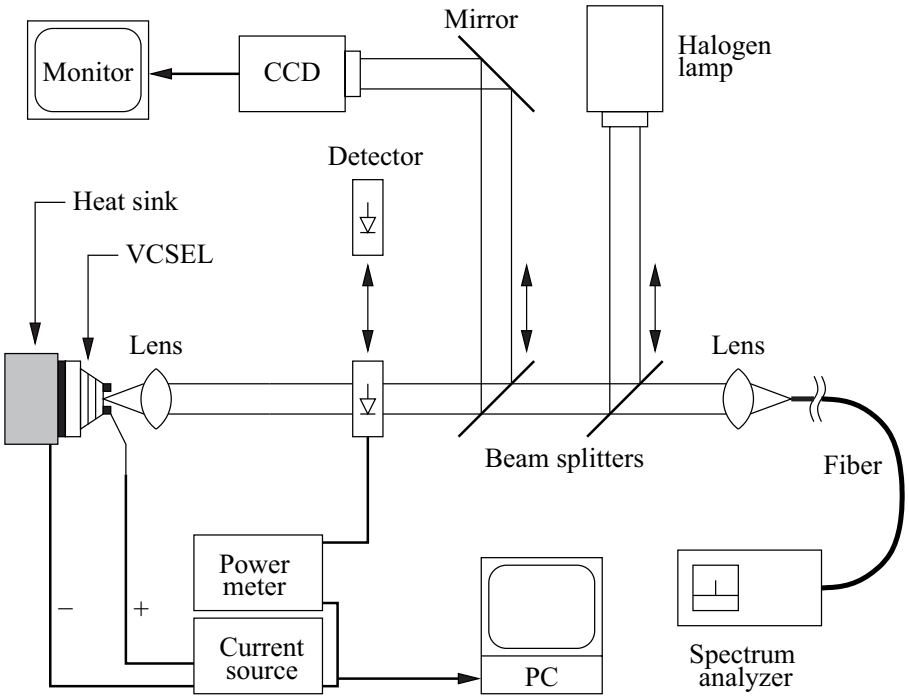

Fig. A.1: Schematic of the setup used for measurements of the LIV curve and the optical spectrum of VCSELs.

To determine output power and voltage drop of the laser diodes in dependence on the current, the experimental setup shown in Fig. A.1 was used. The sample is mounted on a vacuum chuck made of copper. Because the fabricated samples have a back side n-contact, the copper holder is also used for electrical contact. On the p-side the VCSEL is contacted by a needle on the bond pad. For current supply a DC source with a maximal output current of 100 mA is used. The emitted light is collimated by a lens and directed to a silicon photodiode, incurring a power loss of about 3 %. The current source and the power meter of the detector are addressed by GPIB (General Purpose Interface Bus), so current and voltage and output power can be set and read by a PC, respectively. The halogen lamp, the beam splitters and the CCD camera are used to get an enlarged image of the sample on a monitor, so the contacted VCSEL can be identified. The beam splitters as well as the detector are placed on rails to enable a spectral analysis. Therefore, the emitted light is focused by a lens and injected into a 50 µm core diameter graded-index multi-mode fiber

by adjusting both lenses. The fiber is connected to a spectrum analyzer (ANDO Electric Corp., model: AQ 6317) with a spectral resolution of 0.05 nm.

Near-field Measurements

The spectrally resolved transverse intensity profiles of the VCSELs were measured by scanning the close proximity of the laser output facet with a lensed single-mode fiber (see Fig. A.2). The ball lens at the fiber tip has a radius of curvature of 6 µm, yielding a focal length of about 12 µm and a spot width in the range of 1.0 to 1.5 µm. The lens is coated with an antireflection layer to prevent optical feedback. A wavelength meter (Agilent Technologies Inc., model: 86120 B, 0.08 nm resolution) connected to the optical fiber determines intensity peaks in the spectra of the coupled light and thus the power levels of the various transverse modes. The fiber is mounted on a 3-D, computer-controlled piezo-positioning system with a resolution of 40 nm, so the spectrally resolved power can be measured at various transverse and longitudinal positions. To examine the VCSEL beam divergence, the distance between fiber and laser is increased after completion of a transverse scan, and the next scan is started. While the longitudinal distance between successive transverse scans is very accurate, the initial distance to the laser surface is not exactly known. It has to be estimated with a stereo microscope, where an accuracy in the range of ±5 µm must be taken into account.

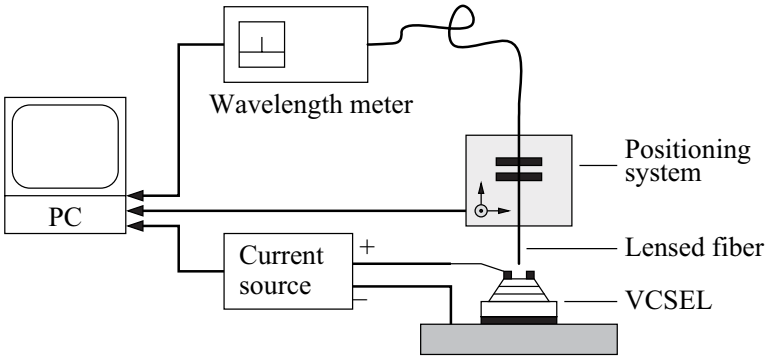

Fig. A.2: Schematic of the near-field measurement setup.

Far-field Measurements

Figure A.3 shows the setup used to measure the far-field intensity distribution. The sample is attached to a copper mount by vacuum and contacted using a probe needle and back side contact. An imaging system consisting of a halogen lamp for illumination and a CCD camera is used for sample alignment. A silicon photodiode is attached to a manually rotatable metal arm, thus it has a constant distance of about 20 cm to the VCSEL. To increase the measurement resolution, the effective area of the photodiode is decreased with a slit aperture. To determine the actual position angle of the photodiode, a potentiometer

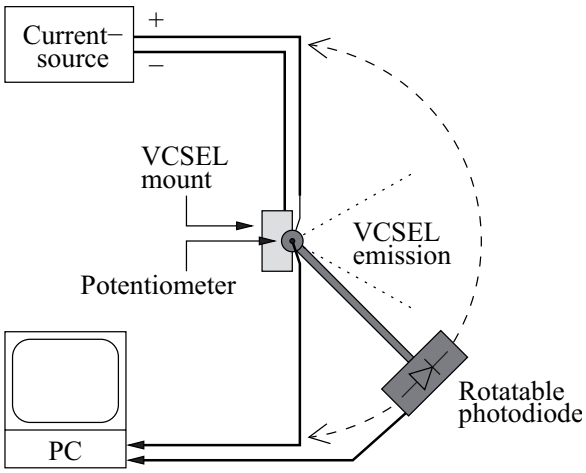

Fig. A.3: Schematic of the far-field measurement setup.

is connected to the axis of the metal arm. Eventually, an A/D-card is used to transfer the signal of photodiode and potentiometer to the computer.

M^2-Measurements

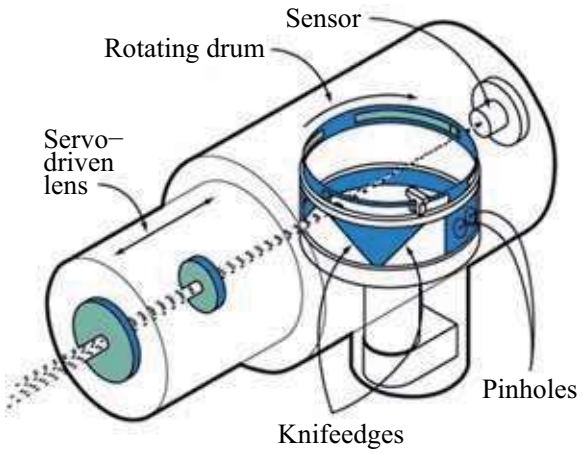

Fig. A.4: Schematic of the so-called ModeMaster used for M^2 measurements (from Coherent ModeMaster data sheet).

To measure the M^2 beam quality factor of the VCSELs, the so-called ModeMaster from Coherent is used (see Fig. A.4). Inside the ModeMaster, a lens focuses the collimated input beam to create an internal beam waist. Two orthogonal knifeedges mounted on a rotating drum together with an optical sensor are used to measure the beam diameter. As the lens is translated along the beam propagation axis, the longitudinal beam shape can be recorded. The ModeMaster software then derives the M^2 factor.

B Mask Layouts

To give an overview on the fabricated densely packed VCSEL arrangements, Fig. B.1 shows the layer for bond pad metalization of the designed lithographic mask. The mask includes large VCSELs of 24 µm mesa diameter and small VCSELs with 22 µm mesa diameter, with target oxide apertures of 8 and 6 µm respectively. Besides individually addressable standard VCSEL arrays, the mask contains mainly VCSELs with inverted surface relief driven in parallel. Here, different tilt angles of the linear arrays are realized.

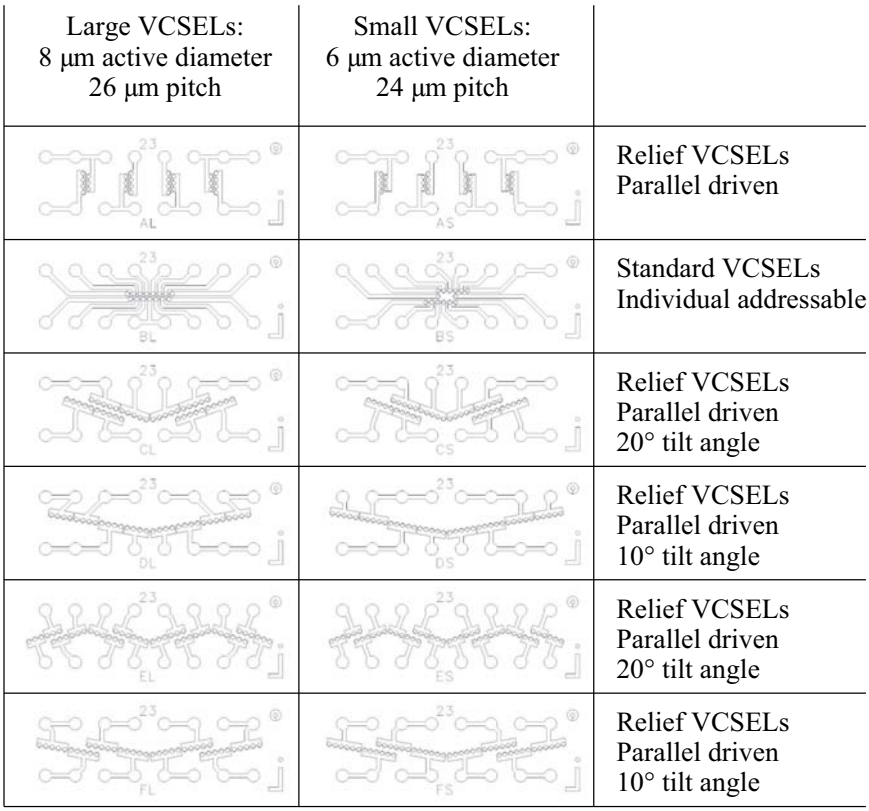

Fig. B.1: Layer for bond pad metalization of the designed lithographic mask for densely packed VCSEL arrays.

C Processing Protocols

VCSEL Arrays: Self-aligned Fabrication Process

In the following, the detailed processing steps for fabrication of densely packed VCSEL arrays with inverted surface relief and integrated microlenses are presented. The process is based on the mask design given in App. B. Each lithographic step is preceded by sample cleaning in acetone and isopropanol and drying on a hot-plate at 120 °C. Unless otherwise noted, a mask aligner (MJB3) with an emission wavelength of 320 nm is used for the exposure steps.

Mesa definition (PMGI process)

· Spin coating:	PMGI SF11, 3000 rpm, 40 s
· Prebake:	hot-plate, 220 °C, 5 min
· Spin coating:	AZ 1512 HS, 6000 rpm, 40 s
· Prebake:	hot-plate, 90 °C, 10 min
· Exposure:	12 mW/cm^2, 12 s, mask: integrated trap 2 / mesa pos
· Developing	AZ 400K : H_2O = 1:4, 19 s
· Flood exposure:	DUV (270–290 nm), 30 min
· Flood exposure:	12 mW/cm^2, 25 s
· Developing:	AZ 400K : H_2O = 1:4, 20–25 s

Surface relief etching

· Spin coating:	TI 35 ES, 9000 rpm, 40 s
· Prebake:	hot-plate, 90 °C, 3 min
· Exposure:	12 mW/cm^2, 0.7 min, mask: integrated trap 2 / contact cov
· Delay:	10 min
· Reverse bake:	hot-plate, 125 °C, 2 min
· Flood exposure:	12 mW/cm^2, 3 min
· Developing:	AZ 400K : H_2O = 1:4, 20 s
· O_2-plasma:	2 min, 10% O_2, 100 W RF
· HCl-dip:	HCl : H_2O = 1:1, 15 s
· Etching:	preparation: citric acid : H_2O = 1:1, then add H_2O_2 1:30 etch rate ≈ 1.3 nm/s ⇒ time: 46 s
· Resist removal:	acetone (cold, 5 min), isopropanol (cold)

P-ring contact

· Spin coating:	TI 35 ES, 6000 rpm, 40 s
· Prebake:	hot-plate, 90 °C, 3 min

· Exposure: 12 mW/cm^2, 0.75 min, mask: integrated trap2 / relief cov
· Delay: 10 min
· Reverse bake: hot-plate, 125 °C, 2 min
· Flood exposure: 12 mW/cm^2, 3 min
· Developing: AZ 400K : H_2O = 1:4, 15–20 s
· O_2-plasma: 2 min, 10% O_2, 100 W RF
· HCl-dip: HCl : H_2O = 1:1, 30 s
· Evaporate: Ti(20 nm)–Pt(50 nm)–Au(150 nm)
· Lift-off: methylpyrrolidone (>100 °C)
· Cleaning: acetone, isopropanol

Facet etching for standard VCSELs
· Spin coating: AZ 1512 HS, 6000 rpm, 40 s
· Prebake: hot-plate, 90 °C, 10 min
· Exposure: 12 mW/cm^2, 14 s, mask: integrated trap / lens
· Developing: AZ 400K : H_2O = 1:4, 19 s
· O_2-plasma: 1 min, 10% O_2, 100 W RF
· HCl-dip: HCl : H_2O 1:1, 15 s
· Etching: preparation: citric acid : H_2O 1:1, then add H_2O_2 1:30
etchrate ≈ 1.3 nm/s ⇒ time: 46 s
· Resist removal: acetone, isopropanol

Passivation of the VCSEL facet
· Spin coating: TI 35 ES, 6000 rpm, 40 s
· Prebake: hot-plate, 90 °C, 3 min
· Exposure: 12 mW/cm^2, 0.5 min, mask: integrated trap2 / facet cov
· Delay: 10 min
· Reverse bake: hot-plate, 125 °C, 2 min
· Developing: AZ 726 MIF, 25–30 s
· Flood exposure: 12 mW/cm^2, 3 min
· Hard bake: hot-plate, 140 °C, 2 min

Mesa etching and oxidation
· Etching: RIE: 90 W, 20 °C, 10 sccm $SiCl_4$, 5 mT, 30 min
· O_2-plasma: 3 min, 20% O_2, 10% CF_4, 100 W RF
· Resist removal: methylpyrrolidone (100 °C)
· Cleaning: acetone, isopropanol
· HF-dip: 0.1% HF, 5 s
· Oxidation: furnace 380 °C, bubbler 96 °C, 0.5 l/min N_2, 14 min

N-contact
Front side process: VCSEL protection
· Spin coating: AZ 9260, 3000 rpm, 40 s
· Prebake: hot-plate, 120 °C, 4 min

Back side process: contact lines

- Spin coating: ma-N 440, 6000 rpm, 40 s
- Prebake: hot-plate, 90 °C, 5 min
- Exposure: 12 mW/cm^2, 0.75 min, mask: mask 3
- Developing: ma-D 332S, 70 s
- HCl-dip: HCl : H_2O = 1:1, 30 s
- Evaporate: Ge(17 nm)–Au(50 nm)–Ni(10 nm)–Au(50 nm)
- Lift-off: methylpyrrolidone (100 °C)
- Cleaning: acetone, isopropanol
- Annealing: ramp up to 400 °C, hold for 10 s, cool down

Passivation (1)

- Spin coating: polyimide 7505, 5000 rpm, 40 s
- Prebake: hot-plate, 100 °C, 3 min
- Exposure: 12 mW/cm^2, 15 s, mask: integrated trap 2 / polyimide
- Postbake: hot-plate, 100 °C, 1 min
- Developing: HTRD2, 90 s, stop with ssopropanol
- Flood exposure: 12 mW/cm^2, 3 min
- Hard bake: ramp up to 300 °C, hold for 1 h, cool down

Bond pads

- Spin coating: TI 35 ES, 4000 rpm, 40 s
- Prebake: hot-plate, 90 °C, 3 min
- Exposure: 12 mW/cm^2, 0.8 min, mask: integrated trap2 / bond pad
- Delay: 10 min
- Reverse bake: hot-plate, 125 °C, 2 min
- Flood exposure: 12 mW/cm^2 (MJB3), 2 min
- Developing: AZ 726 MIF, 30 s
- O_2-plasma: 1 min, 10% O_2, 100 W RF
- Evaporate: Ni(20 nm) Au(150 nm), rotating
- Lift-off: methylpyrrolidone (100 °C)
- Cleaning: acetone, isopropanol

Passivation (2)

- Spin coating: polyimide 7505, 9000 rpm, 40 s
- Prebake: hot-plate, 100 °C, 3 min
- Exposure: 12 mW/cm^2, 15 s, mask: integrated trap / passivation
- Postbake: hot-plate, 100 °C, 1 min
- Developing: HTRD2, 90 s, stop with isopropanol
- Flood exposure: 12 mW/cm^2, 3 min
- Hard bake: ramp up to 400 °C, hold for 10 s

Lenses

- Spin coating: PMGI SF15, 5000 rpm, 40 s

· Prebake:	hot-plate, 220 °C, 5 min
· Spin coating:	AZ 1512 HS, 6000 rpm, 40 s
· Prebake:	hot-plate, 90 °C, 10 min
· Exposure:	12 mW/cm^2, 10 s, mask: integrated trap / lens
· Developing:	AZ 400K : H_2O = 1:4, 19 s
· Flood exposure:	DUV, 90 min
· Flood exposure:	12 mW/cm^2, 25 s
· Developing:	AZ 400K : H_2O = 1:4, 30 s
· Reflow:	hot-plate, 250 °C, 20 min, cool down on hot-plate

Microfluidic Chip Fabrication by Soft Lithography

Soft lithography requires a master wafer, which can be used several times for channel molding. A comparatively cheap silicon wafer serves as substrate. When fabricating standard microfluidic chips, the channels are sealed with a common cover glass. In case of the integrated trap structure, this has to be substituted with a 30 µm thin glass slide.

Master wafer

· Cleaning:	acetone, isopropanol
· Drying:	hot-plate, 120 °C, 15 min
· Spin coating:	SU-8 50, 3000 rpm, 40 s
· Prebake:	hot-plate, 65 °C, 5 min, ramp up to 95 °C, leave for 21 min
· Exposure:	405 nm, 12 mW/cm^2, 7×5 s, 30 s delay between exposures
· Postbake:	hot-plate, 65 °C, 1 min, ramp up to 95 °C, leave for 5 min
· Developing:	mr-Dev 600, 4 min, stop with isopropanol

Channel molding

· PDMS mixing:	PDMS base : curing agent = 10:1, stir for 5 min
· Outgassing:	vacuum cap, 20 min
· Preparation:	put master wafer into pouring form, include stamp for reservoirs
· Pouring:	pour PDMS over the master wafer, avoid air bubbles
· Curing:	furnace, 65 °C, 1 h
· Delay:	≈ 12 h

Channel sealing

· Glass cleaning:	acetone, isopropanol, O_2-Plasma (10 min, 10 % O_2, 150 W RF)
· PDMS peeling:	peel PDMS from master wafer and cut it to size (scalpel)
· PDMS cleaning:	isopropanol (5 s)
· Activate surface:	O_2-plasma, 30 s, 10 % O_2, 60 W RF
· Sealing:	join microfluidic chip and glass surface immediately
· Bake-out:	furnace, 65 °C, 12 h

Integration of VCSEL Chip and Microfluidic Chip

To perform lithographic processes on the glass side of the microfluidic chip, the standard procedure must be slightly varied. First, the channel inlets must be sealed with a PDMS

plug to protect the channels. Second, a furnace instead of a hot-plate must be used for all heating processes. Furthermore, evaporation of the fan-out metalization must be substituted by sputtering.

Fan-out tracks on glass side

· Protect channels:	seal channel inlets
· Cleaning:	acetone, isopropanol
· Drying:	furnace, 100 °C, 10 min
· Spin coating:	ma-N 440, 6000 rpm, 40 s
· Prebake:	furnace, 100 °C, 10 min
· Exposure:	12 mW/cm^2, 0,75 min, mask: integrated trap / glass-contact
· Developing:	ma-D 332 S, 90 s
· Metalization:	sputter Ti(30 nm)–Ni(50 nm)–Au(160 nm)
· Lift-off:	acetone (50 °C)
· Cleaning:	acetone, isopropanol

Glass passivation

· Cleaning:	acetone, isopropanol
· Drying:	furnace, 100 °C, 15 min
· Spin coating:	polyimide 7505, 6000 rpm, 40 s
· Prebake:	furnace, 100 °C, 10 min
· Exposure:	12 mW/cm^2, 10 s, mask: matrix / p glass
· Postbake:	furnace, 100 °C, 6 min
· Developing:	HTR-D2, 80 s, stop with isopropanol
· Hard bake:	ramp up to 300 °C, hold for 1 h, cool down

Indium bumps on glass side

· Cleaning:	acetone, isopropanol
· Drying:	furnace, 110 °C, 10 min
· Spin coating:	AZ nLOF 2070, 2000 rpm, 40 s
· Prebake:	furnace, 110 °C, 10 min
· Exposure:	12 mW/cm^2, 10 s, mask: integrated trap/bumps
· Post Bake:	furnace, 110 °C, 7 min
· Developing:	AZ MIF 826, 110 s
· Evaporate:	In (6 µm)
· Lift-off:	acetone (50 °C)
· Cleaning:	acetone, isopropanol

Flip-chip bonding

· Adjust:	adjust VCSEL chip to fan-out using infrared microscope
· Bonding:	heat up until indium markers start to melt, keep bonding time short
· Cool down:	$\approx$ 10 min

D Calculation of Light Forces

The quantities Q_s and Q_g give the fraction of the momentum transfer per second from an incident light ray to a particle in forward and transverse direction, respectively, as already defined in (2.5) and (2.6) as

$$F_\mathrm{sr} = \frac{\bar{n}_\mathrm{m} P_\mathrm{r}}{c} Q_\mathrm{s}, \tag{D.1}$$

$$F_\mathrm{gr} = \frac{\bar{n}_\mathrm{m} P_\mathrm{r}}{c} Q_\mathrm{g}, \tag{D.2}$$

where P_r is the power of the ray and $\bar{n}_\mathrm{m}$ is the refractive index of the surrounding medium. To determine the scaling factors, Fig. D.1 has to be considered. The incident ray hits the particle surface under an angle θ_i and splits into the reflected ray of power $P_\mathrm{r}\mathcal{R}$ and an infinite number of emergent refracted rays of decreasing powers $P_\mathrm{r}\mathcal{T}^2, P_\mathrm{r}\mathcal{T}^2\mathcal{R}, P_\mathrm{r}\mathcal{T}^2\mathcal{R}^2, \ldots$ [22]. The quantities $\mathcal{R}$ and $\mathcal{T}$ are the Fresnel coefficients for reflection and transmission, respectively, at the interface under an angle θ_i [105], namely

$$\mathcal{R}_\parallel = \frac{\left(\bar{n}_\mathrm{p}\cos\theta_\mathrm{i} - \bar{n}_\mathrm{m}\cos\theta_\mathrm{t}\right)^2}{\left(\bar{n}_\mathrm{p}\cos\theta_\mathrm{i} + \bar{n}_\mathrm{m}\cos\theta_\mathrm{t}\right)^2} \quad \text{and} \quad \mathcal{R}_\perp = \frac{\left(\bar{n}_\mathrm{m}\cos\theta_\mathrm{i} - \bar{n}_\mathrm{p}\cos\theta_\mathrm{t}\right)^2}{\left(\bar{n}_\mathrm{m}\cos\theta_\mathrm{i} + \bar{n}_\mathrm{p}\cos\theta_\mathrm{t}\right)^2}, \tag{D.3}$$

$$\mathcal{T}_\parallel = \frac{4\bar{n}_\mathrm{m}\bar{n}_\mathrm{p}\cos\theta_\mathrm{i}\cos\theta_\mathrm{t}}{\left(\bar{n}_\mathrm{p}\cos\theta_\mathrm{i} + \bar{n}_\mathrm{m}\cos\theta_\mathrm{t}\right)^2} \quad \text{and} \quad \mathcal{T}_\perp = \frac{4\bar{n}_\mathrm{m}\bar{n}_\mathrm{p}\cos\theta_\mathrm{i}\cos\theta_\mathrm{t}}{\left(\bar{n}_\mathrm{m}\cos\theta_\mathrm{i} + \bar{n}_\mathrm{p}\cos\theta_\mathrm{t}\right)^2}, \tag{D.4}$$

where the subscripts $\parallel$ and $\perp$ refer to parallel and perpendicular polarization of the light in respect to the plane of incidence, respectively. Furthermore, $\bar{n}_\mathrm{p}$ denotes the refractive index of the particle and θ_t is the angle of refraction, given by Snell's law as $\sin\theta_\mathrm{t} = \sin\theta_\mathrm{i}\,\bar{n}_\mathrm{m}/\bar{n}_\mathrm{p}$, where $\bar{n}_\mathrm{m} < \bar{n}_\mathrm{p}$ is assumed. Owing to their symmetric structure, the Fresnel coefficients are identical for incidence from the outside to the inside of the sphere or vice versa.

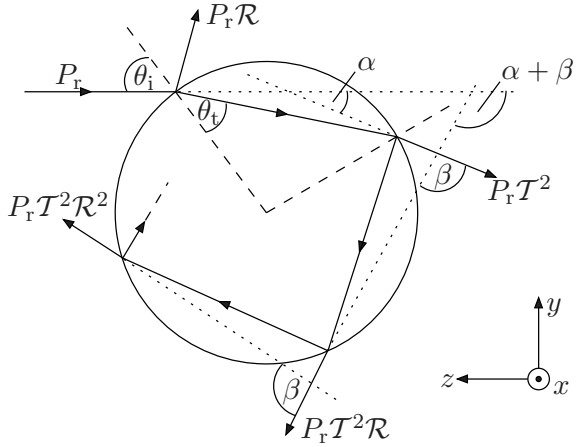

Fig. D.1: Momentum transfer of a single ray of power P_r to a spherical particle: The ray hits the sphere under an angle θ_i and splits into one reflected ray and an infinite number of refracted rays (adapted from [22]).

The transfer of momentum per second to the particle is equal to the difference between the incident momentum and the total momentum of all output rays per second. To consider the angle of propagation of the rays γ, the complex force F_{cr} is defined as [22]

$$F_{\mathrm{cr}} = F_{\mathrm{sr}} + iF_{\mathrm{gr}} = |F_{\mathrm{cr}}|e^{i\gamma}, \tag{D.5}$$

where i is the imaginary number. The exerted force therefore is

$$F_{\mathrm{cr}} = \frac{\bar{n}_{\mathrm{m}}}{c}\left[P_{\mathrm{r}} - P_{\mathrm{r}}\mathcal{R}e^{i\gamma_{\mathrm{R0}}} - P_{\mathrm{r}}\mathcal{T}^2e^{i\gamma_{\mathrm{T0}}} - P_{\mathrm{r}}\mathcal{T}^2\mathcal{R}e^{i\gamma_{\mathrm{T1}}} \ldots - P_{\mathrm{r}}\mathcal{T}^2\mathcal{R}^n e^{i\gamma_{\mathrm{T}n}}\right], \tag{D.6}$$

where γ_{R0} is the angle of the reflected ray and $\gamma_{\mathrm{T}n}$ is the angle of the n-th emergent refracted ray. By geometrical considerations, it is found that $\gamma_{\mathrm{R0}} = \pi - 2\theta_{\mathrm{i}}$ and $\gamma_{\mathrm{T}n} = -(\alpha + n\beta)$, with $\alpha = 2\theta_{\mathrm{i}} - 2\theta_{\mathrm{t}}$ and $\beta = \pi - 2\theta_{\mathrm{t}}$ (see Fig D.1). Equation (D.6) becomes

$$F_{\mathrm{cr}} = \frac{\bar{n}_{\mathrm{m}}P_{\mathrm{r}}}{c}\left[1 + \mathcal{R}e^{-i2\theta_{\mathrm{i}}} - \mathcal{T}^2e^{-i\alpha}\sum_{n=0}^{\infty}\mathcal{R}^n e^{-in\beta}\right], \tag{D.7}$$

and since the sum over n is a geometric series

$$F_{\mathrm{cr}} = \frac{\bar{n}_{\mathrm{m}}P_{\mathrm{r}}}{c}\left[1 + \mathcal{R}e^{-i2\theta_{\mathrm{i}}} - \frac{\mathcal{T}^2e^{-i\alpha}}{1 - \mathcal{R}e^{-i\beta}}\right]. \tag{D.8}$$

By division into real and imaginary part and taking (D.1) and (D.2) into account, the scaling factors Q_{s} and Q_{g} can be determined as [22]

$$Q_{\mathrm{s}} = 1 + \mathcal{R}\cos(2\theta_{\mathrm{i}}) - \frac{\mathcal{T}^2\left[\cos(2\theta_{\mathrm{i}} - 2\theta_{\mathrm{t}}) + \mathcal{R}\cos(2\theta_{\mathrm{i}})\right]}{1 + \mathcal{R}^2 + 2\mathcal{R}\cos(2\theta_{\mathrm{t}})}, \tag{D.9}$$

$$Q_{\mathrm{g}} = -\mathcal{R}\sin(2\theta_{\mathrm{i}}) + \frac{\mathcal{T}^2\left[\sin(2\theta_{\mathrm{i}} - 2\theta_{\mathrm{t}}) + \mathcal{R}\sin(2\theta_{\mathrm{i}})\right]}{1 + \mathcal{R}^2 + 2\mathcal{R}\cos(2\theta_{\mathrm{t}})}. \tag{D.10}$$

Each position on the side of the sphere facing the incident ray can be described by a cylindrical coordinate system with the components r and φ as shown in Fig. D.2a. Using $\sin(\theta_{\mathrm{i}}) = 2r/a$, where a is the diameter of the sphere, the Q-factors can be given in dependence on the position of the ray on the sphere as $Q_{\mathrm{s}}(r,\varphi)$ and $Q_{\mathrm{g}}(r,\varphi)$.

Caused by the polarization dependence of the Fresnel coefficients, the incident electric field $\boldsymbol{E}$ has to be separated into components parallel and orthogonal to the plane of incidence. Assuming polarization in x-direction, these components are $E_{\parallel} = |\boldsymbol{E}|\cos\varphi$ and $E_{\perp} = |\boldsymbol{E}|\sin\varphi$ (see Fig. D.2b). Since the Q-values are scaling factors for the incident power, this has to be considered by

$$Q_{\mathrm{s}} = Q_{\mathrm{s}\parallel}\cos^2\varphi + Q_{\mathrm{s}\perp}\sin^2\varphi, \tag{D.11}$$

$$Q_{\mathrm{g}} = Q_{\mathrm{g}\parallel}\cos^2\varphi + Q_{\mathrm{g}\perp}\sin^2\varphi, \tag{D.12}$$

where the subscripts $\parallel$ and $\perp$ imply the use of the corresponding Fresnel coefficients.

In the example in Sect. 2.1.2, the particle is illuminated by a parallel, transverse Gaussian beam, whose power density distribution is given by

$$S(\hat{r}) = \frac{2P}{\pi w_0}\,exp\left(\frac{-2\hat{r}^2}{w_0^2}\right), \tag{D.13}$$

where P is the total optical power of the beam and w_0 is the beam radius. Since $\hat{r}$ marks a coordinate system whose origin is located at the beam center, a transition to the particle coordinate system of r and φ is required. Geometrical considerations (see Fig. D.2c) lead to

$$\hat{r}^2 = s^2 + r^2 - 2sr\cos(\phi - \varphi), \tag{D.14}$$

where s and ϕ are length and angle of the offset between particle and beam center.

The scattering and gradient force per area on the particle can now be calculated by

$$F_{\mathrm{sa}}(r,\varphi) = \frac{\bar{n}_{\mathrm{m}}}{c}\, S(r,\varphi)\, Q_{\mathrm{s}}(r,\varphi), \tag{D.15}$$

$$F_{\mathrm{ga}}(r,\varphi) = \frac{\bar{n}_{\mathrm{m}}}{c}\, S(r,\varphi)\, Q_{\mathrm{g}}(r,\varphi). \tag{D.16}$$

To determine the total radiation force on the particle, the force per area has to be integrated over the projected area of the particle. In case of the gradient force, this has to be done separately for the components in x- and y-direction, where $F_{\mathrm{ga}\,x} = F_{\mathrm{ga}}\cos\varphi$ and $F_{\mathrm{ga}\,y} = F_{\mathrm{ga}}\sin\varphi$

$$F_{\mathrm{s}} = \int_0^{2\pi}\int_0^{a/2} F_{\mathrm{sa}}(r,\varphi)\, r\mathrm{d}r\,\mathrm{d}\varphi, \tag{D.17}$$

$$F_{\mathrm{g}\,x} = \int_0^{2\pi}\int_0^{a/2} F_{\mathrm{ga}\,x}(r,\varphi)\, r\mathrm{d}r\,\mathrm{d}\varphi, \tag{D.18}$$

$$F_{\mathrm{g}\,y} = \int_0^{2\pi}\int_0^{a/2} F_{\mathrm{ga}\,y}(r,\varphi)\, r\mathrm{d}r\,\mathrm{d}\varphi. \tag{D.19}$$

The total gradient force thus is

$$F_{\mathrm{g}} = \sqrt{(F_{\mathrm{g}\,x})^2 + (F_{\mathrm{g}\,y})^2}, \tag{D.20}$$

with the orientation

$$\varphi_{\mathrm{g}} = \arctan\frac{F_{\mathrm{g}\,y}}{F_{\mathrm{g}\,x}}. \tag{D.21}$$

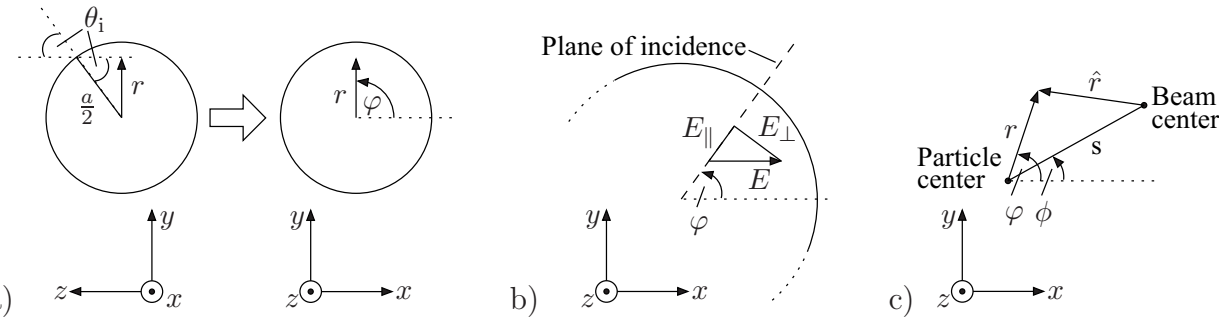

Fig. D.2: Sketches of the examined beam versus particle arrangement necessary for geometrical considerations: transfer of the angle of incidence to cylindrical coordinates (a), splitting of the ray into its polarization components (b), transfer of the coordinate system of the beam to the coordinate system of the particle (c).

E ABCD Matrix Method

In a ray optical model, an individual ray at a certain position z along the propagation axis can be described by a vector, which is composed of the ray's distance $r_1(z)$ and angle $\alpha_1(z)$ to the optical axis. Propagation of the ray through an optical system is calculated by

$$\begin{pmatrix} r_2 \\ \alpha_2 \end{pmatrix} = \begin{pmatrix} A & B \\ C & D \end{pmatrix} \begin{pmatrix} r_1 \\ \alpha_1 \end{pmatrix}, \tag{E.1}$$

where the resulting vector contains the distance and the angle to the optical axis of the ray after passing the optical system. The so-called ABCD transfer matrix describes the optical system. Table E.1 gives the matrices for free-space propagation, refraction at a dielectric interface and transition through a thin lens. More complicated optical systems can be described by combining individual optical elements by means of matrix multiplication, which must be carried out from right (first element) to left (last element).

In contrast to the ray optical model, a Gaussian output beam at the entrance is not described by distance and propagation angle, but by its beam radius $w(z)$ and the radius of curvature $R(z)$ of the wavefront, which are [98]

$$w^2(z) = w_0^2 \left(1 + \frac{z^2}{z_\mathrm{R}^2}\right) \quad \text{and} \quad R(z) = z \left(1 + \frac{z_\mathrm{R}^2}{z^2}\right), \tag{E.2}$$

with

$$z_\mathrm{R} = \frac{\pi w_0^2 \bar{n}}{\lambda M^2} \tag{E.3}$$

being the Rayleigh length, that is the position of maximum radius of curvature of the wavefront [97]. The quantity w_0 is the beam radius at the beam waist, λ is the wavelength of light and $\bar{n}$ is the refractive index of the surrounding medium. Inclusion of the beam quality factor M^2, as introduced in Sect. 5.2.3, enables the description of a real Gaussian beam.

Table E.1: Transfer matrices of basic optical elements.

Beam propagation	Dielectric interface	Thin lens
$\begin{pmatrix} 1 & z \\ 0 & 1 \end{pmatrix}$	$\begin{pmatrix} 1 & 0 \\ 0 & \bar{n}_1/\bar{n}_2 \end{pmatrix}$	$\begin{pmatrix} 1 & 0 \\ -1/f & 1 \end{pmatrix}$
z: propagation length	$\bar{n}_1$, $\bar{n}_2$: refractive indices	f: focal length (in air)

Beam radius and radius of curvature can be combined in the complex beam parameter $q(z)$ at the entrance of an optical system by

$$\frac{1}{q(z)} = \frac{1}{R(z)} - i\frac{\lambda M^2}{\pi w^2(z)}. \tag{E.4}$$

Thus, the propagation of a Gaussian beam is completely described by the complex beam parameter.

Transition of a Gaussian beam through an optical system can be calculated using the ABCD transfer matrix [98, 99]

$$q_2 = \frac{Aq_1 + B}{Cq_1 + D}, \tag{E.5}$$

where q_1 and q_2 are the complex beam parameters at the entrance and at the end of the optical system, respectively. By separation of q_2 into real and imaginary part, beam diameter and radius of curvature of the Gaussian beam leaving the optical system can be determined.

F Index of Mathematical Symbols and Abbreviations

Within this thesis, the following notations are used: The quantities x, y, and z are the spatial coordinates of the Cartesian coordinate system and $\boldsymbol{e}_x$, $\boldsymbol{e}_y$, and $\boldsymbol{e}_z$ are the corresponding unit vectors. All vectors are set in bold type, like $\boldsymbol{B}$, with B_x, B_y, and B_z being its spatial components. The notation $\dot{x}$ names the temporal derivative of x.

a	particle diameter
A	area, channel cross-section
A, B, C, D	elements of the ABCD transfer matrix in App. E
c	vacuum velocity of light
c_{faxen}	scaling factor to consider the proximity of a static surface
d_{active}	active diameter of a VCSEL
D	characteristic geometry
D_{f}	damping constant exerted by a fluid
D_{i}	diameter of the resist island before reflow
D_{l}	bottom diameter of the resist lens after reflow
$\boldsymbol{E}, E$	electric field
$E_{\parallel}$	parallel polarized component of the electric field
$E_{\perp}$	perpendicular polarized component of the electric field
E_{ph}	energy of a single photon
f	focal length of a lens
$f_{\mathrm{collimation}}$	focal length of the collimating objective
$f_{\mathrm{immersion}}$	focal length of the immersion objective
$\boldsymbol{F}, F$	radiation force
$F_{\mathrm{A}}, F_{\mathrm{B}}$	radiation force of ray A and B, respectively
F_{cr}	complex radiation force of a single ray
F_{drag}	fluidic drag force
$\boldsymbol{F}_{\mathrm{ex}}$	external force on a fluid
$\boldsymbol{F}_{\mathrm{g}}, F_{\mathrm{g}}$	gradient force
F_{ga}	gradient force per area
F_{gr}	gradient force from a single ray
F_{R}	friction force
$\boldsymbol{F}_{\mathrm{s}}, F_{\mathrm{s}}$	scattering force
F_{sa}	scattering force per area
F_{sr}	scattering force from a single ray

F_{trap}	trapping force, maximum gradient force
g	gravitational constant
$\hbar$	reduced Planck constant
H_{i}	height of the resist island before reflow
H_{l}	maximum height of the resist lens after reflow
$\mathcal{I}$	optical intensity
I	electrical current
I_{th}	threshold current
l	distance between particle center and static surface
L	pipe length
m	ratio of refractive indices of a particle and its surrounding medium
m_{p}	particle mass
M^2	beam quality factor
n	positive integer
$\bar{n}$	refractive index
$\bar{n}_{\mathrm{i}}$	refractive index of the immersion oil
$\bar{n}_{\mathrm{m}}$	refractive index of the medium surrounding a particle
$\bar{n}_{\mathrm{p}}$	refractive index of a particle
$\bar{n}_{\mathrm{PMGI}}$	refractive index of PMGI resist
N	number of photons
NA	numerical aperture
p	pressure
P	optical power of a laser beam
P_{dis}	dissipated power
P_{max}	maximum output power
P_{r}	optical power of a single ray
q	elementary charge (Chap. 3) or complex beam parameter (App. E)
q_1, q_2	complex beam parameter before and after passing an optical system
Q	overall scaling factor for the trapping force
Q_{g}	scaling factor for the gradient force from a single ray
$Q_{\mathrm{g}\parallel}$, $Q_{\mathrm{g}\perp}$	gradient force scaling factor from a single ray for parallel and perpendicular polarized light, respectively
Q_{s}	scaling factor for the scattering force from a single ray
$Q_{\mathrm{s}\parallel}$, $Q_{\mathrm{s}\perp}$	scattering force scaling factor from a single ray for parallel and perpendicular polarized light, respectively
Q_{V}	volume flow rate
$\mathcal{R}$	Fresnel coefficient for reflection
$\mathcal{R}_{\parallel}$	Fresnel coefficient for reflection for parallel polarized light
$\mathcal{R}_{\perp}$	Fresnel coefficient for reflection for perpendicular polarized light
$\hat{r}$	radial component for a coordinate system with its origin at the beam center
r_1, r_2	distance of an optical ray to the optical axis before and after passing an optical system

R	pipe radius (Chap. 4) or radius of curvature of a Gaussian beam (App. E)
R_c	radius of curvature of a lens
Re	Reynolds number
R_TH	thermal resistance
s	distance from beam center to particle center
S	power density distribution
t	time
$\mathcal{T}$	Fresnel coefficient for transmission
$\mathcal{T}_\parallel$	Fresnel coefficient for transmission for parallel polarized light
$\mathcal{T}_\perp$	Fresnel coefficient for transmission for perpendicular polarized light
$\boldsymbol{v}, v$	fluid velocity (Chap. 4) or particle velocity (Chap. 7)
v_{x0}, v_{y0}	initial particle velocity in x and y direction
$\boldsymbol{v}_\mathrm{f}, v_\mathrm{f}$	fluid velocity
v_max	maximum fluid velocity along the channel cross-section
v_stage	sample stage velocity in the optical tweezers setup
$v_\mathrm{stage,max}$	maximum stage velocity at which a particle remains trapped
V_i	volume of the resist island before reflow
V_l	volume of the resist lens after reflow
V_setup	magnification of the optical tweezers setup
V_F	trapping potential
w	radius of a Gaussian beam
w_0	beam radius at the beam waist of a real beam
$\bar{w}_0$	beam radius at the beam waist of an ideal beam
z_R	Rayleigh length
α	auxiliary angle for geometrical considerations (see Fig. D.1)
α_1, α_2	angle between propagation direction of a beam and the optical axis before and after passing an optical system
α_p	polarizability
β	auxiliary angle for geometrical considerations (see Fig. D.1)
Δh	height difference between channel inlet and outlet
Δp	difference in pressure between channel inlet and outlet
Δp_ph	change in momentum of a single photon
Δt	time period
ΔT	increase of the internal laser temperature in regard to room temperature
γ	angle of the complex radiation force
γ_R0	angle of the ray that is reflected at the particle surface
$\gamma_{\mathrm{T}n}$	angle of the n-th emergent ray that was refracted at the particle surface
η	dynamic viscosity
η_d	differential quantum efficiency
φ_g	orientation of the gradient force
ϕ	azimuthal component for a coordinate system with origin at the beam center

θ	propagation angle
θ_{FF}	far-field angle of a real beam
$\bar{\theta}_{\mathrm{FF}}$	far-field angle of an ideal beam
θ_{i}	angle of incidence
θ_{t}	angle of refraction
κ	trap stiffness
λ	wavelength
ρ	mass density
σ	standard deviation
τ	shear stress
ω	angular frequency
∇	nabla operator

AFM	atomic force microscope
APC	antigen-presenting cell
CAIBE	chemically-assisted ion beam etching
CW	continuous wave
DNA	deoxyribonucleic acid
DUV	deep ultra violet
E. coli	Escherichia coli
FACS	fluorescent-activated cell sorting
FWHD	full-width-at-half-maximum
GPC	generalized phase contrast
GPIB	general purpose interface bus
IV	current–voltage
LI	light–current
LIV	light–current–voltage
LP	linearly polarized
MBE	molecular beam epitaxy
PDMS	polydimethylsiloxane
PMGI	polymethylglutarimide
PMMA	polymethylmethacrylate
RIE	reactive-ion etching
RNA	ribonucleic acid
SEM	scanning electron microscope
SLM	spatial light modulator
SMSR	side-mode suppression ratio
VCSEL	vertical-cavity surface-emitting laser
µTAS	micro total analysis system

Publications

1. J.M. Ostermann, P. Debernardi, C. Jalics, A. Kroner, M.C. Riedl, and R. Michalzik, "Surface gratings for polarization control of single- and multi-mode oxide-confined vertical-cavity surface-emitting lasers", *Optics Communications*, vol. 246, pp. 511–519, 2005.

2. A. Kroner, I. Kardosh, F. Rinaldi, and R. Michalzik, "Towards ultra-compact optical tweezers without external optics", in Proc. *Conf. on Lasers and Electro-Optics Europe, CLEO/Europe 2005*, paper CL4-2-FRI. Munich, Germany, June 2005.

3. A. Kroner, I. Kardosh, F. Rinaldi, and R. Michalzik, "Towards VCSEL-based integrated optical traps for biomedical applications", *Electron. Lett.*, vol. 42, pp. 93–94, 2006.

4. A. Kroner, J.F. May, I. Kardosh, F. Rinaldi, H. Roscher, and R. Michalzik, "Novel concepts of vertical-cavity laser-based optical traps for biomedical applications", in *Biophotonics and New Therapy Frontiers*, R. Grzymala, O. Haeberlé (Eds.), Proc. SPIE 6191, pp. 619112-1–12, 2006.

5. F. Rinaldi, J.M. Ostermann, A. Kroner, M.C. Riedl, and R. Michalzik, "760 nm high-performance VCSEL growth and characterization", in *Micro-Optics, VCSELs, and Photonic Interconnects II: Fabrication, Packaging, and Integration*, H. Thienpont, M.R. Taghizadeh, P. Van Daele, J. Mohr (Eds.), Proc. SPIE 6185, pp. 61850X-1–7, 2006.

6. H. Roscher, P. Gerlach, F.N. Khan, A. Kroner, M. Stach, A. Weigl, and R. Michalzik, "Toward more efficient fabrication of high-density 2-D VCSEL arrays for spatial redundancy and/or multi-level signal communication", in *Micro-Optics, VCSELs, and Photonic Interconnects II: Fabrication, Packaging, and Integration*, H. Thienpont, M.R. Taghizadeh, P. Van Daele, J. Mohr (Eds.), Proc. SPIE 6185, pp. 61850V-1–12, 2006.

7. A. Kroner, A. Gadallah, I. Kardosh, F. Rinaldi, and R. Michalzik, "Integrated VCSEL trap arrays for microfluidic particle separation and sorting", in Proc. *EOS Topical Meeting on Biophotonics and Biomedical Optics*, pp. 140–141. Paris, France, Oct. 2006.

8. R. Michalzik, A. Kroner, J.M. Ostermann, M. Riedl, F. Rinaldi, H. Roscher, and M. Stach, "High-performance vertical-cavity laser diodes enabling new applications" (invited), in Proc. *Eighth International Conf. on Optoelectronics, Fiber Optics and Photonics, Photonics 2006*, vol. 2, p. 246. Hyderabad, India, Dec. 2006.

9. F. Rinaldi, J.M. Ostermann, A. Kroner, and R. Michalzik, "High-performance AlGaAs-based VCSELs emitting in the 760 nm wavelength range", *Optics Communications*, vol. 270, pp. 310–313, 2007.

10. A. Kroner, F. Rinaldi, J.M. Ostermann, and R. Michalzik, "High-performance single fundamental mode AlGaAs VCSELs with mode-selective mirror reflectivities", *Optics Communications*, vol. 270, pp. 310–313, 2007.

11. A. Kroner, F. Rinaldi, R. Rösch, and R. Michalzik, "Densely packed VCSEL arrays tailored for optical particle manipulation", in Proc. (CD ROM) *Conf. on Lasers and Electro-Optics Europe, CLEO/Europe 2007*, paper CB4-1-TUE. Munich, Germany, June 2007.

12. J.M. Ostermann, P. Debernardi, A. Kroner, and R. Michalzik, "Polarization-controlled surface grating VCSELs under externally induced anisotropic strain", *IEEE Photon. Technol. Lett.*, vol. 19, pp. 1301–1303, 2007.

13. S. Hövel, A. Bischoff, N.C. Gerhardt, M.R. Hofmann, T. Ackemann, A. Kroner, and R. Michalzik, "Optical spin manipulation of electrically pumped vertical-cavity surface-emitting lasers", *Appl. Phys. Lett.*, vol. 92, pp. 041118-1–3, 2008.

14. A. Kroner, F. Rinaldi, R. Rösch, I. Kardosh, and R. Michalzik, "Towards a compact particle manipulation system based on arrays of vertical-cavity laser diodes", in Proc. *Nonlinear Microscopy and Optical Control, NMOC 2008*, p. 47. Münster, Germany, Feb. 2008.

15. A. Kroner, F. Rinaldi, R. Rösch, and R. Michalzik, "Optical particle manipulation by application-specific densely packed VCSEL arrays", *Electron. Lett.*, vol. 44, pp. 353–354, 2008.

16. A. Kroner, C. Schneck, F. Rinaldi, R. Rösch, and R. Michalzik, "Application of vertical-cavity laser-based optical tweezers for particle manipulation in microfluidic channels", in *Nanophotonics II*, D.L. Andrews, J.-M. Nunzi, A. Ostendorf (Eds.), Proc. SPIE 6988, pp. 69881R-1-12, 2008.

17. A. Gadallah, A. Kroner, I. Kardosh, F. Rinaldi, and R. Michalzik, "Oblong-shaped VCSELs with pre-defined mode patterns", in *Semiconductor Lasers and Laser Dynamics III*, K.P. Panayotov, M. Sciamanna, A.A. Valle, R. Michalzik (Eds.), Proc. SPIE 6997, pp. 69971R-1–9, 2008.

18. A. Kroner, F. Rinaldi, R. Rösch, I. Kardosh, and R. Michalzik, "Ultra-miniaturized optical particle manipulation using densely integrated laser arrays", in *Digest 1st Int.'l Sympos. on Optical Tweezers in Life Sciences*, poster 26. Berlin, Germany, May 2008.

19. P. Debernardi, A. Kroner, F. Rinaldi, and R. Michalzik, "Hot-cavity model for non-circular VCSELs", in Proc. *21st IEEE Int.'l Semicond. Laser Conf.*, pp. 91–92. Sorrento, Italy, Sept. 2008.

20. N.C. Gerhardt, S. Hövel, M. Li, H. Jaehme, M.R. Hofmann, T. Ackemann, A. Kroner, and R. Michalzik, "Ultrafast spin dynamics in spin-polarized vertical-cavity surface-emitting laser devices", in Proc. *Conf. on Lasers and Electro-Optics, CLEO 2009*, paper CMRR6. Baltimore, MD, USA, May/June 2009.

21. P. Debernardi, A. Kroner, F. Rinaldi, and R. Michalzik, "Surface relief vs. standard VCSELs: a comparison between experimental and hot-cavity model results", *IEEE J. Select. Topics Quantum Electron.*, vol. 15, pp. 828–837, 2009.

22. R. Michalzik, A. Kroner, A. Bergmann, and F. Rinaldi, "VCSEL-based optical trapping for microparticle manipulation" (invited), in *Vertical-Cavity Surface-Emitting Lasers XIII*, K.D. Choquette, C. Lei (Eds.), Proc. SPIE 7229, pp. 722908-1–13, 2009.

Bibliography

[1] Y. Arai, R. Yasuda, K. Akashi, Y. Harada, H. Miyata, K. Kinosita, Jr., and H. Itoh, "Tying a molecular knot with optical tweezers", *Nature*, vol. 399, pp. 446–448, 1999.

[2] C. Xie, M.A. Dinno, and Y. Li, "Near-infrared Raman spectroscopy of single optically trapped biological cells", *Opt. Lett.*, vol. 27, pp. 249–251, 2002.

[3] K. Kitamura, M. Takunaga, A.H. Iwane, and T. Yanagida, "A single myosin head moves along an actin filament with regular steps of 5.3 nanometres", *Nature*, vol. 397, pp. 129–134, 1999.

[4] K. Dholakia, P. Reece, and M. Gu, "Optical micromanipulation", *Chem. Soc. Rev.*, vol. 37, pp. 42–55, 2008.

[5] N.-T. Nguyen, *Mikrofluidik*. Wiesbaden: Teubner Verlag, 2004.

[6] J. Cooper McDonald and G.M. Whitesides, "Poly(dimethylsiloxane) as a material for fabricating microfluidic devices", *Acc. Chem. Res.*, vol. 35, pp. 491–499, 2002.

[7] M.M. Wang, E. Tu, D.E. Raymond, J.M. Yang, H. Zhang, N. Hagen, B. Dees, E.M. Mercer, A.H. Forster, I. Kariv, P.J. Marchand, and W.F. Butler, "Microfluidic sorting of mammalian cells by optical force switching", *Nat. Biotech.*, vol. 23, pp. 83–87, 2005.

[8] R.W. Applegate, Jr., J. Squier, T. Vestad, J. Oakey, D.W.M. Matt, P. Bado, M.A. Dugan, and A.A. Said, "Microfluidic sorting system based on optical waveguide integration and diode laser bar trapping", *Lab Chip*, vol. 6, pp. 422–426, 2006.

[9] B. Shao, S. Zlatanovic, M. Ozkan, A.L. Birkbeck, and S.C. Esener, "Manipulation of microspheres and biological cells with multiple agile VCSEL traps", *Sensors and Actuators B*, vol. 113, pp. 866–874, 2006.

[10] A.L. Birkbeck, R.A. Flynn, M. Ozkan, D. Song, M. Gross, and S.C. Esener, "VCSEL array as micromanipulators in chip-based biosystems", *Biomed. Microdevices*, vol. 5, pp. 47–54, 2003.

[11] Y. Ogura, T. Beppu, F. Sumiyama, and J. Tanida, "Toward photonic DNA computing: developing optical techniques for parallel manipulation of DNA", in *Photonics for Space Environments X*, E.W. Taylor (Ed.), Proc. SPIE 5897, pp. 34–43, 2005.

[12] D. Sands, *Diode Lasers*. London: Institute of Physics Publishing, 2005.

[13] A. Ashkin, "History of optical trapping and manipulation of small-neutral particles, atoms, and molecules", *IEEE J. Select. Topics Quantum Electron.*, vol. 6, pp. 841–856, 2000.

[14] A. Rohrbach, "Switching and measuring a force of 25 femtonewtons with an optical trap", *Optics Express*, vol. 13, pp. 9695–9701, 2005.

[15] A. Ashkin, "Acceleration and trapping of particles by radiation pressure", *Phys. Rev. Lett.*, vol. 24, pp. 156–159, 1970.

[16] A.D. May, E.G. Rawson, and E.H. Hara, "Propulsion and angular stabilization of dust particles in a laser cavity. II", *J. Appl. Phys.*, vol. 38, pp. 5290–5292, 1967.

[17] A. Ashkin, J.M. Dziedzic, J.E. Bjorkholm, and S. Chu, "Observation of a single-beam gradient force optical trap for dielectric particles", *Opt. Lett.*, vol. 11, pp. 288–290, 1986.

[18] A. Ashkin, J.M. Dziedzic, and T. Yamane, "Optical trapping and manipulation of single cells using infrared laser beams", *Nature*, vol. 330, pp. 769–771, 1987.

[19] J.P. Gordon, "Radiation forces and momenta in dielectric media", *Phys. Rev. A*, vol. 8, pp. 14–21, 1973.

[20] K.C. Neuman and S.M. Block, "Optical trapping", *Rev. Sci. Instrum.*, vol. 75, pp. 2787–2809, 2004.

[21] P.N. Prasad, *Introduction to Biophotonics*. Hoboken: John Wiley and Sons, 2003.

[22] A. Ashkin, "Forces of a single-beam gradient laser trap on a dielectric sphere in the ray optics regime", *Biophys. J.*, vol. 61, pp. 569–582, 1992.

[23] K. Henkel, *Die Mikrofibel*. Dachau: Mikrobiologische Vereinigung München e. V., 2003.

[24] G. Göke, *Moderne Methoden der Lichtmikroskopie*. Stuttgart: Franckh´sche Verlagshandlung, 1988.

[25] D. McGloin, V. Garces-Chavez, and K. Dholakia, "Touchless tweezing", *SPIE's oemagazine*, pp. 42–44, Jan. 2003.

[26] D. McGloin and K. Dholakia, "Bessel beams: diffraction in a new light", *Contemporary Physics*, vol. 46, pp. 15–28, 2005.

[27] V.R. Daria, P.J. Rodrigo, and J. Glückstad, "Dynamic array of dark optical traps", *Appl. Phys. Lett.*, vol. 84, pp. 323–325, 2004.

[28] P.J. Rodrigo, V.R. Daria, and J. Glückstad, "Real-time three-dimensional optical micromanipulation of multiple particles and living cells", *Opt. Lett.*, vol. 29, pp. 2270–2272, 2004.

[29] Y. Tanaka, A. Murakami, Y. Kinouchi, and H. Misawa, "On-demand micro droplets manipulation system using laser trapping", *Electron. Lett.*, vol. 39, pp. 1023–1024, 2003.

[30] K. Visscher, S.P. Gross, and S.M. Block, "Construction of multiple-beam optical traps with nanometer-resolution position sensing", *IEEE J. Select. Topics Quantum Electron.*, vol. 2, pp. 1066–1076, 1996.

[31] E. Dufresne and D.G. Grier, "Optical tweezer arrays and optical substrates created with diffractive optics", *Rev. Sci. Instrum.*, vol. 69, pp. 1974–1977, 1998.

[32] M. Reicherter, T. Haist, E.U. Wagemann, and H.J. Tiziani, "Optical particle trapping with computer-generated holograms written on a liquid-crystal display", *Opt. Lett.*, vol. 24, pp. 608–610, 1999.

[33] J.E. Curtis, B.A. Koss, and D.G. Grier, "Dynamic holographic optical tweezers", *Optics Communications*, vol. 207, pp. 169–175, 2002.

[34] S.H. Tao, X.-C. Yuan, and B.S. Ahluwalia, "The generation of an array of non-diffracting beams by a single composite computer generated hologram", *J. Opt. A: Pure Appl. Opt.*, vol. 7, pp. 40–46, 2005.

[35] P.A. Prentice, M.P. MacDonald, T.G. Frank, A. Cuschieri, G.C. Spalding, W. Sibbett, P.A. Campbell, and K. Dholakia, "Manipulation and filtration of low index particles with holographic Laguerre-Gaussian optical trap arrays", *Optics Express*, vol. 12, pp. 593–600, 2004.

[36] P.J. Rodrigo, V.R. Daria, and J. Glückstad, "Real-time interactive optical micromanipulation of a mixture of high- and low-index particles", *Optics Express*, vol. 12, pp. 1417–1425, 2004.

[37] J. Glückstad, P.J. Rodrigo, and I. P.-Nielsen, "GPC-driven optical micro-manipulation", in *Optical Trapping and Optical Micromanipulation II*, K. Dholakia, G.C. Spalding (Eds.), Proc. SPIE 5930, pp. 59300Z-1–8, 2005.

[38] P.J. Rodrigo, I.R. Perch-Nielsen, C.A. Alonzo, and J. Glückstad, "GPC-based optical micromanipulation in 3D real-time using a single spatial light modulator", *Optics Express*, vol. 14, pp. 13107–13112, 2006.

[39] J. Plewa, E. Tanner, D.M. Mueth, and D.G. Grier, "Processing carbon nanotubes with holographic optical tweezers", *Optics Express*, vol. 12, pp. 1978–1981, 2004.

[40] G. Whyte, G. Gibson, J. Leach, and M. Padgett, "An optical trapped microhand for manipulating micron-sized objects", *Optics Express*, vol. 14, pp. 12497–12502, 2006.

[41] K. Ladavac, K. Kasza, and D.G. Grier, "Sorting mesoscopic objects with periodic potential landscapes: optical fractionation", *Phys. Rev. E*, vol. 70, pp. 010901-1–4, 2004.

[42] K. Svoboda and S.M. Block, "Biological applications of optical forces", *Annu. Rev. Biophys. Biomol. Struct.*, vol. 23, pp. 247–285, 1994.

[43] A.D. Lucio, R.A.S. Santos, and O.N. Mesquita, "Measurements and modeling of water transport and osmoregulation in a single kidney cell using optical tweezers and videomicroscopy", *Phys. Rev. E*, vol. 68, pp. 041906-1–6, 2003.

[44] X. Wei, B.J. Tromberg, and M.D. Cahalan, "Mapping the sensitivity of T cells with an optical trap: polarity and minimal number of receptors for Ca^{2+} signaling", *Proc. Natl. Acad. Sci. USA*, vol. 96, pp. 8471–8476, 1999.

[45] P.R.T. Jess, V. Garcés-Chávez, D. Smith, M. Mazilu, L. Paterson, A. Riches, C.S. Herringtion, W. Sibbett, and K. Dholakia, "Dual beam fibre trap for Raman microspectroscopy of single cells", *Optics Express*, vol. 14, pp. 5779–5791, 2006.

[46] J. Guck, R. Ananthakrishnan, H. Mahmood, T.J. Moon, C.C. Cunningham, and J. Käs, "The optical stretcher: a novel tool to micromanipulate cells", *Biophys. J.*, vol. 81, pp. 767–784, 2001.

[47] J.M. Nascimento, E.L. Botvinick, L.Z. Shi, B. Durrant, M.W. Berns, "Analysis of sperm motility using optical tweezers", *J. Biomed. Optics*, vol. 11, pp. 044001-1–8, 2006.

[48] D. Wiedenmann, M. Grabherr, R. Jäger, and R. King, "High volume production of single-mode VCSELs", in *Vertical-Cavity Surface-Emitting Lasers X*, C. Lei, K.D. Choquette (Eds.), Proc. SPIE 6132, pp. 613202-1–12, 2006.

[49] S. Knappe, V. Shah, P.D.D. Schwindt, L. Hollberg, J. Kitching, L.-A. Liew, and J. Moreland, "A microfabricated atomic clock", *Appl. Phys. Lett.*, vol. 85, pp. 1460–1462, 2004.

[50] E. Thrush, O. Levi, K. Wang, M.A. Wistey, J.S. Harris Jr., and S.J. Smith, "Integrated semiconductor fluorescent detection system for biochip and biomedical applications", in *Biomedical Nanotechnology Architectures and Applications*, D.J. Bornhop, et al. (Eds.), Proc. SPIE 4626, pp. 289–297, 2002.

[51] R. Michalzik, *Modellierung und Design von Laserdioden mit Vertikalresonator*. Ph.D. thesis, Ulm University, Ulm, Germany, 1996.

[52] R. Michalzik and K.J. Ebeling, "Operating Principles of VCSELs", Chap. 3 in *Vertical-Cavity Surface-Emitting Laser Devices*, H. Li and K. Iga (Eds.), pp. 53–98. Berlin: Springer-Verlag, 2003.

[53] F. Rinaldi, *MBE Growth and Characterization of Multilayer Structures for Vertically Emitting Laser Devices*. Ph.D. thesis, Ulm University, Ulm, Germany, 2009.

[54] M. Miller, M. Grabherr, R. King, R. Jäger, R. Michalzik, and K.J. Ebeling, "Improved output performance of high-power VCSELs", *IEEE J. Select. Topics Quantum Electron.*, vol. 7, pp. 210–216, 2001.

[55] M. Grabherr, *Oberflächenemittierende Leistungsdiodenlaser mit Vertikalresonator*. Ph.D. thesis, Ulm University, Ulm, Germany, 2000.

[56] K. Faltin, *Untersuchungen zur Nahfeldverteilung von Transversalmoden in Laserdioden mit Vertikalresonator*. Ph.D. thesis, Ulm University, Ulm, Germany, 1999.

[57] H.J. Unold, S.W.Z. Mahmoud, R. Jäger, M. Golling, M. Kicherer, F. Mederer, M.C. Riedl, T. Knödl, M. Miller, R. Michalzik, and K.J. Ebeling, "Single-mode VCSELs", in *Vertical-Cavity Surface-Emitting Lasers VI*, C. Lei, S.P. Kilcoyne (Eds.), Proc. SPIE 4649, pp. 218–229, 2002.

[58] D. Zhou and L.J. Mawst, "High-power single-mode antiresonant reflecting optical waveguide-type vertical-cavity surface-emitting lasers", *IEEE J. Quantum Electron.*, vol. 38, pp. 1599–1606, 2002.

[59] A. Furukawa, S. Sasaki, M. Hoshi, A. Matsuzono, K. Moritoh, and T. Baba, "High-power single-mode vertical-cavity surface-emitting lasers with triangular holey structure", *Appl. Phys. Lett.*, vol. 85, pp. 5161–5163, 2004.

[60] I. Kardosh, F. Demaria, F. Rinaldi, S. Menzel, and R. Michalzik, "High-power single transverse mode vertical-cavity surface-emitting lasers with monolithically integrated curved dielectric mirrors", *IEEE Photon. Technol. Lett.*, vol. 20 , pp. 2084–2086, 2008.

[61] Å. Haglund, J.S. Gustavsson, J. Vukusic, P. Modh A. Larsson, "Single fundamental mode output power exceeding 6 mW from VCSELs with a shallow surface relief", *IEEE Photon. Technol. Lett.*, vol. 16, pp. 368–370, 2004.

[62] A. Kroner, F. Rinaldi, J.M. Ostermann, and R. Michalzik, "High-performance single fundamental mode AlGaAs VCSELs with mode-selective mirror reflectivities", *Optics Communications*, vol. 270, pp. 310–313, 2007.

[63] R.A. Flynn, M. Birkbeck, M. Gross, M. Ozkan, B. Shao, M.M. Wang, and S.C. Esener, "Parallel transport of biological cells using individually addressable VCSEL arrays as optical tweezers", *Sensors and Actuators B*, vol. 87, pp. 239–243, 2002.

[64] Y. Ogura, K. Kagawa, and J. Tanida, "Optical manipulation of microscopic objects by means of vertical-cavity surface-emitting laser array sources", *Appl. Optics*, vol. 40, pp. 5430–5435, 2001.

[65] Y. Ogura, K. Watanabe, and J. Tanida, "Parallel translation of microscopic objects in three-dimensional traps by sequential change of emitting vertical-cavity surface-emitting lasers", *Jap. J. Appl. Phys.*, vol. 45, pp. 2603–2605, 2006.

[66] F. Sumiyama, Y. Ogura, and J. Tanida, "Stacking and translation of microscopic particles by means of 2×2 beams emitted from a vertical-cavity surface-emitting laser array", *Appl. Phys. Lett.*, vol. 82, pp. 2969–2971, 2003.

[67] Y. Ogura, F. Sumiyama, T. Kawakami, and J. Tanida, "Manipulation of DNA molecules using optical techniques for optically assisted DNA computing", in *Nano-engineering: Fabrication, Properties, Optics and Devices*, E.A. Dobisz, L.A. Eldada (Eds.), Proc. SPIE 5515, pp. 100–108, 2004.

[68] B. Shao, S. Zlatanovic, and S.C. Esener, "Microscope-integrated micromanipulator based on multiple VCSEL traps", in *Optical Trapping and Optical Micromanipulation*, K. Dholakia, G.C. Spalding (Eds.), Proc. SPIE 5514, pp. 62–72, 2004.

[69] S. Guha, F. Agahi, B. Pezeshki, J.A. Kash, D.W. Kisker, and N.A. Bojarczuk, "Microstructure of AlGaAs-oxide heterolayers formed by wet oxidation", *Appl. Phys. Lett.*, vol. 68, pp. 906–908, 1996.

[70] K.D. Choquette, K.M. Geib, H.C. Chui, B.E. Hammons, H.Q. Hou, T.J. Drummond, and R. Hull, "Selective oxidation of buried AlGaAs versus AlAs layers", *Appl. Phys. Lett*, vol. 69, pp. 1385–1387, 1996.

[71] M. Ochiai, G.E. Giudice, H. Temkin, J.W. Scott, and T.M. Cockerill, "Kinetics of thermal oxidation of AlAs in water vapor", *Appl. Phys. Lett.*, vol. 68, pp. 1898–1900, 1996.

[72] C.I.H. Ashby, M.M. Bridges, A.A. Allermann, B.E. Hammons, and H.Q. Hou, "Origin of the time dependence of wet oxidation of AlGaAs", *Appl. Phys. Lett.*, vol. 75, pp. 73–75, 1999.

[73] H.P. Le, "Progress and trends in ink-jet printing technology", *Journal of Imaging Science and Technology*, vol. 42, pp. 49–62, 1998.

[74] S. Steven, *Fundamentals of BioMEMS and Medical Microdevices*. Bellingham: SPIE Press, 2006.

[75] H. Stöker, *Taschenbuch der Physik*. Frankfurt am Main: Verlag Harri Deutsch, 1998.

[76] V. Lien, K. Zhao, Y. Berderdichevsky, and Y.-H. Lo, "High-sensitivity cytometric detection using fluidic-photonic integrated circuits with array waveguides", *IEEE J. Select. Topics Quantum Electron.*, vol. 11, pp. 827–834, 2005.

[77] H.M. Shapiro, *Practical Flow Cytometry*. New York: Wiley-Liss, 2003.

[78] A.Y. Fu, H.-P. Chou, C. Spence, F.H. Arnold, and S.R. Quake, "An integrated microfabricated cell sorter", *Anal. Chem.*, vol. 74, pp. 2451–2457, 2002.

[79] L.R. Huang, E.C. Cox, R.H. Austin, and J.C. Sturm, "Continuous particle separation through deterministic lateral displacement", *Science*, vol. 304, pp. 987–990, 2004.

[80] P.S. Dittrich and P. Schwille, "An integrated microfluidic system for reaction, high-sensitivity detection, and sorting of fluorescent cells and particles", *Anal. Chem.*, vol. 75, pp. 5767–5774, 2003.

[81] S. Fiedler, S.G. Shirley, T. Schnelle, and G. Fuhr, "Dielectrophoretic sorting of particles and cells in a microsystem", *Anal. Chem.*, vol. 70, pp. 1909–1915, 1998.

[82] P.C.H. Li and D.J. Harrison, "Transport, manipulation, and reaction of biological cells on-chip using electrokinetic effects", *Anal. Chem.*, vol. 69, pp. 1564–1568, 1997.

[83] M. Ozkan, M. Wang, C. Ozkan, R. Flynn, A. Birkbeck, and S. Esener, "Optical manipulation of objects and biological cells in microfluidic devices", *Biomed. Microdevices*, vol. 5, pp. 61–67, 2003.

[84] M.P. MacDonald, G.C. Spalding, and K. Dholakia, "Microfluidic sorting in an optical lattice", *Nature*, vol. 426, pp. 421–424, 2003.

[85] K. Dholakia, W.M. Lee, L. Paterson, M.P. MacDonald, R. McDonald, I. Andreev, P. Mthunzi, C.T.A. Brown, R.F. Marchington, and A.C. Riches, "Optical separation of cells on potential energy landscapes: enhancement with dielectric tagging", *IEEE J. Select. Topics Quantum Electron.*, vol. 13, pp. 1646–1654, 2007.

[86] W. Mu, Z. Li, L. Luan, P. West, H. Kyriazes, G.C. Spalding, G. Wang, A. Feinerman, and J.B. Ketterson, "Force measurement and optical assisted particle separation in an optical standing wave", in *Optical Trapping and Optical Micromanipulation IV*, K. Dholakia, G.C. Spalding (Eds.), Proc. SPIE 6644, pp. 66440R-1–8, 2007.

[87] F.C. Cheong, C.H. Sow, A.T.S. Wee, P. Shao, A.A. Bettiol, J.A. van Kan, and F. Watt, "Optical travelator: transport and dynamic sorting of colloidal microspheres with an asymmetrical line optical tweezers", *Appl. Phys. B*, vol. 23, pp. 121–125, 2006.

[88] Y.Y. Sun, J. Bu, L.S. Ong, and X.-C. Yuan, "Transport and separation of microspheres with lensless imaging", in *Optical Trapping and Optical Micromanipulation IV*, K. Dholakia, G.C. Spalding (Eds.), Proc. SPIE 6644, pp. 66440S-1–7, 2007.

[89] Y.Y. Sun, L.S. Ong, and X.-C. Yuan, "Composite-microlens-array-enabled microfluidic sorting", *Appl. Phys. Lett.*, vol. 89, pp. 141108-1–3, 2006.

[90] F. Merenda, J. Rohner, J.-M. Fournier, and R.-P. Salathé, "Miniaturized high-NA focusing-mirror multiple optical tweezers", *Optics Express*, vol. 15, pp. 6075–6086, 2007.

[91] R.F. Marchington, M. Mazilu, S. Kuriakose, V. Garcés-Chávez, P.J. Reece, T.F. Krauss, M. Gu, and K. Dholakia, "Optical deflection and sorting of microparticles in a near-field optical geometry", *Optics Express*, vol. 16, pp. 3712–3726, 2008.

[92] C. Jensen-McMullin, H.P. Lee, and E.R. Lyons, "Demonstration of trapping, motion control, sensing and fluorescence detection of polystyrene beads in a multi-fiber optical trap", *Optics Express*, vol. 7, pp. 2634–2642, 2005.

[93] S. Kühn, P. Measor, E.J. Lunt, A.R. Hawkins, and H. Schmidt, "Particle manipulation with integrated optofluidic traps", in Proc. *IEEE/LEOS Summer Topical Meeting on Optofluidics*, pp. 187–188. Acapulco, Mexico, July 2008.

[94] S. McGreehin, K. Dholakia, and F. Krauss, "Monolithic integration of microfluidic channels and semiconductor lasers", *Optics Express*, vol. 14, pp. 7723–7729, 2006.

[95] D.N. Nikogosyan, *Properties of Optical and Laser-Related Materials*. West Sussex: John Wiley and Sons, 1997.

[96] A.J. Wright, T.A. Wood, M.R. Dickinson, H.F. Gleeson, and T. Mullin, "The transverse trapping force of an optical trap: factors affecting its measurement", *J. Mod. Opt.*, vol. 50, pp. 1521–1532, 2003.

[97] A.E. Siegman, "Defining the effective radius of curvature for a nonideal optical beam", *IEEE J. Quantum Electron.*, vol. 27, pp. 1146–1148, 1991.

[98] W. Glaser, *Photonik für Ingenieure*. Berlin: Verlag Technik GmbH, 1997.

[99] P.A. Bélanger, "Beam propagation and the ABCD ray matrices", *Opt. Lett.*, vol. 16, pp. 196–198, 1991.

[100] M. Miller, *Aufbautechnik, Leistungsskalierung und Strahlformung oberflächenemittierender Halbleiterdiodenlaser*. PhD thesis, Ulm University, Ulm, Germany, 2002.

[101] S. Sinzinger and J. Jahns, *Microoptics*. Weinheim: Wiley-VCH, 1999.

[102] I.N. Bronstein, K. A. Semendjajew, G. Musiol, and H. Mühlig, *Taschenbuch der Mathematik* (4th edition). Frankfurt am Main: Verlag Harri Deutsch, 1999.

[103] P. Debernardi, A. Kroner, F. Rinaldi, and R. Michalzik, "Surface relief versus standard VCSELs: a comparison between experimental and hot-cavity model results", *IEEE J. Select. Topics Quantum Electron.*, vol. 15, pp. 828–837, 2009.

[104] J. Ng Lee, C. Park, and G.M. Whitesides, "Solvent compatibility of poly(dimethylsiloxane)-based microfluidic devices", *Anal. Chem.*, vol. 75, pp. 6544–6554, 2003.

[105] M. Born and E. Wolf, *Principles of Optics* (6th edition). Oxford: Pergamon Press, 1989.

Curriculum Vitae

Personal Data

09.10.1978 born in Ulm, Germany

Employment

since 01/10	research engineer, Philips Technologie GmbH U-L-M Photonics, Ulm, Germany
01/09 – 12/09	parental leave
04/04 – 12/08	academic employee, Institute of Optoelectronics, Ulm University
12/03 – 03/04	research assistant, Institute of Optoelectronics, Ulm University

Education

since 04/04	PhD student in electrical engineering at Ulm University
11/03	diploma in electrical engineering
05/03 – 11/03	diploma thesis, Institute of Optoelectronics, Ulm University
06/02 – 08/02	semester thesis, Signals and Systems, Uppsala University, Sweden
10/98 – 11/03	student in electrical engineering at Ulm University
09/89 – 06/98	Bertha-von-Suttner Gymnasium high school in Neu-Ulm, Germany

Scholarships

since 02/01	member of the German National Academic Foundation
01/05 – 12/07	PhD scholarship from the German National Academic Foundation
05/04 – 12/04	PhD scholarship from the Landesgraduiertenförderung of Baden-Württemberg

Ulm, August 2010 Andrea Kroner

Danksagung

Zum Abschluss möchte ich mich bei allen bedanken, die auf sehr unterschiedliche Weise zum Entstehen dieser Arbeit beigetragen haben. Beginnen will ich mit PD. Dr-Ing. Rainer Michalzik, dem ich für die hervorragende Betreuung während der vergangenen sechs Jahre danke. Ich freue mich sehr, dass ich als einer seiner ersten Doktoranden promovieren durfte. Danken möchte ich auch Prof. Pfleiderer für das große Interesse an meiner Arbeit, sowie den weiteren Mitgliedern der Prüfungskommission Prof. Bossert und Prof. Hoffmann. Prof. Ebeling möchte ich dafür danken, dass er mich zu Beginn meiner Zeit am Institut für Optoelektronik als Doktorand angenommen hat.

Besonders wertvoll war die Unterstützung und Zusammenarbeit, die ich im Institut für Optoelektronik erleben durfte. Den Gruppenleitern Prof. Peter Unger, Prof. Ferdinand Scholz und PD. Dr-Ing. Rainer Michalzik und allen Kollegen möchte ich dafür herzlich danken. Einige Ereignisse sind mir dabei in besonderer Erinnerung geblieben. Ich danke Johannes Michael Ostermann dafür, dass er mir die VCSEL-Herstellung beigebracht und mich zu dieser Arbeit motiviert hat. Fernando Rinaldi und Dietmar Wahl für das sehr gute Epimaterial, das die Grundlage der gesamten Arbeit war. Dr.-Ing. Frank Demaria und Dr.-Ing. Steffen Lorch danke ich für weise Ratschläge und den Blick fürs Wesentliche. Dr.-Ing. Philipp Gerlach hat mir Einblicke in die Welt der Bastler gewährt, danke für unendlich hilfreiche Drahtigel. Wolfgang Schwarz möchte ich für die entscheidenden vier Bonddrähte danken und Michael Riedl für den Einsatz an der Oxidationsanlage. Vielen Dank an Ihab Kardosh für die Einführung in den Linsenprozess und die Unterstützung beim Zusammenschreiben. Hendrik Roscher hat das VCSEL Array mit großem Bauteilabstand zur Verfügung gestellt und mich regelmäßig mit Snacks versorgt, vielen Dank dafür. Besonders danken möchte ich Anna Bergmann für ihre große Hilfe, viele Denkanstöße und die nötige Ablenkung, wenn es mal nicht mehr richtig weiter ging.

Ich möchte Dr.-Ing. Jürgen Mähnß für Diskussionen, Ratschläge und einen funktionierenden Reinraum danken. Zusammen mit Rudi Rösch habe ich lange, frustrierende und dann doch erfolgreiche Zeiten an RIE, REM und Flip-Chip Bonder durchlebt, vielen Dank dafür, ohne ihn hätte es nicht geklappt. Susanne Menzel danke ich für die Unterstützung in allen Bereichen und die wirklich entscheidenden Tipps im Reinraum. Ich danke Rainer Blood für das häufige Reparieren des REMs und Josef Theisz für die große Geduld bei kleinen Fitzelarbeiten. Bei Sükran Kilic und Hilde Mack möchte ich mich für Aufmunterungen, Papierkram und fürs Babysitten bedanken. Danke an Dr.-Ing. Peter Brückner für Sushi, Frank Lipski für Fußball und alle anderen für die wirklich schöne Zeit.

Bedanken möchte ich mich auch bei allen Studenten, mit denen ich in den vergangenen Jahren zusammenarbeiten durfte, vor allem bei Johanna May, Carolin Schneck und Anna Bergmann. Mit ihren Diplomarbeiten haben sie einen wichtigen Beitrag geleistet, allen dreien danke ich vielmals für ihren großen Einsatz.

Institutsübergreifend möchte ich mich bei den Mitarbeitern des Instituts für Elektronische Bauelemente und Schaltungen (EBS) für die Hilfe bei Belichter und Sputteranlage bedanken. Yakiv Men vom EBS und Klaus Mammel vom Mikroelektronik Technikum danke ich für die Maskenherstellung für die mikrofluidischen Kanäle. Robert Rieger vom Institut für Biophysik gab mir zu Beginn meiner Arbeit eine Einführung und wichtige Tipps zur Herstellung mikrofluidischer Chips, vielen Dank dafür. My special thanks go to Pierluigi Debernardi from Politecnico di Torino, who gave me new insights in the mysterious insides of the VCSEL.

Diese Arbeit wäre nicht möglich gewesen ohne die nötige finanzielle Unterstützung. Dafür möchte ich der Landesgraduiertenförderung Baden-Württemberg, der Studienstiftung des deutschen Volkes und der deutschen Forschungsgemeinschaft danken.

Großer Dank gilt meiner Familie und allen anderen, die immer daran geglaubt haben, dass diese Arbeit irgendwann noch fertig wird. Das ständige Nachbohren war nervig aber hilfreich. Den schwersten Part an dieser Arbeit hatte allerdings mein Partner Andi. Vielen Dank fürs Aushalten, Durchhalten, Aufbauen und den etwas anderen Blickwinkel auf die Dinge.

Hanna danke ich dafür, dass sie so wunderbar ist und dafür, dass diese Arbeit nicht noch ein Jahr länger gedauert hat.